Exploring the inhibitory potential of South African natural compounds against *Mycobacterium tuberculosis* fatty acyl-AMP ligase

by

Mbali Matshoba

209514331

A dissertation submitted in fulfillment of the academic requirements for the degree of

Master of Medical Science

College of Health Sciences

School of Laboratory Medicine & Medical Sciences

Department of Medical Biochemistry

University of KwaZulu-Natal, Durban 4000, South Africa

2025

Exploring the inhibitory potential of South African natural compounds against *Mycobacterium tuberculosis* fatty acyl-AMP ligase.

by

Mbali Matshoba

209514331

A dissertation submitted in fulfillment of the academic requirements for the degree of

Master of Medical Science

2025

This is the thesis in which the chapters are written as a set of discrete research publications, with an overall introduction and final summary. Typically, these chapters will have been published in internationally recognized, peer-reviewed journals.

This is to certify that the contents of this thesis are the original research work of Miss **Mbali Matshoba.**

Supervisor:

As the candidate's supervisor, I have approved this thesis/dissertation for submission.

Name: **Dr Ndumiso N. Mhlongo** Signature: [redacted] Date: 07/04/2026

PREFACE

This thesis is divided into five chapters, and they are outlined as follows:

- **Chapter 1 (Introduction)**

This chapter offers an overview and contextual information regarding the research, including its aims, objectives, hypothesis, and research questions.

- **Chapter 2 (Literature review)**

This chapter provides a comprehensive foundation of previous research on TB, a detailed understanding of FadD23's role in TB pathogenesis, the therapeutic potential of natural compounds, and the application of *in silico* methods for drug discovery.

- **Chapter 3 (Methodology)**

This chapter describes the research design by providing an in-depth understanding of the principles behind the methods, procedures, and techniques used to conduct the study.

- **Chapter 4 (Manuscript)**

This chapter is entitled Exploring the inhibitory potential of South African natural compounds against *Mycobacterium tuberculosis* fatty acyl-AMP ligase

.

.

- **Chapter 5 (Conclusion and future work)**

This chapter summarizes the key findings of the research while providing insight into how the findings can be used in the context of future studies and drug development.

DECLARATION I – PLAGIARISM

I, **Mbali Matshoba**, declare that

1. The research reported in this thesis, except where otherwise indicated, is my original research.

2. This thesis has not been submitted for any degree or examination at any other university.

3. This thesis does not contain other persons data, pictures, graphs or other information, unless specifically acknowledged as being sourced from other persons.

4. This thesis does not contain other persons writing unless specifically acknowledged as being sourced from other researchers. Where other written sources have been quoted, then:

   a. Their words have been rewritten, but the general information attributed to them has been referenced.
   b. Where their exact words have been used, then their writing has been placed in italics and inside quotation marks and referenced.

5. This thesis does not contain text, graphics, or tables copied and pasted from the internet, unless specifically acknowledged, and the source being detailed in the thesis and in the reference sections.

A detailed contribution to publications that form part or/and include research presented in this thesis is stated (include publications submitted, accepted, in press and published).

6. Author Contributions were as follows:

- Miss Mbali Matshoba: Manuscript writing and data analysis, conducted MD simulations and trajectory analysis calculations.
- Dr Ndumiso N. Mhlongo.: Supervisor, manuscript proofreading, assisted with MD calculations.

- Miss Mbali Matshoba Signature: [redacted] Date: 07/04/2026
- Dr Ndumiso N. Mhlongo Signature [redacted] Date: 07/04/2026

ACKNOWLEDGMENTS

I want to express my heartfelt gratitude to my supervisor, Dr. Ndumiso N. Mhlongo, for his invaluable expertise, guidance, and encouragement throughout this project. I am deeply thankful to my wonderful family for their unwavering support, and I also wish to acknowledge God and my amazing ancestors for their protection and guidance.

LIST OF ABBREVIATIONS

Abbreviations	Full Name
α	Alpha
β	Beta
Å	Angstrom
°	Degree
µm	micrometer
%	Percentage
γ	Gamma
3D	Three-Dimensional
23S rRNA	23S Ribosomal RNA
ADMET	Absorption, Distribution, Metabolism, Excretion, and Toxicity
AG	Arabinogalactan
AIDS	Acquired immunodeficiency syndrome
AMP-PNP	Adenylyl-imidodiphosphate
ANP	Phosphoaminophosphonic acid-adenylate ester
Anti-TB	Anti-Tuberculosis
ATP	Adenosine triphosphate
BDLLfxC	bedaquiline (B), delamanid (D), linezolid (L), levofloxacin (Lfx), and clofazimine (C)
BDQ	Bedaquiline
BEAT	Building Evidence for Advancing New Treatment for Tuberculosis
BFGS	Broyden Fletcher Goldfarb Shanno
BLMZ	bedaquiline, linezolid, moxifloxacin, and Pyrazinamide
BPaL	bedaquiline, pretomanid and linezolid
BPaLM	bedaquiline, pretomanid, linezolid and moxifloxacin
CDC	Centers for Disease Control and Prevention
Chp1	Calcineurin homologous protein 1
COVID-19	Coronavirus disease
CRISPR	Clustered regularly interspaced short palindromic repeats
CTL	Cytotoxic T lymphocytes
Ddn	deazaflavin (F420)-dependent nitroreductase
DNA	Deoxyribonucleic acid
DPA	Decaprenyl-phosphoryl-β-D-arabinose
DprE	Decaprenylphosphoryl-D-ribose 20-epimerase
DR-TB	Drug-resistant tuberculosis

E	Ethambutol
Emb	Ethambutol resistance gene
EMBL-EBI	European Bioinformatics Institute
F420	Fluorescent coenzyme with peak emission at 420 nm
FAAL	Fatty Acyl-AMP Ligase
Fab	fatty acid biosynthesis gene
FACL	Fatty Acyl-CoA Ligase
FAS	Fatty Acid Synthase
FDA	Food and Drug Administration
Fq	Fluoroquinolones
GI	Gastrointestinal
GlfT	Galactofuranosyltransferase
GUI	Graphical User Interface
Had	Hydroxyacyl-ACP dehydratase
HIV	Human Immunodeficiency Virus
IL	Interleukin
INF-γ	Interferon gamma
Inh /H	Isoniazid
KatG	Catalase-peroxidase
LAM	Lipoarabinomannan
LTBI	Latent TB infection
M. tuberculosis	Mycobacterium Tuberculosis
MDR-TB	Multidrug-Resistant tuberculosis
MGIT 960	Mycobacteria Growth Indicator Tube 960
MIC	Minimal inhibitory concentrations
MM-PBSA/MM-GBSA	Mechanics Poisson–Boltzmann Surface Area / Molecular Mechanics Generalized Born Surface Area
MMCoA	Methylmalonyl-CoA
MmpL	Mycobacterial membrane protein large.
Mur	UDP-N-acetylmuramate
NAD	Nicotinamide adenine dinucleotide
NagA	N-acetylglucosamine-6-phosphate deacetylase

PAIN	Pan-Assay Interference
PAMPs	pathogen-associated molecular patterns
PapA	Polyketide-associated protein A
PBPs	Penicillin-binding proteins
PDB	Protein Data Bank
PDIM	Phthiocerol Dimycocerosate
PG	Peptidoglycan
PhU-AMS	5'-O-[N-(11-phenoxyundecanoyl) sulfamoyl] adenosine
PI3P	phosphatidylinositol 3-phosphate
PKS	Polyketide Synthase
PLM	Palmitic
P-loop	Phosphate-binding loop
POA	Pyrazinoic acid
PonA1 /PonA2	Penicillin-binding protein A1/Penicillin-binding protein A2
PZA /Z	Pyrazinamide
R	Rifampicin/rifampin
RAVs	Resistance-associated variants
RNAP	RNA polymerase
ROS	Reactive Oxygen Species
RpsA	ribosomal protein S1
RR-TB	Rifampicin-resistant tuberculosis
SANCDB	South African Natural Compounds Database
SL-1	Sulfolipid-1
SMILES	Simplified Molecular Input Line Entry System
Th	T-helper
TLR	Toll-like receptor
T2S	trehalose-2-sulfate
Tb	Tuberculosis
TDM	Trehalose dimycolate
TM-score	Template modeling score
TMM	Trehalose monomycolate

TPSA	Topological Polar Surface Area
VMD	Visual molecular dynamics
WHO	World Health Organization
XDR-TB	Extensively Drug-Resistant TB

LIST OF FIGURES

LIST OF TABLES

ABSTRACT

Background: Tuberculosis is one of the leading infectious diseases causing mortality worldwide. Factors such as the increasing prevalence of drug-resistant strains and toxicity profiles of current drugs have made it nearly impossible to eradicate TB. This calls for urgent discovery and development of potent and safe tuberculosis drug candidates with a novel mechanism of action. Usage of natural compounds and their derivatives is being prioritized for drug development owing to their accessibility, potency, and safety profiles.

Aim: To identify natural inhibitors of *M. tuberculosis* FadD23 and characterize their potential mechanism of inhibition.

Methodology: A crystal structure of FaD23 (PDB ID 8hdf) with a resolution of 2.2 Å was obtained from RCSB Protein Data Bank. Virtual screening of seven antitubercular compounds from the South African Natural Compounds Database (SANCDB), namely SANC00937, SANC00520, SANC00522, SANC00519, SANC00834, SANC01098, and SANC01097, was performed using molecular docking principles to identify potential inhibitors of FadD23. FadD23-docked compounds underwent 130 ns molecular dynamics (MD) simulation using Amber18 software package. MD trajectories from simulations were used to calculate MM/GBSA binding free energy to determine binding affinities of compounds to FadD23. Various metrics, including root mean square deviation (RMSD), root mean square fluctuation (RMSF), radius of gyration (Rg), hydrogen bonding, and secondary structure elements, were used to characterise conformational dynamics between FadD23-ligand complexes under simulated physiological conditions. The safety profile of the simulated compounds was also evaluated using the SwissADME and ProTox 3.0 servers.

Results: The docking results identified compound SANC00937, a flavonoid, as a top candidate that effectively binds at the ATP-binding site of FadD23 with the highest docking score of -8.4 kcal/mol, stabilized by hydrophobic and hydrogen-bond interactions. To achieve accuracy of docking results, all docked compounds were subjected to 130 ns MD simulations to further characterize their interaction with the protein. MM/GBSA calculations revealed SANC01098 to have the highest binding affinity of -28.86 kcal/mol to the protein with reference to ANP. However, SANC01098 resided adjacent to the ATP binding site. SANC00937 showed a second highest binding affinity of -27.83 kcal/mol with reference to ANP, and interacted with key ATP-binding site residues Ala328, Asp222, Gly330, and Ser300 which significantly contributed to a stronger binding affinity and a more stable interaction with FadD23. All complexes exhibited RMSd values below 2 Å highlighting stable association of ligands with the protein. However, the average Rg and RMSd values indicated that SANC01098 forms a more stable association with FadD23 than ANP, suggesting a possibility of competitive binding between SANC00937 and ATP. The secondary structure analysis revealed that SANC00937 deforms the Pi structural component of FadD23, optimizing its binding affinity within the binding site. This was also supported by large hydrophobic interactions and few hydrogen bonds that stabilized FadD23-

SANC00937 complex. Pharmacokinetic evaluation showed that SANC01097 exhibits optimal oral drug-like properties, characterized by a high bioavailability score, minimal interference with major Cytochrome P-450 enzymes.

Conclusion: This study has identified SANC00937 as a potential ligand to interfere with FadD23 function by competing and displacing ATP in the active site. This opens an interest in experimental evaluation of this natural compound for drug-like properties against FadD23. A positive outcome of such evaluation could potentially lead to the development of novel, alternative and naturally safe TB therapeutics that are accessible in abundance to Africans. In absence of an approved FadD23 inhibitors, these results provide a lead baseline for further laboratory-based experiments to confirm the biological relevance of both SANC00937 and SANC01098 compounds as potential inhibitors of FadD23.

Keywords: Tuberculosis, FadD23 inhibition, SANCDB, molecular docking, MD simulations, *M. tuberculosis* FadD23, drug discovery.

Table of Contents

1. Chapter One

Introduction

1.1. Background and rationale of this study

Tuberculosis (TB) is one of the most deadly, highly contagious, yet preventable and typically curable airborne infectious diseases in the world [1, 2], caused by the highly complex and adaptable pathogen *Mycobacterium tuberculosis* (*M. tuberculosis*) [3]. With an estimated 10.8 million infections and 1.25 million deaths reported in 2023, TB overtook COVID-19 as the leading infectious disease killer worldwide [2]. This infectious disease is the most significant opportunistic killer among people living with HIV and a major contributor to antimicrobial resistance-related deaths [2]. Treatment options include a combination of first-line antibiotics that target various physiological components of the bacterium.

The World Health Organisation (WHO) currently recommends a 6-month course of treatment that includes pyrazinamide, isoniazid, rifampicin, and ethambutol for drug-susceptible TB (pulmonary and extrapulmonary) [2]. All four drugs are administered together for the first two months, after which isoniazid and rifampicin are administered separately for the remaining four months [2]. Because these drugs target essential bacterial functions, improper use, stopping treatment, or noncompliance can reduce their effectiveness, leading to drug resistance and, in some cases, fatal outcomes. Drug-resistant TB (DR-TB) is still a threat to public health, in 2023 an estimated 400,000 cases of multidrug-resistant [4] TB (MDR-TB) or rifampicin-resistant TB (RR-TB) were reported worldwide [2].

With resistance levels ranging from specific drug resistance to resistance against multiple drug classes, such as rifampicin, fluoroquinolones, bedaquiline, or linezolid, the WHO has classified drug-resistant TB into five groups: isoniazid-resistant TB, RR-TB, MDR-TB, pre-extensively drug-resistant TB (pre-XDR-TB), and extensively drug-resistant TB (XDR-TB) [2]. The most recent guidelines for treating drug-resistant TB contain three primary regimen types. The first category includes 6-month all-oral regimens for individuals with MDR/RR-TB (with or without fluoroquinolone resistance) [2]. The second category includes many short, all-oral regimens lasting nine months for individuals with MDR/RR-TB who are not fluoroquinolone-resistant [2]. The third category consists of longer regimens lasting 18–20 months, which may include injectable drugs such as amikacin [2]. Compared to the shorter 6-month regimens, longer regimens are regarded as a last resort [2]. Unfortunately, these treatment options present a serious health risk because of their length and complexity. Patients frequently find it difficult to follow them, which may result in

inadequate care and heightened resistance [5]. Patients often have difficulties coping with the severity of the adverse effects caused by the medication used to treat DR-TB [6]. For many DR-TB patients, the lack of access to critical healthcare treatments leads to worse outcomes [6]. As a result of the high expense of treatment, patients and their families may face severe financial and social difficulties [6]. The ongoing TB crisis is largely driven by these underlying factors. The emergence of MDR and XDR TB strains makes it very challenging to treat and eradicate TB, especially in patients with co-infections such as HIV, diabetes, and other diseases [7]. XDR-TB has evolved into drug-incurable or programmatically incurable TB in certain TB-endemic countries [8]. The rise in DR-TB highlights the pressing need for novel treatment drugs with distinct modes of action to successfully combat *M. tuberculosis* and reduce the incidence of TB globally.

The bacterium's remarkable ability to evade the immune system is largely due to its unique cell wall composition and specialized virulence factors [9]. One such virulent component is sulfolipid-1 (SL-1), a lipid present in the cell wall of *M. tuberculosis* that plays a significant role in mitochondrial oxidative phosphorylation inhibition, preventing phagosome-lysosome fusion within the macrophages, and allowing the bacterium to survive and replicate within the host cell [10].

The fatty acid adenylyl transferase (FadD23) is a key enzyme in the biosynthesis of SL-1 (see Figure 1.1) [10]. It activates long-chain fatty acids by converting them into acyl-adenylates, which are then used as starter units by polyketide synthase 2 (Pks2) to synthesize multiple methyl-branched fatty acids [10]. This activation step is vital for downstream metabolic biosynthetic pathways like phthiocerol dimycocerosate (PDIM) and polyacyltrehaloses (PATs), which are also essential virulence-associated lipids in *M. tuberculosis* [9, 11]. Inhibiting FadD23 will interfere with lipid biosynthesis, weakening the *M. tuberculosis* cell envelope and increasing its susceptibility to immune clearance [9]. This approach presents FadD23 as a promising target for antituberculosis drug development [10]. While synthetic inhibitors of FadD23 have been explored, the potential of natural compounds remains largely under-examined [12].

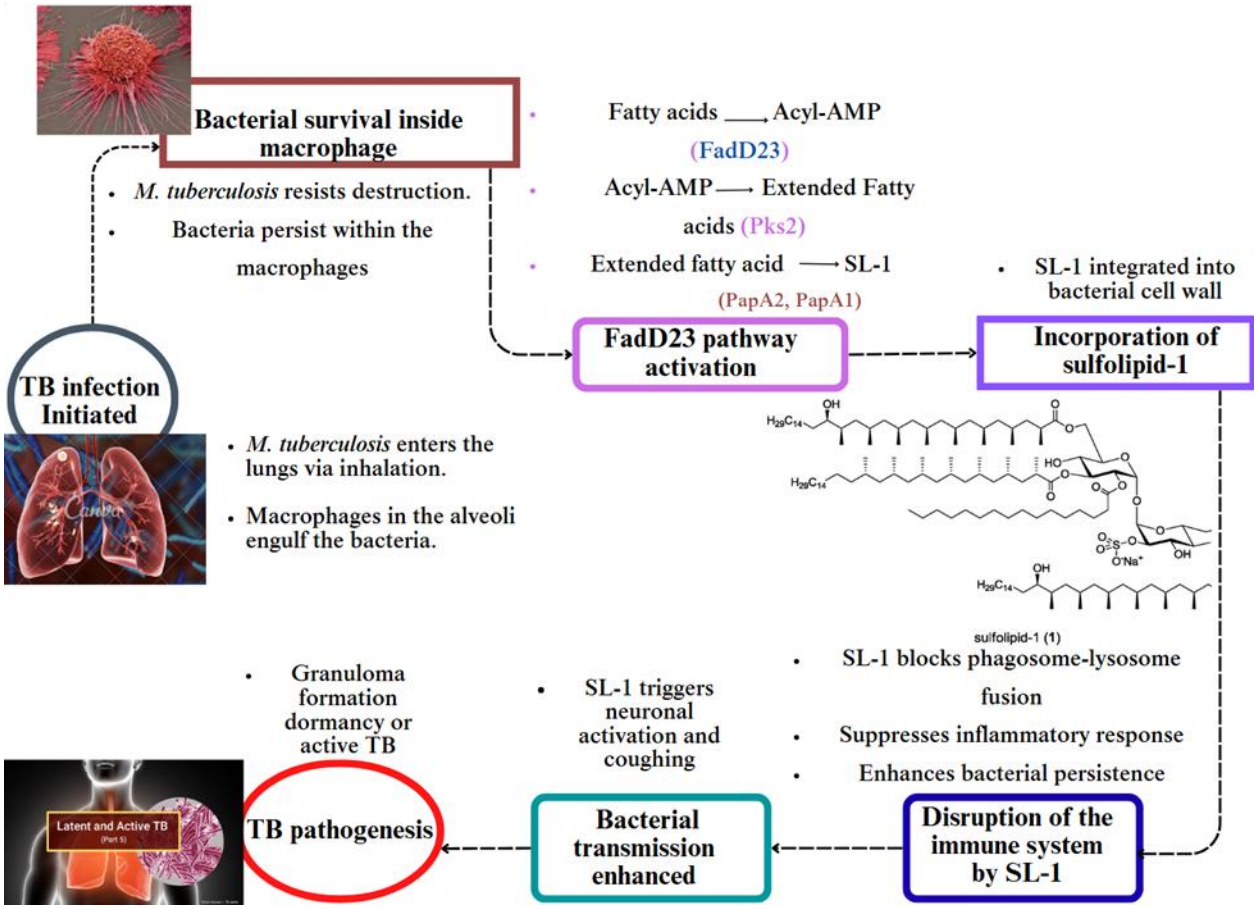

Figure 1.1: The role of FadD23 in the TB pathogenesis: SL-1 biosynthesis and immune evasion. *M. tuberculosis* enters the lungs via inhalation, where infection is initiated and survives inside the macrophage. The bacterium activates the FadD23 pathway to produce SL-1, which blocks phagosome-lysosome fusion, suppresses immune responses, and promotes bacterial persistence, ultimately contributing to the pathogenesis of TB.

In addition to having a variety of chemical structures, natural products often exhibit favorable bioactivity and safety profiles [13]. For centuries, people have depended on natural products with therapeutic properties to treat and prevent infections. Natural products usually have no adverse side effects, unlike conventional antibacterial treatments [14]. Evolutionary processes have endowed them with unique structural complexity, chemical diversity, and biological specificity that is not commonly found in purely synthetic compounds [15].

South Africa, renowned for its rich biodiversity, has a long history of utilizing plant-based remedies for medicinal purposes. The South African Natural Compounds Database (SANCDB; https://sancdb.rubi.ru.ac.za/) is the only comprehensive and fully referenced database of natural chemical compounds derived from South African flora and fauna [15]. This database, with approximately 1,012 compounds, serves as a valuable resource for identifying potential

antimicrobial agents, including anti-TB compounds [15]. Many of these plant extracts and marine-derived compounds have demonstrated antimycobacterial, antibacterial, and anti-TB properties, making them valuable candidates in the search for new therapeutic inhibitors [15].

The process of drug discovery is lengthy, costly, and fraught with difficulties. However, applications of *in silico* techniques, including the use of artificial intelligence, have facilitated this process [16, 17]. Such techniques include virtual screening of compound databases for the identification of specific inhibitors of drug targets, and molecular dynamics simulations to study the thermodynamic properties of molecules [18]. These computational approaches offer efficient strategies for identifying possible drug candidates for experimental validation [18, 19].

In this study, we virtually screened the SANCDB to identify novel inhibitors of *M. tuberculosis* FadD23 in search of drug candidates for the treatment of TB. We further characterized the thermodynamic properties of candidate molecules and their contribution to the inhibitory potential through molecular dynamics calculations. To the extent of our knowledge, there is no existence of approved inhibitor of FadD23, and this study is the first to seek FadD23 inhibitors from this database.

1.2. Problem Statement

DR-TB remains a significant global health issue despite advancements in TB treatment. Current TB regimens like rifampicin, ethambutol, isoniazid, and pyrazinamide are lengthy, often requiring months to years of administration, and frequently linked to severe side effects, leading to treatment interruptions and decreased efficacy [20]. While treatment for drug-resistant TB remains expensive, options like bedaquiline and linezolid have been associated with serious cross-resistance [5, 21] and severe side effects. Furthermore, *M. tuberculosis* possesses a complex lipid metabolism that is essential for its survival, virulence, and drug tolerance. Even though some existing front-line drugs like isoniazid and ethionamide are able to successfully target essential lipid biosynthesis pathways, the bacterium's ability to reprogram its metabolism to utilize host lipids (eg cholesterol) for survival, together with the development of resistance strains (MDR-TB and XDR-TB) calls for urgent identification of antituberculosis agents with long-term novel mechanisms of action [13]. Moreover, agents that can successfully target multiple lipid pathways to shorten treatment and overcome drug resistance.

1.3. Novelty and significance of this study

Despite having international initiatives like the WHO's End TB Initiative [2], factors such as delayed diagnosis, poor treatment plans, structural flaws in healthcare delivery, and drug resistance cripple the efforts of TB eradication. In light of this, there is a demand not only for new diagnostic tools, patient-centred treatment strategies, and a renewed political commitment to ending TB [22], but also, consideration of complementary medicine as an alternative treatment strategy, essentially herbal medicine.

South Africa is rich in a variety of natural resources that are traditionally used as alternative medicine for disease treatment and management. The efficiency of this practice has led to the development of a database (SANCDB) where isolated active ingredients from these medicines are deposited. SANCDB was selected for this study as it is the only fully referenced repository that offers novel natural compounds derived from South Africa's rich biodiversity. This database is smaller, allowing for faster screening. While global databases like Pubchem or Zinc contains large number of compounds that are redundant, synthetic, and already well studied. By exploring the therapeutic potential of these ingredient compounds, we are encouraging their isolation from natural resources, characterization for drug-like properties, and development into safe, readily accessible, and affordable TB therapeutics. This also promotes the preservation of these medicinal resources to prevent their extinction. Fatty acids in *M. tuberculosis* are a major virulence factor in TB pathogenesis [10], as they play a major role in mycobacterial cell defence systems. Furthermore, FadD23 is not present in human metabolic pathways, which allows for selective inhibition with minimal host toxicity. Therefore, targeting these pathways

with natural molecules, given their notable therapeutic properties, presents a novel yet nature-based approach to attenuate TB. With this study, we hope to contribute to addressing socioeconomic barriers that hinder TB eradication and the associated crisis resonating from lack of treatment availability and affordability.

1.4. Research aims and objectives

1.4.1. Aim of the study

To identify novel natural inhibitors of *M. tuberculosis* FadD23 and characterize their inhibitory potential through the application of *in silico* methods.

1.4.2. Objectives

- To virtually screen the SANCDB for the identification of *M. tuberculosis* FadD23 inhibitors.
- To generate FadD23-natural compound complexes to identify the mechanism of binding.
- To perform molecular dynamics simulations to characterize the FadD23-compound interaction.
- To characterize drug-like properties of the candidate compound as a FadD23 potential inhibitor.

1.5. Hypothesis

Compounds from the SANCDB possess inhibitory potential against *M. tuberculosis* FadD23 enzyme, which could potentially impair FadD23 function and consequently mycobacterial virulence.

1.6. Research Questions

1. Which compounds from the SANCDB bind to FadD23 and with what binding mode?

2. Which compounds exhibit the highest inhibitory potential against FadD23?

3. How does the binding affinity of the selected natural compounds compare to that of established reference inhibitors, and what implications does this have for their potential as therapeutic agents?

4. Which structural components of the protein and ligands contribute to the binding affinity of ligands, and how?

5. What drug-like properties does the selected compound possess?

References

1. Koch, R., T.D. Brock, and E.B. Fred, *The Etiology of Tuberculosis.* Reviews of Infectious Diseases, 1982. **4**(6): p. 1270–1274.
2. World Health, O., *Global tuberculosis report 2024*. 2024, Geneva: World Health Organization.
3. Daniel, T.M., *Pioneers of medicine and their impact on tuberculosis*. 2000: University Rochester Press.
4. Yan, F., X. Liu, S. Zhang, Q. Zhang, and J. Chen, *Understanding conformational diversity of heat shock protein 90 (HSP90) and binding features of inhibitors to HSP90 via molecular dynamics simulations.* Chemical Biology & Drug Design, 2019. **95**: p. 87–103.
5. Ismail, N.A., S.V. Omar, L. Joseph, N. Govender, L. Blows, F. Ismail, H. Koornhof, A.W. Dreyer, K. Kaniga, and N. Ndjeka, *Defining Bedaquiline Susceptibility, Resistance, Cross-Resistance and Associated Genetic Determinants: A Retrospective Cohort Study.* EBioMedicine, 2018. **28**: p. 136–142.
6. World Health, O., *Key updates to the treatment of drug-resistant tuberculosis: rapid communication, June 2024*. 2024, World Health Organization: Geneva.
7. Pal, R., M.K. Bisht, and S. Mukhopadhyay, *Secretory proteins of Mycobacterium tuberculosis and their roles in modulation of host immune responses: focus on therapeutic targets.* Febs j, 2022. **289**(14): p. 4146–4171.
8. Heidary, M., M. Shirani, M. Moradi, M. Goudarzi, R. Pouriran, T. Rezaeian, and S. Khoshnood, *Tuberculosis challenges: Resistance, co-infection, diagnosis, and treatment.* Eur J Microbiol Immunol (Bp), 2022. **12**(1): p. 1–17.
9. Trivedi, O.A., P. Arora, A. Vats, M.Z. Ansari, R. Tickoo, V. Sridharan, D. Mohanty, and R.S. Gokhale, *Dissecting the mechanism and assembly of a complex virulence mycobacterial lipid.* Mol Cell, 2005. **17**(5): p. 631–43.
10. Yan, M., L. Cao, L. Zhao, W. Zhou, X. Liu, W. Zhang, and Z. Rao, *The Key Roles of Mycobacterium tuberculosis FadD23 C-terminal Domain in Catalytic Mechanisms.* Frontiers in Microbiology, 2023. **14**.
11. Seeliger, J.C., C.M. Holsclaw, M.W. Schelle, Z. Botyanszki, S.A. Gilmore, S.E. Tully, M. Niederweis, B.F. Cravatt, J.A. Leary, and C.R. Bertozzi, *Elucidation and chemical modulation of sulfolipid-1 biosynthesis in Mycobacterium tuberculosis.* J Biol Chem, 2012. **287**(11): p. 7990–8000.
12. Yan, M., M. Ma, R. Chen, Y. Cao, W. Zhang, and X. Liu, *Structural basis for the development of potential inhibitors targeting FadD23 from Mycobacterium tuberculosis.* Acta Crystallogr F Struct Biol Commun, 2023. **79**(Pt 8): p. 208–216.

13. Sulyman, A.O., J. Fulcher, S. Crossley, A.A. Fatokun, and F.J. Olorunniji, *Shikonin and Juglone Inhibit Mycobacterium tuberculosis Low-Molecular-Weight Protein Tyrosine Phosphatase a (Mt-PTPa).* BioTech, 2023. **12**(3): p. 59.
14. Kedar Pandurangrao Patki , M.M.A.M., Dr. Jameel Ahmed, *Herbal Medicine Used in Treatment of Tuberculosis: A Review.* Ijnrd - International Journal Of Novel Research And Development, 2024. **Volume 9**(Issue 9,): p. e79–e85.
15. Hatherley, R., D. Brown, T. Musyoka, D. Penkler, N. Faya, K. Lobb, and O. Tastan Bishop, *SANCDB: A South African natural compound database.* Journal of cheminformatics, 2015. **7**.
16. Andries, K., P. Verhasselt, J. Guillemont, H.W.H. GöHlmann, J.-M. Neefs, H. Winkler, J. Van Gestel, P. Timmerman, M. Zhu, E. Lee, P. Williams, D. De Chaffoy, E. Huitric, S. Hoffner, E. Cambau, C. Truffot-Pernot, N. Lounis, and V. Jarlier, *A Diarylquinoline Drug Active on the ATP Synthase of Mycobacterium tuberculosis.* Science, 2005. **307**(5707): p. 223–227.
17. Chakraborty, S. and K.Y. Rhee, *Tuberculosis Drug Development: History and Evolution of the Mechanism-Based Paradigm : Figure 1.* Cold Spring Harbor Perspectives in Medicine, 2015. **5**(8): p. a021147.
18. Swain, A., S.S. Senapati, and A. Pan, *In silico screening of natural compounds as potential inhibitors against SecA protein of Acinetobacter baumannii.* Molecular Diversity, 2025.
19. Roney, M. and M.F.F. Mohd Aluwi, *The importance of in-silico studies in drug discovery.* Intelligent Pharmacy, 2024.
20. Capela, R., R. Félix, M. Clariano, D. Nunes, M. Perry, and F. Lopes, *Target Identification in Anti-tuberculosis Drug Discovery*. 2023.
21. Hartkoorn, R.C., S. Uplekar, and S.T. Cole, *Cross-resistance between clofazimine and bedaquiline through upregulation of mmpl5 in mycobacterium tuberculosis.* Antimicrobial Agents and Chemotherapy, 2014. **58**(5): p. 2979–2981.
22. Olivier, C. and L. Luies, *WHO Goals and Beyond: Managing HIV/TB Co-infection in South Africa.* SN Comprehensive Clinical Medicine, 2023. **5**(1).

2. Chapter Two

Literature Review

2.1. Introduction to Tuberculosis

TB is a bacterial infection caused by *M. tuberculosis* [1]. It was formerly known as the "white death" [2] or the "great white plague" [3] in the 17th century, phthisis [4] and consumption [5] from Hippocrates until the 18th century [4], tabes in ancient Roman, and schachepheth in ancient Hebrew [1], or wasting disease [6-9]. Although it can spread to other organs, it usually affects the lungs [10]. When an infected person coughs or sneezes, the virus spreads through airborne droplets, making it extremely contagious [10, 11]. Because of its infectious nature, complex immune response, chronic progression, and the need for extended treatment. TB continues to be a major global health concern, even though it is preventable and treatable [12]. This infectious disease has continuously afflicted humans for thousands of years, with evidence from human isolates of tubercle bacilli found in East Africa [13] and ancient mummies, indicating its long-standing presence in human history [9, 14-16]. In 1834, Dr. Johann Lukas Schonlein formally introduced the term "tuberculosis" for this deadly infectious disease [8].

The bacterial cause of this disease was only discovered in 1882, despite its long-standing presence in human history. An important turning point in the knowledge of this deadly bacterium was reached when the German microbiologist Robert Koch formally announced this discovery on March 24, 1882. [17, 18]. His discovery was later validated by highly effective staining techniques created by Ziehl-Neelsen (1883) [19] and Ehrlich (1887) [19-21]. In addition to providing insight into the causative agent, Koch's discovery shaped our current knowledge of *M. tuberculosis,* its classification, and laid the foundation for modern TB diagnostics and treatment strategies [17].

Because of *M. tuberculosis's* ability to hold onto some dyes even after being washed with acid-alcohol, it is known as an acid-fast bacillus [22]. Koch's bacillus, another name for this mycobacterium, is a member of the family *Mycobacteriaceae*, phylum *Actinobacteria*, order *Mycobacteriales*, and domain Bacteria [23, 24]. Above all, the bacterium's unique and complex structure allows it to thrive in diverse environments, both inside and outside the human host [25, 26]. *M. tuberculosis* is an extremely aerobic organism, hence it requires high levels of oxygen for survival [24]. Compared to other bacterial infections, this mycobacterium grows slowly under ideal conditions, doubling every 12 to 24 hours, which slows the progression of the disease [27]. *M. tuberculosis* appears to have a rod-shaped morphology (A) when viewed under a light microscope, usually measuring between 0.2 and 0.6 μm in diameter and 1 to 10 μm in length (B) (Figure 2.1) [20]. Furthermore, *M. tuberculosis* is characterized by a unique cell envelope composed of long-chain fatty acids, glycolipids, and other components also

crucial for its survival and pathogenicity (C-D) as shown in Figure 2.1. These ultimately provide resilience against host immune defenses and environmental stressors [26, 28].

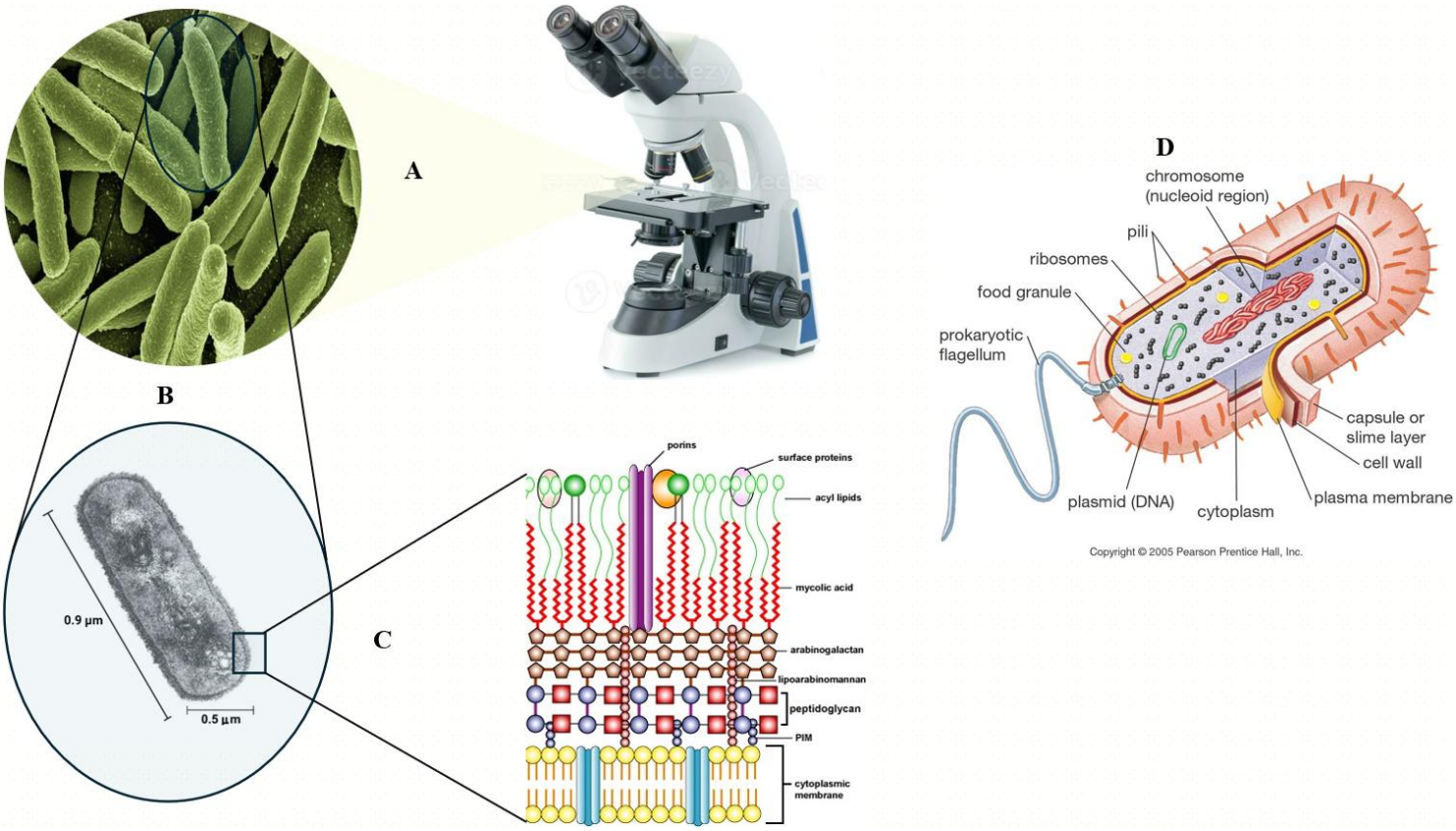

Figure 2.1: Microscopic view of a typical *M. tuberculosis* cell structure, showing rod-shaped bacteria (**A**), highlighting its morphological features (**B**), and its complex multilayered cell wall architecture (**C**). External and internal structure of the bacterium and its cell components (**D**).

In addition to its structural strength, *M. tuberculosis* possesses a special ability that allows it to enter a state of inactivity, or latency, in response to adverse conditions like low pH, low oxygen levels, nutrient deficiency, and oxidative stress [29-31]. This characteristic is essential during an infection because it enables the bacterium to use hypoxia-inducible genes to suppress its metabolic activity, preventing the host immune system from killing it [31]. This ultimately enables the mycobacterium to survive in granulomas, which are specialized immune responses in the lungs [14]. *M. tuberculosis* can stay dormant for long periods and frequently progress to latent TB infection (LTBI) due to its capacity to evade host defences [32]. When the immune system is weakened as a result of malnutrition, infections, and certain medications, LTBI reactivates, allowing the TB bacteria to multiply, progressing from latent to an active, contagious state [29, 32-34]. This reactivation leads to active TB disease. Because of this, TB flourishes and continues to wreak havoc in parts of the world, resulting in millions of new cases and fatalities documented each year [2].

2.2. Global Burden of TB

In 2024, the WHO Global Tuberculosis Report stated that TB had once again become the world's most common cause of death, exceeding COVID-19 and HIV/AIDS related deaths that were recorded in the previous years [10]. Despite years of hard work in the fight against this infectious disease, eliminating TB remains a serious challenge, especially in developing countries where many people still struggle to access good-quality healthcare and effective treatment [10]. The battle against TB is complicated by several challenging risk factors, which make the fight against TB even more difficult. These include alcohol and tobacco use, poor nutrition, long treatment times, diabetes, and the strong link between TB and HIV; all of these weaken the immune system and reduce the chances of recovery [10]. On top of that, the rise of drug-resistant TB strains has made treatment more complicated and less effective [10]. Another major hurdle is funding. The WHO has warned that without sufficient financial support, countries that rely heavily on international aid, especially those in the African region, could face serious jeopardy [10, 35]. With drug-resistant TB on the rise, there's an urgent need for better diagnostic tools, new medications, and stronger public health systems to turn the tide, as previously highlighted by Liebenberg and colleagues [36].

2.2.1 Global Incidence and Mortality Rate

According to the WHO, an estimated 10.8 million people fell ill with TB in 2023, of whom 55% were men, 33% were women, 12% were children, and young adolescents [10]. This was a further increase from the 10.7 million reported in 2022, 10.4 million in 2021, and 10.1 million in 2020 [10]. Among those, 8.2 million were reported as newly diagnosed [10]. This was an overwhelming increase from 7.5 million in 2022, 6.4 million in 2021, and 5.8 million in 2020 [10]. Despite this overwhelming trend, the global rise in the number of people falling ill with TB each year has slowed and started to stabilize following the surge observed during the COVID-19 pandemic [10]. The global incidence rate stood at 134 new cases per 100,000 population, which represents an 8.3% reduction since 2015, as shown in Figure 2.2 [10]. However, this decline remains insufficient to meet the global TB elimination targets [10].

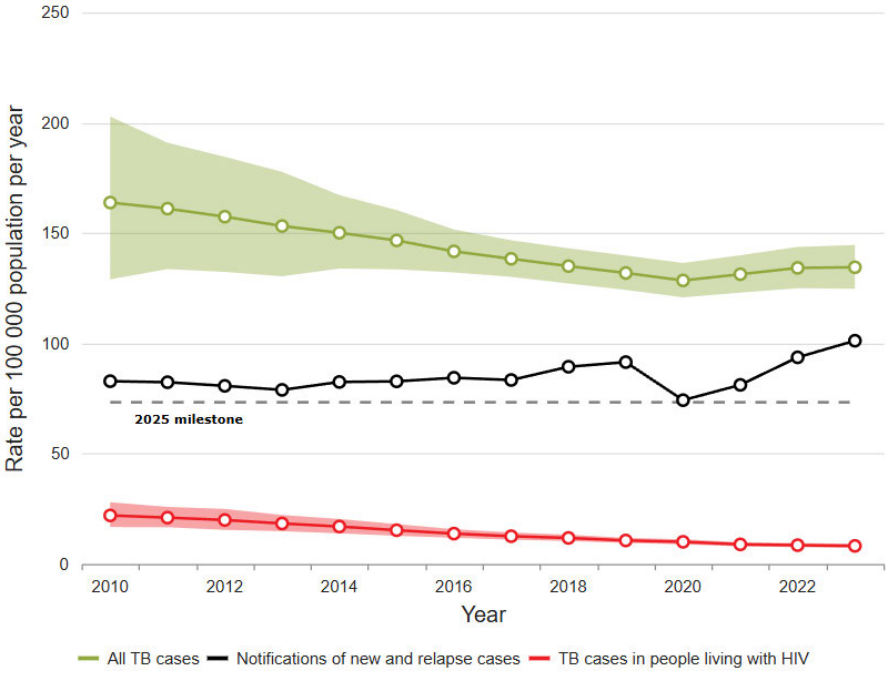

Figure 2.2: Global TB incidence rate between 2015 and 2023, highlighting changes in disease burden over time and reflecting the impact of public health interventions, diagnostic improvements, and treatment strategies on TB control worldwide.

TB-related mortality remains a concern, with approximately 1.25 million deaths reported in 2023, reinforcing the compelling need for intensified efforts towards TB prevention, diagnosis, and treatment [10]. As illustrated in Figure 2.3 the disease predominantly affected regions in South-East Asia, Africa, and the Western Pacific, with countries like India (26%), Indonesia (10%), China (6.8%), the Philippines

(6.8%), Pakistan (6.3%), Nigeria (4.6%), Bangladesh (3.5%) and the Democratic Republic of the Congo (3.1%) bearing the highest burdens [10].

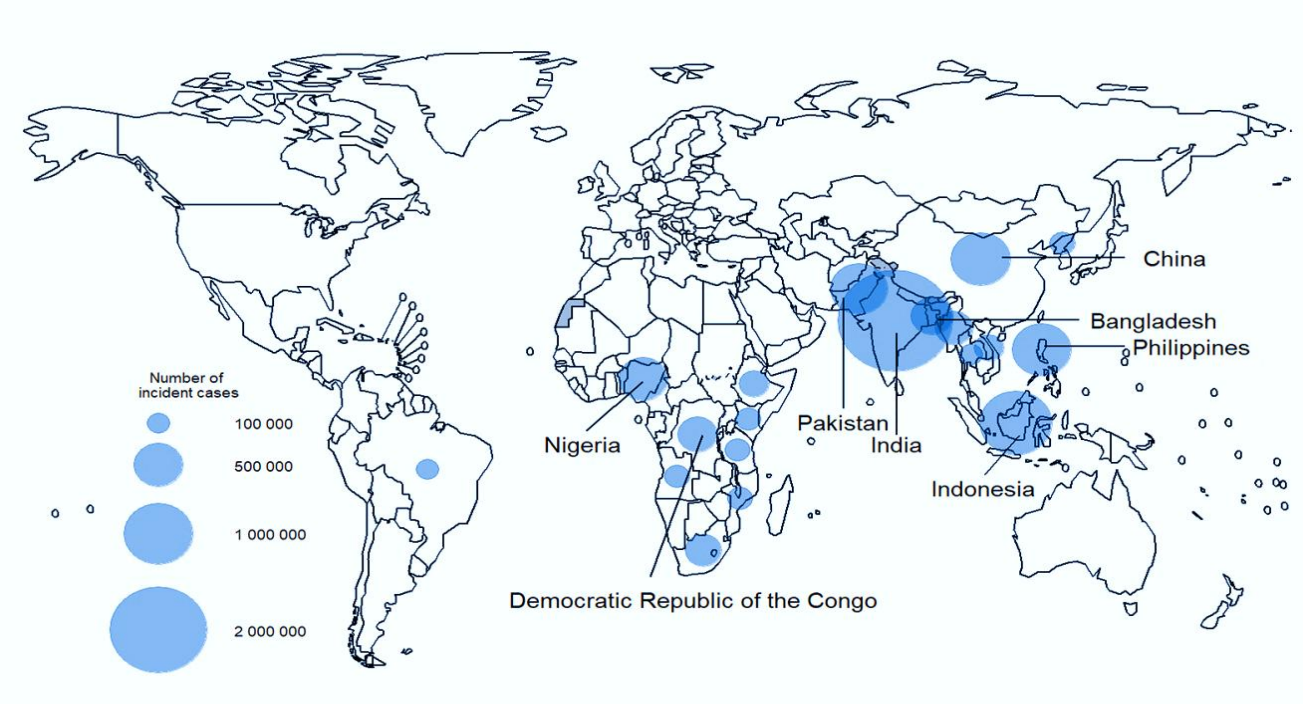

Figure 2.3: Estimated number of incident TB cases in 2023 for countries with at least 100,000 incident cases, highlighting the eight countries that accounted for about two-thirds of the global number of people estimated to have developed TB [10].

2.2.2 Global Incidences of MDR/RR-TB

In addition to the overall burden of TB, drug-resistant forms of the disease continue to pose a serious global health concern, especially with the increasing prevalence of MDR-TB and RR-TB [10]. In 2023, 400,000 people developed DR-TB [10]. Of these, only 175,923 cases received diagnosis and treatment, accounting for just 44% of the estimated total [10]. MDR-TB is characterized by resistance to at least isoniazid and rifampicin, the two primary first-line anti-TB drugs [10, 37]. The treatment success rate for DR-TB showed a gradual improvement in 2023, reaching 68%, up from 64% in 2020 and 60% in 2019 [10, 37]. Although these findings seem encouraging, more can be done to guarantee better results for everyone who is affected. In addition to MDR-TB, XDR-TB increases resistance to fluoroquinolones and at least one injectable second-line medication (amikacin, streptomycin) [10]. Since capreomycin and kanamycin have been prohibited since 2020, treatment options have become even more limited [10, 37].

The WHO Global Tuberculosis Report 2024 also stipulated that in 2023, the majority of MDR/RR-TB cases originated from the Russian Federation and several countries across Eastern Europe and Central Asia [10]. As illustrated in Figure 2.4, five countries, India (27%), the Russian Federation (7.4%), Indonesia (7.4%), China (7.3%), and the Philippines (7.2%), accounted for over half of all reported MDR/RR-TB cases globally during that year [10].

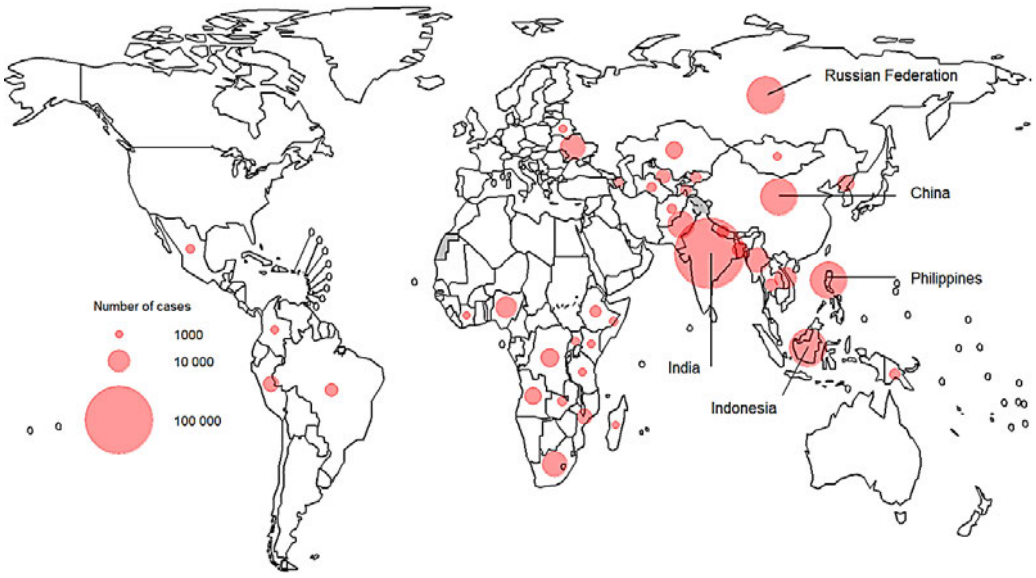

Figure 2.4: Estimated number of people who developed MDR/RR-TB (incident cases) in 2023 for countries with at least 1000 incident cases, highlighting the top five affected countries [10].

These statistics illustrate the ongoing TB control challenge and the critical need for targeted intervention, especially in high-burden countries, to combat TB and DR-TB efficiently.

2.2.3 TB Burden in Southern Africa

According to the South African Health Review (2023), South Africa continues to bear a significant burden of TB, and this places it among the countries with the highest incidence rates [10, 38]. Despite this, the WHO Global Tuberculosis Report 2024 highlighted South Africa as one of just 13 countries to have achieved a 50% reduction in TB incidence between 2015 and 2023, exceeding the 2025 target of the "End TB" strategy [10]. Remarkably, it was the only high-burden country to have reached this milestone [10].

Sadly, despite this noteworthy achievement, the dual burden of TB and HIV continues to be a profound challenge in this region, as it is worsened by long-standing inequalities, inadequate healthcare access,

and various complex political challenges [39]. The co-epidemic of TB and HIV is too grave in the sub-Saharan African region, where approximately 20% of the newly reported TB cases occur among people living with HIV/ AIDS [10, 40]. This vulnerability is largely due to the weakened immune systems of people with HIV, making them highly susceptible to opportunistic infections like TB, as it is difficult for their bodies to control the multiplication and spread of the tubercle bacilli [41]. Moreover, the situation is highly difficult in Southern Africa, where in certain countries, more than half of the people with TB are co-infected with HIV, as depicted in

Figure 2.5 [10]. South Africa is one of the few countries that appear on all three high-burden lists for TB, HIV-associated TB, and multidrug-resistant/rifampicin-resistant TB [10, 38]. According to the South African National Recovery Plan 4.0 report, the impact of TB varies across provinces and districts [42]. In 2024, four provinces (Eastern Cape, Gauteng, KwaZulu-Natal, and Western Cape) were responsible for approximately 77% of people diagnosed with laboratory-confirmed pulmonary TB, with Eastern Cape and Western Cape alone accounting for 46% [42].

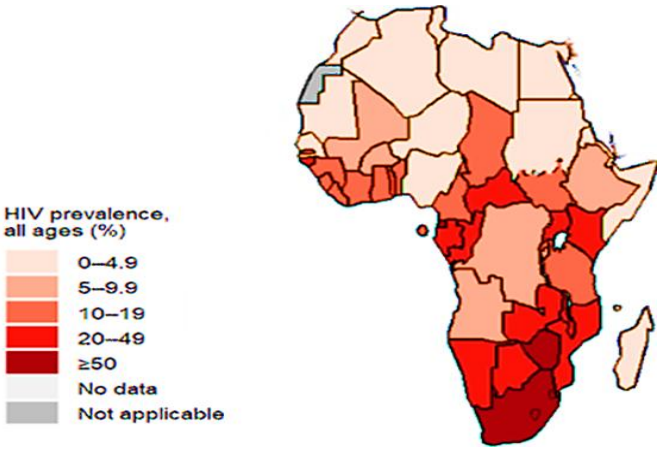

Figure 2.5: Estimated HIV prevalence in people with a new episode of TB (new or relapse cases), 2023, in the Sub-Saharan region [10].

These disturbing findings emphasize the importance of integrating HIV and TB care strategies to effectively fight the dual epidemic and enhance general health outcomes in the Sub-Saharan region, especially in countries like South Africa and Zimbabwe, which are severely impacted, as shown in

Figure 2.5. To effectively prevent and treat TB, it is essential to understand its pathogenesis and mode of transmission.

2.3. Transmission and Pathogenesis

2.3.1. Bacterial Transmission

TB is spread primarily through airborne droplets when someone with active pulmonary TB releases tiny respiratory droplets by coughing, sneezing, speaking, or even singing. (Figure 2.6) [43, 44]. These droplets, containing *M. tuberculosis*, are incredibly small, usually between 1-5 microns in size, and can stay airborne for long periods, especially in poorly ventilated spaces [41, 43, 44]. When a susceptible person inhales these droplets, most of the larger droplets remain lodged in the upper respiratory tract (the nose and throat), where infection is most unlikely to develop [41]. However, smaller droplet nuclei may reach the small air sacs of the lung (the alveoli) and initiate the infection process [41, 43]. The likelihood of transmission varies based on several factors, like the infectiousness of the patient, the duration and proximity of contact, ventilation conditions, and the immune state of the exposed person [43, 44]. Overcrowded living conditions and inadequate healthcare resources further increase transmission risks, making TB a significant issue, especially in low-resource environments [43, 44]. According to Zhuang et al (2024), TB is not only an infectious disease but also an immune-mediated disease [45].

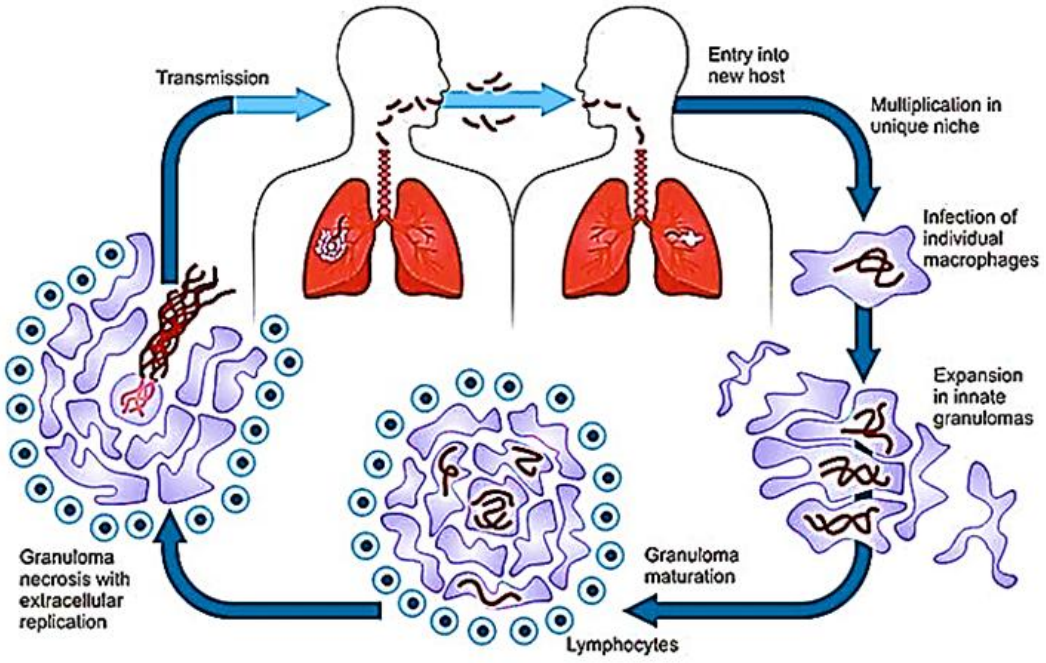

Figure 2.6: Life Cycle and transmission of *M. tuberculosis* [46].

2.3.2. Pathogenesis of Tuberculosis

Within the lungs, *M. tuberculosis* is engulfed by alveolar macrophages but survives by blocking phagosome-lysosome fusion, enabling its replication [30, 47]. In response, the immune system sends more macrophages, dendritic cells, and lymphocytes to the infected area, leading to the formation of granulomas (Figure 2.6) [11, 30, 47]. These granulomas encase the bacteria, preventing their spread and resulting in LTBI, where the bacteria remain dormant without causing symptoms [11, 41, 47]. Most individuals with LTBI do not progress to active disease or transmit it, yet approximately 5–10% may experience reactivation, especially with compromised immunity [11, 41, 47, 48].

Immunosuppressants like HIV or malnutrition can cause granulomas to deteriorate (break down), allowing *M. tuberculosis* to proliferate and spread [28, 48]. This deterioration results in secondary (reactivation) TB, which is characterized by lung lesions and tissue damage [28, 47]. The bacteria may spread through the bloodstream, leading to extrapulmonary TB, which can affect organs like lymph nodes, bones (Pott's disease), meninges (TB meningitis), and the genitourinary system [49]. In severe cases, *M. tuberculosis* can disseminate extensively throughout the body, resulting in miliary TB, a potentially life-threatening condition [49].

Lung TB typically shows symptoms such as a persistent cough lasting over three weeks, chest pain or discomfort, and coughing up blood-streaked mucus [50]. Besides these respiratory signs, an infected individual might also experience systemic symptoms like fever, night sweats, persistent fatigue, unexplained weight loss, and loss of appetite [50]. When TB affects organs outside the lungs, symptoms vary based on the affected area [48, 50]. For instance, lymph node TB may cause swelling, spinal TB can result in back pain and stiffness, TB meningitis leads to headaches, confusion, and neck stiffness, while TB of the kidneys or reproductive organs may cause blood in the urine or pelvic pain [48, 50].

The immune response to TB involves both innate and adaptive elements, as shown in Figure 2.7 [11, 49]. The innate response includes macrophages and neutrophils producing reactive oxygen species (ROS) and inflammatory signals like TNF-α, IL-1, and IL-6 to control bacterial growth [45, 51]. Concurrently, the adaptive immune response activates T-helper (Th) cells, cytotoxic T lymphocytes (CTLs), and B cells, which release antibodies and cytokines like interferon-gamma (IFN-γ), interleukins (IL-4 and IL-17) to enhance the immune defense [45, 51]. Innate cells like neutrophils, macrophages, and dendritic cells rapidly activate defense mechanisms, working with adaptive cells like $CD4^+$ T cells, $CD8^+$ T cells, and B cells [45]. Alveolar macrophages and dendritic cells play an immense role in the initial defense, while T-helper 1 (Th1) cells produce IFN-γ to stimulate macrophages to eliminate the bacteria [45, 47, 51, 52].

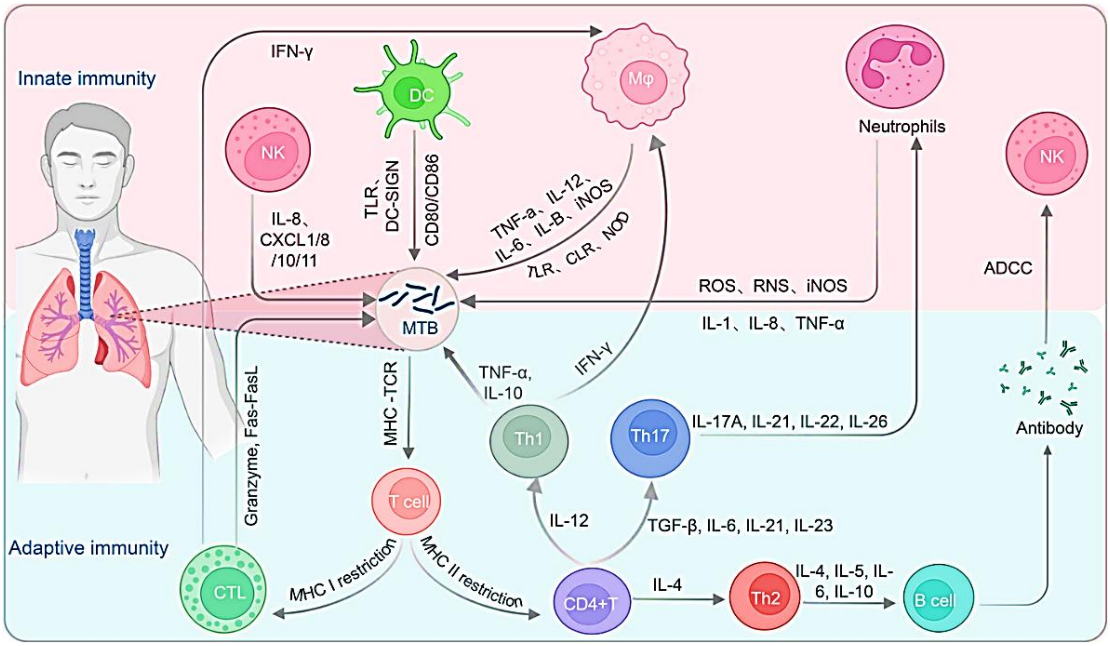

Figure 2.7: Illustration of the Immune System's Response to TB [45].

Cytotoxic T cells and granuloma formation are important for controlling the infection [45]. The granulomas rupture when the immune system is less active, which leads to active TB and increased bacterial transmission [45]. Controlling and stopping the spread of infection requires prompt diagnosis and efficient treatment.

2.4. Diagnosis

The diagnosis of TB has undergone tremendous changes, as illustrated in

Figure 2.8. Initially, diagnosis began with the use of microscopic methods (A), like Ziehl-Neelsen and acid-fast staining [53, 54]. Although these techniques were widely accepted and suitable for low-resource settings, they had sensitivity limitations, especially in patients with co-infections and low bacterial loads.[48, 55]. This resulted in some false positives [55]. To overcome these issues, scientists introduced bacterial culture to supplement the staining method, though it also had its drawbacks [55]. Solid media culture (B), such as the Löwenstein-Jensen method, proved to be highly specific and accurate for confirming *M. tuberculosis* and testing drug susceptibility [55]. Its main drawback was the time it took for colonies to grow, often several weeks [55]. In contrast, liquid media culture systems, like the MGIT 960, provide faster results, around 10 days, and have higher sensitivity, speeding up diagnosis [55]. However, they are more prone to contamination and require advanced laboratory infrastructure [55]. Over time, TB diagnosis has experienced a significant revolution with the development of new tools that make detection quicker, simpler, and more precise. Today, rapid tests like GeneXpert (D) and Truenat can detect TB in less than two hours [56]. Targeted DNA sequencing (E) helps clinicians make swift treatment decisions [57]. Simple urine tests, like the Fujifilm SILVAMP TB lipoarabinomannan (LAM) assay (C), serve as alternative methods for TB testing in HIV patients (especially with low CD4 counts) and when sputum samples cannot be obtained [58]. AI-powered X-ray tools (F) and portable scanners facilitate rapid diagnosis even in remote or crowded locations [55, 59, 60].

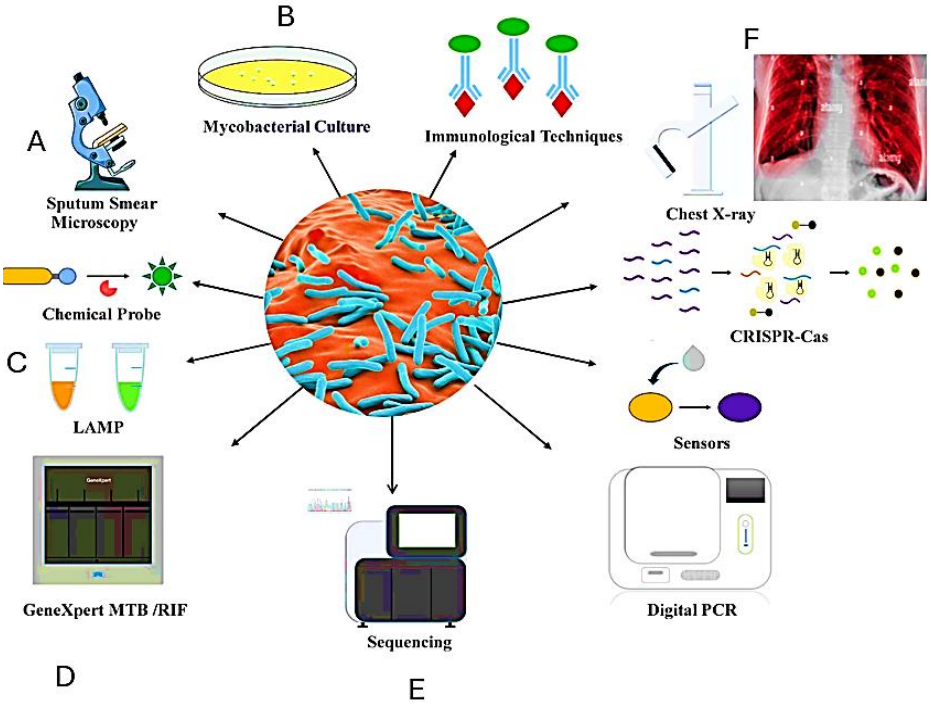

Figure 2.8: Common Diagnostic Methods for TB.

In African countries like Tanzania and Ethiopia, trained African giant pouched rats called HeroRATs are being used to detect TB in sputum samples [61]. For underdiagnosed children, a clinical algorithm known as the TB Treatment Decision Algorithms for Children (TDA4Child) has been invented [55, 62, 63]. TDA4Child is endorsed by the WHO and used in several African countries. It has improved detection rates by up to 258% in some parts of Africa [64].

2.5. TB Treatment

Over the past centuries, the treatment of TB has changed tremendously. Before the discovery of antibiotics, TB had been managed through sanatoriums, where patients were isolated and treated with rest, fresh air, and healthy food [65]. Although these actions offered some comfort, they did not heal the illness [65]. After Alexander Fleming discovered penicillin in 1928, many hoped it would be a cure-all for bacterial infections, including TB. However, *M. tuberculosis* proved to be a tough opponent; its uniquely structured, waxy cell wall made it hard for penicillin to penetrate it and perform its function [66]. In 1921, Albert Calmette and Camille Guérin developed the Bacille Calmette-Guérin (BCG) vaccine [65]. This was the first significant advancement in TB prevention. Although BCG remains the only licensed TB vaccine to date, its effectiveness is limited, offering partial protection mainly in children while showing variable efficacy in adults [67, 68].

2.5.1.1 Antibiotic revolution and drug resistance

In 1943, Selman Waksman and his associates discovered streptomycin, the first ever effective antibiotic against *M. tuberculosis* [69]. This breakthrough transformed TB management from symptomatic care to targeted antimicrobial therapy. However, streptomycin was later removed as a first-line drug due to side effects and its ineffectiveness, which increased the risk of developing DR-TB [70].

2.5.1.2 Current Antibiotic Treatment

Following the discovery of streptomycin and its limitations, it became clear that a more reliable and effective treatment approach was needed. This realization led to the development of combination therapy, which includes drugs like isoniazid, rifampicin, pyrazinamide, and ethambutol [71]. This combination therapy is considered to be the standard first-line treatment for TB [71, 72]. This first-line regimen is approved by the U.S. Food and Drug Administration (FDA) and backed by the WHO [71, 72]. To effectively reduce the bacterial load and enhance patient outcomes, this regimen has to be administered for a minimum of six months [10]. The implementation of this regimen marked a new era in TB treatment, shortening treatment duration and minimizing the development of resistance. **Error! Reference source not found.** outlines the recommended regimens for the different TB classifications based on the latest WHO recommendations, while Table 2.2 provides an overview of the FDA-approved anti-TB drugs, along with their mechanism [10, 73].

Table 2.1: Updated treatment regimens for each disease classification based on the latest WHO recommendations [10, 37, 74, 75].

Disease Classification	Treatment Regimen	Length of Treatment	All-Oral	Age Recommendation
Drug-Susceptible TB (Both Pulmonary and Extrapulmonary)	**H, R, E, and Z	2 months of HREZ followed by 4 months of H and R (6 months total)	Yes	All ages
Drug-Susceptible Pulmonary Tb	**P, H, Z, and M	4-months	Yes	12 years and older
Non-severe TB (and without suspicion or evidence of resistance to R and H)	**H, R, Z and sometimes also E	2 months of H, R, Z and sometimes also E, followed by 2 months of H, and R (4 months total)	Yes	3 months - 16 years
MDR/RR-TB or pre-XDR-TB	BPaLM (fluoroquinolone-susceptible)	6-month (standardized treatment duration)	Yes	14 years and older
	*BDLLfxC (Unknown susceptibility to fluoroquinolones) *BDLLfx (FQ susceptibility) BDLC (FQ resistance)	6-month (standardized treatment duration)	Yes	All ages, pregnant or breastfeeding
	BPaL (Fluoroquinolone-resistant)	6-9 months (Extension to 9 months applies if sputum culture is positive, months 4 – 6)	Yes	14 years and older
	*BLMZ, BLLfxCZ, and BDLLfxZ (fluoroquinolone-susceptible)	9 months	Yes	
	Injectable drug (amikacin). (Individualized longer treatment based on drug susceptibility)	18–20 months	No	All

NB: BPaLM/BPaL- Not recommended for pregnant and lactating women due to safety data.

* BEAT- TB trial in South Africa (New updates).

** Isoniazid -(H), Rifampicin (R), Ethambutol (E), Pyrazinamide (Z)

Table 2.1 summarizes the WHO's latest recommended TB treatment regimens, including those for drug-susceptible, MDR, Pre-XDR, and XDR TB based on the WHO Global Tuberculosis Report 2024, Updated WHO consolidated guidelines on DR-TB treatment 2025, and the Key Updates to the Treatment of drug-resistant Tuberculosis Rapid Communication 2024.

Table 2.2: Current FDA-approved TB drugs and their mechanism of action.

First-Line TB drugs		
Generic name of the antibiotic	**Structure**	**Mechanism**
Isoniazid	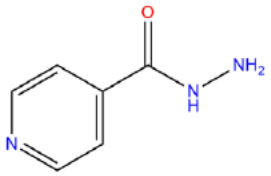	Isoniazid (INH) is a pro-drug that becomes active through the bacterial enzyme KatG, which helps convert it into a form that binds to the NAD cofactor and inhibits the InhA enzyme [76]. This action blocks the production of mycolic acid, a critical component of the *M. tuberculosis* cell wall, making INH bactericidal [76].
Rifampicin	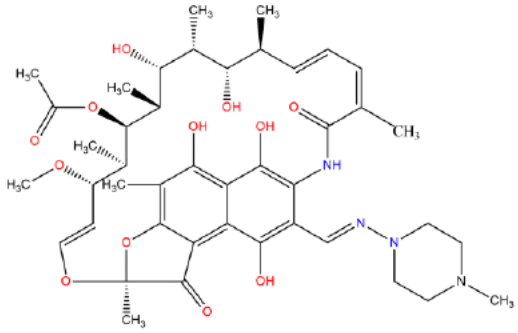	Rifampicin binds to the beta-subunit of microbial DNA-dependent RNA polymerase (RNAP); this action ultimately leads to the inhibition of the enzyme and impedes RNA synthesis [77]. Overall, it reduces the affinity of RNAP for short RNA transcripts [78].
Pyrazinamide	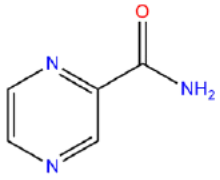	Pyrazinamide (PZA) is a prodrug converted into its active form, pyrazinoic acid (POA), by the mycobacterial enzyme pyrazinamidase (encoded by the pncA gene) [79]. POA interferes with the trans-translation process by binding to ribosomal protein S1 (RpsA) [80].
Ethambutol	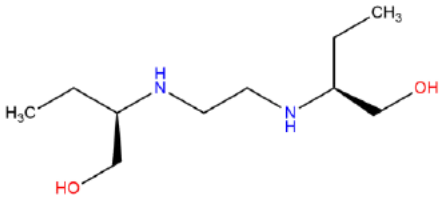	This antibiotic inhibits the arabinosyltransferases (embA, embB, and embC), preventing the formation of the cell wall components such as arabinogalactan and lipoarabinomannan, and even cell division [79].
Second Line Treatment (Drug-resistant Anti-TB)		
Bedaquiline	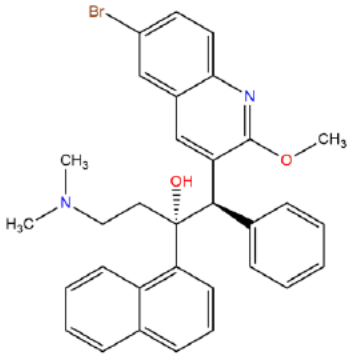	Bedaquiline is a "diarylquinoline antimycobacterial drug that inhibits mycobacterial ATP (adenosine 5'-triphosphate) synthase, by binding to subunit c of the enzyme that is essential for the generation of energy in *M. tuberculosis*" [81].

Pretomanid	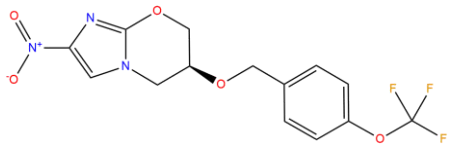	Pretomanid, a nitroimidazole, is activated through deazaflavin-dependent nitroreductase (Ddn), producing nitric oxide that acts as a respiratory poison in low-oxygen conditions. Additionally, it inhibits mycolic acid synthesis, killing replicating *M. tuberculosis* [82].
Linezolid	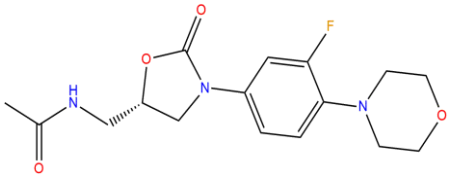	It is responsible for inhibiting bacterial protein translation by binding to the 23S rRNA of the 50S ribosomal subunit. Preventing the formation of the 70S initiation complex, halting bacterial reproduction and division. Point mutations in bacterial 23S rRNA can result in linezolid resistance [83].
Streptomycin	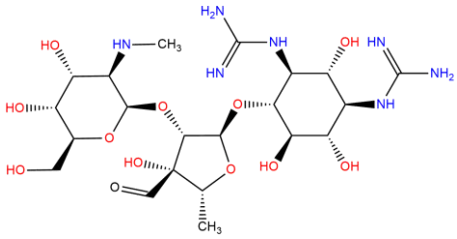	Streptomycin is a bactericidal and broad-spectrum aminoglycosidic antibiotic that inhibits protein synthesis in bacterial cells by binding to the side of 16S rRNA located on the smaller 30S subunit of ribosomes [84]. It induces structural changes, which interfere with the recognition site of the codon-anticodon interaction, resulting in the misreading of the genetic message carried by messenger RNA (mRNA) [84].
Delamanid	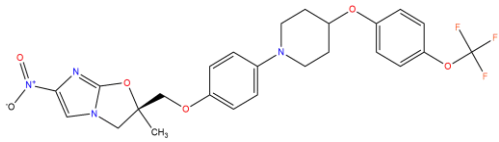	A prodrug that requires biotransformation via the mycobacterial F420 system. Targets both growing and non-growing mycobacteria. Linked to mutations in F420-related genes. Inhibits cell wall synthesis (methoxy-mycolic and keto-mycolic acids) and generates reactive nitrogen species. Does not affect alpha-mycolic acid (unlike isoniazid) [85].
Clofazimine	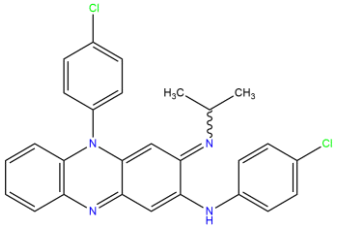	Repurposed drug. Disrupts bacterial cell membranes and generates reactive oxygen species, which contribute to its antimycobacterial effects [86].
Fluoroquinolones/Levofloxacin	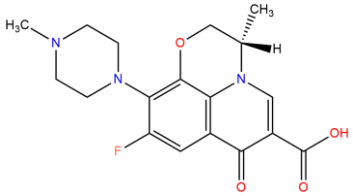	• Binds to DNA gyrase and topoisomerase IV. • Disrupts the supercoiled structure of bacterial DNA. • Inhibits bacterial cell division. [87]
Moxifloxacin	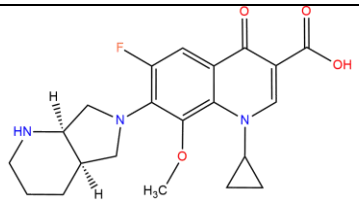	• Binds to DNA gyrase and topoisomerase IV. • Disrupts the supercoiled structure of bacterial DNA. • Inhibits bacterial cell division. [88]

Table 2.2 presents an overview of the FDA-approved anti-TB treatment regimens, listing the generic names of antibiotics, their chemical structures, and their mechanisms of action. Together, these drugs form a potent combination therapy that effectively targets different physiological aspects of *M. tuberculosis*, including cell wall synthesis, energy production, and protein synthesis [89].

Despite these significant advancements in TB treatment, *M. tuberculosis* continues to evolve, leading to the emergence of MDR-TB, XDR-TB, and TDR-TB, ultimately causing substantial setbacks to global TB control [89]. MDR-TB strains exhibit resistance to at least isoniazid and rifampicin, the two most potent anti-TB drugs [10]. Managing MDR-TB and RR-TB requires second-line drugs, which are generally less effective, more toxic, and significantly more expensive than first-line treatments [37, 74, 90]. Moreover, treatment durations are longer, often extending up to two years [37]. In contrast, XDR-TB strains exhibit additional resistance to fluoroquinolones and second-line injectable drugs, complicating treatment options further [10, 37].

In response to the growing threat of DR-TB, the WHO and national TB programs reintroduced and reclassified streptomycin as a second-line TB drug in the late 1990s [70, 91]. This decision aimed to provide additional treatment options when amikacin was unavailable or there was confirmed resistance [84, 92]. Streptomycin's mechanism, which involves inhibiting bacterial protein synthesis, made it an ideal alternative for blocking resistant strains and improving efficacy against DR-TB [84].

2.5.1.3 Latest Drug-Resistant TB Recommendations

Recognizing the ongoing challenges of DR-TB, the WHO continues to refine treatment strategies. In March 2025, the organization released updated consolidated guidelines, introducing new recommendations to improve treatment efficacy and patient outcomes (Table 2.1 and Table 2.2) [37, 75, 91]. The latest guidelines recommend a six-month BDLLfxC regimen (bedaquiline, delamanid, linezolid, levofloxacin, and clofazimine) for MDR/RR-TB patients with or without fluoroquinolone resistance [75, 91]. These recommendations apply to individuals with MDR/RR-TB or pre-XDR-TB, including both pulmonary and extrapulmonary forms (excluding CNS, osteoarticular, or disseminated TB), regardless of age or HIV status, including pregnant or breastfeeding women [75, 91]. These also apply to individuals with less than one month of exposure to specific drugs such as bedaquiline, linezolid, or delamanid, or when drug resistance is excluded [75, 91]. Moreover, these recommendations are relevant for children and adolescents with a high likelihood of MDR/RR-TB, even in the absence of bacteriological confirmation [75, 91]. Adjustments to this regimen (BDLLfx, BDLC) depend on fluoroquinolone (Fq) resistance status [75, 91]. The updated recommendations now prioritize a nine-month all-oral regimen over longer treatments for fluoroquinolone-susceptible MDR/RR-TB [75, 91]. Among these regimen updates, BLMZ

is preferred over BLLfxCZ, and BLLfxCZ is also preferred over BDLLfxZ for fluoroquinolone-susceptible treatment [75, 91]. The Centers for Disease Control and Prevention (CDC) continues to support the six-month BPaLM (bedaquiline, pretomanid, linezolid, moxifloxacin) for fluoroquinolone-susceptible TB and BPaL (without moxifloxacin) for fluoroquinolone-resistant TB [75, 91]. These regimens represent a shift toward shorter, more effective, and patient-friendly treatments.

Nonetheless, despite the significant advancements in the treatment of DR-TB, a significant gap still exists within the healthcare system. While the six-month BDLLfxC regimen and its variations are designed to improve patient outcomes [75]. There are still serious concerns over drug toxicity, particularly with linezolid, which, through clinical studies, was reported to have been linked to severe side effects, like myelosuppression and peripheral neuropathy; these can hinder patient adherence and necessitate increased clinical monitoring [93]. While shorter regimens like the nine-month all-oral treatment for fluoroquinolone-susceptible MDR/RR-TB and the six-month BPaLM/BPaL regimens endorsed by the CDC are designed to improve adherence, they remain costly and inaccessible in many low-resource areas where TB is most prevalent [75, 91].

Another growing concern in the fight against DR-TB is the rise of resistance to mandatory prescriptions like bedaquiline (BDQ), and the potential for cross-resistance between clofazimine (CFZ) and BDQ [94]. Several *in vitro* and clinical studies have found that *M. tuberculosis* strains develop drug resistance exclusively through the selection of spontaneous chromosomal variants, and the mechanisms of resistance include mutations in the *atpE* [95], *Rv0678* [96], and *pepQ* [97] genes [98, 99]. A study by Hartkoorn et al. (2014) aimed to investigate the mechanism behind the resistance of CFZ in *M. tuberculosis* using *in vitro* evolution and genomic analysis to identify mutations in the transcriptional regulator *Rv0678* [94]. They discovered mutants that were not only resistant to CFZ but also showed unexpected cross-resistance to BDQ [94]. This was linked to increased activity of the MmpL*5* gene [94]. According to Ismail et al (2018), this strong correlation between BDQ and CFZ, especially in isolates with Rv0678 RAV, suggests that CFZ and BDQ probably share a common biochemical pathway [100]. Shared resistance pathways have the potential to undermine treatment strategies and increase the failure of multiple key drugs all at once. Furthermore, drugs that share similar pathways tend to have similar therapeutic uses and an increased risk of adverse effects [101, 102]. If a strain of *M. tuberculosis* becomes resistant to one drug, it may automatically become resistant to the other, and losing effectiveness in one drug often means losing the other as well. This can severely restrict available treatment choices.

Rv0678 mutations are a major driver of resistance, and this was further elucidated by a recent study conducted by L. Sonnenkalb et al. (2023) where they set out to understand how *M. tuberculosis* develops resistance to BDQ and CFZ [103]. The study employed rigorous methodology, utilizing lab-grown strains, genomic sequencing, and computer-based (*in silico)* analyses [103]. *M. tuberculosis* was subjected to low levels of both drugs to trigger resistance [103]. They found 265 mutations linked to BDQ resistance, most

of which affected the *Rv0678* gene that controls an efflux pump [103]. Interestingly, new resistance mechanisms involving a major rearrangement of the bacterial genome were also uncovered [103]. The study included data from over 14,000 global clinical TB samples, helping to confirm the lab findings [103]. Structural modeling of Rv0678 (PDB:4NB5) further revealed how these mutations affect the function of resistance-related proteins through impaired DNA binding, disruption of dimerization, and alteration in ligand binding [103].

The cross-resistance between BDQ and CFZ can lead to significant pharmacological effects. BDQ is classified as a group A drug for the treatment of MDR-TB, meaning it is considered to be one of the most important and effective options available [104, 105]. CFZ is classified as a group B drug for MDR-TB (second-line priority drugs) [86]. The increased global use of these drugs raises the risk of reduced effectiveness, jeopardizing the ability to treat resistant TB [104]. With more people around the world using these treatments, there's a growing risk that they might not work as well as they should. This is especially troubling for patients dealing with DR-TB as it could result in longer treatment plans, more difficult to endure, and less effective, especially for those who don't have many other options. The rise of drug resistance poses a serious risk to the future effectiveness of these newer treatments. [104, 105].

Furthermore, no form of any mutation in the fadD23 gene has been reported that would make the bacterium resistant to drugs, thus far. Moreover, there are currently no FDA-approved drugs or inhibitors that specifically target FadD23.

2.6. Mechanism of Drug Resistance

Drug resistance is a challenging issue that stems from a range of biological mechanisms. These mechanisms can be intrinsic, meaning they are naturally present in the organism, or acquired, arising from mutations or the transfer of genes [106]. Drug resistance reduces the effectiveness of anti-TB medication in curing or controlling the spread of TB [106]. It often arises when *M. tuberculosis* modifies itself to resist antibiotics, further complicating treatment options [106]. Intrinsic resistance is the natural ability of *M. tuberculosis* to resist certain drugs as a result of its cell wall (limiting drug penetration), efflux pumps (pumping out drugs), formation of a protective barrier (biofilm), and metabolic adaptability (dormancy), happening even without previous exposure to the medication [106]. Acquired resistance develops from genetic mutations or gene transfer from other bacteria as a result of prolonged drug exposure [106]. This occurs when there's a change in the bacterial DNA as a result of mutation or chromosomal changes that alter drug target genes (e.g., *katG*, *rpoB*), making them ineffective [106]. Unlike intrinsic resistance, acquired resistance appears during treatment and differs by strain [106]. This form of resistance has become a major concern because *M. tuberculosis* does not transfer resistance

genes via plasmids, like other bacteria, but develops mutations against essential drugs, leading to MDR-TB, XDR-TB, or even totally drug-resistant (TDR-TB) strains [106]. Figure 2.9 illustrates how the bacterium evades the effects of several antibiotics using the drug-resistant mechanism [106].

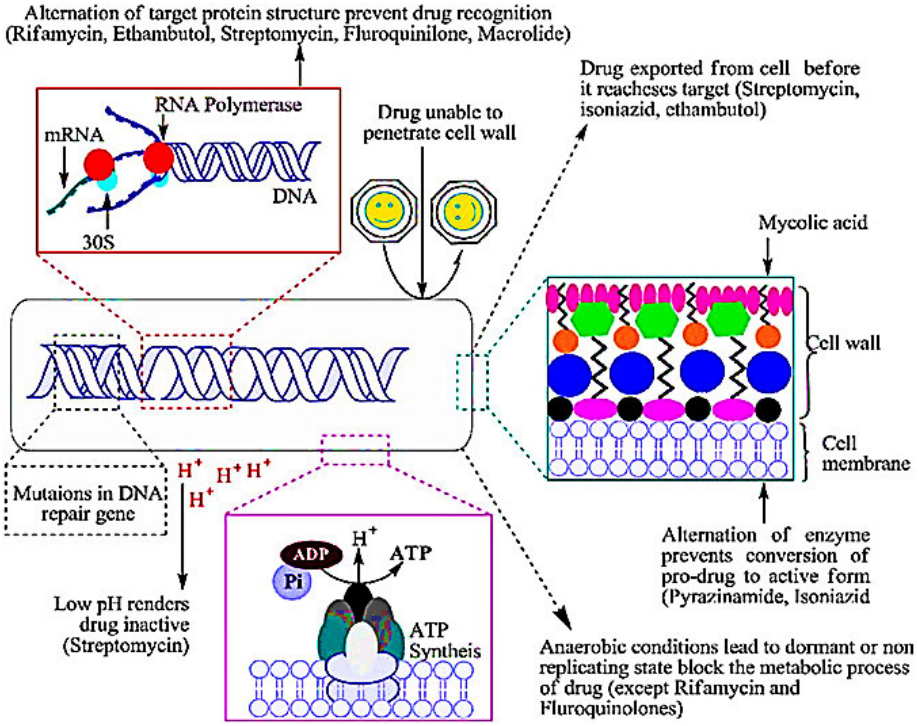

Figure 2.9: Schematic representation of the drug-resistant mechanism of *M. tuberculosis* [106].

As drug resistance continues to evolve, there will always be a need for continuous monitoring, pharmacovigilance, and development of novel therapeutic strategies to sustain progress in DR-TB treatment [105]. The key factor to *M. tuberculosis's* resistance to antibiotics is its unique cell envelope, which serves as a formidable barrier against drug penetration [107].

2.7. Mycobacterial Cell Envelope

The cell envelope of *M. tuberculosis* is a complex, multilayered structure that is essential for the bacterium's survival, virulence, and resistance to antibiotics [26]. Unlike many other bacteria, *M. tuberculosis* has a highly complex and lipid-rich cell wall that is primarily made up of mycolic acids, peptidoglycan, and arabinogalactan [26]. This unique structure forms a highly impermeable hydrophobic barrier that protects the bacterium from hostile environments, including the host immune system and antibiotics [108]. This corroborates its significant role in the pathogen's ability to evade immune responses and resist antimicrobial agents. Trivedi et al. (2005) once described the mycobacterial cell envelope as a "treasure house of biologically active lipids of fascinating molecular architecture" [109]. This is because the cell envelope of tubercle bacilli is enriched with complex lipids, many of which play an important role in its pathogenesis [109].

2.7.1 Structural Organization of the Mycobacterial Cell Envelope

The mycobacterial cell envelope consists of three major layers, as shown in Figure 2.10 which contribute to the cell rigidity and impermeability, [110]Figure 2.10. The plasma membrane is the innermost layer and consists of a phospholipid bilayer [26, 89]. It contains membrane-bound proteins that play major roles in nutrient uptake, electron transport, and the biosynthesis of cell wall components. [26, 89]. Above this lies the peptidoglycan-arabinogalactan complex, where the peptidoglycan (PG) layer provides structural integrity and rigidity [26, 111]. Unlike Gram-positive bacteria, mycobacterial PG is highly resistant to degradation by lysozymes due to its being extensively cross-linked, with muramic acid residues modified by *N-glycolylation* instead of the more common *N-acetylation* [110, 111]. The arabinogalactan (AG) polymer, which is a branched polysaccharide, serves as a crucial linker, covalently attaching the PG to the outer mycolic acid layer, thereby strengthening the cell wall permeability barrier [26].

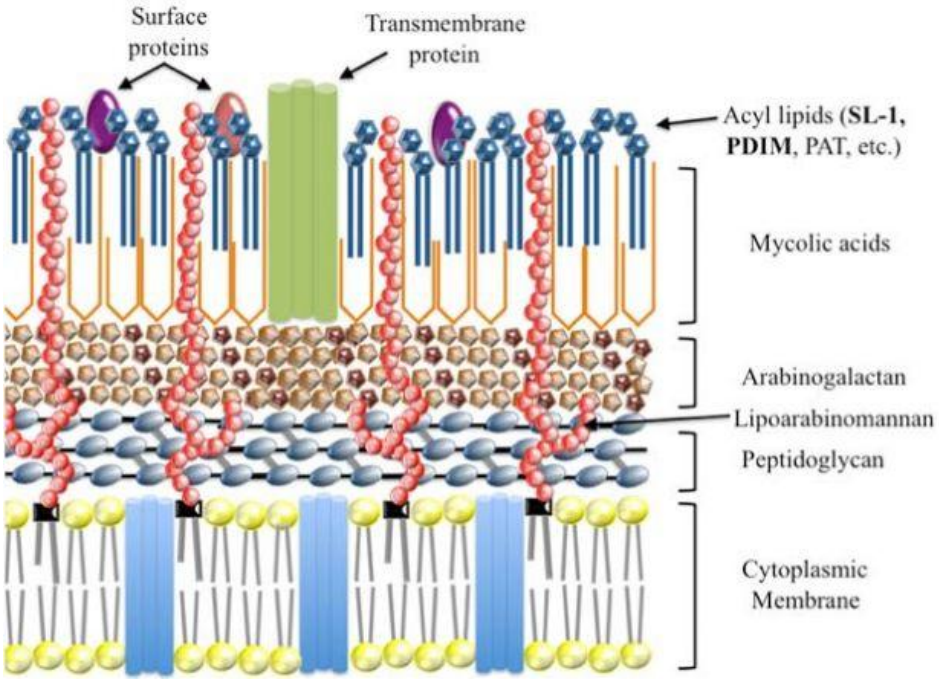

Figure 2.10: Illustrates the structural organization of the mycobacterial cell envelope, highlighting its multilayered composition and the role of each component in bacterial survival and pathogenicity [26].

The outer mycolic acid layer is a defining feature of mycobacteria. This layer consists of extremely long-chain fatty acids (60–90 carbons) that create a hydrophobic barrier, which reduces permeability to antibiotics and host immune factors [112]. Furthermore, this outer layer includes additional lipids that enhance its impermeability and facilitate interactions with the external environment. Collectively, these are also known as virulence-associated or acyl lipids and include phthiocerol dimycocerosates (PDIMs), phenolic glycolipids (PGLs), trehalose dimycolate (TDM), SL-1, and lipoarabinomannan (LAM). All of these contribute to immune modulation, virulence, and macrophage survival [110, 112]. Surrounding this structure is a capsule-like layer composed of polysaccharides and proteins, which aids in biofilm formation and host immune evasion [26, 89].

2.7.2 Important Biosynthesis Enzymes in the Mycobacterial Cell Envelope

The biosynthesis of this complex cell envelope is facilitated by several specialized enzymes, many of which serve as potential drug targets. Figure 2.11 illustrates the structural organization of the mycobacterial cell envelope, highlighting its multilayered architecture and key lipid components [113]. Peptidoglycan biosynthesis involves key enzymes such as MurA–MurF, which catalyze the formation of the UDP-N-acetylmuramyl-pentapeptide (UDP-MurNAc-pentapeptide), a crucial nucleotide-activated monosaccharide-peptide, while D-alanine racemase (Alr) and D-Ala: D-Ala ligase (DdlA)

synthesize D-alanine residues, which are essential for peptidoglycan cross-linking [112, 114]. "The sequential Mur ligase pathway is the major contributor to the biosynthesis of PG" [25]. Penicillin-binding proteins (PBPs) such as PonA1/PBP1 and PonA2/PBP2 play a crucial role in peptidoglycan polymerization and remodeling, which directly influence cell wall strength, stability, and integrity [111, 112].

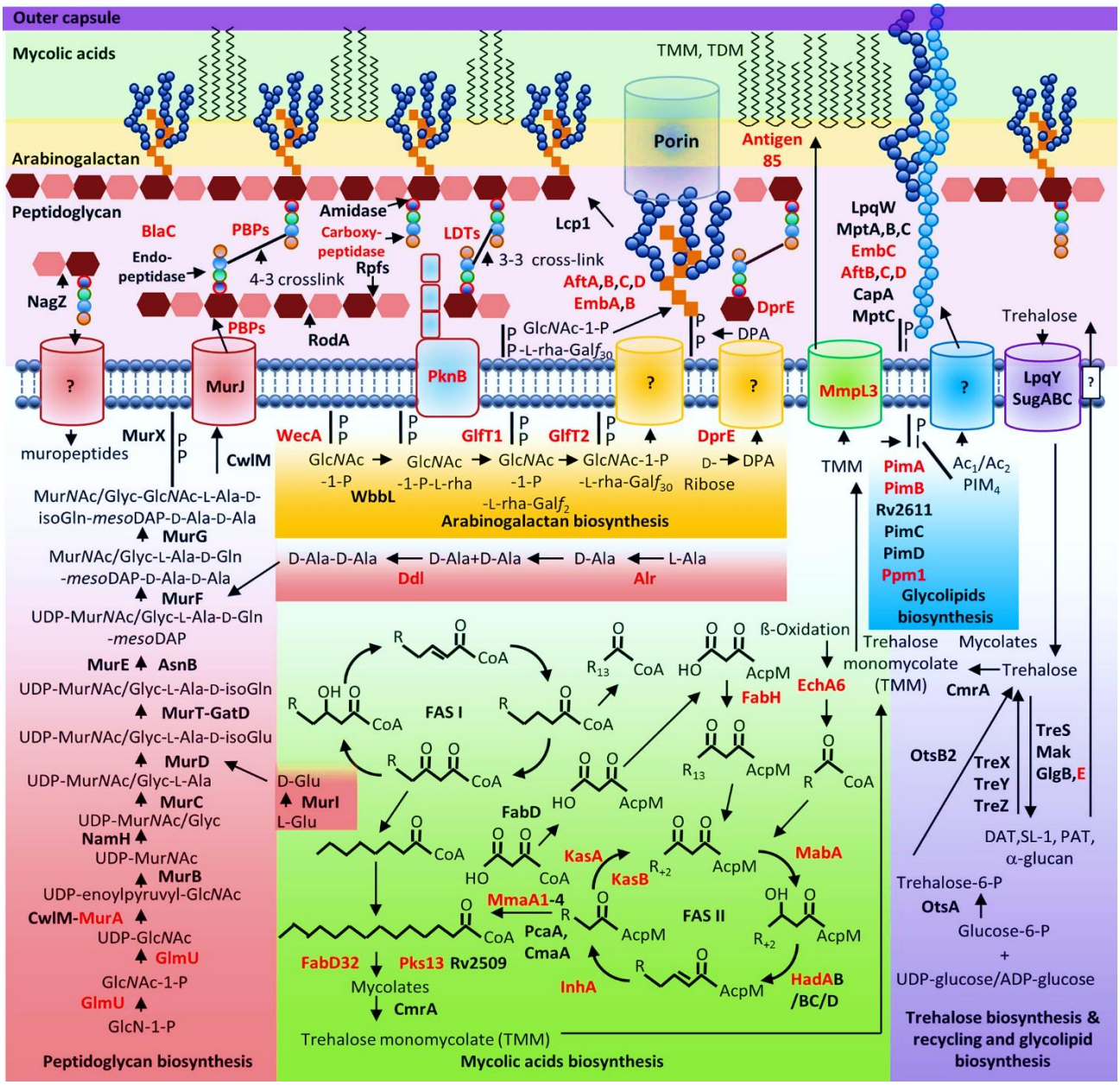

Figure 2.11: A visual representation of the mycobacterial cell envelope, illustrating the biosynthetic pathways of key lipid components, and also highlighting potential drug targets [114].

Arabinogalactan biosynthesis is another crucial pathway, involving decaprenyl-phosphoryl-β-D-arabinose (DPA) synthesis enzymes, such as DprE1/DprE2, which are essential for arabinogalactan

assembly and are validated drug targets [25, 115]. EmbA, EmbB, and EmbC (arabinosyltransferases) also catalyze the addition of arabinose units to form arabinogalactan [115]. These arabinosyltransferases are drug targets for one of the first-line antimycobacterial drugs, ethambutol, and this highlights their clinical significance [116, 117]. Meanwhile, galactan synthesis is mediated by glycosyltransferases such as GlfT1 and GlfT2, which catalyze galactofuranose units' sequential addition to the linear galactan backbone [25, 112].

The biosynthesis of mycolic acids is a defining feature of the mycobacterial cell wall and is mediated by two distinct fatty acid synthase systems, ie. Fatty Acid Synthase I (FAS-I) and Fatty Acid Synthase II (FAS-II) [25, 111]. FAS-I is responsible for generating C_{16}–C_{26} fatty acids, which are subsequently elongated by FAS-II to produce extremely long-chain mycolic acids that contribute to the impermeability and resilience of *M. tuberculosis's* cell wall [111, 112, 118]. Within this pathway, β-ketoacyl-ACP synthase enzymes such as FabH and FabD play a critical role in initiating the elongation of fatty acid precursors, while FabG, HadAB, and InhA facilitate further elongation and modification [119-121]. FabH is especially crucial in controlling the specificity of acyl chain elongation, while FabD (malonyl-CoA: ACP transacylase) ensures malonyl-ACP availability for chain elongation [119-121]. Polyketide synthase 13 (Pks13) catalyzes the condensation of fatty acid precursors, a key step in mycolic acid biosynthesis [112]. Once synthesized, mycolic acids are transported to the cell surface by MmpL3, an essential transporter that also serves as a validated drug target [112].

Due to the critical role of biosynthetic enzymes, they have become prime targets for developing new anti-TB drugs. Recent studies have identified inhibitors targeting some of these biosynthetic enzymes and pathways. For example, research on the mycolic acid biosynthesis pathway has highlighted β-ketoacyl-ACP synthase III (FabH) as a promising target, with inhibitors like thiolactomycin and its derivatives showing efficacy in disrupting mycolic acid synthesis (Figure 2.12) [122, 123]. Furthermore, a whole-genome CRISPR interference screening study has identified N-acetylglucosamine-6-phosphate deacetylase (NagA), a key enzyme in amino sugar metabolism, as a potential drug target [124]. Inhibiting NagA disrupts amino sugar metabolism, impairing the production of essential precursors required for cell wall integrity [124].

Targeting these biosynthetic enzymes offers a promising strategy for developing novel TB therapies, potentially overcoming drug resistance and improving treatment outcomes.

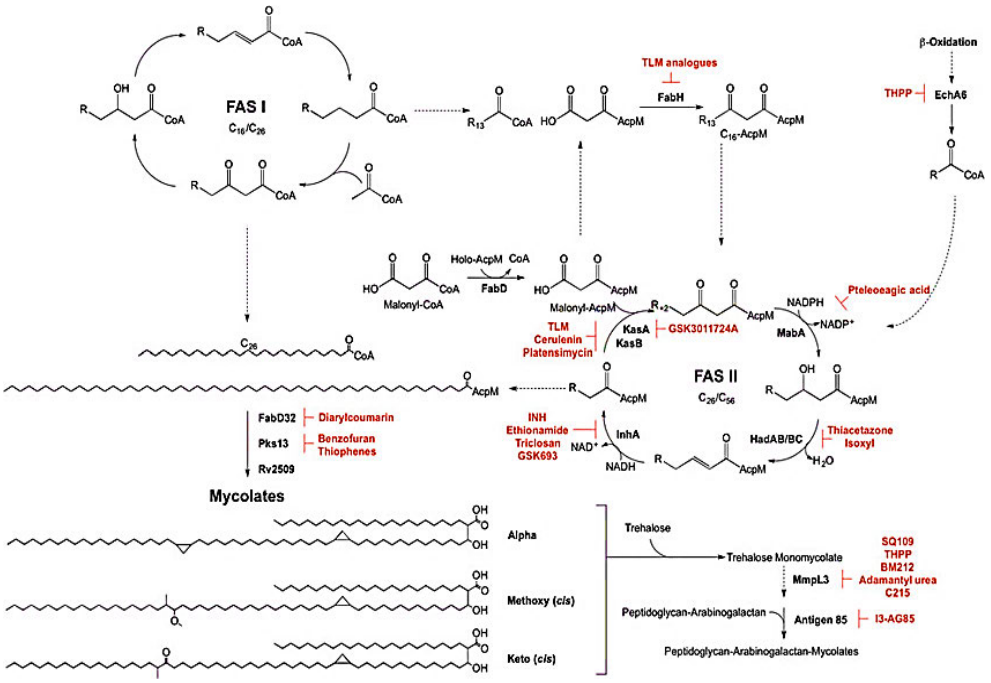

Figure 2.12: Known inhibitors of Mycolic acid. The enzymes involved in the mycolic acid biosynthetic pathway are marked in red [111].

Beyond structural integrity, *M. tuberculosis* also uses virulence-associated lipids, like sulfolipids and PDIMs, to evade the host immune system and enhance intracellular survival, further contributing to the persistence of *M. tuberculosis* within the host [125]. The bacterium's ability to survive and thrive within the human host, together with the rise of MDR-TB and XDR-TB, reinforces the compelling need for new and effective therapeutic strategies.

In response to the growing problem of DR-TB treatment, targeting FadD23 and other enzymes involved in fatty acid biosynthesis offers a potential avenue for developing new and effective therapeutics.

2.8. FadD23 Role in Pathogenesis

FadD23 is a fatty acyl-AMP ligase (FAAL) that plays an important role in the pathogenesis of *M. tuberculosis* through its involvement in lipid metabolism and the synthesis of virulence-related lipids [126]. FadD23 is one of the 34 fatty acid adenylating enzymes (FadDs) from the adenylate-forming enzyme superfamily found in *M. tuberculosis* [126-129]. This enzyme features an N-terminal AMP-binding domain with the conserved A-motif [117, 130-132], along with a C-terminal domain that stabilizes the enzyme's conformation and promotes substrate binding [117, 126, 129, 133, 134]. The conserved motif found in the adenylation domain of FadD23 is a characteristic feature of fatty acyl-AMP ligases (FAALs) and other enzymes in the adenylate-forming enzyme superfamily [126, 130, 131]. This motif is responsible for activating long-chain fatty acids by binding ATP and converting carboxylate substrates into acyl-AMP intermediates [126]. These activated intermediates are then utilized in polyketide biosynthesis, including the synthesis of sulfolipids [117, 126].

Previous studies have also highlighted an interconnection between the biosynthetic pathways of PDIM and SL-1, through their dependence on shared metabolic precursors, like the propionyl-CoA derived from the degradation of cholesterol via methylmalonyl-CoA (MMCoA) [117, 135, 136]. Research has demonstrated that manipulating one pathway can influence the activity or abundance of the other; for instance, a reduction in PDIM synthesis can lead to an increased flux of MMCoA towards the SL-1 biosynthetic pathway, subsequently enhancing SL-1 production [137]. Moreover, PDIMs are essential for the pathogenicity of *M. tuberculosis* and are synthesized through polyketide synthases, which rely on acyl-AMP substrates provided by FadD23 [117, 137]. As a key player in this process, FadD23 plays a central role in the synthesis of both SL-1 and PDIMs, which are vital components of the bacterial cell wall [126]. Together, SL-1 and PDIMs play an immense role in preserving the integrity of the *M. tuberculosis* cell wall and ensuring bacterial virulence, while facilitating immune evasion [117].

SL-1 is a tetraacyl-sulfotrehalosed glycolipid characterized by a trehalose-2-sulfate (T2S) core that is modified by four acyl groups: a straight-chain fatty acid, like palmitate or stearate, and three multi-methyl-branched (hydroxy) phthioceranoic acids [126, 138]. This glycolipid is both abundantly and uniquely found in the *M. tuberculosis cell* envelope and plays a vital role in aiding bacterial survival within human cells by obstructing the immune response [126, 138]. Various studies involving cell culture models have proposed that SL-1 achieves this disruption of host cell functions by altering phagosome-lysosome fusion and disrupting mitochondrial oxidative phosphorylation, which is essential for ATP production via the electron transport chain in mitochondria [138-143]. However, the interaction between SL-1 and mitochondrial components remains fully elucidated, as there hasn't been any evidence supporting a direct link [138]. Several *in vitro* studies suggest that SL-1 influences mitochondrial activity through indirect mechanisms, possibly by activating host cell signaling pathways that influence mitochondrial function. For instance, SL-1 has been shown to activate human neutrophils, generating

superoxide (O_2^-) and priming these cells for subsequent responses to other metabolic agonists [144, 145]. These effects involve the generation of diacylglycerol (DAG), increased calcium ion availability, and the activation of guanine nucleotide-binding proteins, which are essential for neutrophil activation and priming [144]. Such cellular responses can lead to alterations in mitochondrial activity, including changes in oxidative phosphorylation.

The presence of SL-1 in the *M. tuberculosis* cell wall has also been linked to the activation and suppression of host immune responses, including the reduction of pro-inflammatory cytokines and reactive oxygen species produced by human leukocytes, which aids in bacterial survival within macrophages [126, 129, 142, 144, 146].

PDIMs are associated with increased resistance to oxidative stress and antibiotics, while Palmitoyltransferases (PATs) play a role in enhancing intracellular survival by preventing the maturation of phagosomes in macrophages [109, 147]. A deeper understanding of FadD23's structural characteristics could provide crucial insight into its function and potential as a target for anti-TB drugs.

2.8.1 Structure of FadD23

According to the RCSB protein databank [148], FadD23 is a single-chained protein with a deposited model that contains a total of 605 residues, including both modeled and unmodeled ones. Out of these, 539 residues are modeled, with 4,234 atoms [148]. FadD23, like other FAALs, consists of functional domains that are essential for its enzymatic activity [149]. According to the latest crystallographic research by Yan. et al (2023) (Figure 2.13), this enzyme features a large N-terminal domain (residue 4–460), a smaller C-terminal domain (residue 473–576), and an active site [117]. The two domains are connected by flexible loops and an anti-parallel β-sheet (residue 465–472) [126]. The N-terminal domain contains the substrate binding pocket and is responsible for binding fatty acid substrates, whilst the C-terminal domain acts as a dynamic lid, covering the substrate binding pocket to facilitate catalysis [126]. The N-terminal domain consists of the adenylation domain and the acyl binding domain (which is specifically located in a hydrophobic tunnel that accommodates long-chain fatty acids) [126].

The adenylation domain, also known as the functional region, is responsible for binding ATP/AMP-PNP and catalyzing the activation of fatty acids into acyl-adenylates [126]. In the crystal structure of FadD23 (pdb;8HDF) [148], the adenylation domain is located at the interface between the N-terminal and C-terminal domains, where ATP or AMP-PNP binds [126]. This domain plays an important role in the enzyme's function, as it facilitates the formation of acyl-AMP intermediates before transferring them to downstream biosynthetic pathways [126, 149]. It is also defined by a phosphate-binding loop (P-loop), also known as the A-motif [126, 150]. Structural studies of FadD23 have confirmed the presence of this motif

on this enzyme through its ATP-binding capability [117, 126]. The N-terminal domain of FadD23 is further subdivided into three distinct regions or subdomains (A-C) [117]:

Region A of the N-terminal domain consists of several beta-sheets, namely, β1, β2, β3, β4, β5, and β6, and four helices, all of which are responsible for maintaining the core structure and contribute to the enzyme's stability [117, 126]. Residue Range 4–152 [117].

Region B of the N-terminal domain is made up of six helices, β7, β8, β9, β10, β11, β12, and β13, which form a continuous sheet that surrounds the substrate-binding cavity [117, 126]. Residue Range 158–344 [117].

Region C mainly consists of flexible loops, which allow conformational changes during substrate binding and catalysis [117, 126]. Residue Range 345–460 [117].

158-344344Figure 2.13 illustrates the 3D structure of FadD23, highlighting its functional domains.

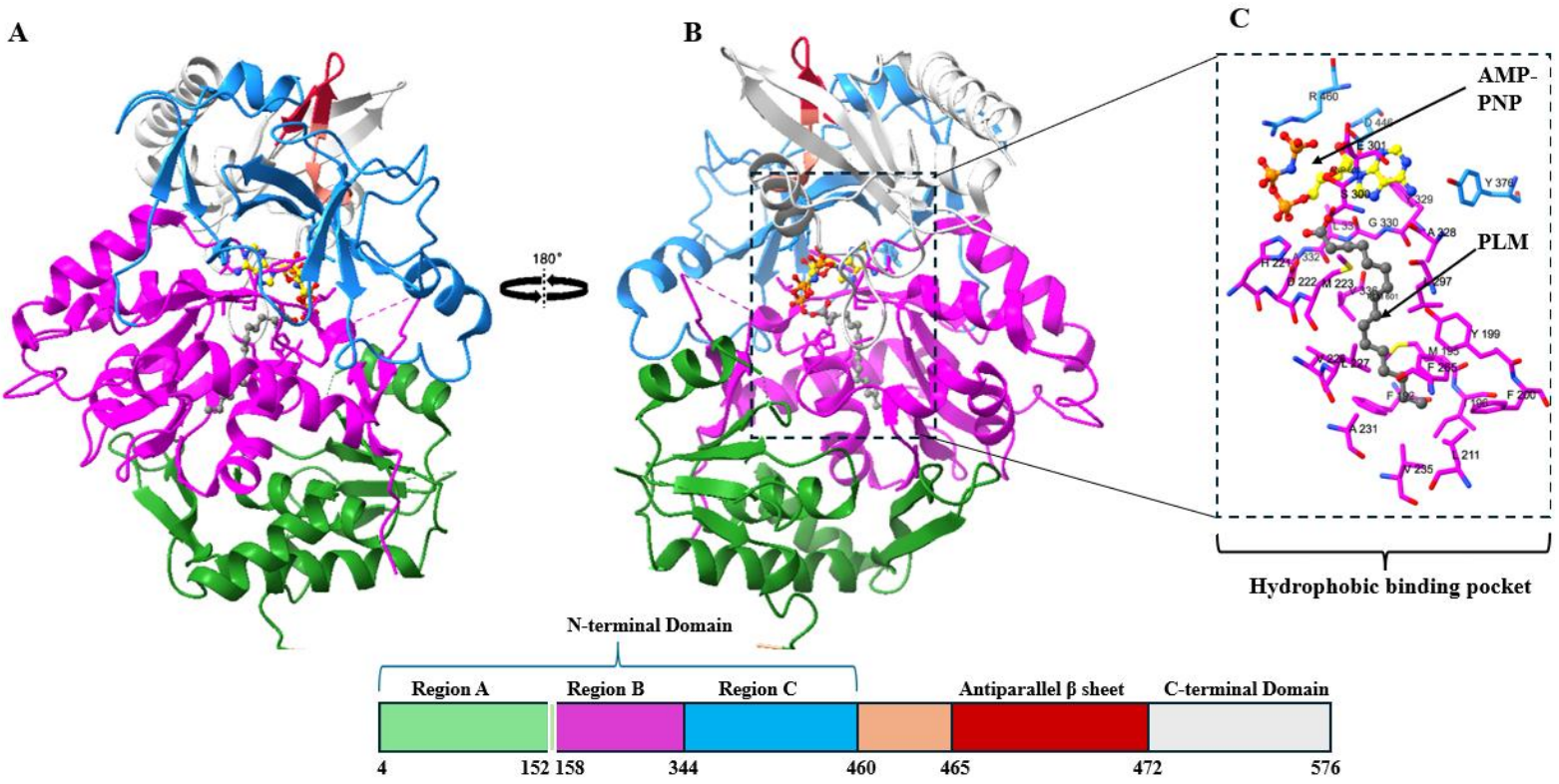

Figure 2.13: (**A**) FadD23 crystal structure showing the N-terminal, the C-terminal domain, and the anti-parallel β-sheet. (**B**) 180°C rotation of the crystal structure to show the (**C**) hydrophobic binding pocket. The N-terminal is divided into three subdomain regions [126].

Furthermore, according to the crystal structure of FadD23 (pdb;8HDF) the adenylation domain is also defined by key residues like His221 (essential for ATP hydrolysis), Ala328, Ala332, Tyr376, and Asp446 (involved in adenosine and ribose recognition), Asp222, Glu301, Arg329, Gly330 and Leu331 (interact

with phosphates and stabilize the protein complex), Arg460 and Ser300 (interact with AMP-PNP), as illustrated in Figure 2.14 [126]. These residues facilitate ATP hydrolysis and substrate activation [126]. The domain undergoes a conformational shift upon substrate binding [126]. FadD23 binds ATP or AMP-PNP (a non-hydrolyzable ATP analog) in a pocket formed by residues from both domains [126]. Biochemical studies suggest that palmitic acid (C16:0) serves as the preferred substrate for FadD23 [117]. However, for the N-terminal domain to perform its catalytic function in binding palmitic acid and other substrates, it requires assistance from the C-terminal domain, signifying a cooperative interaction between the two domains [126].

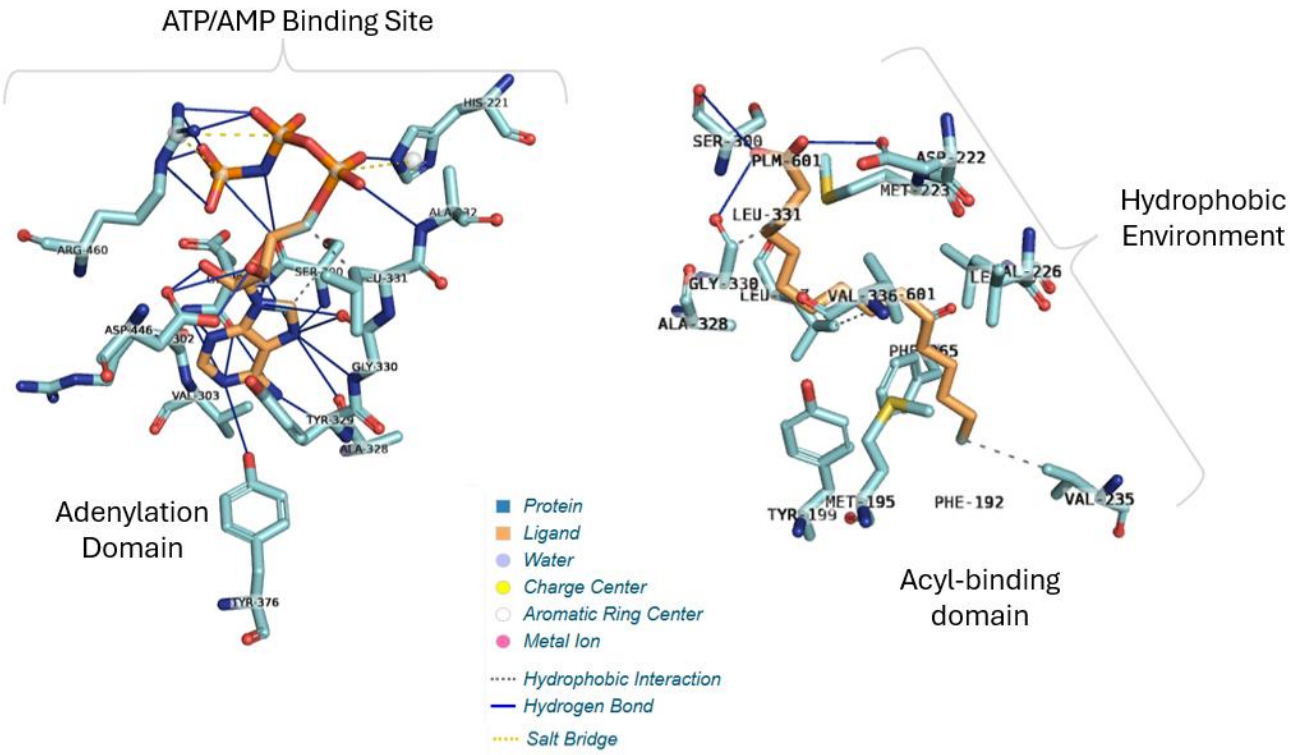

Figure 2.14: 2D interaction maps illustrating the interaction between the FadD23 protein and its ligands (AMP-PNP (ANP) and PLM) at the binding regions. (On the left) The adenylation domain, which facilitates ATP binding, is characterized by extensive hydrogen bonding, salt bridges, and polar contacts that help stabilize ligand binding. (On the right) The hydrophobic acyl-binding domain stabilizes fatty acids before activation, features PLM and key residues that contribute to nonpolar interactions. Protein residues are depicted in cyan, while the ligand is shown in orange. Interaction types are represented as hydrophobic contacts (dark dashed lines), hydrogen bonds (blue lines), salt bridges (yellow dotted lines), and aromatic interactions (white dots).

The acyl-binding domain provides a hydrophobic environment that stabilizes the fatty acid chain before activation, as shown in Figure 2.14 [126]. This domain is lined with hydrophobic residues such as Met223, Ala328, and Val336 near the base of adenosine's hydrophobic pocket, Met195, Tyr199, Val226, Leu227,

and Leu297 in the middle of the pocket, while the amino acid residues Phe192, Ile196, Phe200, Leu211, Ala231, Val235, and Phe265 line the end of the pocket, forming a semi-enclosed barrel [126]. These residues comprise the binding pocket for fatty acid substrates and, therefore, play a crucial role in substrate anchoring and specificity [126]. The C-terminal catalytic domain, located within the core of FadD23, consists of three peripheral helices and three inner β-sheets [126]. This terminal domain acts as a lid domain closing over the binding pocket, ensuring proper substrate binding and enzymatic activity [126]. The active site is positioned at the junction of the N-terminal and C-terminal domains and houses highly conserved residues, like histidine, glycine, serine, alanine, arginine, and aspartate, which participate in the catalytic mechanism [126]. This site is responsible for binding both ATP and fatty acid substrates [126]. Structural studies imply that FadD23 may require metal ions such as Mg^{2+} or Mn^{2+} for effective ATP binding and enzymatic function[126].

Recently, Yan et al. (2023) investigated the critical role of the C-terminal domain in enzymatic activity, further validating the structural features of FadD23 [126, 130, 150]. In their research, they identified the 2.68 Å crystal structure of *M. tuberculosis* FadD23 bound to ATP and the 2.25 Å crystal structure bound to AMP-PNP [126]. They concluded that the 2.68 Å FadD23 structure depicts the enzyme's conformation in the initial activation phase, while the 2.25 Å structure captures the enzyme with AMP-PNP [117, 126]. Their research provides important new information about the conformational changes of the enzyme during catalysis[117, 126]. The second structure provides insight into understanding how FadD23 changes shape during catalytic activity [117]. These structures offer important information about how FadD23 functions and how potential inhibitors might target it. These structures are listed in the Protein Data Bank (PDB entries: 8HDF, 8HCZ, and 8HD4) [126].

Comparative structural analyses and homology modeling indicate that FadD23 (8HDF) shares a high degree of structural and functional similarity with other FAAL enzymes, like FadD10 (4ISB), FadD26 (AF_AFP9WQ43F1), and FadD28 (3E53), and all of which are implicated in mycobacterial lipid biosynthesis [109]. According to Yan et al. (2023), FadD23 and FadD28 share a 66% sequence similarity and both belong to the same evolutionary branch [126]. The FadD23 C-terminal domain is structurally similar to that of FadD32 (5HM3) when in complex with a substrate, and both these enzymes possess similar fatty acid binding tunnels [126]. These FadD enzymes play a crucial role in activating and transferring long-chain fatty acids to cognate polyketide synthases, which are later incorporated into complex lipids essential for *M. tuberculosis* virulence and survival [109, 126].

2.8.2 Biosynthesis and Functional Role of FadD23

FadD23 catalyzes the ATP-dependent activation of fatty acids, particularly medium and long-chain fatty acids, converting them into acyl-AMP intermediates [126]. Unlike fatty acyl-CoA synthetases (FACS), FAALs like FadD23 ensure that these fatty acids are utilized specifically for specialized lipid biosynthesis rather than central metabolism [109].

FadD23, like other FAALs, exhibits dynamic conformational flexibility and adopts two main conformations during catalysis: adenylation and thiolation, with the C-terminal domain undergoing a 140° shift to complete catalysis [126, 150]. In this dynamic motion, the enzyme undergoes significant structural rearrangements, transitioning between different conformational states and serving as a "lid" to facilitate substrate binding, intermediate formation, and product release. According to Figure 2.15, this process is divided into four unique stages [126, 150].

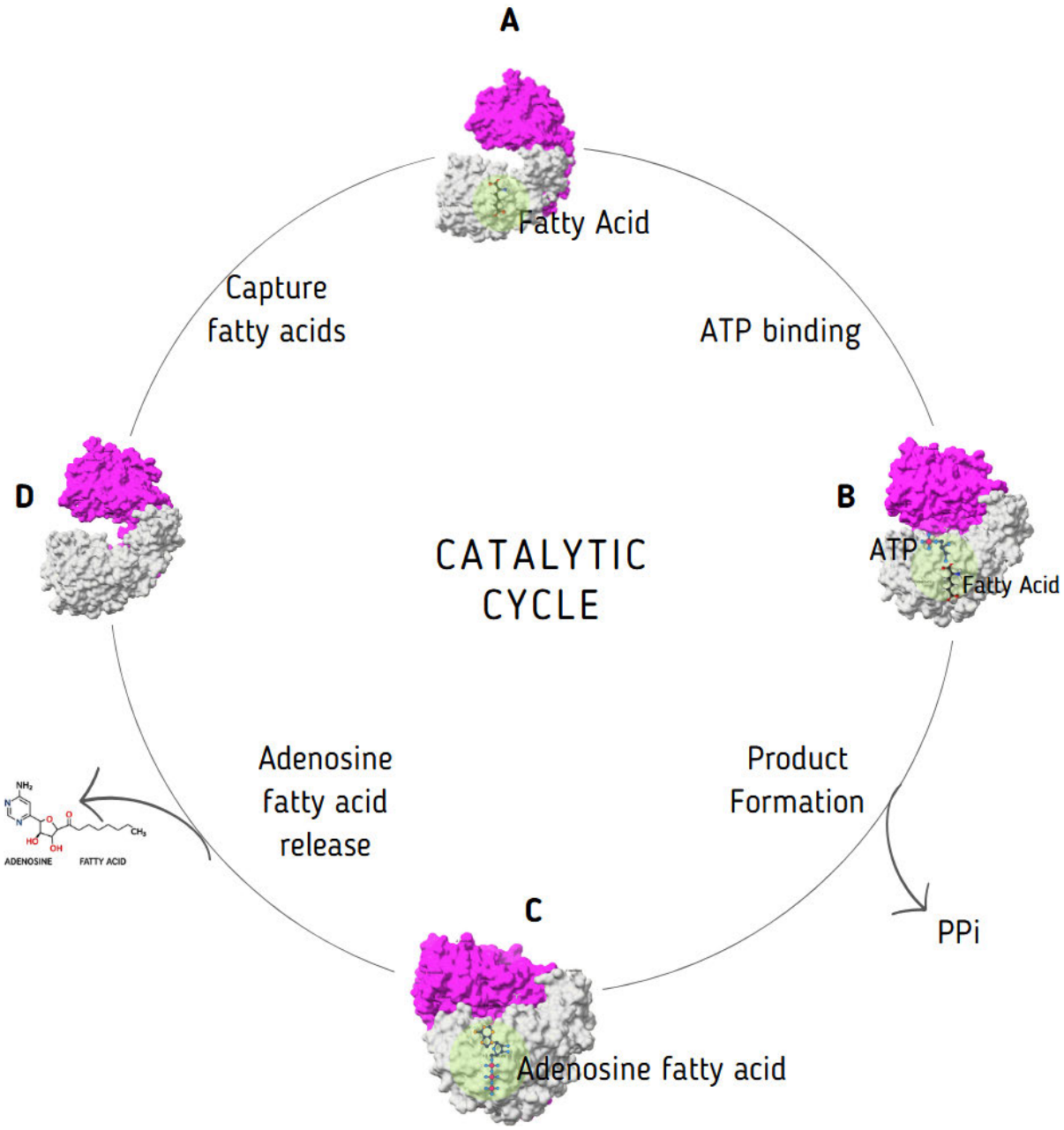

Figure 2.15: The catalytic cycle of FadD23 consists of four distinct stages. It begins with the *in vivo* capturing of fatty acids by FadD23 (**A**), followed by the binding of ATP, which triggers structural changes, such as rotation in the C-terminal domain (magenta) (**B**). As a result, the N-terminal (grey) and C-terminal (magenta) ends of the protein move closer together, facilitating the formation of the product (**C**). Finally, the products are released (**D**), allowing the cycle to commence again [126].

These conformational changes ensure that the enzyme can process various acyl-CoA substrates effectively [126, 150]. The key residues involved in substrate binding include His221, Ala328, Tyr376, Asp446, and Arg460 [126].

The general mechanism of FAALs follows a two-step enzymatic reaction, as illustrated in Figure 2.16. First, the fatty acyl-adenylate (acyl-AMP) intermediate (fatty acid + ATP → fatty acyl-AMP intermediate) is formed, followed by the transfer of the activated fatty acid (acyl group) to a polyketide synthase (PKS) or carrier proteins, which elongates and modifies the lipid structure [79, 109, 149, 151]. In the elucidated SL-1 biosynthesis, these FadD23-activated fatty acids (methyl-branched (hydroxy) phthioceranoyl chains) are then transferred by the acyltransferase PapA1 to the 3'-position of SL659, forming the diacylated intermediate SL1278 [138]. PapA1 and PapA2 have been shown to inhibit phagosome maturation and suppress host immune responses, thereby promoting *M. tuberculosis's* ability to persist within the macrophages [126, 129, 138]. The final steps of SL-1 biosynthesis involve additional acylations at the 6- and 6'-positions of SL_{1278}, which is catalyzed by the membrane-associated acyltransferase Chp1 [126, 138]. The membrane-associated protein Saps and the sulfolipid transporter MmpL8 are essential for SL-1 transport across the bacterial cell envelope [138]. Mutant strains lacking SL-1 exhibit reduced virulence and altered macrophage interaction, reinforcing the importance of this pathway in TB pathogenesis [126, 152].

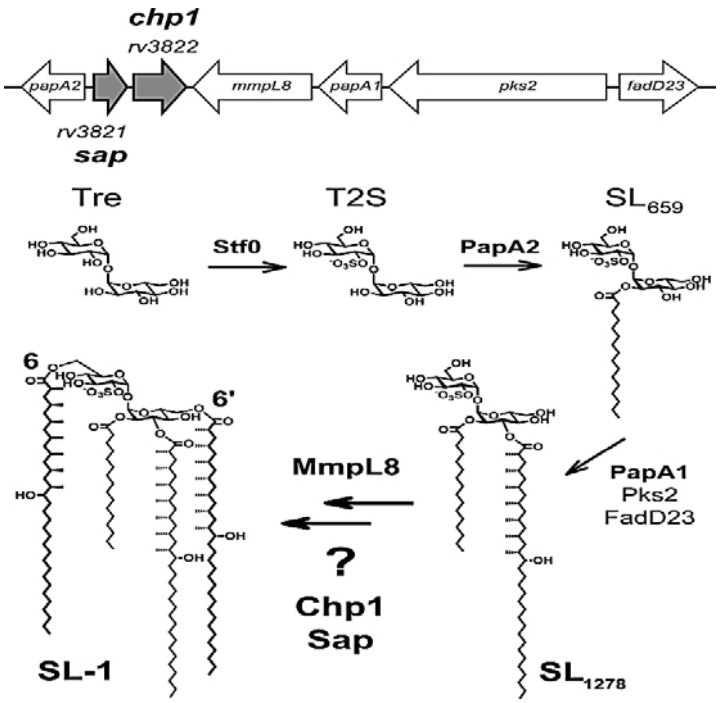

Figure 2.16: Biosynthetic pathway of SL-1 in *M. tuberculosis* showing the role of FadD23 and associated Enzymes [138].

This pathway illustrates the connection between lipid biosynthesis and transmembrane transport, with various proteins operating at the interface between the membrane and the cytosol. [138]. PDIMs contribute to *M. tuberculosis* virulence through multiple mechanisms. They disrupt phagosome maturation by interfering with phosphatidylinositol 3-phosphate (PI3P) signaling, thereby blocking phagosome-lysosome fusion [153]. PDIMs also mask pathogen-associated molecular patterns (PAMPs), reducing

Toll-like receptor (TLR2/4) recognition and subsequent NF-κB activation, which interferes with pro-inflammatory cytokine production (e.g., TNF-α, IL-12) [153]. PDIMs also scavenge reactive oxygen species (ROS), protecting *M. tuberculosis* from oxidative stress in macrophages [153]. According to previous research, the deletion of FadD23 attenuated the virulence of *M. tuberculosis* in murine models, with the mutants exhibiting increased lysosomal colocalization and susceptibility to nitric oxide-mediated killing [154].

2.8.3 Therapeutic Potential of FadD23

FadD23 is a promising target for developing anti-TB drugs, as it plays an important role in the production of virulence factors that are crucial for the survival and pathogenicity of *M. tuberculosis* [126]. Inhibiting this enzyme could interfere with SL-1 production, subsequently impacting the overall lipid composition of the bacterial cell wall [126]. However, creating specific inhibitors for FadD23 presents a difficult challenge as a result of its substrate specificity and the complex structure of its active site, both of which must be carefully considered during drug development [126].

Despite these challenges, it is important to note that, unlike *M. tuberculosis*, humans do not synthesize SL-1, nor do they possess the enzymatic machinery required for its biosynthesis, including FadD23, which is absent in human cells [126]. Because of this, we can conclude that FadD23 possesses a unique function in mycobacteria that is absent in humans, making it an appealing selective target [109]. This distinction significantly lowers the risk of off-target effects, enabling the development of selective drugs that can impede bacterial growth while safeguarding the integrity of human cells, and thus minimizing side effects [109].

Furthermore, unlike enzymes involved in central metabolism, FadD23 specifically plays a central role in the biosynthesis of virulence-associated lipids [126]. Therefore, selective inhibition of this enzyme could weaken *M. tuberculosis* by compromising its cell wall integrity and virulence without affecting human metabolism, making the bacterium more susceptible to immune responses and antibiotics [109]. This could enhance treatment efficacy against tubercular strains.

Another promising strategy for inhibiting FadD23 involves targeting the ATP-binding site with small-molecule inhibitors. These inhibitors could compete with ATP for binding to the ATP site of FadD23, potentially disrupting fatty acid activation and halting the synthesis of essential virulence lipids. [128, 155]. This strategy could disrupt the bacterium’s defense mechanisms, increasing its vulnerability to host immunity and standard antibiotic treatments. The FadD23 active site includes conserved residues like His221, which play a significant role in substrate binding and catalysis [126]. Mutations in these residues can significantly impair enzymatic activity, which highlights their importance in the enzyme's function

[126]. Previous research has identified several molecular targets within *M. tuberculosis*, leading to the development of newer drugs like bedaquiline[156] (targeting ATP synthase) and delamanid (inhibiting mycolic acid synthesis) [72, 157].

Despite the lack of extensively documented inhibitors specifically targeting FadD23, ongoing research on structurally related enzymes could provide valuable insights for drug development. Crystallographic analysis by Yan and colleagues revealed key information about the active site interactions of FadD23, particularly its interaction with 5'-O-[N-(11-phenoxyundecanoyl) sulfamoyl]adenosine (PhU-AMS), a known inhibitor of fatty acid adenylating enzymes [117]. While PhU-AMS binds effectively to FadD23, it does not inhibit its adenylation activity. Instead, it appears to obstruct the transfer of the acyl chain to Pks2, a downstream enzyme in the SL-1 biosynthetic pathway [117].

Structural studies have further shown that the C-terminal domain of FadD23 is essential for its enzymatic activity, with its absence rendering the enzyme nearly inactive [126]. This reinforces the importance of targeting the full enzymatic structure in drug design. Inhibiting FadD23 could impair the biosynthesis of mycolic acids and complex lipids, thereby compromising the integrity of the *M. tuberculosis* cell wall. Such disruption would not only weaken the bacterium's defense against host immune responses but also increase its susceptibility to existing antibiotics. Given FadD23's role in lipid-mediated drug resistance, targeting this enzyme holds significant potential for treating MDR and XDR strains of TB.

While current strategies have been centered on synthetic inhibitors like PhU-AMS, their narrow scope presents certain limitations. By focusing on a single synthetic compound, we risk missing the broader therapeutic potential that other compounds may offer. Natural compounds, often characterized by greater structural diversity, better bioavailability, and historical success in antimicrobial drug discovery, present a compelling alternative [158, 159]. Furthermore, recent findings indicate that FadD23 utilizes long-chain saturated fatty acids as substrates and that mutations in its active site significantly disrupt function [126]. This reinforces the enzyme's vulnerability and further supports the idea that natural compounds might serve as more effective modulators of FadD23, presenting an important direction for future research.

FadD23 emerges as a highly promising target for the development of new TB treatments. Its critical role in lipid biosynthesis, specificity to bacterial systems, and lower likelihood of off-target effects make it an attractive candidate for therapeutic intervention. By widening the scope of research to include a broader spectrum of natural inhibitors alongside synthetic options, we open new avenues for innovation. Addressing the current research gaps holds the potential to drive the discovery of more effective, targeted treatments offering hope in the global fight against TB.

2.9. Natural Compounds as Potential Inhibitors

Natural compounds have been the cornerstone of medicine for centuries, serving as the primary source of therapeutic agents. Early civilizations, such as those in China, Egypt, and India, recorded the application of plant-based medicine in texts like the Ebers, Papyrus, and the Ayurveda, outlining various herbal remedies [160]. African medicine has a long and rich traditional history of natural products, with healers utilizing plant-based treatments to combat and eliminate diseases, including TB, long before modern antibiotics were discovered [161]. This began with the use of *Aspalathus linearis* (rooibos) for its anti-inflammatory properties and *Artemisia* species for respiratory issues [161]. The extraction of bioactive compounds, particularly morphine from *Papaver somniferum* (poppy) during the 19th century, established the foundation of modern pharmacology and highlighted the remarkable therapeutic capabilities of natural products [162].

Natural compounds derived from plants, marine life, and microbial sources exhibit significant antimycobacterial properties, with several already incorporated into TB therapies [157, 163-166]. The rich biodiversity of Africa, which is characterized by its extensive array of medicinal plants, fungi, and marine species, offers a critical resource for discovering new anti-TB medications [167]. One example is the extract from *Pelargonium sidoides*, which has been commercialized as the herbal medicine Umckaloabo for treating respiratory infections [168].

The SANCDB is a valuable resource for pinpointing bioactive compounds that could have anti-TB effects [163, 167]. A variety of natural compounds, such as alkaloids, phenols, terpenoids, and flavonoids, have shown strong anti-inflammatory, antimycobacterial, anti-TB, and antioxidant activities, making them attractive options for therapeutic development (Figure 2.17) [163, 164, 167]. These secondary metabolites are generated by organisms to promote health benefits, fulfill ecological roles, or defend themselves against danger, highlighting their various biological functions [169, 170]. The focus on utilizing natural compounds for the prevention and treatment of various diseases has gained more recognition in recent years. Presently, these compounds play a crucial role in pharmaceuticals, with numerous medications derived from plants, fungi, and marine organisms [163, 164, 166].

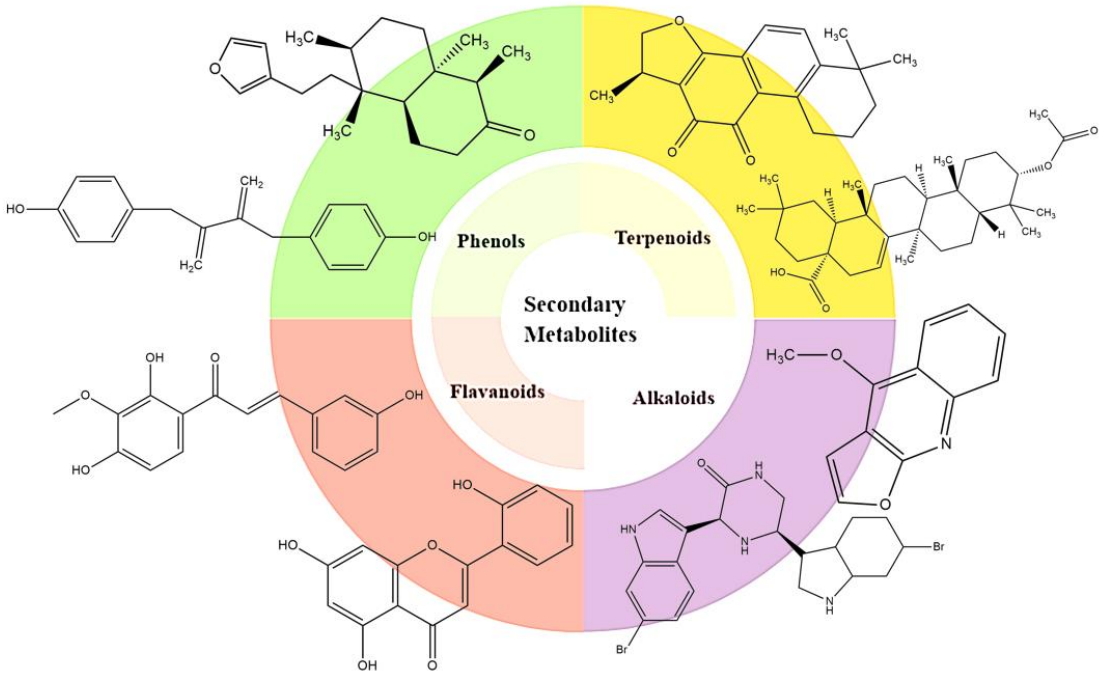

Figure 2.17: Classification of plants, marine life, and microbial-derived secondary metabolites is divided into four major groups: phenols, terpenoids, flavonoids, and alkaloids. This classification includes representative chemical structures that highlight their structural diversity and functional significance in biological and pharmacological processes.

A series of studies have pinpointed various South African natural compounds that may possess anti-*M. tuberculosis* properties, in aiding drug discovery efforts [163, 164]. Quinoline-based structures, found in numerous natural products, have shown moderate activity against TB, with the quinoline ring being viewed as a promising scaffold for creating new TB medications [171]. Likewise, diterpenoids, a category of phytochemicals, have demonstrated notable antimicrobial effects, including against *M. tuberculosis* [172].

Gladiolin, a polyketide natural product from *Burkholderia gladioli*, has shown encouraging efficacy against *M. tuberculosis*, including resistant strains, and offers greater structural stability compared to similar compounds, thus boosting its therapeutic potential [173]. Calanolide A, initially recognized for its anti-HIV activity, has also demonstrated effectiveness against both drug-susceptible and drug-resistant *M. tuberculosis*, underlining its promise as a versatile therapeutic agent [174].

Considering the limitations of current TB treatments and the emergence of drug resistance, the search for novel TB inhibitors from natural sources is becoming increasingly important [166]. This growing interest in natural compounds stems from their structural diversity, biological relevance, and evolutionary fine-tuning, which provides them with therapeutic advantages over synthetic drugs [163, 175].

Natural compounds tend to result in lower mortality rates among TB patients due to reduced toxicity and fewer side effects [170, 176].

In contrast, synthetic medications, frequently used for treating various metabolic and degenerative conditions, can be costly and lead to significant side effects [176]. Natural options are generally more affordable and accessible than conventional drugs, offering a practical solution, particularly in resource-limited areas [177]. Moreover, developing tolerance and experiencing relapses can restrict the long-term benefits of synthetic treatments [170]. Natural products, derived from plant-based foods or traditional medicine, could serve as lead compounds or templates for designing potentially superior alternatives [175]. These natural compounds often strengthen the body's natural healing processes, contributing to their overall efficacy [176]. This approach could lead to better treatment results and enhanced patient adherence, as many individuals prefer herbal remedies for their gentle, non-invasive nature compared to traditional pharmaceuticals [176].

Past research has also highlighted natural products that have the potential to inhibit *M. tuberculosis* proteins, and these include biotin synthase, ATP synthase, and 1,4-dihydroxy-2-naphthoate prenyltransferase, representing novel avenues for TB drug development [157]. Exploration of these natural compounds offers promising directions for new anti-TB therapies, particularly in addressing the growing challenge of drug resistance, non-adherence, and side effects. However, integrating them with synthetic modifications enhances their drug-like properties (synergistic effect).

Advances in computer-aided drug discovery, crystallographic studies of molecules, and synthetic biology have further enhanced the potential of natural products, ensuring their continued relevance in the development of new and effective treatments for TB and other diseases [159].

2.10. Computer-Aided Drug Discovery Approach

Drug discovery is a long and complicated journey that begins with understanding the biological cause of a disease [178]. As shown in

Figure 2.18, scientists begin by pinpointing a molecule (target) in the body that plays a role in the disease (stage 1). Once the target is confirmed, researchers search for chemical compounds that can affect its function (stage 1) [178, 179]. Promising compounds are then improved through careful design and testing [179]. Before any human testing can begin, these candidates are evaluated in lab and animal studies to evaluate their safety and effectiveness (stage 2). If a positive outcome is obtained, the drug then moves into human clinical trials, which take place in multiple phases to ensure the drug works and is safe (stage 3) [179]. After completing these trials, the drug needs to be reviewed and approved by health authorities like the FDA (stage 4) [179]. Only after passing all these steps is the medicine made available to the public (stage 5) [180]. The full process usually takes a decade or more.

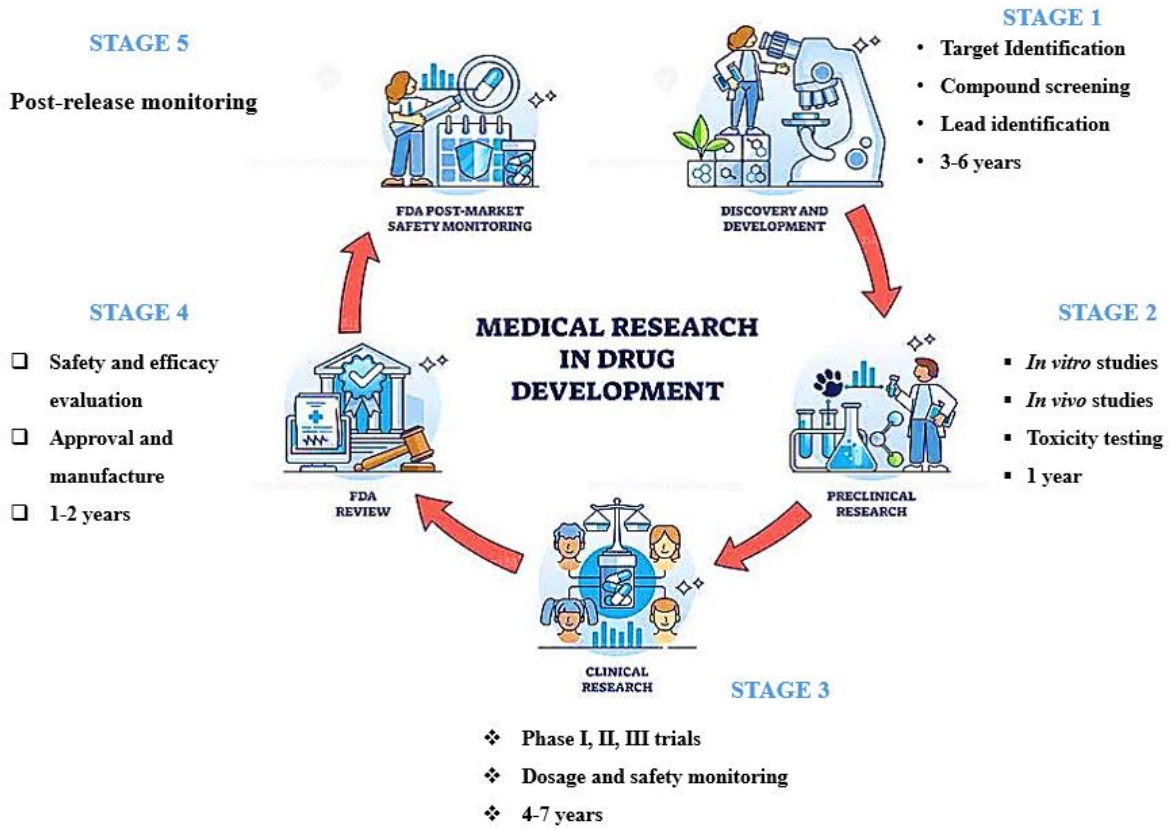

Figure 2.18: Schematic illustration of the complex journey that entails bringing a new pharmaceutical from the lab to the patient begins with laboratory discovery (stage 1), followed by laboratory validations (stage 2), clinical trials (stage 3), FDA review (stage 4), and long-term safety monitoring.[181]

Computational chemistry accelerates the drug discovery process through molecular modeling, a computational technique commonly used in drug design as a standard technique in the field. The identification of bedaquiline exemplifies this, the first anti-drug-resistant TB drug, through *in-silico* screening combined with structure-based design [72, 95, 182]. This technique allows researchers to rapidly evaluate thousands of compounds, streamlining the pathway to developing new treatments. Molecular modeling provides insight into the physical properties, interactions, and dynamics [183]. Molecular modeling is a subset of *in-silico* techniques.

The *in-silico* technique is a computational approach that enables researchers to scan through thousands of chemical compounds to find those that can interact well with a specific protein or enzyme. [184]. Once promising candidates have been identified, molecular docking is used to see how well these molecules fit into the target's binding site and what kind of interactions might take place. [184]. This allows for the selection of the most promising candidate based on binding scores [184]. To ensure the reliability of these findings, the best-fitting compounds are then tested further using simulations that mimic real biological conditions, helping scientists understand how stable the molecule-target complex would be over time [184]. These findings are further reaffirmed through binding free energy calculations using MM-PBSA/MM-GBSA, which provides more accurate insights into the strength and stability of these interactions [185]. In comparison to the lengthy and expensive process of traditional drug development, this method offers a quicker, more cost-effective route to narrowing down potential drug candidates [185, 186]. Figure 2.19 outlines the limitations and benefits of conventional drug discovery and the *in-silico* method.

In silico drug discovery has become a fundamental aspect of modern pharmaceutical research, working side by side with traditional screening methods to improve the likelihood of identifying effective drug candidates [184]. Researchers can now quickly identify, design, and examine the therapeutic potential of new compounds, using computational tools [184]. The most important step in drug discovery, ADMET drug-likeness evaluation, predicts toxicity and helps to identify potential adverse effects early, ultimately saving time and resources [184]. Virtual ligand screening, molecular modeling, and docking-based virtual screening shed light on binding mechanisms and interactions, opening doors to exciting and innovative drug discoveries [184].

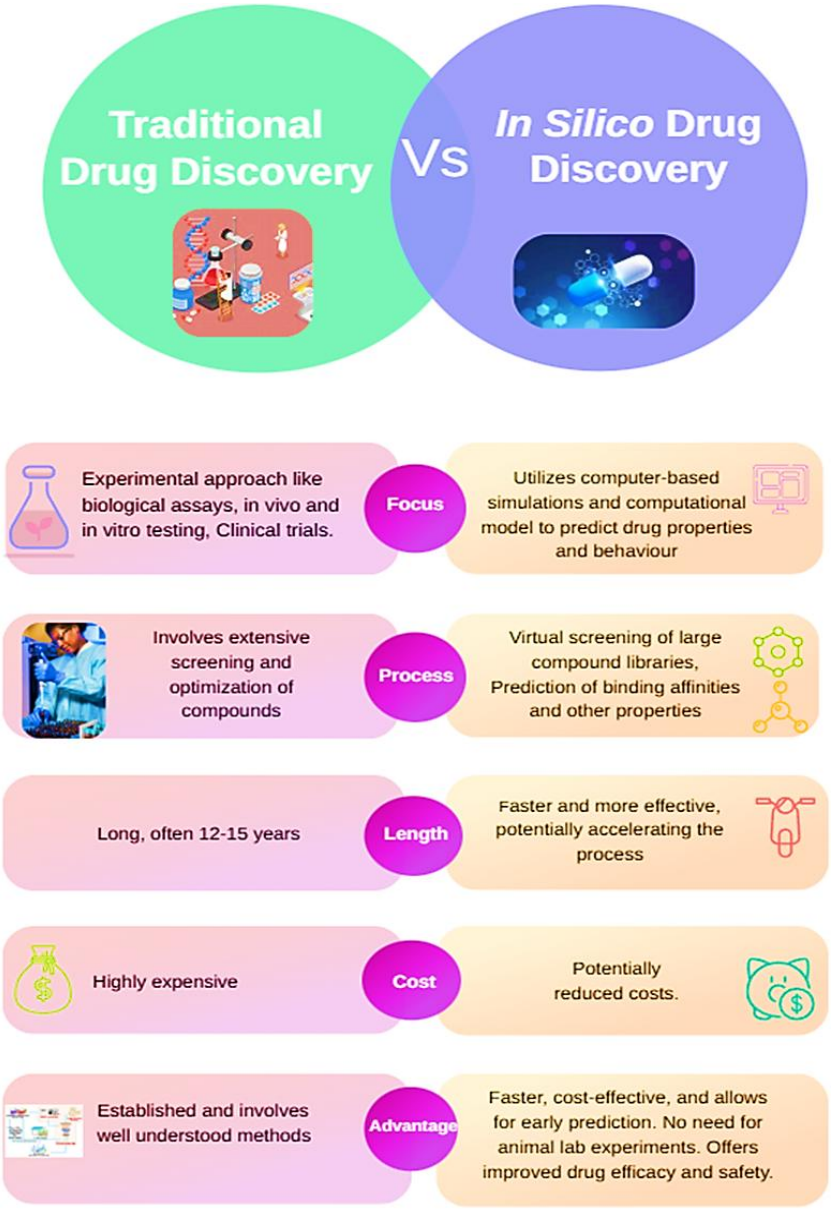

Figure 2.19: "Finding Your Way in Drug Discovery: Mixing New Ideas with Real-Life Challenges in Creating Life-Saving Medicines."

While many studies have demonstrated the potential of computational techniques in drug discovery over the years,[187] several limitations persist, hindering the full potential use of this methodology. Many *in silico* findings stop at the computer screen and are not validated through experimental assays, limiting translational value [188]. Others use generic compound libraries that ignore the unique biodiversity of compounds in regions like South Africa. Very often, studies focus on single molecular targets when what we need are multi-target approaches that reflect the complexity of drug-resistant strains. Pharmacokinetic and toxicity predictions are often not integrated into early-stage screening [189], leading to false positives.

References

1. Daniel, V.S. and T.M. Daniel, *Old Testament biblical references to tuberculosis.* Clin Infect Dis, 1999. **29**(6): p. 1557–8.
2. Dormandy, T., *The White Death: A History of Tuberculosis*. 2000: NYU Press.
3. Dubos, R.J. and J. Dubos, *The White Plague: Tuberculosis, Man and Society*. 1952: Little, Brown.
4. Hippocrates, T. Coar, and L. Verhoofd, *The aphorisms of Hippocrates: with a translation into Latin and English*. 1982: Classics of Medicine Library.
5. Major, R.H., *Classic Descriptions of Disease: With Biographical Sketches of the Authors*. 1932: Charles C. Thomas.
6. Prevention, C.f.D.C.a. *Clinical Overview of Tuberculosis*. 2025 [cited 2025 03/02]; Available from:https://www.cdc.gov/tb/hcp/clinical-overview/index.html?form=MG0AV3&form=MG0AV3.
7. National Center for HIV/AIDS, V.H., STD, and TB Prevention (U.S.). Division of Tuberculosis Elimination. *History of World TB Day*. World TB Day 2018 [cited 2025 29/03]; Available from: https://stacks.cdc.gov/view/cdc/52419.
8. *History of World TB Day.* 2018.
9. Daniel, T.M., *The history of tuberculosis.* Respiratory Medicine, 2006. **100**(11): p. 1862–1870.
10. World Health, O., *Global tuberculosis report 2024*. 2024, Geneva: World Health Organization.
11. Fogel, N., *Tuberculosis: a disease without boundaries.* Tuberculosis (Edinb), 2015. **95**(5): p. 527–31.
12. Barberis, I., N. Bragazzi, L. Galluzzo, and M. Martini, *The history of tuberculosis: From the first historical records to the isolation of Koch's bacillus.* Journal of preventive medicine and hygiene, 2017. **58**: p. 9–12.
13. Gutierrez, M.C., S. Brisse, R. Brosch, M. Fabre, B. Omaïs, M. Marmiesse, P. Supply, and V. Vincent, *Ancient Origin and Gene Mosaicism of the Progenitor of Mycobacterium tuberculosis.* PLoS Pathogens, 2005. **1**(1): p. e5.
14. Cambier, C.J., S. Falkow, and L. Ramakrishnan, *Host Evasion and Exploitation Schemes of Mycobacterium tuberculosis.* Cell, 2014. **159**(7): p. 1497–1509.
15. Zink, A.R., C. Sola, U. Reischl, W. Grabner, N. Rastogi, H. Wolf, and A.G. Nerlich, *Characterization of Mycobacterium tuberculosis complex DNAs from Egyptian mummies by spoligotyping.* J Clin Microbiol, 2003. **41**(1): p. 359–67.
16. Hershkovitz, I., H.D. Donoghue, D.E. Minnikin, H. May, O.Y.C. Lee, M. Feldman, E. Galili, M. Spigelman, B.M. Rothschild, and G.K. Bar-Gal, *Tuberculosis origin: The Neolithic scenario.* Tuberculosis, 2015. **95**: p. S122–S126.

17. Barnes, D.S., *Historical perspectives on the etiology of tuberculosis.* Microbes and Infection, 2000. **2**(4): p. 431–440.
18. Koch, R., T.D. Brock, and E.B. Fred, *The Etiology of Tuberculosis.* Reviews of Infectious Diseases, 1982. **4**(6): p. 1270–1274.
19. Bishop, P.J. and G. Neumann, *The history of the Ziehl-Neelsen stain.* Tubercle, 1970. **51**(2): p. 196–206.
20. Velayati, A. and P. Farnia, *Morphological Characterization of Mycobacterium tuberculosis*. 2012.
21. Jay, V., *Paul Ehrlich.* Archives of Pathology & Laboratory Medicine, 2001. **125**(6): p. 725–725.
22. Talbot, E.A. and B.J. Raffa, *Chapter 92 - Mycobacterium tuberculosis*, in *Molecular Medical Microbiology (Second Edition)*, Y.-W. Tang, et al., Editors. 2015, Academic Press: Boston. p. 1637–1653.
23. Gupta, R.S., B. Lo, and J. Son, *Phylogenomics and Comparative Genomic Studies Robustly Support Division of the Genus Mycobacterium into an Emended Genus Mycobacterium and Four Novel Genera.* Front Microbiol, 2018. **9**: p. 67.
24. Koch, A. and V. Mizrahi, *Mycobacterium tuberculosis.* Trends Microbiol, 2018. **26**(6): p. 555–556.
25. Jankute, M., J.A. Cox, J. Harrison, and G.S. Besra, *Assembly of the Mycobacterial Cell Wall.* Annu Rev Microbiol, 2015. **69**: p. 405–23.
26. Daffé, M. and H. Marrakchi, *Unraveling the Structure of the Mycobacterial Envelope.* Microbiology Spectrum, 2019. **7**(4): p. 10.1128/microbiolspec.gpp3–0027–2018.
27. Delogu, G., M. Sali, and G. Fadda, *The Biology of Mycobacterium Tuberculosis Infection.* Mediterranean Journal of Hematology and Infectious Diseases, 2013. **5**(1): p. e2013070.
28. Kaufmann, S.H.E., *How can immunology contribute to the control of tuberculosis?* Nature Reviews Immunology, 2001. **1**(1): p. 20–30.
29. Rastogi, N., E. Legrand, and C. Sola, *The mycobacteria: an introduction to nomenclature and pathogenesis.* Rev Sci Tech, 2001. **20**(1): p. 21–54.
30. Allué-Guardia, A., J.I. García, and J.B. Torrelles, *Evolution of Drug-Resistant Mycobacterium tuberculosis Strains and Their Adaptation to the Human Lung Environment.* Frontiers in Microbiology, 2021. **12**.
31. Singh, P.R., A.K. Vijjamarri, and D. Sarkar, *Metabolic Switching of Mycobacterium tuberculosis during Hypoxia Is Controlled by the Virulence Regulator PhoP.* J Bacteriol, 2020. **202**(7).
32. Tufariello, J.M., J. Chan, and J.L. Flynn, *Latent tuberculosis: mechanisms of host and bacillus that contribute to persistent infection.* The Lancet Infectious Diseases, 2003. **3**(9): p. 578–590.
33. Kiazyk, S. and T.B. Ball, *Latent tuberculosis infection: An overview.* Can Commun Dis Rep, 2017. **43**(3-4): p. 62–66.
34. Tobin, E.H. and D. Tristram, *Tuberculosis*, in *StatPearls*. 2024, StatPearls Publishing

35. Organization, W.H. *WHO calls for urgent action to address worldwide disruptions in tuberculosis services putting millions of lives at risk*. 2025 20/03/2025 [cited 2025 22/03]; Available from: https://www.who.int/news/item/20-03-2025-who-calls-for-urgent-action-to-address-worldwide-disruptions-in-tuberculosis-services-putting-millions-of-lives-at-risk.
36. Liebenberg, D., B.G. Gordhan, and B.D. Kana, *Drug resistant tuberculosis: Implications for transmission, diagnosis, and disease management.* Front Cell Infect Microbiol, 2022. **12**: p. 943545.
37. World Health, O., *Key updates to the treatment of drug-resistant tuberculosis: rapid communication, June 2024*. 2024, World Health Organization: Geneva.
38. Ndlovu, N., A. Gray, N. Blose, and M. Mokganya, *Health and Related Indicators, 2023.* South African Health Review, 2024. **26**.
39. Olivier, C. and L. Luies, *WHO Goals and Beyond: Managing HIV/TB Co-infection in South Africa.* SN Comprehensive Clinical Medicine, 2023. **5**(1).
40. World Health Organization. Regional Office for, A., *Tuberculosis in the WHO African Region: 2023 progress update*. 2023, World Health Organization. Regional Office for Africa: Brazzaville.
41. *Transmission and pathogenesis of tuberculosis.* 2016.
42. Health, N.D.o., *National TB Recovery Plan 4.0 April 2025 – March 2026.*, N.D.o. Health, Editor. 2025.
43. Heemskerk, D., M. Caws, B. Marais, and J. Farrar, *Wellcome Trust–Funded Monographs and Book Chapters*, in *Tuberculosis in Adults and Children*. 2015, Springer

44. Tuberculosis, C. *Tuberculosis: Causes and How It Spreads*. 2025 17/01/2025 [cited 2025 03/30]; Available from: https://www.cdc.gov/tb/causes/index.html.
45. Zhuang, L., L. Yang, L. Li, Z. Ye, and W. Gong, *Mycobacterium tuberculosis: immune response, biomarkers, and therapeutic intervention.* MedComm, 2024. **5**(1).
46. Cusabio. *Tuberculosis--A Resurgent*. 2025 [cited 2025 01/04]; Available from: https://www.cusabio.com/c-21087.html.
47. Gideon, H.P. and J.L. Flynn, *Latent tuberculosis: what the host "sees"?* Immunologic Research, 2011. **50**(2-3): p. 202–212.
48. Cruz-Knight, W. and L. Blake-Gumbs, *Tuberculosis: an overview.* Prim Care, 2013. **40**(3): p. 743–56.
49. Golden, M.P. and H.R. Vikram, *Extrapulmonary tuberculosis: an overview.* Am Fam Physician, 2005. **72**(9): p. 1761–8.

50. Prevention, C.f.D.C.a. *Signs and Symptoms of Tuberculosis*. Tuberculosis (TB) 2025 17/01 [cited 2025 01/07]; Available from: https://www.cdc.gov/tb/signs-symptoms/index.html.
51. O'Garra, A., P.S. Redford, F.W. McNab, C.I. Bloom, R.J. Wilkinson, and M.P. Berry, *The immune response in tuberculosis.* Annu Rev Immunol, 2013. **31**: p. 475–527.
52. Ravesloot-Chávez, M.M., E. Van Dis, and S.A. Stanley, *The Innate Immune Response to Mycobacterium tuberculosis Infection.* Annu Rev Immunol, 2021. **39**: p. 611–637.
53. Azadi, D., T. Motallebirad, K. Ghaffari, and H. Shojaei, *Mycobacteriosis and Tuberculosis: Laboratory Diagnosis.* Open Microbiol J, 2018. **12**: p. 41–58.
54. Caulfield, A.J. and N.L. Wengenack, *Diagnosis of active tuberculosis disease: From microscopy to molecular techniques.* J Clin Tuberc Other Mycobact Dis, 2016. **4**: p. 33–43.
55. Zaporojan, N., R.A. Negrean, H. Ramona, C. Zaporojan, A. Csep, and D. Zaha, *Evolution of Laboratory Diagnosis of Tuberculosis*. 2023.
56. Ssengooba, W., A. Katamba, J. Sserubiri, D. Semugenze, A. Nyombi, R. Byaruhanga, S. Turyahabwe, and M.L. Joloba, *Performance evaluation of Truenat MTB and Truenat MTB-RIF DX assays in comparison to gene XPERT MTB/RIF ultra for the diagnosis of pulmonary tuberculosis in Uganda.* BMC Infectious Diseases, 2024. **24**(1): p. 190.
57. Matteo, M.J., M.C. Latini, D.N. Martinovic, and M. Bottiglieri, *Update of diagnostic methods in tuberculosis (TB).* Rev Argent Microbiol, 2025. **57**(1): p. 49–53.
58. Gaba, D.P., *Fujifilm SILVAMP TB LAM: A Breakthrough Urine Test for Tuberculosis Diagnosis in HIV Patients*. 2025, labdecoded.blogspot.com.
59. Khalifa, M. and M. Albadawy, *AI in diagnostic imaging: Revolutionising accuracy and efficiency.* Computer Methods and Programs in Biomedicine Update, 2024. **5**: p. 100146.
60. Jalloul, M., D. Alkhulaifat, M. Miranda-Schaeubinger, L. De Leon Benedetti, H.J. Otero, and F. Dako, *Artificial Intelligence in Chest Radiology: Advancements and Applications for Improved Global Health Outcomes.* Current Pulmonology Reports, 2024. **13**(1): p. 1–9.
61. Agizew, T.B., J. Soka, C.D. Fast, S. Mwimanzi, G. Mwesiga, N. Edward, M. Stephen, R. Kondo, R. Burny, C. Cox, and N. Beyene, *Increased tuberculosis case detection in Tanzanian children and adults using African giant pouched rats.* BMC Infectious Diseases, 2024. **24**(1): p. 401.
62. Gunasekera, K.S., O. Marcy, J. Muñoz, E. Lopez-Varela, M.P. Sekadde, M.F. Franke, M. Bonnet, S. Ahmed, F. Amanullah, A. Anwar, O. Augusto, R.B. Aurilio, S. Banu, I. Batool, A. Brands, K.P. Cain, L. Carratalá-Castro, M. Caws, E.S. Click, . . . J.A. Seddon, *Development of treatment-decision algorithms for children evaluated for pulmonary tuberculosis: an individual participant data meta-analysis.* Lancet Child Adolesc Health, 2023. **7**(5): p. 336–346.
63. World Health, O., *WHO operational handbook on tuberculosis: module 5: management of tuberculosis in children and adolescents*. 2022, Geneva: World Health Organization.
64. TDR.who.int *Enhancing TB diagnosis and treatment for children in Africa*. 2025.

65. Patriarca, C., G. Lo Bello, S. Zannella, and S.A. Agati, *Tuberculosis: the sanatorium season in the early 20th century.* Pathologica, 2022. **114**(4): p. 342–346.
66. Abraham, E.P., E.B. Chain, C.M. Fletcher, A.D. Gardner, N.G. Heatley, M.A. Jennings, and H. Florey, *Further Observations on Penicillin.* The Lancet, 1941. **238**: p. 177–189.
67. World Health, O., *Global tuberculosis report 2023*. 2023, Geneva: World Health Organization.
68. Rahlwes, K.C., D.B.R. S., C.P. C., A.-A. Samuel, and M.U. and Shiloh, *Pathogenicity and virulence of Mycobacterium tuberculosis.* Virulence, 2023. **14**(1): p. 2150449.
69. Schatz, A., E. Bugle, and S.A. Waksman, *Streptomycin, a Substance Exhibiting Antibiotic Activity Against Gram-Positive and Gram-Negative Bacteria.∗†.* Proceedings of the Society for Experimental Biology and Medicine, 1944. **55**: p. 66 – 69.
70. Thida Oo, N.A., L.L. San, J. Thapa, K.S. Aye, W.W. Aung, C. Nakajima, and Y. Suzuki, *Characterization of mutations conferring streptomycin resistance to multidrug-resistant Mycobacterium tuberculosis isolates from Myanmar.* Tuberculosis, 2018. **111**: p. 8–13.
71. Somasundaram, S., A. Ram, and L. Sankaranarayanan, *Isoniazid and Rifampicin as Therapeutic Regimen in the Current Era: A Review.* Journal of Tuberculosis Research, 2014. **02**: p. 40–51.
72. Bandodkar, B., R.K. Shandil, J. Bhat, and T.S. Balganesh, *Two Decades of TB Drug Discovery Efforts—What Have We Learned?* Applied Sciences, 2020. **10**(16): p. 5704.
73. Heidary, M., M. Shirani, M. Moradi, M. Goudarzi, R. Pouriran, T. Rezaeian, and S. Khoshnood, *Tuberculosis challenges: Resistance, co-infection, diagnosis, and treatment.* Eur J Microbiol Immunol (Bp), 2022. **12**(1): p. 1–17.
74. World Health, O., *WHO consolidated guidelines on tuberculosis: module 1: prevention: tuberculosis preventive treatment*. 2nd ed. 2024, Geneva: World Health Organization.
75. Mirzayev, F., *Updated WHO consolidated guidelines on DR-TB treatment 2025*. 2025.
76. Timmins, G.S. and V. Deretic, *Mechanisms of action of isoniazid.* Molecular Microbiology, 2006. **62**(5): p. 1220–1227.
77. Abulfathi, A.A., E.H. Decloedt, E.M. Svensson, A.H. Diacon, P. Donald, and H. Reuter, *Clinical Pharmacokinetics and Pharmacodynamics of Rifampicin in Human Tuberculosis.* Clin Pharmacokinet, 2019. **58**(9): p. 1103–1129.
78. Beloor Suresh, A., A. Rosani, P. Patel, and R. Wadhwa, *Rifampin*, in *StatPearls*. 2025, StatPearls Publishing

79. Zhang, Y., W. Shi, W. Zhang, and D. Mitchison, *Mechanisms of Pyrazinamide Action and Resistance.* Microbiol Spectr, 2013. **2**(4): p. 1–12.
80. Shi, W., X. Zhang, X. Jiang, H. Yuan, J.S. Lee, C.E. Barry, 3rd, H. Wang, W. Zhang, and Y. Zhang, *Pyrazinamide inhibits trans-translation in Mycobacterium tuberculosis.* Science, 2011. **333**(6049): p. 1630–2.

81. Fox, G.J. and D. Menzies, *A Review of the Evidence for Using Bedaquiline (TMC207) to Treat Multi-Drug Resistant Tuberculosis.* Infect Dis Ther, 2013. **2**(2): p. 123–44.
82. Thompson, A.M., M. Bonnet, H.H. Lee, S.G. Franzblau, B. Wan, G.S. Wong, C.B. Cooper, and W.A. Denny, *Antitubercular Nitroimidazoles Revisited: Synthesis and Activity of the Authentic 3-Nitro Isomer of Pretomanid.* ACS Med Chem Lett, 2017. **8**(12): p. 1275–1280.
83. Azzouz, A. and C.V. Preuss, *Linezolid*, in *StatPearls*. 2025, StatPearls Publishing

Copyright © 2025, StatPearls Publishing LLC.: Treasure Island (FL).

84. Waters, M. and P. Tadi, *Streptomycin*, in *StatPearls*. 2025, StatPearls Publishing

Copyright © 2025, StatPearls Publishing LLC.: Treasure Island (FL).

85. Sloan, D. and J. Lewis, *The role of delamanid in the treatment of drug-resistant tuberculosis.* Therapeutics and Clinical Risk Management, 2015: p. 779.
86. Stadler, J.A.M., G. Maartens, G. Meintjes, and S. Wasserman, *Clofazimine for the treatment of tuberculosis.* Frontiers in Pharmacology, 2023. **14**.
87. Fish, D.N. and A.T. Chow, *The clinical pharmacokinetics of levofloxacin.* Clin Pharmacokinet, 1997. **32**(2): p. 101–19.
88. Ginsburg, A.S., N. Hooper, N. Parrish, K.E. Dooley, S.E. Dorman, J. Booth, M. Diener-West, W.G. Merz, W.R. Bishai, and T.R. Sterling, *Fluoroquinolone resistance in patients with newly diagnosed tuberculosis.* Clin Infect Dis, 2003. **37**(11): p. 1448–52.
89. Schami, A., M.N. Islam, J.T. Belisle, and J.B. Torrelles, *Drug-resistant strains of Mycobacterium tuberculosis: cell envelope profiles and interactions with the host.* Front Cell Infect Microbiol, 2023. **13**: p. 1274175.
90. Saukkonen, J.J., R. Duarte, S.S. Munsiff, C.A. Winston, M.J. Mammen, I. Abubakar, C. Acuña-Villaorduña, P.M. Barry, M.L. Bastos, W. Carr, H. Chami, L.L. Chen, T. Chorba, C.L. Daley, A.J. Garcia-Prats, K. Holland, I. Konstantinidis, M. Lipman, G. Battista Migliori, . . . P. Nahid, *Updates on the Treatment of Drug-Susceptible and Drug-Resistant Tuberculosis: An Official ATS/CDC/ERS/IDSA Clinical Practice Guideline.* American Journal of Respiratory and Critical Care Medicine, 2025. **211**(1): p. 15–33.
91. World Health, O., *WHO consolidated guidelines on tuberculosis: module 4: treatment and care*. 2025, Geneva: World Health Organization.
92. World Health, O., *Consolidated guidelines on differentiated HIV testing services*. 2024, Geneva: World Health Organization.
93. Conradie, F., A.H. Diacon, N. Ngubane, P. Howell, D. Everitt, A.M. Crook, C.M. Mendel, E. Egizi, J. Moreira, J. Timm, T.D. McHugh, G.H. Wills, A. Bateson, R. Hunt, C. Van Niekerk, M. Li, M. Olugbosi, and M. Spigelman, *Treatment of Highly Drug-Resistant Pulmonary Tuberculosis.* New England Journal of Medicine, 2020. **382**(10): p. 893–902.

94. Hartkoorn, R.C., S. Uplekar, and S.T. Cole, *Cross-resistance between clofazimine and bedaquiline through upregulation of mmpl5 in mycobacterium tuberculosis.* Antimicrobial Agents and Chemotherapy, 2014. **58**(5): p. 2979–2981.

95. Andries, K., P. Verhasselt, J. Guillemont, H.W.H. GöHlmann, J.-M. Neefs, H. Winkler, J. Van Gestel, P. Timmerman, M. Zhu, E. Lee, P. Williams, D. De Chaffoy, E. Huitric, S. Hoffner, E. Cambau, C. Truffot-Pernot, N. Lounis, and V. Jarlier, *A Diarylquinoline Drug Active on the ATP Synthase of Mycobacterium tuberculosis.* Science, 2005. **307**(5707): p. 223–227.

96. Hoffmann, H., T.A. Kohl, S. Hofmann-Thiel, M. Merker, P. Beckert, K. Jaton, L. Nedialkova, E. Sahalchyk, T. Rothe, P.M. Keller, and S. Niemann, *Delamanid and Bedaquiline Resistance in Mycobacterium tuberculosis Ancestral Beijing Genotype Causing Extensively Drug-Resistant Tuberculosis in a Tibetan Refugee.* American Journal of Respiratory and Critical Care Medicine, 2016. **193**(3): p. 337–340.

97. Andries, K., C. Villellas, N. Coeck, K. Thys, T. Gevers, L. Vranckx, N. Lounis, B.C. De Jong, and A. Koul, *Acquired Resistance of Mycobacterium tuberculosis to Bedaquiline.* PLoS ONE, 2014. **9**(7): p. e102135.

98. Nguyen, T.V.A., R.M. Anthony, A.-L. Bañuls, T.V.A. Nguyen, D.H. Vu, and J.-W.C. Alffenaar, *Bedaquiline Resistance: Its Emergence, Mechanism, and Prevention.* Clinical Infectious Diseases, 2018. **66**(10): p. 1625–1630.

99. Böttger, E.C. and B. Springer, *Tuberculosis: drug resistance, fitness, and strategies for global control.* European Journal of Pediatrics, 2008. **167**(2): p. 141–148.

100. Ismail, N.A., S.V. Omar, L. Joseph, N. Govender, L. Blows, F. Ismail, H. Koornhof, A.W. Dreyer, K. Kaniga, and N. Ndjeka, *Defining Bedaquiline Susceptibility, Resistance, Cross-Resistance and Associated Genetic Determinants: A Retrospective Cohort Study.* EBioMedicine, 2018. **28**: p. 136–142.

101. Li, C., D. Shang, Y. Wang, J. Li, J. Han, S. Wang, Q. Yao, Y. Wang, Y. Zhang, C. Zhang, Y. Xu, W. Jiang, and X. Li, *Characterizing the Network of Drugs and Their Affected Metabolic Subpathways.* PLoS ONE, 2012. **7**(10): p. e47326.

102. Zhou, M., M. Xu, X. Zhang, X. Xing, Y. Li, G. Wang, and G. Yan, *HPRNA: Predicting synergistic drug combinations for angina pectoris based on human pathway relationship network algorithm.* PLOS ONE, 2025. **20**(2): p. e0318368.

103. Sonnenkalb, L., J.J. Carter, A. Spitaleri, Z. Iqbal, M. Hunt, K.M. Malone, C. Utpatel, D.M. Cirillo, C. Rodrigues, K.S. Nilgiriwala, P.W. Fowler, M. Merker, S. Niemann, I. Barilar, S. Battaglia, E. Borroni, A.P. Brandao, A. Brankin, A.M. Cabibbe, . . . B. Zhu, *Bedaquiline and clofazimine resistance in Mycobacterium tuberculosis: an in-vitro and in-silico data analysis.* The Lancet Microbe, 2023. **4**(5): p. e358–e368.

104. Chesov, E., D. Chesov, F.P. Maurer, S. Andres, C. Utpatel, I. Barilar, A. Donica, M. Reimann, S. Niemann, C. Lange, V. Crudu, J. Heyckendorf, and M. Merker, *Emergence of bedaquiline resistance in a high tuberculosis burden country.* Eur Respir J, 2022. **59**(3).

105. Singla, R., S. Khan, A. Silsarma, V. Chavan, R. Mahajan, H. Mansoor, R.K. Devan, N. Singla, M. Bhalla, G. Kumar, P. Singh, A. Iyer, M. Morales, S.C. Devkota, A. Dalal, H. Spencer, and P. Isaakidis, *Bedaquiline Resistance and Treatment Outcomes Among Patients With Tuberculosis Previously Exposed to Bedaquiline in India: A Multicentric Retrospective Cohort Study.* Clinical Infectious Diseases, 2025.

106. Brammachary, U., V. Ramachandra, S. Palavesam, V. Raj Cuppusamy Kapalamurthy, A. Muralidhar, and M. Muthaiah, *Mechanisms and Action of Drug Resistance on Mycobacterium tuberculosis*. 2025, IntechOpen.

107. Gygli, S.M., S. Borrell, A. Trauner, and S. Gagneux, *Antimicrobial resistance in Mycobacterium tuberculosis: mechanistic and evolutionary perspectives.* FEMS Microbiology Reviews, 2017. **41**(3): p. 354–373.

108. Brennan, P.J. and H. Nikaido, *The envelope of mycobacteria.* Annu Rev Biochem, 1995. **64**: p. 29–63.

109. Trivedi, O.A., P. Arora, A. Vats, M.Z. Ansari, R. Tickoo, V. Sridharan, D. Mohanty, and R.S. Gokhale, *Dissecting the mechanism and assembly of a complex virulence mycobacterial lipid.* Mol Cell, 2005. **17**(5): p. 631–43.

110. Team, B. *Mycobacteria Cell Wall Insights: Composition and Function*. 2025 [cited 2025 20/03/2025]; Available from: https://biologyinsights.com/mycobacteria-cell-wall-insights-composition-and-function/.

111. Abrahams, K.A. and G.S. Besra, *Mycobacterial cell wall biosynthesis: a multifaceted antibiotic target.* Parasitology, 2018. **145**(2): p. 116–133.

112. Shetye, G.S., S.G. Franzblau, and S. Cho, *New tuberculosis drug targets, their inhibitors, and potential therapeutic impact.* Translational Research, 2020. **220**: p. 68–97.

113. Gokhale, R., P. Saxena, T. Chopra, and D. Mohanty, *Versatile Polyketide Enzymatic Machinery for the Biosynthesis of Complex Mycobacterial Lipids.* Natural product reports, 2007. **24**: p. 267–77.

114. Shaku, M., C. Ealand, and B.D. Kana, *Cell Surface Biosynthesis and Remodeling Pathways in Mycobacteria Reveal New Drug Targets.* Front Cell Infect Microbiol, 2020. **10**: p. 603382.

115. Zhang, L., Y. Zhao, Y. Gao, L. Wu, R. Gao, Q. Zhang, Y. Wang, C. Wu, F. Wu, S.S. Gurcha, N. Veerapen, S.M. Batt, W. Zhao, L. Qin, X. Yang, M. Wang, Y. Zhu, B. Zhang, L. Bi, . . . Z. Rao, *Structures of cell wall arabinosyltransferases with the anti-tuberculosis drug ethambutol.* Science, 2020. **368**(6496): p. 1211–1219.

116. Das, N., P.K. Jena, and S.K. Pradhan, *Arabinosyltransferase C enzyme of Mycobacterium tuberculosis, a potential drug target: An insight from molecular docking study.* Heliyon, 2020. **6**(2): p. e02693.

117. Yan, M., M. Ma, R. Chen, Y. Cao, W. Zhang, and X. Liu, *Structural basis for the development of potential inhibitors targeting FadD23 from Mycobacterium tuberculosis.* Acta Crystallogr F Struct Biol Commun, 2023. **79**(Pt 8): p. 208–216.

118. Duan, X., X. Xiang, and J. Xie, *Crucial components of mycobacterium type II fatty acid biosynthesis (Fas-II) and their inhibitors.* FEMS Microbiology Letters, 2014. **360**(2): p. 87–99.

119. Guo, Q., C. Zhong, H. Dong, J.E. Cronan, and H. Wang, *Diversity in fatty acid elongation enzymes: The FabB long-chain β-ketoacyl-ACP synthase I initiates fatty acid synthesis in Pseudomonas putida F1.* Journal of Biological Chemistry, 2024. **300**(2): p. 105600.

120. Lai, C.-Y. and J.E. Cronan, *β-Ketoacyl-Acyl Carrier Protein Synthase III (FabH) Is Essential for Bacterial Fatty Acid Synthesis *.* Journal of Biological Chemistry, 2003. **278**(51): p. 51494–51503.

121. Cantaloube, S., R. Veyron-Churlet, N. Haddache, M. Daffé, and D. Zerbib, *The Mycobacterium Tuberculosis FAS-II Dehydratases and Methyltransferases Define the Specificity of the Mycolic Acid Elongation Complexes.* PloS one, 2011. **6**: p. e29564.

122. Kumar, N., R. Srivastava, R.K. Mongre, C.B. Mishra, A. Kumar, R. Khatoon, A. Banerjee, M. Ashraf-Uz-Zaman, H. Singh, A.M. Lynn, M.S. Lee, and A. Prakash, *Identifying the Novel Inhibitors Against the Mycolic Acid Biosynthesis Pathway Target "mtFabH" of Mycobacterium tuberculosis.* Front Microbiol, 2022. **13**: p. 818714.

123. Schaeffer, M.L., G. Agnihotri, C. Volker, H. Kallender, P.J. Brennan, and J.T. Lonsdale, *Purification and biochemical characterization of the Mycobacterium tuberculosis beta-ketoacyl-acyl carrier protein synthases KasA and KasB.* J Biol Chem, 2001. **276**(50): p. 47029–37.

124. Wang, X., W.J. Jowsey, C.Y. Cheung, C.J. Smart, H.R. Klaus, N.E. Seeto, N.J. Waller, M.T. Chrisp, A.L. Peterson, B. Ofori-Anyinam, E. Strong, B. Nijagal, N.P. West, J.H. Yang, P.C. Fineran, G.M. Cook, S.A. Jackson, and M.B. McNeil, *Whole genome CRISPRi screening identifies druggable vulnerabilities in an isoniazid resistant strain of Mycobacterium tuberculosis.* Nat Commun, 2024. **15**(1): p. 9791.

125. Mohanty, D., R. Sankaranarayanan, and R.S. Gokhale, *Fatty acyl-AMP ligases and polyketide synthases are unique enzymes of lipid biosynthetic machinery in Mycobacterium tuberculosis.* Tuberculosis, 2011. **91**(5): p. 448–455.

126. Yan, M., L. Cao, L. Zhao, W. Zhou, X. Liu, W. Zhang, and Z. Rao, *The Key Roles of Mycobacterium tuberculosis FadD23 C-terminal Domain in Catalytic Mechanisms.* Frontiers in Microbiology, 2023. **14**.

127. Cole, S.T., R. Brosch, J. Parkhill, T. Garnier, C. Churcher, D. Harris, S.V. Gordon, K. Eiglmeier, S. Gas, C.E. Barry, F. Tekaia, K. Badcock, D. Basham, D. Brown, T. Chillingworth, R. Connor, R. Davies, K. Devlin, T. Feltwell, . . . B.G. Barrell, *Deciphering the biology of Mycobacterium tuberculosis from the complete genome sequence.* Nature, 1998. **393**(6685): p. 537–544.

128. Baran, M., K.D. Grimes, P.A. Sibbald, P. Fu, H.I.M. Boshoff, D.J. Wilson, and C.C. Aldrich, *Development of small-molecule inhibitors of fatty acyl-AMP and fatty acyl-CoA ligases in Mycobacterium tuberculosis.* Eur J Med Chem, 2020. **201**: p. 112408.

129. Kumar, P., M.W. Schelle, M. Jain, F.L. Lin, C.J. Petzold, M.D. Leavell, J.A. Leary, J.S. Cox, and C.R. Bertozzi, *PapA1 and PapA2 are acyltransferases essential for the biosynthesis of the Mycobacterium tuberculosis virulence factor sulfolipid-1.* Proc Natl Acad Sci U S A, 2007. **104**(27): p. 11221–6.

130. Goyal, A., P. Verma, M. Anandhakrishnan, R.S. Gokhale, and R. Sankaranarayanan, *Molecular Basis of the Functional Divergence of Fatty Acyl-AMP Ligase Biosynthetic Enzymes of Mycobacterium tuberculosis.* Journal of Molecular Biology, 2012. **416**(2): p. 221–238.

131. Bateman, A., M.-J. Martin, S. Orchard, M. Magrane, A. Adesina, S. Ahmad, E.H. Bowler-Barnett, H. Bye-A-Jee, D. Carpentier, P. Denny, J. Fan, P. Garmiri, L.J.D.C. Gonzales, A. Hussein, A. Ignatchenko, G. Insana, R. Ishtiaq, V. Joshi, D. Jyothi, . . . J. Zhang, *FadD23 - Long-chain-fatty-acid--AMP ligase FadD23 - Mycobacterium tuberculosis (strain ATCC 25618 / H37Rv)*. 2025, uniprot: uniprot.

132. Bateman, A., M.-J. Martin, S. Orchard, M. Magrane, A. Adesina, S. Ahmad, E.H. Bowler-Barnett, H. Bye-A-Jee, D. Carpentier, P. Denny, J. Fan, P. Garmiri, L.J.D.C. Gonzales, A. Hussein, A. Ignatchenko, G. Insana, R. Ishtiaq, V. Joshi, D. Jyothi, . . . J. Zhang, *UniProt: the Universal Protein Knowledgebase in 2025.* Nucleic Acids Research, 2025. **53**(D1): p. D609–D617.

133. Patil, G.S., P. Kinatukara, S. Mondal, S. Shambhavi, K.D. Patel, S. Pramanik, N. Dubey, S. Narasimhan, M.K. Madduri, B. Pal, R.S. Gokhale, and R. Sankaranarayanan, *A universal pocket in fatty acyl-AMP ligases ensures redirection of fatty acid pool away from coenzyme A-based activation.* eLife, 2021. **10**: p. e70067.

134. Li, W., S. Gu, J. Fleming, and L. Bi, *Crystal structure of FadD32, an enzyme essential for mycolic acid biosynthesis in mycobacteria.* Scientific Reports, 2015. **5**(1): p. 15493.

135. Kruh, N.A., J.G. Borgaro, B.P. Ruzsicska, H. Xu, and P.J. Tonge, *A Novel Interaction Linking the FAS-II and Phthiocerol Dimycocerosate (PDIM) Biosynthetic Pathways.* Journal of Biological Chemistry, 2008. **283**(46): p. 31719–31725.

136. Mendum, T.A., H. Wu, A.M. Kierzek, and G.R. Stewart, *Lipid metabolism and Type VII secretion systems dominate the genome scale virulence profile of Mycobacterium tuberculosis in human dendritic cells.* BMC Genomics, 2015. **16**(1).

137. Agarwal, N., H. Gogoi, Eeba, L. Augustin, M.Y. Khan, Y. Kumar, S.K. Bhowmick, and B. Dey, *Identifying a novel mechanism of L-leucine uptake in Mycobacterium tuberculosis using a chemical genomic approach*. 2025, eLife Sciences Publications, Ltd.

138. Seeliger, J.C., C.M. Holsclaw, M.W. Schelle, Z. Botyanszki, S.A. Gilmore, S.E. Tully, M. Niederweis, B.F. Cravatt, J.A. Leary, and C.R. Bertozzi, *Elucidation and chemical modulation of sulfolipid-1 biosynthesis in Mycobacterium tuberculosis.* J Biol Chem, 2012. **287**(11): p. 7990–8000.

139. Gilmore, S.A., M.W. Schelle, C.M. Holsclaw, C.D. Leigh, M. Jain, J.S. Cox, J.A. Leary, and C.R. Bertozzi, *Sulfolipid-1 Biosynthesis Restricts Mycobacterium tuberculosis Growth in Human Macrophages.* ACS Chemical Biology, 2012. **7**(5): p. 863–870.

140. Goren, M.B., P. D'Arcy Hart, M.R. Young, and J.A. Armstrong, *Prevention of phagosome-lysosome fusion in cultured macrophages by sulfatides of Mycobacterium tuberculosis.* Proceedings of the National Academy of Sciences, 1976. **73**(7): p. 2510–2514.

141. Pabst, M.J., J.M. Gross, J.P. Brozna, and M.B. Goren, *Inhibition of macrophage priming by sulfatide from Mycobacterium tuberculosis.* J Immunol, 1988. **140**(2): p. 634–40.

142. Brozna, J.P., M. Horan, J.M. Rademacher, K.M. Pabst, and M.J. Pabst, *Monocyte responses to sulfatide from Mycobacterium tuberculosis: inhibition of priming for enhanced release of superoxide, associated with increased secretion of interleukin-1 and tumor necrosis factor alpha, and altered protein phosphorylation.* Infect Immun, 1991. **59**(8): p. 2542–8.

143. Sachdeva, K., M. Goel, M. Sudhakar, M. Mehta, R. Raju, K. Raman, A. Singh, and V. Sundaramurthy, *Mycobacterium tuberculosis (Mtb) lipid mediated lysosomal rewiring in infected macrophages modulates intracellular Mtb trafficking and survival.* Journal of Biological Chemistry, 2020. **295**(27): p. 9192–9210.

144. Zhang, L., D. English, and B.R. Andersen, *Activation of human neutrophils by Mycobacterium tuberculosis-derived sulfolipid-1.* J Immunol, 1991. **146**(8): p. 2730–6.

145. Brozna, J.P., M. Horan, J.M. Rademacher, K.M. Pabst, and M.J. Pabst, *Monocyte responses to sulfatide from Mycobacterium tuberculosis: inhibition of priming for enhanced release of superoxide, associated with increased secretion of interleukin-1 and tumor necrosis factor alpha, and altered protein phosphorylation.* Infection and Immunity, 1991. **59**(8): p. 2542–2548.

146. Ruhl, C.R., B.L. Pasko, H.S. Khan, L.M. Kindt, C.E. Stamm, L.H. Franco, C.C. Hsia, M. Zhou, C.R. Davis, T. Qin, L. Gautron, M.D. Burton, G.L. Mejia, D.K. Naik, G. Dussor, T.J. Price, and M.U. Shiloh, *Mycobacterium tuberculosis Sulfolipid-1 Activates Nociceptive Neurons and Induces Cough.* Cell, 2020. **181**(2): p. 293–305.e11.

147. Marrakchi, M., X. Liu, and S. Andreescu, *Oxidative stress and antibiotic resistance in bacterial pathogens: state of the art, methodologies, and future trends.* Adv Exp Med Biol, 2014. **806**: p. 483–98.

148. Berman, H.M., J. Westbrook, Z. Feng, G. Gilliland, T.N. Bhat, H. Weissig, I.N. Shindyalov, and P.E. Bourne, *The Protein Data Bank.* Nucleic Acids Research, 2000. **28**(1): p. 235–242.

149. Arora, P., A. Goyal, V.T. Natarajan, E. Rajakumara, P. Verma, R. Gupta, M. Yousuf, O.A. Trivedi, D. Mohanty, A. Tyagi, R. Sankaranarayanan, and R.S. Gokhale, *Mechanistic and functional insights into fatty acid activation in Mycobacterium tuberculosis.* Nat Chem Biol, 2009. **5**(3): p. 166–73.

150. Reger, A.S., R. Wu, D. Dunaway-Mariano, and A.M. Gulick, *Structural characterization of a 140 degrees domain movement in the two-step reaction catalyzed by 4-chlorobenzoate:CoA ligase.* Biochemistry, 2008. **47**(31): p. 8016–25.

151. Gande, R., K.J.C. Gibson, A.K. Brown, K. Krumbach, L.G. Dover, H. Sahm, S. Shioyama, T. Oikawa, G.S. Besra, and L. Eggeling, *Acyl-CoA Carboxylases (accD2 and accD3), Together with a Unique Polyketide Synthase (Cg-pks), Are Key to Mycolic Acid Biosynthesis in Corynebacterianeae Such as Corynebacterium glutamicum and Mycobacterium tuberculosis*.* Journal of Biological Chemistry, 2004. **279**(43): p. 44847–44857.

152. Sachdeva, K., M. Goel, M. Sudhakar, M. Mehta, R. Raju, K. Raman, A. Singh, and V. Sundaramurthy, *Mycobacterium tuberculosis (Mtb) lipid mediated lysosomal rewiring in infected macrophages modulates intracellular Mtb trafficking and survival.* J Biol Chem, 2020. **295**(27): p. 9192–9210.

153. Quigley, J., V.K. Hughitt, C.A. Velikovsky, R.A. Mariuzza, N.M. El-Sayed, and V. Briken, *The Cell Wall Lipid PDIM Contributes to Phagosomal Escape and Host Cell Exit ofMycobacterium tuberculosis.* mBio, 2017. **8**(2): p. e00148–17.

154. Lynett, J. and R.W. Stokes, *Selection of transposon mutants of Mycobacterium tuberculosis with increased macrophage infectivity identifies fadD23 to be involved in sulfolipid production and association with macrophages.* Microbiology (Reading), 2007. **153**(Pt 9): p. 3133–3140.

155. Breen, M.E. and M.B. Soellner, *Small molecule substrate phosphorylation site inhibitors of protein kinases: approaches and challenges.* ACS Chem Biol, 2015. **10**(1): p. 175–89.

156. Chakraborty, S. and K.Y. Rhee, *Tuberculosis Drug Development: History and Evolution of the Mechanism-Based Paradigm : Figure 1.* Cold Spring Harbor Perspectives in Medicine, 2015. **5**(8): p. a021147.

157. Han, J., X. Liu, L. Zhang, R.J. Quinn, and Y. Feng, *Anti-mycobacterial natural products and mechanisms of action.* Natural Product Reports, 2022. **39**(1): p. 77–89.

158. Newman, D.J. and G.M. Cragg, *Natural Products as Sources of New Drugs over the Nearly Four Decades from 01/1981 to 09/2019.* Journal of Natural Products, 2020. **83**(3): p. 770–803.

159. Harvey, A.L., R. Edrada-Ebel, and R.J. Quinn, *The re-emergence of natural products for drug discovery in the genomics era.* Nature Reviews Drug Discovery, 2015. **14**(2): p. 111–129.

160. Naidoo, K. and R. Coopoosamy, *Review on herbal remedies used by the 1860 South African Indian settlers.* Afr J Biotechnol, 2010. **10**.

161. Van Wyk, B.E., *The potential of South African plants in the development of new medicinal products.* South African Journal of Botany, 2011. **77**(4): p. 812–829.
162. Cordell, G.A., *Fifty years of alkaloid biosynthesis in Phytochemistry.* Phytochemistry, 2013. **91**: p. 29–51.
163. Hatherley, R., D. Brown, T. Musyoka, D. Penkler, N. Faya, K. Lobb, and O. Tastan Bishop, *SANCDB: a South African natural compound database.* Journal of cheminformatics, 2015. **7**.
164. Atanasov, A.G., S.B. Zotchev, V.M. Dirsch, and C.T. Supuran, *Natural products in drug discovery: advances and opportunities.* Nat Rev Drug Discov, 2021. **20**(3): p. 200–216.
165. Cazzaniga, G., M. Mori, L.R. Chiarelli, A. Gelain, F. Meneghetti, and S. Villa, *Natural products against key Mycobacterium tuberculosis enzymatic targets: Emerging opportunities for drug discovery.* European Journal of Medicinal Chemistry, 2021. **224**: p. 113732.
166. Kumar, G. and A. C, *Natural products and their analogues acting against Mycobacterium tuberculosis: A recent update.* Drug Dev Res, 2023. **84**(5): p. 779–804.
167. Diallo, B.N., M. Glenister, T.M. Musyoka, K. Lobb, and Ö. Tastan Bishop, *SANCDB: an update on South African natural compounds and their readily available analogs.* J Cheminform, 2021. **13**(1): p. 37.
168. Kolodziej, H., O. Kayser, O.A. Radtke, A.F. Kiderlen, and E. Koch, *Pharmacological profile of extracts of Pelargonium sidoides and their constituents.* Phytomedicine, 2003. **10 Suppl 4**: p. 18–24.
169. Zhang, A., H. Sun, and X. Wang, *Recent advances in natural products from plants for treatment of liver diseases.* Eur J Med Chem, 2013. **63**: p. 570–7.
170. Al-Sayed, E., I. Somasundaram, D. Dhamecha, and H. Hagar, *Natural Products for Ameliorating Degenerative Diseases.* Evidence-Based Complementary and Alternative Medicine, 2018. **2018**(1): p. 1–2.
171. Casal, J. and S.E. Asis, *Natural and Synthetic Quinoline Derivatives as Anti- tuberculosis Agents.* Austin Tuberculosis: Research & Treatment, 2017. **2**: p. 2017.
172. Ndjoubi, K.O., R. Sharma, and A.A. Hussein, *The Potential of Natural Diterpenes Against Tuberculosis: An Updated Review.* Curr Pharm Des, 2020. **26**(24): p. 2909–2932.
173. Song, L., M. Jenner, J. Masschelein, C. Jones, M.J. Bull, S.R. Harris, R.C. Hartkoorn, A. Vocat, I. Romero-Canelon, P. Coupland, G. Webster, M. Dunn, R. Weiser, C. Paisey, S.T. Cole, J. Parkhill, E. Mahenthiralingam, and G.L. Challis, *Discovery and Biosynthesis of Gladiolin: A Burkholderia gladioli Antibiotic with Promising Activity against Mycobacterium tuberculosis.* Journal of the American Chemical Society, 2017. **139**(23): p. 7974–7981.
174. Xu, Z.-Q., W.W. Barrow, W.J. Suling, L. Westbrook, E. Barrow, Y.-M. Lin, and M.T. Flavin, *Anti-HIV natural product (+)-calanolide A is active against both drug-susceptible and drug-resistant strains of Mycobacterium tuberculosis.* Bioorganic & Medicinal Chemistry, 2004. **12**(5): p. 1199–1207.

175. Aware, C.B., D.N. Patil, S.S. Suryawanshi, P.R. Mali, M.R. Rane, R.G. Gurav, and J.P. Jadhav, *Natural bioactive products as promising therapeutics: A review of natural product-based drug development.* South African Journal of Botany, 2022. **151**: p. 512–528.
176. Kedar Pandurangrao Patki , M.M.A.M., Dr. Jameel Ahmed, *Herbal Medicine Used in Treatment of Tuberculosis: A Review.* Ijnrd - International Journal Of Novel Research and Development, 2024. **Volumeo 9**(Issue 9,): p. e79–e85.
177. Maiolini, M., S. Gause, J. Taylor, T. Steakin, G. Shipp, P. Lamichhane, B. Deshmukh, V. Shinde, A. Bishayee, and R.R. Deshmukh, *The War against Tuberculosis: A Review of Natural Compounds and Their Derivatives.* Molecules, 2020. **25**(13): p. 3011.
178. Wang, N. and Q. He, *1.02 - Artificial Intelligence and Bioinformatics Applications in Precision Medicine and Future Implications*, in *Comprehensive Precision Medicine (First Edition)*, K.S. Ramos, Editor. 2024, Elsevier: Oxford. p. 9–24.
179. Singh, N., P. Vayer, S. Tanwar, J.-L. Poyet, K. Tsaioun, and B.O. Villoutreix, *Drug discovery and development: introduction to the general public and patient groups.* Frontiers in Drug Discovery, 2023. **3**.
180. Institute of Medicine Committee on Conflict of Interest in Medical Research, E. and Practice, *The National Academies Collection: Reports funded by National Institutes of Health*, in *Conflict of Interest in Medical Research, Education, and Practice*, B. Lo and M.J. Field, Editors. 2009, National Academies Press (US)

181. VectorMine, *Medical research in drug development and new medicine study outline diagram*. 2018, VectorMine SIA: vectormine.com.
182. Cohen, J., *Approval of Novel TB Drug Celebrated—With Restraint.* Science, 2013. **339**(6116): p. 130–130.
183. Tripathi, M.K., S. Ahmad, R. Tyagi, V. Dahiya, and M.K. Yadav, *Fundamentals of molecular modeling in drug design*. 2022, Elsevier. p. 125–155.
184. Roney, M. and M.F.F. Mohd Aluwi, *The importance of in-silico studies in drug discovery.* Intelligent Pharmacy, 2024.
185. Genheden, S. and U. Ryde, *The MM/PBSA and MM/GBSA methods to estimate ligand-binding affinities.* Expert Opin Drug Discov, 2015. **10**(5): p. 449–61.
186. Wang, C., P.H. Nguyen, K. Pham, D. Huynh, T.B.N. Le, H. Wang, P. Ren, and R. Luo, *Calculating protein–ligand binding affinities with MMPBSA: Method and error analysis.* Journal of Computational Chemistry, 2016. **37**(27): p. 2436–2446.
187. Mugumbate, G., B. Nyathi, A. Zindoga, and G. Munyuki, *Application of Computational Methods in Understanding Mutations in Mycobacterium tuberculosis Drug Resistance.* Frontiers in Molecular Biosciences, 2021. **8**.

188. Timo, G.O., R.S.S.V.D. Reis, A.F.D. Melo, T.V.L. Costa, P.D.O. Magalhães, and M. Homem-De-Mello, *Predictive Power of In Silico Approach to Evaluate Chemicals against M. tuberculosis: A Systematic Review.* Pharmaceuticals, 2019. **12**(3): p. 135.
189. Khambhawala, A., C.H. Lee, S. Pahari, and J.S.-I. Kwon, *Minimizing late-stage failure in drug development with transformer models: Enhancing drug screening and pharmacokinetic predictions.* Chemical Engineering Journal, 2025. **508**: p. 160423.

3. Chapter Three

Principles of Molecular Modelling

3.1. Introduction

Molecular modeling is a collective term used to describe the use of computation to study 3D structures of biological macromolecules [1]. The combination of aspects of bioinformatics and biophysics allows researchers to construct, demonstrate, and model the behavior of these macromolecules [2, 3] in order to examine their 3D structures and interactions [1]. Molecular modeling is widely used, especially in fields such as biochemistry, computational chemistry, drug design, and material science [4]. All molecular modeling techniques are initiated with the same idea of studying molecules by focusing on their atoms [5]. Each atom is treated as a tiny building block.

There are two basic methods for computing the energy of a molecule: Quantum Mechanical (QM) [6] and Molecular Mechanics [7] (MM) methods [8, 9]. While QM solves equations based on quantum theory to describe electronic structures and molecular properties [8], MM uses force fields to approximate molecular interactions and is used to simulate large biomolecules such as proteins [8]. Together, they give a better understanding of how biological processes and reactions occur at the molecular level [8]; in fact, researchers can use this to predict how potential drugs will bind to their targets and help design compounds [10].

According to the SIB Swiss Institute of Bioinformatics, Saquinavir (HIV protease inhibitor) [11, 12], was the first FDA-approved drug to be designed using bioinformatic programs in 1995 [1, 3, 13, 14]. Molecular modeling includes a variety of computational techniques that can be used in analyzing molecular structures and their properties [8]. These include quantum mechanics, molecular mechanics, molecular docking, molecular dynamics, Monte Carlo simulations, homology modeling, pharmacophore modeling, structure-activity relationships, and visualization tools [8].

3.2. Quantum Mechanics

Quantum Mechanics (QM) is a very important concept in physics, which helps us understand the behavior of atoms and molecules [8, 15]. The information acquired from QM is essential when aiming to design effective and targeted pharmaceutical compounds [16]. QM makes use of Ab initio methods like Hartree-Fock (to determine the electronic density and energy of the system), and Density Functional Theory (DFT) [16]. These Ab initio methods help researchers to be able to calculate electronic properties

like partial charges on atoms, molecular orbitals, and reaction energies, so as to predict how strongly a drug binds to its target. QM also enables scientists to study reaction pathways, transition states, and energy barriers, all at an atomic level [17]. QM consists of semi-empirical methods that allow researchers to be able to solve the Schrödinger equation and obtain electronic structures [18], in turn giving us valuable insights into the molecular properties. At its core, the principles of quantum mechanics include the following:

3.2.1. Wavefunction & Probability Interpretation

Quantum mechanics starts with the idea of the wave function, which is represented by the Greek symbol Ψ [15]. The function explains the wave-like nature of particles, eg movement of electrons in a molecule [15]. This function holds all the important information about the system, including the positions and energies of particles [15]. For molecular systems, the Ψ is written as a mathematical expression that depends on the locations of all the electrons and often the nuclei. Overall, it enables scientists to be able to grasp how multiple particles interact and behave together, giving us a more complete picture of the system [15]. In molecular quantum mechanics, Ψ can depend on the coordinates of multiple particles.

$$\Psi=\Psi\ (r1, r2\ldots, rn)$$

However, Ψ does not convey a direct physical meaning by itself [19]. Hence, Max Born, a German physicist, was fascinated by his colleague Franck's experiments on the collisions of atoms and molecules [20] and decided to expand on Einstein's earlier ideas on the relation of light waves and photons [21], according to which the square of the wave amplitude was to be interpreted as the probability for the appearance of photons [19]. Max then suggested that the probability density of locating a particle in a given region of space be denoted by $|\Psi|^2$ [15, 19]. For the wavefunction to describe a physically acceptable system, it ought to be normalized [22], ensuring that the total probability of finding the particle anywhere in space is equal to one [15].

3.3. Molecular mechanics

Molecular Mechanics (MM) is a computational technique that helps scientists create models of molecular systems based on the principles of classical physics [23]. It also enables them to visualise atoms as balls and the bonds between them as springs [23]. Furthermore, the technique uses mathematical equations to capture the geometry and energy of these systems, making it highly effective for studying large and complex structures like proteins and DNA. The key components of MM include:

3.3.1. Potential Energy Functions

The potential energy of a molecular system refers to the energy stored in a system as a result of its atoms or molecules [4]. It encompasses energy terms that detail interactions between bonded atoms (including bonds, angles, and torsions) and those that describe non-bonded interactions, such as van der Waals and electrostatic forces interactions as shown in **Equation** 1 [8]. The equation summarizes all these interaction terms in the system, with the first three components describing the bonded interactions, whereas the final two terms capture the non-bonded forces.

$$V(r\hat{}N) = \sum_{all\ bonds} kl(l-lo)\hat{}2 + \sum_{all\ angles} k\theta(\theta-\theta\_0)\hat{}2 + \sum_{all\ torsions} \frac{1}{2} Vn[1+cos(n\omega-\gamma)]$$
$$+\sum_{J=1}^{N}\sum_{i=j+1}^{N}\{\varepsilon ij\left[\left(\frac{r0ij}{rij}\right)\hat{}6\right] + \frac{qjqi}{4\pi\varepsilon 0rij} \qquad \textbf{Equation } 1$$

Bond Stretching (l)

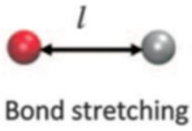

Bond stretching

Energy that occurs as a result of deviation from the equilibrium bond length and is written out as

$$\sum_{\text{all bonds}} \text{kl(l} - \text{lo)}\hat{}2$$

Angle Bending (Θ)

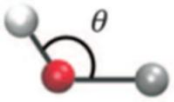

Angle bending

Deviations from the equilibrium bond are mathematically written as

$$\sum_{\text{all angles}} \text{k}\theta(\theta - \theta_0)^2$$

Dihedral (Torsional) Angles (Ω)

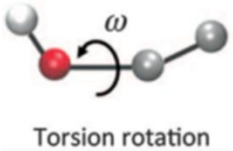

Torsion rotation

The energy from the rotation of bonds is mathematically expressed as

$$\sum_{all\ torsions} \frac{1}{2} \text{Vn}[1 + \cos(\text{n}\omega - \gamma)]$$

Non-bonded interaction

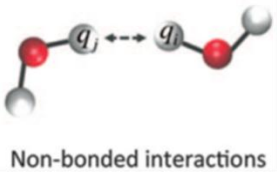

Non-bonded interactions

The Van der Waals interaction is written as

$$\sum_{\text{J=1}}^{\text{N}} \sum_{\text{i=j+1}}^{\text{N}} \{ \varepsilon\text{ij}\left[\left(\frac{\text{r0ij}}{\text{rij}}\right)\hat{}6\right]$$

Electrostatic interaction expressed by Coulomb's Law

$$\sum \frac{\text{qjqi}}{4\pi\varepsilon 0\text{rij}}$$

In

These

3.4. Molecular Docking

Molecular

Autodock

3.5. Molecular Dynamics Simulation

Molecular dynamics simulations (MD) are computational methods that enable us to track the physical movement of proteins, ligands, and other biomolecules at the atomic level over time by solving Newton's law of motion [4]. This technique was originally introduced in the late 1950s by Alder and Wainwright [38]. It operates on the principle of Newton's second law of motion, which defines force (**F)** as the product of an object's mass (**m**) and its acceleration (**a)**, as shown in$F=m\vec{a}$ = m$\frac{d\hat{}2q}{dt\hat{}2}$ **Equation** [8, 39].

$\vec{F} = m\vec{a}$ = m$\frac{d\hat{}2q}{dt\hat{}2}$ **Equation *5***

In molecular dynamics, acceleration is also expressed as d^2q/dt^2; this expression defines how atoms and molecules move over time [8]. Where q is the position vector of an atom, and t^2 is time [8, 39].

MD simulations offer a more realistic view of how a drug candidate interacts with its target under physiological conditions by including water effects, changes in the protein's shape over time, and the dynamic behavior of the complex [10]. The most important part of any MD simulation is the force field, which offers the mathematical functions and parameters used to describe how atomic interactions. Selecting the correct force field is of utmost importance as it ensures the simulated system reflects realistic chemical and physiological conditions, eg, FF14SB for proteins or GAFF for small-molecule ligands. MD studies are supported by powerful biomolecular simulation software packages like Amber [40], GROMOS [41]. Charmm [42], and so forth. These tools enable scientists to explore protein flexibility, compute binding free energies, evaluate ligand stability, and investigate molecular mechanisms that are not easily accessible experimentally. Amber 18, used in this study, is a computationally efficient software package that employs the Amber FF14SB force field for biomolecular simulations [43-45].

3.5.1. Molecular Dynamics Analysis

The dynamic behavior and structural changes of the generated trajectories are studied using the PTRAJ and CPPTRAJ modules [46] of Amber 18 by calculating the root mean square deviation (RMSd) and root mean square fluctuation (RMSf) [45], radius of gyration (Rg), MM-PBSA (molecular mechanics Poisson–Boltzmann surface area), Per-residue free energy decomposition analysis, and h-bond analysis.

Root-Mean-Square Deviation (RMSD)

RMSd is a quantitative measure that allows scientists to assess the structural stability of a protein-ligand complex over time. RMSd is one of the most fundamental metrics of MD simulation, obtained by measuring the average distance between the backbones of two superimposed structures using equation 6.

$$RMSD = \sqrt{\frac{1}{N}\sum_N r\_i(t\_0) - \left| \; r\_i(t))\text{^}2} \qquad \textbf{Equation 6}$$

Where N is the number of atoms being compared, $r_i(t_0)$ is the position of atom *i* in the reference structure at time t, while $r_i t$ is the position of atom *i* in the target structure at time t. RMSD is calculated in units of Angstrom (Å).

The change in the RMSd values over time indicates possible conformational changes in the enzyme structure due to the inhibitor attachment [47]. Generally, a low RMSd (<2Å) suggests structural stability [48, 49], while a high RMSd (>3Å) [50] suggests structural instability accompanied by major conformational changes. While RMSd is important for measuring geometric differences, it cannot distinguish between a molecule with both very rigid and very flexible parts, and one where all regions have a similar, moderate level of flexibility [50]. Hence, RMSF calculations are performed to acquire this information.

Root-Mean-Square Fluctuation (RMSF)

RMSf analysis is one of the key techniques in MD simulations that allows researchers to quantify and characterize local flexibility or movement of specific atoms or residues within a molecule over a certain space of time. The RMSf provides an estimate of how much an atom or residue fluctuates around its average position during the simulation [51] and is given by e$RMSF = \frac{1}{T}\sum_T (r(t) - r)^2$ **Equation** .

$$RMSF = \frac{1}{T}\sum_T (r(t) - r)^2 \qquad \textbf{Equation 7}$$

Where T is the total time of the simulation, and r is the average position of an atom or residue over the simulation [39]. High RMSF values (peaks in the plot) indicate regions of the structure with greater flexibility or motion, while Low RMSF values (troughs in the plot) indicate more rigid and stable areas, typically found in secondary structures like (alpha)-helices, (beta)-sheets, or ligand-binding sites [47]. RMSF calculations are often calculated using common software packages like GROMACS [52], VMD [53], DESMOND [54], and MD Analysis [55].

Radius of Gyration (Rg)

Rg is commonly calculated to measure the compactness of protein molecules during the simulation [56]. Smaller Rg values indicate a more compact or folded structure, and larger Rg values suggest extended or flexible conformations during the simulation. Rg is defined according to equation 8 as the root mean square distance of a molecule's atoms from its center of mass.:

$$Rg = \sqrt{\frac{1}{N}\sum_{i=1}^{N} \left| r_i - r_{com} \right|^2} \qquad \textbf{Equation 8}$$

Where :

N = number of atoms

ri = position vector of atom i

rcom = center mass of molecules

Binding Free Energy

The binding affinity between the ligand and a protein is often estimated using MM-PBSA or MM/-GBSA. This method was originally defined by Srinivasan and colleagues [57]. This method is very popular in molecular dynamics because of its simplicity and computational efficiency as opposed to other Poisson-Boltzmann methods [45]. However, despite its popularity, it has limitations, such as reduced accuracy for charged molecules [58] and often neglects the entropic contribution to binding free energy. This omission can impact prediction accuracy, especially when dealing with flexible ligands and proteins [59]. For this technique, snapshot structures are extracted from the equilibrated parts of the trajectory, and the free-energy components, which include the computation of van der Waals, electrostatic, polar solvation, and non-polar solvation.

Per-residue Binding Free Energy Decomposition

Per residue analysis involves calculating the energy contribution of single residues by summing their interactions over all residues in the system [45]. The MM-PBSA method estimates the composition of each amino acid to the total free binding energy using the equation below.

$$\Delta G_{\text{inhibitor-residue}} = \Delta G_{\text{VdW}} + \Delta G_{\text{ele}} + \Delta G_{\text{polar}} + \Delta G_{\text{nonopolar}} \qquad \textbf{Equation 9}$$

The Adaptive Poisson-Boltzmann Solver (APBS), a molecular software, was used to calculate the electrostatic energy, van der Waals energy, and polar solvation energy [60]. Equation 9 represents the energy interaction between the ligands and amino acid residues as the sum of Van der Waals forces (ΔG_{vdW}), electrostatic effects (ΔG_{ele}), as well as polar and non-polar contributions ($\Delta G_{\text{polar}} + \Delta G_{\text{nonopolar}}$).

H-bond Formation

H-bond analysis allows researchers to track the formation, breaking, and strength of hydrogen bonds over time and, in turn, give valuable insight into the dynamics, stability, and, most importantly, molecular interaction of the protein. The analysis is often carried out using software like GROMACS, Amber, etc. In Amber, the analysis is initiated with the creation of a cpptraj input script that loads the simulation's topology and trajectory files [45]. Followed by the definition of the donor and acceptor atom masks, as well as the geometric criteria, which include a maximum donor-acceptor distance, typically set at 3.0 Å, and a minimum angle, usually 135° [45]. The cpptraj h-bond command provides data on h-bond frequency, average distance, and angle, which is instrumental in evaluating the structural stability and interactions within the system [45].

Dictionary of Secondary Structure of Proteins (DSSP)

DSSP is a widely used tool for assigning secondary structure elements in proteins [61] following the Kabsch and Sander method [62]. The analysis involved evaluating structural changes of the FadD23 protein caused by ligand binding over time by examining the local folded conformations, which are mainly stabilized by backbone hydrogen bonds [61, 63, 64]. The secstruct command helps to identify backbone hydrogen bonds and assign secondary structure types as either helices, sheets, turns, or coils [45, 64]. By default, cpptraj searches for atoms named N, H, C, and O. This analysis provides detailed insights into how the residues' structures change over time, the frequency of each structure type, and the dominant structure for each residue [45]. Various options, like the ptrajformat and betadetail options, are employed to differentiate various beta structures, such as β-strands and β-bridges [45]. All these steps

enhanced our understanding of the protein's stability and dynamic shape throughout the simulation. The results are then visualized and analyzed to assess structural stability across the simulated trajectories.

3.6. Pharmacokinetics

To ensure that the selected compounds are not only strong binders but also possess qualities that allow them to work as effective medicine in the body, pharmacokinetic analysis is conducted. The evaluation of drug-likeness is often conducted using software like SwissADME [65] that utilises Lipinski, Veber, and Ghose criteria. To minimise safety risks, toxicity predictions are also generated. This is made possible by using software like Admetlab 2.0 [66] or Protox3.0 [67].

References

1. Forster, M.J., *Molecular modelling in structural biology.* Micron, 2002. **33**(4): p. 365–384.
2. Leach, A.R., *Molecular modelling : principles and applications*. 2. , [Nachdr.] ed. 2009, Harlow: Pearson Prentice Hall.
3. Bioinformatics, S.S.I.o. *What is molecular modelling?* Precision Medicine [cited 2025 23/04]; Available from: https://www.precisionmed.ch/en/what-is-molecular-modelling/.
4. Saxena, A., D. Wong, K. Diraviyam, and D. Sept, *The basic concepts of molecular modeling.* Methods Enzymol, 2009. **467**: p. 307–334.
5. Casadesús, R., *Molecular Modeling*, in *Encyclopedia of Sciences and Religions*, A.L.C. Runehov and L. Oviedo, Editors. 2013, Springer Netherlands: Dordrecht. p. 1344–1346.
6. Foresman, J.B., A.E. Frisch, and I. Gaussian, *Exploring Chemistry with Electronic Structure Methods*. 1996: Gaussian, Incorporated.
7. Burkert, U. and N.L. Allinger, *Molecular Mechanics*. 1982: American Chemical Society.
8. Genheden, S., A. Reymer, P. Saenz-Méndez, and L.A. Eriksson, *Computational Chemistry and Molecular Modelling Basics*, in *Computational Tools for Chemical Biology*, S. Martín-Santamaría, Editor. 2017, The Royal Society of Chemistry. p. 0.
9. Corcho Sánchez, F.J., *Computational Studies on the Structure and Dynamics of Bioactive Peptides*. 2004: Universitat Politècnica de Catalunya.
10. Adelusi, T.I., A.-Q.K. Oyedele, I.D. Boyenle, A.T. Ogunlana, R.O. Adeyemi, C.D. Ukachi, M.O. Idris, O.T. Olaoba, I.O. Adedotun, O.E. Kolawole, Y. Xiaoxing, and M. Abdul-Hammed, *Molecular modeling in drug discovery.* Informatics in Medicine Unlocked, 2022. **29**: p. 100880.
11. Noble, S. and D. Faulds, *Saquinavir. A review of its pharmacology and clinical potential in the management of HIV infection.* Drugs, 1996. **52**(1): p. 93–112.
12. Roberts, N.A., J.A. Martin, D. Kinchington, A.V. Broadhurst, J.C. Craig, I.B. Duncan, S.A. Galpin, B.K. Handa, J. Kay, A. Kröhn, R.W. Lambert, J.H. Merrett, J.S. Mills, K.E.B. Parkes, S. Redshaw, A.J. Ritchie, D.L. Taylor, G.J. Thomas, and P.J. Machin, *Rational Design of Peptide-Based HIV Proteinase Inhibitors.* Science, 1990. **248**(4953): p. 358–361.
13. Weber, I.T., Y.-F. Wang, and R.W. Harrison, *HIV Protease: Historical Perspective and Current Research.* Viruses, 2021. **13**(5): p. 839.
14. Chen, D. and X. Bu, *Chapter 11 - Discovery and development of the human immunodeficiency virus protease inhibitor Saquinavir*, in *Medicinal Chemistry and Drug Development*, G. Liu, Editor. 2025, Elsevier. p. 245–264.
15. Adelman, S.A., *Basic Molecular Quantum Mechanics*. 2020, Crc Press: Boca Raton.

16. Crespo, A., A. Rodriguez-Granillo, and V.T. Lim, *Quantum-Mechanics Methodologies in Drug Discovery: Applications of Docking and Scoring in Lead Optimization.* Curr Top Med Chem, 2017. **17**(23): p. 2663–2680.
17. Lodola, A. and M. De Vivo, *The increasing role of QM/MM in drug discovery.* Adv Protein Chem Struct Biol, 2012. **87**: p. 337–62.
18. Lewars, E.G., *Semiempirical Calculations*, in *Computational Chemistry: Introduction to the Theory and Applications of Molecular and Quantum Mechanics*, E.G. Lewars, Editor. 2024, Springer International Publishing: Cham. p. 433–492.
19. Kemmer, N. and R. Schlapp, *Max Born, 1882-1970.* Biographical Memoirs of Fellows of the Royal Society, 1971. **17**(0): p. 17–52.
20. Gearhart, C.A., *The Franck-Hertz Experiments, 1911–1914 Experimentalists in Search of a Theory.* Physics in Perspective, 2014. **16**(3): p. 293–343.
21. Cheng, T.-P. and T.-P. Cheng, *50Einstein's proposal of light quanta*, in *Einstein's Physics: Atoms, Quanta, and Relativity - Derived, Explained, and Appraised*. 2013, Oxford University Press. p. 0.
22. *Index*, in *Introduction to Quantum Mechanics*, D.J. Griffiths and D.F. Schroeter, Editors. 2018, Cambridge University Press: Cambridge. p. 486–495.
23. Dulta, K., A.K. Virk, P. Chauhan, P. Bohara, and P.K. Chauhan, *Chapter 8 - Nanotechnology and applications*, in *Applications of Computational Intelligence in Multi-Disciplinary Research*, A.A. Elngar, et al., Editors. 2022, Academic Press. p. 129–141.
24. Jorgensen, W.L. and J. Tirado-Rives, *Potential energy functions for atomic-level simulations of water and organic and biomolecular systems.* Proc Natl Acad Sci U S A, 2005. **102**(19): p. 6665–70.
25. Meng, X.Y., H.X. Zhang, M. Mezei, and M. Cui, *Molecular docking: a powerful approach for structure-based drug discovery.* Curr Comput Aided Drug Des, 2011. **7**(2): p. 146–57.
26. Singh, S. and V.K. Singh, *Molecular Dynamics Simulation: Methods and Application*, in *Frontiers in Protein Structure, Function, and Dynamics*, D.B. Singh and T. Tripathi, Editors. 2020, Springer Singapore: Singapore. p. 213–238.
27. Stefaniu, A., *Introductory Chapter: Molecular Docking and Molecular Dynamics Techniques to Achieve Rational Drug Design*, in *Molecular Docking and Molecular Dynamics*, A. Stefaniu, Editor. 2019, IntechOpen: London.
28. Berman, H.M., J. Westbrook, Z. Feng, G. Gilliland, T.N. Bhat, H. Weissig, I.N. Shindyalov, and P.E. Bourne, *The Protein Data Bank.* Nucleic Acids Research, 2000. **28**(1): p. 235–242.
29. Kim, S., J. Chen, T. Cheng, A. Gindulyte, J. He, S. He, Q. Li, Benjamin A. Shoemaker, Paul A. Thiessen, B. Yu, L. Zaslavsky, J. Zhang, and Evan E. Bolton, *PubChem 2025 update.* Nucleic Acids Research, 2024. **53**(D1): p. D1516–D1525.

30. Irwin, J.J., K.G. Tang, J. Young, C. Dandarchuluun, B.R. Wong, M. Khurelbaatar, Y.S. Moroz, J. Mayfield, and R.A. Sayle, *ZINC20—A Free Ultralarge-Scale Chemical Database for Ligand Discovery.* Journal of Chemical Information and Modeling, 2020. **60**(12): p. 6065–6073.
31. Diallo, B.N., M. Glenister, T.M. Musyoka, K. Lobb, and Ö. Tastan Bishop, *SANCDB: an update on South African natural compounds and their readily available analogs.* J Cheminform, 2021. **13**(1): p. 37.
32. Trott, O. and A.J. Olson, *AutoDock Vina: Improving the speed and accuracy of docking with a new scoring function, efficient optimization, and multithreading.* Journal of Computational Chemistry, 2010. **31**(2): p. 455–461.
33. Tietze, S. and J. Apostolakis, *GlamDock: development and validation of a new docking tool on several thousand protein-ligand complexes.* J Chem Inf Model, 2007. **47**(4): p. 1657–72.
34. Friesner, R.A., J.L. Banks, R.B. Murphy, T.A. Halgren, J.J. Klicic, D.T. Mainz, M.P. Repasky, E.H. Knoll, M. Shelley, J.K. Perry, D.E. Shaw, P. Francis, and P.S. Shenkin, *Glide: a new approach for rapid, accurate docking and scoring. 1. Method and assessment of docking accuracy.* J Med Chem, 2004. **47**(7): p. 1739–49.
35. Eberhardt, J., D. Santos-Martins, A.F. Tillack, and S. Forli, *AutoDock Vina 1.2.0: New Docking Methods, Expanded Force Field, and Python Bindings.* J Chem Inf Model, 2021. **61**(8): p. 3891–3898.
36. Head, J.D. and M.C. Zerner, *A Broyden—Fletcher—Goldfarb—Shanno optimization procedure for molecular geometries.* Chemical Physics Letters, 1985. **122**(3): p. 264–270.
37. Tang, S., R. Chen, L. Mengru, L. Qingde, Z. Yanxiang, W. Jiansheng, H. Haifeng, and M. Ling, *Accelerating AutoDock VINA with GPUs*. 2021.
38. Alder, B.J. and T.E. Wainwright, *Studies in Molecular Dynamics. I. General Method.* The Journal of Chemical Physics, 1959. **31**(2): p. 459–466.
39. Saenz-Méndez, P., S. Genheden, A. Reymer, and L. Eriksson, *Computational Chemistry and Molecular Modelling Basics*. 2017. p. 1–38.
40. salomon ferrer, R., D. Case, and R. Walker, *An overview of the AMBER biomolecular simulation package.* Wiley Interdisciplinary Reviews: Computational Molecular Science, 2013. **3**.
41. Schmid, N., A.P. Eichenberger, A. Choutko, S. Riniker, M. Winger, A.E. Mark, and W.F. van Gunsteren, *Definition and testing of the GROMOS force-field versions 54A7 and 54B7.* Eur Biophys J, 2011. **40**(7): p. 843–56.
42. Brooks, B.R., C.L. Brooks, 3rd, A.D. Mackerell, Jr., L. Nilsson, R.J. Petrella, B. Roux, Y. Won, G. Archontis, C. Bartels, S. Boresch, A. Caflisch, L. Caves, Q. Cui, A.R. Dinner, M. Feig, S. Fischer, J. Gao, M. Hodoscek, W. Im, . . . M. Karplus, *CHARMM: the biomolecular simulation program.* J Comput Chem, 2009. **30**(10): p. 1545–614.
43. Wang, J., R.M. Wolf, J.W. Caldwell, P.A. Kollman, and D.A. Case, *Development and testing of a general amber force field.* Journal of Computational Chemistry, 2004. **25**(9): p. 1157–1174.

44. Tian, C., K. Kasavajhala, K.A.A. Belfon, L. Raguette, H. Huang, A.N. Migues, J. Bickel, Y. Wang, J. Pincay, Q. Wu, and C. Simmerling, *ff19SB: Amino-Acid-Specific Protein Backbone Parameters Trained against Quantum Mechanics Energy Surfaces in Solution.* Journal of Chemical Theory and Computation, 2020. **16**(1): p. 528–552.
45. Case, D., I. Ben-Shalom, S.R. Brozell, D.S. Cerutti, T. Cheatham, V.W.D. Cruzeiro, T. Darden, R. Duke, D. Ghoreishi, M. Gilson, H. Gohlke, A. Götz, D. Greene, R. Harris, N. Homeyer, Y. Huang, S. Izadi, A. Kovalenko, T. Kurtzman, and P.A. Kollman, *Amber 2018*. 2018.
46. Roe, D.R. and T.E. Cheatham, 3rd, *PTRAJ and CPPTRAJ: Software for Processing and Analysis of Molecular Dynamics Trajectory Data.* J Chem Theory Comput, 2013. **9**(7): p. 3084–95.
47. Ghahremanian, S., M.M. Rashidi, K. Raeisi, and D. Toghraie, *Molecular dynamics simulation approach for discovering potential inhibitors against SARS-CoV-2: A structural review.* J Mol Liq, 2022. **354**: p. 118901.
48. Jain, A.N., *Bias, reporting, and sharing: computational evaluations of docking methods.* Journal of Computer-Aided Molecular Design, 2008. **22**(3): p. 201–212.
49. Amaro, R.E., J. Baudry, J. Chodera, Ö. Demir, J.A. McCammon, Y. Miao, and J.C. Smith, *Ensemble Docking in Drug Discovery.* Biophysical Journal, 2018. **114**(10): p. 2271–2278.
50. Maia, E.H.B., L.C. Assis, T.A. de Oliveira, A.M. da Silva, and A.G. Taranto, *Structure-Based Virtual Screening: From Classical to Artificial Intelligence.* Frontiers in Chemistry, 2020. **Volume 8 - 2020**.
51. Bagewadi, Z., Y.K. T.M, B. Gangadharappa, A. Kamalapurkar, S. Shamsudeen, and D. Yaraguppi, *Molecular Dynamics and Simulation Analysis against Superoxide Dismutase (SOD) Target of Micrococcus luteus with Secondary Metabolites from Bacillus licheniformis Recognized by Genome Mining Approach.* Saudi Journal of Biological Sciences, 2023. **30**: p. 103753.
52. Van Der Spoel, D., E. Lindahl, B. Hess, G. Groenhof, A.E. Mark, and H.J. Berendsen, *GROMACS: fast, flexible, and free.* J Comput Chem, 2005. **26**(16): p. 1701–18.
53. Humphrey, W., A. Dalke, and K. Schulten, *VMD: visual molecular dynamics.* J Mol Graph, 1996. **14**(1): p. 33–8, 27–8.
54. *Proceedings of the 2006 ACM/IEEE conference on Supercomputing*. 2006, Tampa, Florida: Association for Computing Machinery.
55. Gowers, R., M. Linke, J. Barnoud, T. Reddy, M. Melo, S.L. Seyler, D. Dotson, J. Domanski, S. Buchoux, and I. Kenney, *MDAnalysis: a Python package for the rapid analysis of molecular dynamics simulations*. 2016.
56. Lobanov, M., N. Bogatyreva, and O. Galzitskaya, *Radius of gyration as an indicator of protein structure compactness.* Mol Biol, 2008. **42**: p. 623–628.

57. Srinivasan, J., T.E. Cheatham, P. Cieplak, P.A. Kollman, and D.A. Case, *Continuum Solvent Studies of the Stability of DNA, RNA, and Phosphoramidate−DNA Helices.* Journal of the American Chemical Society, 1998. **120**(37): p. 9401–9409.
58. Poli, G., C. Granchi, F. Rizzolio, and T. Tuccinardi, *Application of MM-PBSA Methods in Virtual Screening.* Molecules, 2020. **25**(8): p. 1971.
59. Genheden, S. and U. Ryde, *The MM/PBSA and MM/GBSA methods to estimate ligand-binding affinities.* Expert Opin Drug Discov, 2015. **10**(5): p. 449–61.
60. Song, L., T.-S. Lee, C. Zhu, D. York, and K. Merz, *Using AMBER18 for Relative Free Energy Calculations.* Journal of chemical information and modeling, 2019. **59**.
61. Reeb, J. and B. Rost, *Secondary Structure Prediction*, in *Encyclopedia of Bioinformatics and Computational Biology*, S. Ranganathan, et al., Editors. 2019, Academic Press: Oxford. p. 488–496.
62. Kabsch, W. and C. Sander, *Dictionary of protein secondary structure: Pattern recognition of hydrogen-bonded and geometrical features.* Biopolymers, 1983. **22**(12): p. 2577–2637.
63. Haghighi, H., J. Higham, and R.H. Henchman, *Parameter-Free Hydrogen-Bond Definition to Classify Protein Secondary Structure.* The Journal of Physical Chemistry B, 2016. **120**(33): p. 8566–8570.
64. Case, D.A., H.M. Aktulga, K. Belfon, D.S. Cerutti, G.A. Cisneros, V.W.D. Cruzeiro, N. Forouzesh, T.J. Giese, A.W. Götz, H. Gohlke, S. Izadi, K. Kasavajhala, M.C. Kaymak, E. King, T. Kurtzman, T.-S. Lee, P. Li, J. Liu, T. Luchko, . . . K.M. Merz, Jr., *AmberTools.* Journal of Chemical Information and Modeling, 2023. **63**(20): p. 6183–6191.
65. Daina, A., O. Michielin, and V. Zoete, *SwissADME: a free web tool to evaluate pharmacokinetics, drug-likeness and medicinal chemistry friendliness of small molecules.* Scientific Reports, 2017. **7**(1): p. 42717.
66. Xiong, G., Z. Wu, J. Yi, L. Fu, Z. Yang, C. Hsieh, M. Yin, X. Zeng, C. Wu, A. Lu, X. Chen, T. Hou, and D. Cao, *ADMETlab 2.0: an integrated online platform for accurate and comprehensive predictions of ADMET properties.* Nucleic Acids Res, 2021. **49**(W1): p. W5–w14.
67. Banerjee, P., E. Kemmler, M. Dunkel, and R. Preissner, *ProTox 3.0: a webserver for the prediction of toxicity of chemicals.* Nucleic Acids Res, 2024. **52**(W1): p. W513–w520.

4. Chapter Four

Research Manuscript

Exploring the inhibitory potential of South African natural compounds against *Mycobacterium tuberculosis* fatty acyl-AMP ligase

Mbali Matshoba and Ndumiso N. Mhlongo*

School of Laboratory Medicine and Medical Sciences, University of KwaZulu-Natal

Durban 4001, South Africa

*Corresponding author: Ndumiso N. Mhlongo

Email: mhlongoN4@ukzn.ac.za

Telephone: +2731 260 2428

Fax: +2731 260 7792

Abstract

Background: Tuberculosis is one of the leading infectious diseases causing mortality worldwide, particularly in resource-limited areas. Most existing medications result in significant side effects and fail to effectively target the lipid metabolism crucial for the survival and virulence of *Mycobacterium tuberculosis*. FadD23, a fatty acid-AMP ligase that is unique to *M. tuberculosis* and not found in humans, presents a promising drug target due to its role in synthesizing the essential virulence glycolipid SL-1. This unique characteristic allows for selective inhibition with minimal toxicity to the host. The lack of approved drugs that specifically target FadD23 within the SL-1 synthetic pathway highlights the need for the identification of potential inhibitors.

Aim: This study aimed to identify natural inhibitors of *M. tuberculosis* FadD23 from the SANCDB and characterize their potential mechanism of inhibition.

Method: A FadD23 crystal structure with a PDB ID 8HDF and a resolution of 2.2 Å was obtained from the Protein Data Bank. A structure-based virtual screening method was employed to identify potential inhibitors from the South African Natural Compounds Database library. The binding interactions between FadD23 and potential ligands were evaluated through molecular docking using AutoDock Vina. To characterize the protein-ligand interactions, 130 ns molecular dynamics simulations were conducted with Amber 18 software, and the results were analyzed using the CPPTRAJ module. The trajectory's behavior, stability, and conformational alterations were assessed through root mean square deviation (RMSd), root mean square fluctuation (RMSf), hydrogen bond analysis, and radius of gyration (Rg). The biological efficacy and drug-likeness profiles of the compounds were evaluated using the Protox 3.0 and SwissADME web servers.

Results: Out of 1,012 compounds, 7 were selected for docking analysis based on their antimycobacterial activity. Docking analysis revealed that SANC00937 demonstrated a stronger binding affinity for the FadD23 ATP binding pocket, stabilized by both hydrophobic and hydrogen bond interactions, yielding a binding energy of -8.4 kcal/mol among the seven compounds screened. The stability and dynamics of these interactions were further validated through molecular dynamics simulations. The RMSd analyses showed that SANC01098 stabilised the protein more effectively, reducing major fluctuations and supporting a more uniform structural behaviour over time. Further, MM/GBSA calculations were conducted on the molecular dynamics' trajectories of the compounds SANC00937, SANC00520, SANC00522, SANC00834, SANC01097, SANC00519, and SANC01098 to evaluate their binding energies to the FadD23 protein. Notably, SANC01098 demonstrated a higher binding affinity compared to all other compounds, including the reference molecule ANP. SANC00937 binding energies were subsequently decomposed into per amino acid residue contribution, whereby ATP binding residues Ala328, Asp222, Gly330 a Ser300 made notable contributions. Average radius of gyration and root of

mean square deviation values showed that SANC01098 formed the most stable association with FadD23 compared to ANP. This suggests a possibility for competitive binding between SANC01098 and ATP under physiological conditions, whereby FadD23 interaction with the former supersedes the latter, and is energetically favoured and sustained by hydrogen bond formation. The dictionary of secondary structure elements calculation revealed that SANC00937 deforms the Pi structural component of FadD23 secondary structure to favour its optimum binding affinity in the binding site. Pharmacokinetic evaluation of the seven compounds revealed SANC01097 as the most favorable due to its high bioavailability score, lack of interference with major Cytochrome P-450 enzymes, and absence of structural alerts.

Conclusion: This study identifies FadD23 as a critical target for drug development, offering a promising strategy for creating safer and more effective treatments for drug-resistant *Mycobacterium tuberculosis*. In the absence of an approved FadD23 inhibitor, these results form a baseline for experimental assays, including enzyme inhibition assays, binding validations, and cell-based assays, ADMET, and toxicity evaluations of SANC00937 and SANC01098 compounds to confirm them as potential FadD23 inhibitors.

Keywords: Tuberculosis, FadD23 inhibition, SANCDB, molecular docking, MD simulation.

4.1. Introduction

Mycobacterium tuberculosis causes tuberculosis (TB), a highly contagious disease that has plagued humans for centuries [1, 2]. Despite effective treatments and preventive measures, TB remains one of the leading causes of death from a single infectious agent globally, especially in low- and middle-income countries [3]. The infectious nature of TB is aggravated by underlying conditions such as HIV co-infection [3], COVID-19 [3, 4], and the emergence of drug-resistant TB strains.

TB drugs, namely isoniazid, rifampicin, and pyrazinamide, alongside the recently recommended drug for resistance cases, linezolid (an oxazolidinone) [5], have been reported to cause hepatotoxicity, peripheral neuropathy, and gastrointestinal disturbances [6]. Clinical studies have also demonstrated that the severe toxicity of linezolid [7, 8] can lead to myelosuppression [9] and mitochondrial damage [10], raising safety concerns. Despite the promising efficacy of drug-resistant TB drugs like bedaquiline (a diarylquinoline) and delamanid, they are expensive and not widely available in some regions [11]. There have also been reports of bedaquiline resistance and cross-resistance between bedaquiline and clofazimine (a riminophenazine) [12, 13], further complicating treatment options. Clofazimine has also been linked to skin discoloration [14]. The growing rates of drug-resistant TB [15], especially MDR-TB, Pre-XDR TB, XDR-TB, and TDR-TB [3, 16], prompt for the identification of new drug targets and novel inhibitors in the treatment of TB.

Apart from being structurally sound, *M. tuberculosis* also makes use of lipids that enhance virulence. One of the crucial virulence factors in TB infection is sulfated glycolipid, sulfolipid-1 (SL-1). This glycolipid plays a key role in the bacterium's ability to evade the immune response [17]. SL-1 disrupts mitochondrial function, modulates cytokine and reactive oxygen species production in human leukocytes [18-23]. SL-1 also modulates host response by affecting phagosome maturation, inhibiting mTORC1 activity, leading to nuclear translocation of the transcription factor TFEB, which promotes lysosomal biogenesis [24, 25]. Furthermore, SL-1 influences the survival of bacteria within macrophages by negatively regulating their intracellular growth and increasing their susceptibility to human antimicrobial peptides like LL-37 [18, 25]. SL-1 also directly stimulates nociceptive neurons in the respiratory tract, initiating a cough reflex [26], a facilitative mechanism of *M. tuberculosis* transmission [26, 27].

Central to SL-1 synthesis is the fatty acyl-AMP ligase (FAAL), namely FadD23. FadD23 activates fatty acids by forming an acyl adenylate intermediate, which is transferred to Pks2 – a participating enzyme in SL-1 synthesis [17]. Inhibition of FadD23 could reduce SL-1 production, potentially impairing biochemical processes implicating SL-1, and consequently attenuating bacterial virulence and survival. FadD23 consists of two functional domains, as presented in Figure 4.1, the N-terminal domain (residue 4–460) that binds fatty acids, and a C-terminal domain (residue 473–576) that has catalytic residues. The

N-terminal domain includes an adenylation domain and an acyl-binding domain. The adenylation domain facilitates the binding of ATP/AMP-PNP and catalyzes the conversion of fatty acids into acyl-adenylates, while the acyl-binding domain provides a hydrophobic environment that stabilizes the fatty acid chain before activation [17]. The C-terminal domain also plays an essential role in fatty acid activation. Despite the role FadD23 plays in TB pathogenesis, there are currently no FDA-approved inhibitors that specifically target this protein. The availability of FadD23 crystallographic structures provides a platform to conduct structure-based identification of its potential inhibitors through the use of *in silico* techniques.

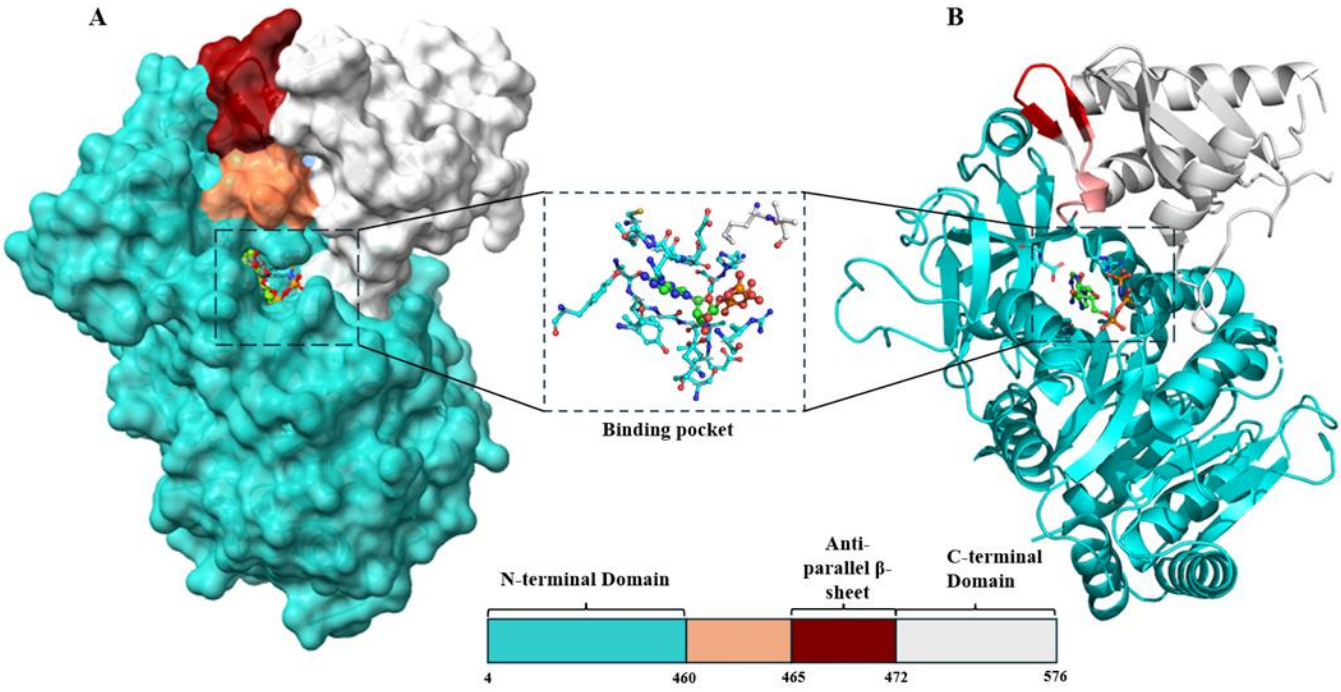

Figure 4.1: Crystal structure of FadD23 in surface form (A) and ribbon form (B) showing its functional domains and the binding pocket.

Natural compounds derived from plants, marine life, and microbial sources have demonstrated significant antimycobacterial properties, with several already incorporated into TB therapies [28-32]. Owing to South Africa's rich biodiversity and its long-term standing history of utilizing natural compounds in medicine, a South African Natural Compound Database (SANCDB) [29, 33] comprising 1012 bioactive compounds from 321 source organisms has been created. Contrary to synthetic compounds, natural compounds are known to exhibit structural diversity, bioactivity, and safety profiles [34] in the treatment of diseases.

This study aims to identify potential inhibitors of *M. tuberculosis* FadD23 from the SANCDB through the application of *in silico* methods, virtual screening, and molecular dynamics simulations.

Identification of compounds with drug-like properties, upon experimental validation, could lay a foundation for the development of TB therapeutics.

4.2. Materials and Methods

4.2.1. Preparation of Target Protein

An X-ray crystal structure of FadD23 (PDB ID: 8HDF [17]) with a resolution of 2.24 Å was obtained from the Protein Data Bank [17, 35]. In preparation for protein-ligand docking, co-crystallised molecules such as ANP, palmitic acid, and water molecules were removed from the protein structure using ChimeraX 1.10 software [36]. The structure had 33 missing residues, which were modelled using Modeller [37] .

4.2.2. Preparation of ligands

The SANCDB [29, 33] was chosen for this study as it is the only fully referenced database containing natural compounds derived from South Africa's biodiversity. Having acquired the 3D structure of FadD23 from the RCSB Protein Data Bank, we utilised Structure-Based Drug Design (SBDD) methods to virtually screen known anti-*M. tuberculosis* compounds from the SANCDB to yield 7 compounds from a total of 1012 compounds. The 2D structures of the 7 compounds were downloaded from the SANCDB, inspected for structural discrepancies, and subjected to energy minimization using the GAFF in Avogadro 1.2.0 software [38]. FadD23 natural substrate phosphoaminophosphonic acid-adenylate ester (ANP) was extracted from the 8HDF structure and used as a reference ligand.

4.2.3. Molecular Docking

Blind docking was performed using AutoDock Vina [39] to predict the binding mode of SANC00937, SANC00519, SANC00520, SANC00522, SANC0834, SANC01097, and SANC01908, on the FadD23 protein structure. This approach screens the entire surface of a protein without having prior knowledge of the target pocket to find the most probable or favourable binding mode and identifies unexplored binding pockets where ligands could bind with optimum binding affinity [40, 41]. Polar hydrogens and Kollman charges (essential for the computation of electrostatic interactions during docking) were added to the protein crystal structure, while Gasteiger partial charges were added to the ligand [42]. A grid box

defined by parameters of x = 84 Å, y = 96 Å, and z = 84 Å for the dimensions and x = 36.083 Å, y = 33.056 Å, and z = 208.278 Å for the center grid, grid spacing of 0.817 Å, and exhaustiveness =10 was generated to encapsulate the whole protein structure for binding site identification. Docking calculations were performed for all seven ligands, and binding affinities and conformations were ranked using the Lamarckian genetic algorithm [43], which generates ligand conformations in descending order based on their docking energy. The docking calculations were performed in triplicate to ensure the accuracy and consistency of the docking method [44]. The top-ranked ligand conformation showing the highest binding energy and a corresponding RMSD value of 0.00 Å2 was selected and saved in complex with the protein structure for subsequent MD calculations. Interatomic interactions between the ligands and FadD23 at the binding site were characterized using Arpeggio [45], an online web server that uses BioPython [46] and OpenBabel [47] to process PDB structure files. The results were visualised using PyMOL v3.1.6.1 [48].

4.2.4. Validation of Docking Protocol

To uphold the reliability and accuracy of the docking results according to Arlsan et al [49], the native ligand of the co-crystallized protein structure, ANP, was removed and redocked into the active site of FadD23 using AutoDock Vina, and using the same docking parameters [44]. This step aimed to evaluate the software's ability to reproduce known binding poses and predict binding affinities within an acceptable range [44]. The docked complex was superimposed with the X-ray co-crystallographic structure of FadD23 bearing the native ligand to generate the RMSD value in ChimeraX 1.10.

4.2.5. Molecular Dynamics Simulations

To characterise protein-ligand interaction, three systems were prepared, namely a free protein (Apo), FadD23 bound to ANP (reference system), and FadD23 bound to a SANC compound. These were subjected to molecular dynamics calculations using AMBER version 18 [50] software. Protein residues were protonated at physiological pH (7.0), using H++ server [51]. The protein was modelled with the ff14SB force field [52], while the ligands were treated using GAFF (General Amber Force Field) [53]. Ligand topology and coordinate parameters were generated using Antechamber [54], and the protein and system coordinates and topology were finalized using LEaP module [54]. Each protein-ligand complex was solvated using a TIP3P model [55], with at least 8 Å of water padding around the solute. To neutralize the system, sodium and chloride ions were added. A 12 Å cutoff for short-range interactions was used, whilst long-range electrostatics were handled with the Particle-Mesh Ewald (PME) [56] method. To speed up the simulations and maintain stability, all bonds involving hydrogen atoms were constrained using

the SHAKE algorithm [57], allowing for a 2-femtosecond (fs) time step sampling. To eliminate steric clashes or unfavorable contacts within the initially prepared solvated complexes, a two-step energy minimization was performed: first, water and ions were relaxed by 2000 steps while keeping the protein-ligand complex restrained; then, the entire system was minimized without restraints [58]. After that, the system was gradually heated from 0 K to 300 K over 200 picoseconds, using a Langevin thermostat [59] to control temperature and apply restraints to the solute. This was followed by a 2-nanosecond equilibration phase at constant temperature and pressure (300 K, 1 atm), using the Berendsen barostat [60]. Finally, we ran 130 nanoseconds of unrestrained production MD under periodic boundary conditions. Snapshots were saved every 2 picoseconds, and the trajectories were analyzed using Cpptraj to assess structural stability and conformational changes.

4.2.6. Post-MD simulation analysis

After the 130ns simulation, the conformational changes of the simulated complexes were analysed from the generated trajectories using the CPPTRAJ module [61] of Amber 18. Assessed conformational elements include root mean square deviation (RMSd), root mean square fluctuation (RMSf), radius of gyration (Rg), MM-PBSA (Molecular Mechanics Poisson–Boltzmann Surface Area), per-residue free energy decomposition analysis, hydrogen bonding analysis, and secondary structure elements analysis [50].

4.2.6.1. Root Mean Square Deviation

The overall structural stability of the protein-ligand complexes was assessed by computing the RMSD of the backbone atoms relative to the starting structure using the following equation.

$$RMSD = \sqrt{\frac{1}{N}\sum_{N} r\_i(t\_0) - \left| \; r\_i(t))\text{^}2} \right.$$

Where N is the number of atoms being compared, $r_i\,(t_0)$ is the position of atom *i* in the reference structure at time t, while $r_i t$ is the position of atom *i* in the target structure at time t. RMSD is calculated in units of Angstrom (Å).

This measurement allows us to see whether the complex settled into a stable arrangement or continued shifting. A stable curve is an indication that the system has reached equilibrium and that the ligand has

maintained a consistent pose. A low RMSD value (< 2Å) suggests structural stability [62, 63], while a high RMSD (> 3Å) value [64], suggests structural instability accompanied by major conformational changes.

4.2.6.2. Root Mean Squared Fluctuation

The flexibility of individual residues over time was assessed by calculating the RMSf. RMSf profile enables us to identify highly dynamic regions (such a loop domains and flexible terminal ends) and rigid areas. The RMSf is computed by estimating how much an atom or residue fluctuates around its average position and is given by the following equation.

$$RMSf = \frac{1}{T}\sum_{T}(r(t) - r)^2$$

Where T is the total time of the simulation, and r is the average position of an atom or residue over the simulation [65]. Higher RMSf values indicate regions that are unstable and flexible, while lower values represent more structurally stable regions.

4.2.6.3. Radius of Gyration

The radius of gyration allows us to gain an overall perspective on the compactness of the complexes during the simulation [66, 67]. Rg is computed using the following equation.

$$Rg = \sqrt{\frac{1}{N}\sum_{i=1}^{N} \left| r_i - r_{com} \right|^2}$$

Where N is the number of atoms, r_i is the position vector of the atom, and r_{com} is the mass center of the molecule. A low Rg value indicates a compact or folded structure, while a high Rg suggests an extended, unfolded, or denatured conformation [66]. Variations in Rg values can signify structural transitions, such as folding, unfolding, or ligand binding [66, 67] .

4.2.6.4. Binding Free Energy

To understand the strength and stability of existing interactions between the ligand and the FadD23 protein, we calculated the Molecular Mechanics Generalized Born Surface Area (MM-GBSA) binding free energy ($\Delta G_{binding}$) of the equilibrated trajectories using the Molecular Mechanics Poisson–Boltzmann surface area (MM-PBSA) [68, 69] program in Amber 18. Snapshots of each complex were

generated at 25-ps intervals throughout the 130 ns of the MD trajectory. The MM-PBSA method estimates the binding free energy of the bound ligand-receptor complex using the equation below [68, 70].

$$\Delta G_{binding} = \Delta E_{ele} + \Delta E_{vdW} + \Delta G_{polar} + \Delta G_{nonopolar} - T\Delta S \quad (1)$$

$\Delta G_{binding}$ in equation 1 denotes the binding free energy of the protein-ligand complex. ΔE_{ele} and ΔE_{vdW} denote the electrostatic effects and the Van der Waals forces of the ligands with the proteins in the gas phase. ΔG_{polar} denotes the polar solvation free energy, and $\Delta G_{nonopolar}$ is the non-polar contribution of solvation free energy, also assumed to be proportional to the solvent accessible surface area (SASA). $T\Delta S$ is the change in molecular movement during binding.

4.2.6.5. Per-residue Free Energy Decomposition analysis

The energy contributions of individual residues involved in the binding mechanism of the FadD23 complexes were computed using the MM-GBSA per-residue free energy decomposition method in Amber 18 [50, 71]. All energy components, including van der Waals, electrostatic, polar solvation, and non-polar solvation terms, were calculated from the snapshots taken from the final 130 ns of the MD trajectory [72].

4.2.6.6. H-bond Analysis

Hydrogen bonds are crucial in determining the binding affinity and stability of protein-ligand complexes. To monitor the protein-ligand hydrogen bonding patterns between FadD23 and the ligands, h-bond analysis using the geometric criteria of hydrogen donor acceptor distance $\leq$ 3.5Å and angle $\geq$ 120° was performed over 130 ns using the CPPTRAJ module [50]. This analysis helps identify when and where hydrogen bonds form between atoms.

4.2.6.7. Dictionary of Secondary Structure Elements (DSSP)

To analyse and monitor protein structural changes in FadD23 during an MD simulation, secondary structure elements properties were evaluated using the DSSP algorithm in CPPTRAJ [50, 73]. These were performed for all simulated complexes.

4.2.7. Drug-likeness and Toxicity Analysis

The selected compounds were further subjected to absorption, distribution, metabolism, and excretion (ADME) profiling to predict their pharmacokinetic, drug-likeness, and medicinal potential properties using the SwissADME server (http://www.swissadme.ch) [74]. This online tool uses a combination of rule-based filters (Lipinski's Rule of Five, Ghose, Veber, Egan, and Muegge filters), predictive models, and cheminformatics algorithms to evaluate the drug-likeness, pharmacokinetic properties, and medicinal chemistry of small molecules [74]. Input structures are often submitted in Simplified Molecular Input Line Entry System (SMILES) format [75]. The *in silico* toxicity profiling of each compound was also predicted using the ProTox 3.0 server (https://tox.charite.de/protox3/index.php) [76]. ProTox 3.0 is a high-profile computational server that predicts acute toxicity, organ-based toxicity, molecular toxicity, molecular initiating events (MIEs), and cytochrome P450 interactions [76]. The compound structure was submitted in a SMILE format, and each prediction was given as a probability score.

4.3. Results and Discussion

The importance of identifying suitable drug candidates in drug discovery cannot be overemphasised. A well-chosen candidate is essential for the success of drug development, as it can greatly impact the efficacy, safety, and overall advancement of the therapeutic agent. In this study, we performed docking-based virtual screening of SANCs to identify candidate compounds as potential inhibitors of FadD23. We further performed MD calculations to characterise the interactions of selected compounds with the FadD23 protein through MD analyses. In the subsequent sections, we present the results from molecular docking and MD trajectory analyses.

4.3.1 Molecular Docking Validation

To ensure the reliability and accuracy of our computational predictions, the co-crystalised ligand, ANP, was separated from the binding pocket of FadD23 and docked back into the binding pocket. Research studies indicate that the binding affinity of ANP with various target proteins typically ranges from -7.8 to -10.5 kcal/mol when using Autodock Vina [77, 78]. Redocking ANP into the FadD23 binding pocket resulted in an RMSd of 3.6 Å, which exceeds the acceptable threshold of 2 Å [79]. These results highlight a limitation of the methodology in accurately prediction of the ANP orientation. To improve the accuracy, the process was repeated three times to eliminate discrepancies. Each time, a consistent RMSd value of 3.6 Å was obtained (Figure 4.2).

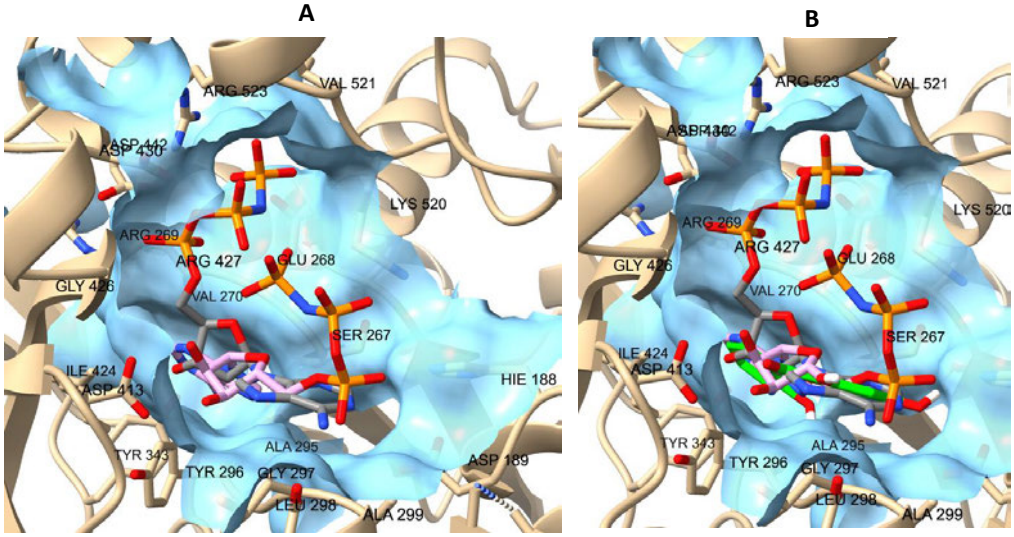

Figure 4.2: Structures of ANP (redocked pose – grey, and crystallographic pose - magenta) [**A**], and SANC00937 (Green) with ANP [**B**] in the ATP binding site of FadD23. ANP was redocked into the binding pocket using the same coordinates for docking SANC00937.

Although the redocked pose of ANP deviates from the reported original pose, the adopted conformation is still residing within the same position of a large ATP-binding pocket. Given that all docking preparations were carried out correctly, the observed deviation in the pose does not inherently imply a failure in the protocol. However, there are several plausible contributing factors to consider, which include grid box dimensions and ligand complexity. For instance, ANP is an adenylate ester with a moderately flexible phosphate tail that often rotates, flips, and extends in different directions. Furthermore, docking programs often encounter challenges in exploring all conformations and accurately positioning the phosphate group, leading to docked poses that deviate from the X-ray pose. According to earlier structural studies by Yan et al (2023), FadD23 may require metal ions such as Mg^{2+} or Mn^{2+} for effective ATP binding and enzymatic function [17, 80]. Lack of these counterions could lead to misplacement of the phosphate, and in turn contribute to a large RMSd. Despite the obtained docking score of ANP, the ligand still resided in the same pocket with alternative orientation of a phosphate moiety, and same interactions with the key active site residues as reported for the original ANP conformation.

4.3.2 SANC00937 binds in the ATP binding site with relatively high binding affinity

The selected natural compounds that were docked into the FadD23 protein to identify their binding pose and binding affinity are presented in Table 4.1. The docking scores of these compounds were compared against the native co-crystallized ligand of FadD23 (ANP), which served as a reference standard. This comparison with ANP provides a baseline for evaluating the binding affinities of the screened compounds. Due to a lack of well-established inhibitors against FadD23, there were no additional positive controls included. The docking scores of the individual ligands were ranked with the most negative value positioned at the top. A conformation with the most negative value and a zero RMSd was chosen from the list. A more negative score indicates a stronger binding affinity between the ligand and the target protein, whereas a zero RMSd value reflects a stable association with the protein [39].

Table 4.1: Docking scores (kcal/mol) of top compounds against FadD23 in comparison with the native ligand (ANP).

Compound Name	SANC ID	Docking Score	2D Structure	Reference
ANP		-7.8 to -10.5	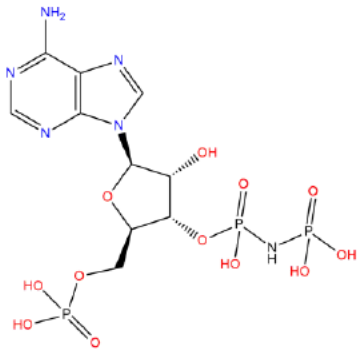	
5,7,2'-Trihydroxyflavone	SANC00937	-8.4	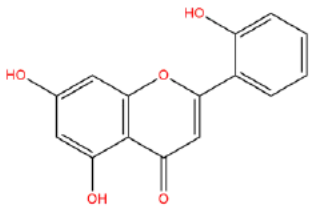	[81]
(2S)-5,7,2'-Trihydroxyflavanone	SANC00520	-7.7	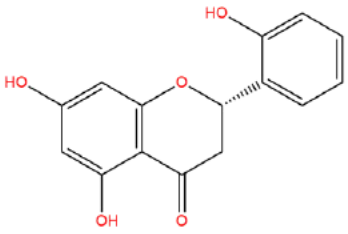	[82]
(E)-2',4'-Dihydroxychalcone	SANC00522	-7.0	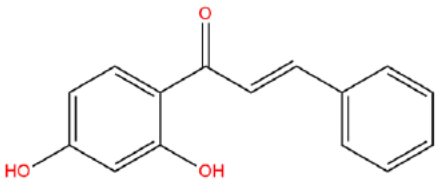	[82]
(E)-3,2',4'-Trihydroxy-3'-methoxychalcone	SANC00519	-6.9	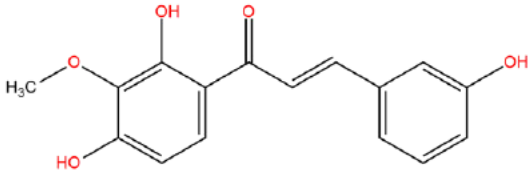	[82]
Alpha-linolenic acid	SANC00834	-5.3		[83]

Linoleic acid	SANC01098	-4.9	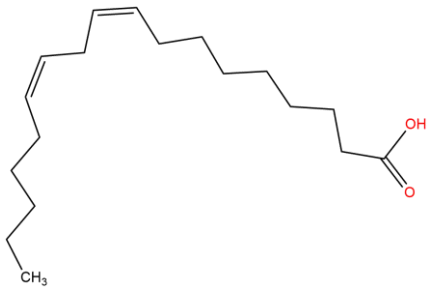	[84]
Lauric acid	SANC01097	-4.8	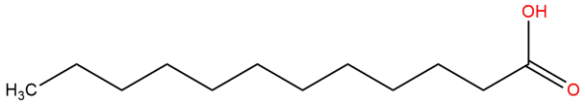	[84]

Compound SANC00937 docked in the ANP binding site (Figure 4.3A) with a highest docking score of -8.4 kcal/mol compared to ANP and the other six SANC docked compounds (Table 4.1). SANC00937 formed a h-bond interaction with Ser300 and His221, and hydrophobic interactions with other residues within its 4 Å radius, namely Asp222, Asp446, Arg460, Ile457, Glu301, Arg302, Gly330, Leu331, Tyr329, and Ala328 (Figure 4.3 B and C).

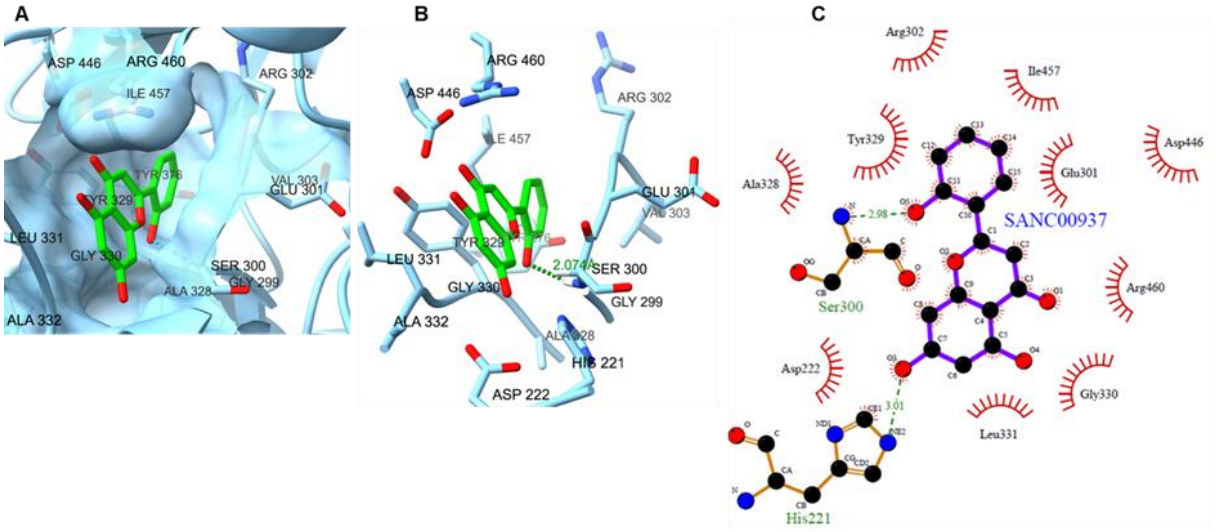

Figure 4.3: A depiction of SANC00937 docked to FadD23 ANP binding site. **A** shows 3D conformation of the ligand (green) in the ANP binding pocket; **B** shows h-bond formation between the ligand and Ser300; and **C** shows ligand interaction with binding pocket residues – h-bond formation with Ser300 and His221, hydrophobic interactions with other residues within a 4 Å radius of the ligand.

A compound with second best binding affinity was SANC00520, which had a docking score of -7.7 kcal/mol. This ligand also docked in the ANP binding site (Figure S.0.1 A), where it formed a single h-bond with Thr444. SANC00520 formed hydrophobic interactions with the rest of the binding pocket

residues. These include Leu331, Glu333, Ser300, Gly330, Glu301, Tyr329, Ile457, Arg460 and Asp446 (Figure S.0.1 B and C). Similar to the latter compound, SANC00522 also docked in the ANP binding site (Figure S.0.2 A) with a docking score of -7.0 kcal/mol. SANC00522 formed a h-bondinteraction with Asp446 (Figure S.0.2 C). Hydrophobic interactions were also observed between the ligand and binding site residues, including Leu331, Glu301, Ser300, Ala328, Tyr329, Tyr376, Ile457, and Arg460.

Compound SANC00519 had an optimum affinity for the ANP binding site (Figure S.0.3 A), where it resided with a docking score of -6.9 kcal/mol. It formed hydrogen bonds with four residues, Arg460, Arg555, Glu301, and Arg302, and hydrophobic interactions with four residues, namely Asp 475, Thr 549, Val554, and Arg556 in the binding site (Figure S.0.3 B and C). Compound SANC00834 optimally docked in the ANP binding site (Figure S.0.4 A) with a docking score of -5.3 kcal/mol. Hydrogen bonds formation and hydrophobic interactions formed a protein-ligand interaction network. The ligand formed a h-bondwith His221 and Asp225, and hydrophobic interactions with residues Gly330, Asp446, Arg460, Ile457, Arg302, Glu301, Tyr329 and Ser300 (Figure S.0.4 B and C).

Unlike the first four compounds presented above, SANC01098 did not bind in the ANP binding site, but adjacent to it (Figure S.0.5 A), where it strictly formed hydrophobic interactions with residues within its vicinity. These include Gln482, Phe271, Leu275, Arg488, Leu248, Glu507 and Glu274 (Figure S.0.5 C). A compound with the least binding affinity for the protein was SANC01097, which had a docking score of -4.8 kcal/mol. SANC01097 optimally docked at the back of the protein structure (Figure S.0.6 A), where it formed hydrogen bonds with four residues, Gln380, Ser381, Gln194, and Tyr337, and hydrophobic interactions with eight residues, namely Pro379, Thr340, Pro377, Gln342, Ser341, Ala201, Ser197, and Ala198 (Figure S.0.6 B and C).

As reflected by the individual docking scores above, SANC00937 was the best compound among the list. Its optimum binding affinity in the ANP binding pocket hints that it could possibly compete with ATP for the binding site. ANP stabilizes the protein by strictly forming hydrophobic interactions with residues in the binding site (Figure S.0.7), whereas SANC00937 forms both hydrogen bonds and hydrophobic interactions. Both ligands interact with Ser300, where SANC00937 forms a h-bond this residue and with His221. SANC00937 rests directly above the PLM tunnel entrance and interacts with numerous residues that have been reported to bind PLM [17]. These include Asp222, Ala328, Leu331 and Gly330.

SANC00937 and SANC00520 are structurally similar, therefore are expected to interact with the protein in a similar manner. However, this was not the case - they adopted differing structural configurations in the binding pocket, which subsequently led to differing interactions with the same residues. SANC00519 and SANC00522 are also structurally similar and are anticipated to similarly interact with the protein, hence the narrow distinction of their docking scores.

Compounds SANC00834, SANC01097, and SANC01098 are fatty acids. SANC00834 and SANC01097 are identical, with a difference in the number of double bonds in the hydrocarbon chain. SANC00834 hydrophobic tail was folded to optimally bind in the ANP binding site, while its oxygen atoms hung directly above the PLM binding site entrance. The folded moiety initiated hydrophobic interactions with hydrophobic side chains of ANP binding site residues, while the two oxygen atoms formed hydrogen bonds with proximal His221 and Asp225. The positioning of these oxygen atoms also presents a possibility of their interaction with the PLM hydroxyl functional group through h-bond formation. On the other hand, SANC01097 and SANC01098, possibly due to hydrocarbon chain differences, could not dock in the ANP site. These three ligands are completely different from ANP, which could also explain their failure to dock in the ANP pocket.

Despite the favourable binding outcome, molecular docking cannot confirm the stability of the generated protein-ligand complexes since they are solely generated in a vacuum from static crystallographic structures and lack physiological environment properties. The generated FadD23-ligand complexes were further subjected to MD calculations to examine structural stability, conformational changes, and binding affinity over time. This analysis is presented in the subsequent sections.

SANC01098 shows relatively dominant inhibitory potential against FadD23

To investigate the inhibitory potential of the docked compounds against FadD23, we performed MM/GBSA-PBSA binding free energy calculations to acquire their binding affinity to the protein. In the absence of an approved FadD23 inhibitor, ANP was used as a reference ligand to trace vital binding site residues participating in native protein-ligand interactions and overall active site activity. The calculated binding energies of natural compounds were therefore compared to those of ANP to identify thermodynamic differences (Table 4.2). Interactions within each protein-ligand complex were examined by estimating the change in binding free energy components, including electrostatic (Ele) and van der Waals (vdW) interaction energies between the ligand and its environment during complex formation [85].

Table 4.2: Binding free energy (kcal/mol) components of the docked complexes over a 130ns trajectory.

Complex	ΔE_{vdw}	ΔE_{ele}	ΔG_{gas}	ΔG_{sol}	ΔG_{Total}
FadD23-ANP	-39.61 ± 0.15	84.49 ± 3.44	44.88 ± 3.43	-62.83 ± 2.88	-17.95 ± 0.63

FadD23-SANC00520	-30.06 ± 0.11	-24.96 ± 0.26	-55.02 ± 0.30	35.19 ± 0.21	-19.84 ± 0.13
FadD23-SANC00522	-31.43 ± 0.11	-27.57 ± 0.24	-58.99 ± 0.23	34.34 ± 0.16	-24.69 ± 0.13
FadD23-SANC00834	-31.36 ± 0.14	-12.78 ± 0.35	-44.13 ± 0.41	20.30 ± 0.31	-23.84 ± 0.16
FadD23-SANC00937	-32.88 ± 0.10	-24.00 ± 0.26	-56.88 ± 0.21	29.05 ± 0.16	-27.83 ± 0.09
FadD23-SANC01097	-16.53 ± 0.30	-7.79 ± 0.24	-24.32 ± 0.50	9.59 ± 0.33	-14.73 ± 0.33
FadD23-SANC01098	-35.11 ± 0.26	-9.33 ± 0.48	-44.3 ± 0.58	15.57 ± 0.44	-28.86 ± 0.26

ΔE_{vdw} = van der Waals; ΔE_{ele} = Electrostatic; ΔG_{gas} = gas-phase energy; ΔG_{sol} = solvation energy; ΔG_{Total} = total binding energy.

Based on the tabulated results above, all SANC compounds exhibited favourable total binding free energies, which were partially offset by a positive solvation term. The positive solvation term indicates a solvation penalty and includes both polar (ΔG_{polar}) and non-polar ($\Delta G_{non\text{-}polar}$) components [70]. Relative to the native ligand ANP (-17.95 kcal/mol), most SANC compounds exhibited higher total binding free energy apart from SANC01097 (-14.73 kcal/mol). This implies that SANC compounds have a stronger binding affinity for the FadD23 binding site. Among all SANC compounds, SANC01098 (-28.86 kcal/mol) displayed the most favourable binding, followed closely by SANC00937 (27.83 kcal/mol), then SANC00522 (24.69 kcal/mol) and SANC00834 (23.84 kcal/mol). This outcome corroborates the favourable docking scores for the SANC compounds (refer to Table 4.1), especially SANC00937, which ranked top during docking and showed the second most favourable binding free energy. The correlation between favourable docking scores and more negative binding free energies illustrates that SANC00937 maintained relative stability and exhibited persistent interactions within the FadD23 binding site even under dynamics and physiological conditions. SANC01098, on the other hand, initially showed moderate binding affinity as evident by the docking scores (Table 4.1), however under molecular dynamics simulations, the compound was able to adapt and form stabilising interactions with the residues in the FadD23 binding site, as indicated by the highly favourable RMSd, Rg, and total free binding energy. In contrast to ANP, the SANC compounds exhibited favourable electrostatic and gas-phase interactions. The negative electrostatic contribution value reflects favourable interactions between opposite charges, such as hydrogen bonds and salt bridges, which further stabilize the complex, especially in polar or charged environments like enzyme active sites [86].

The Van der Waals interactions made a consistent and favourable contribution across all complexes, reflecting good shape complementarity between the ligands and the binding pocket. These non-polar contacts help stabilise the complexes and are a common feature within hydrophobic binding sites [87]. ANP also displayed a large unfavourable electrostatic of 84.49 kcal/mol and gas contribution of 44.88 kcal, which weakened the overall binding strength of the complex despite the favourable solvation energy. The positive electrostatic value indicates poor dipole or charge alignment, which could lead to

destabilization [87]. The gas phase interaction energy, also known as the sum of electrostatic and van der Waals interactions [70], indicates loss of energy in the gas phase due to binding.

The ANP, overall, exhibits spontaneous, favourable binding driven by shape complementarity (van der Waals forces) and solvent effects (solvation), while electrostatic repulsion and gas-phase energetic penalties hindered binding. Both SANC00937 and FadD23 exhibit a strong natural affinity primarily due to the gas phase term, van der Waals, and electrostatic forces, which enable the protein and ligand to fit well and form favorable interactions. However, the environmental solvent makes binding more difficult, possibly because it stabilizes them when they are apart. Nonetheless, the intrinsic ligand-protein interactions were strong enough to overcome this water resistance, resulting in overall favorable binding.

Overall, the binding energy analysis showed that the ANP complex exhibits transient or unstable interactions, which could contribute to poor binding accompanied by significant conformational changes. Contrary to this, SANC compounds exhibit enhanced binding affinities, with SANC01098 and SANC00937 showing the most favourable binding free energies driven by gas-phase, van der Waals, and electrostatic contributions. Furthermore, the stability of the total binding energy across all simulation frames shows consistency with RMSd, RMSF, and Rg analyses, which further confirms the suitability of SANCs as a potential lead compound in drug discovery.

SANC01098 binding in the ATP binding site stabilizes the FadD23 protein structure.

Protein dynamics in complex simulations are partly driven by conformational changes of the bound ligand. To understand conformational changes and stability of ligands in complexed systems, we calculated RMSd of the individual ligands (Figure 4.4 A) to examine their conformational evolution within the binding site over time.

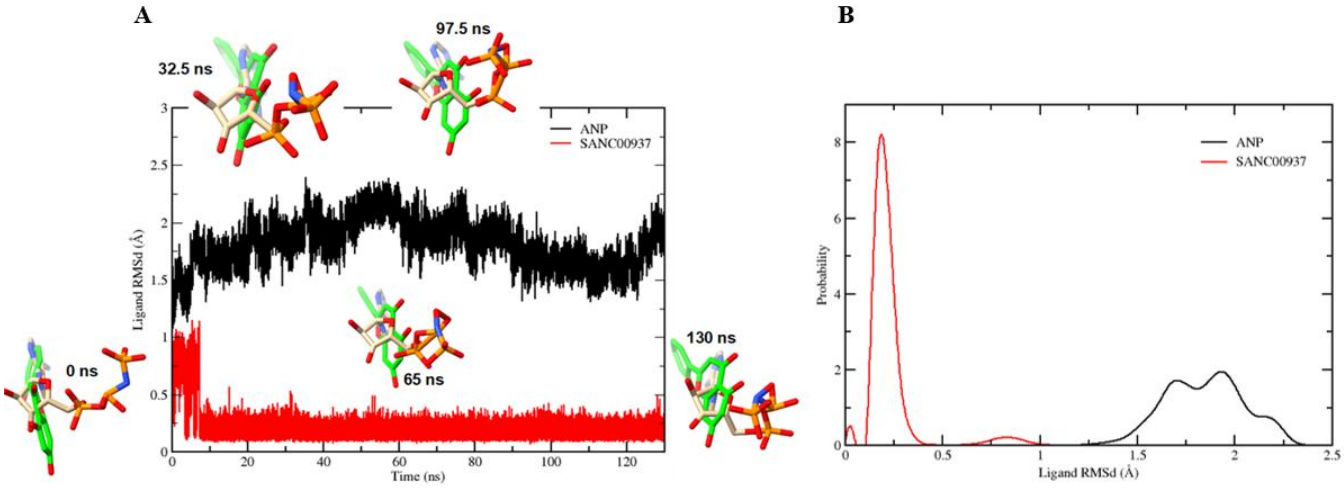

Figure 4.4: (**A**) Graph showing time evolution of ligand RMSd values from complex MD simulations, and snapshots of ligands taken at stipulated time frames. (**B**) Ligand RMSd probability distributions of ANP and SANC00937 during molecular dynamics simulations, illustrating internal stability of ANP and SANC00937 as standalone entities.

A low RMSd value indicates that the structures share greater similarity with the reference structure, both in terms of shape and position [88]. The calculated average RMSd values for ANP and SANC00937 ligands were 1.82 Å and 0.21 Å, respectively. A lower RMSd value for SANC00937 suggests a more stable residence conformation of a ligand in the binding site over 130 ns period, compared to ANP. As noted in Figure 4.5 A, SANC00937 structure (indicated as red) adapts to the binding site landscape at ~ 8 ns, where it resides in a constant conformation until the end of the simulation. This may be due to positional restriction of the ligand by proximal residue sidechains in the binding site. In contrast, ANP (indicated as black) structural configuration constantly evolves with time within the binding site, particularly the phosphate moiety.

This behavior was further corroborated by the distribution plot (D), which demonstrated multiple broad peaks around 1.5-2.4 Å, confirming that ANP indeed exhibits several distinct conformational sub-states. ANP displayed behavioural patterns consistent with those of an unconstrained or flexible ligand, which often fluctuates extensively in the absence of a stabilizing interaction [89, 90].

The conformational trend displayed by SANC00937 alludes a relatively high degree of structural stability in the binding site and an evident tendency to retain its initial conformation throughout the simulation trajectory. The distribution plot for SANC00937 (Figure 4.4 D) corroborated this, showcasing a sharp, well-defined, narrow peak centred around 0.2 Å, corresponding to the average RMSd value of the SANC00937 ligand, which suggests an energetically favourable conformation. The peak is accompanied by a steep drop-off that reflects low RMSd, increased structural stability, and minimal conformational changes. In contrast to ANP, SANC00937 demonstrates behavioural patterns

consistent with those of an inherently rigid ligand. Inherent ligand stability upon binding is associated with a consistently low RMSd, which implies that the ligand is well accommodated in the binding pocket of the protein [91, 92]. These RMSd findings suggest that SANC00937 establishes stronger, more persistent interactions with FadD23 as opposed to ANP, which underwent considerable positional adjustments during the simulation.

Examination of the stability of simulated complexes prior to further analysis is essential to ensure the reliability of the sampled data. To achieve this, we calculated average RMSd values of complexes from respective MD trajectories of 130 ns and graphically presented the results in Figure 4.5 C-N. The estimated average RMSd values for FadD23-ANP, FadD23-SANC00937, and FadD23_Apo were respectively 1.86 Å, 0.97 Å, and 1.88 Å. The average RMSd values for FadD23-SANC00520, FadD23-SANC00522, FadD23-SANC01098, FadD23-SANC00834, and FadD23-SANC01097 were 1.010 Å, 0.96 Å, 0.89 Å, 1.26 Å, and 1.04 Å, respectively. The average RMSd for ANP and the Apo remained constant across all graphs. All systems were evidently stable, which was supported by RMSd values below 2 Å, with the SANC01098 complex being the most stable, closely followed by SANC00522, then SANC00937. In liganded systems, these values imply not only the formation of stable conformations of ligands within the binding pocket of the protein, and formation of stable interactions with residues in the vicinity, but they essentially signify energetic convergence of these systems. All three systems displayed minor fluctuations throughout all the simulations, with FadD23_Apo showing its inherent flexibility through moderate fluctuations, while the binding of the SANC compounds significantly reduced structural deviations, leading to early stabilization of the protein. The FadD23-ANP system displayed larger fluctuations, consistent with ligand-induced conformational changes towards the end of the simulation, which, according to a study by Hussain et al., are attributed to the intrinsic flexibility of the protein–ligand complex, alongside the thermal motion and the gradual formation of stabilising intermolecular contacts [91].

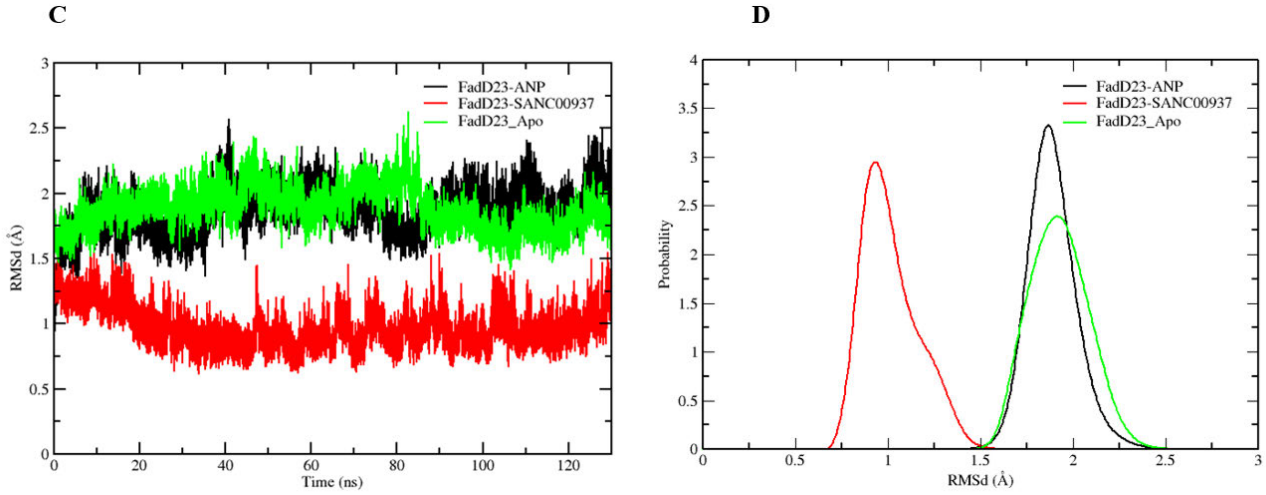

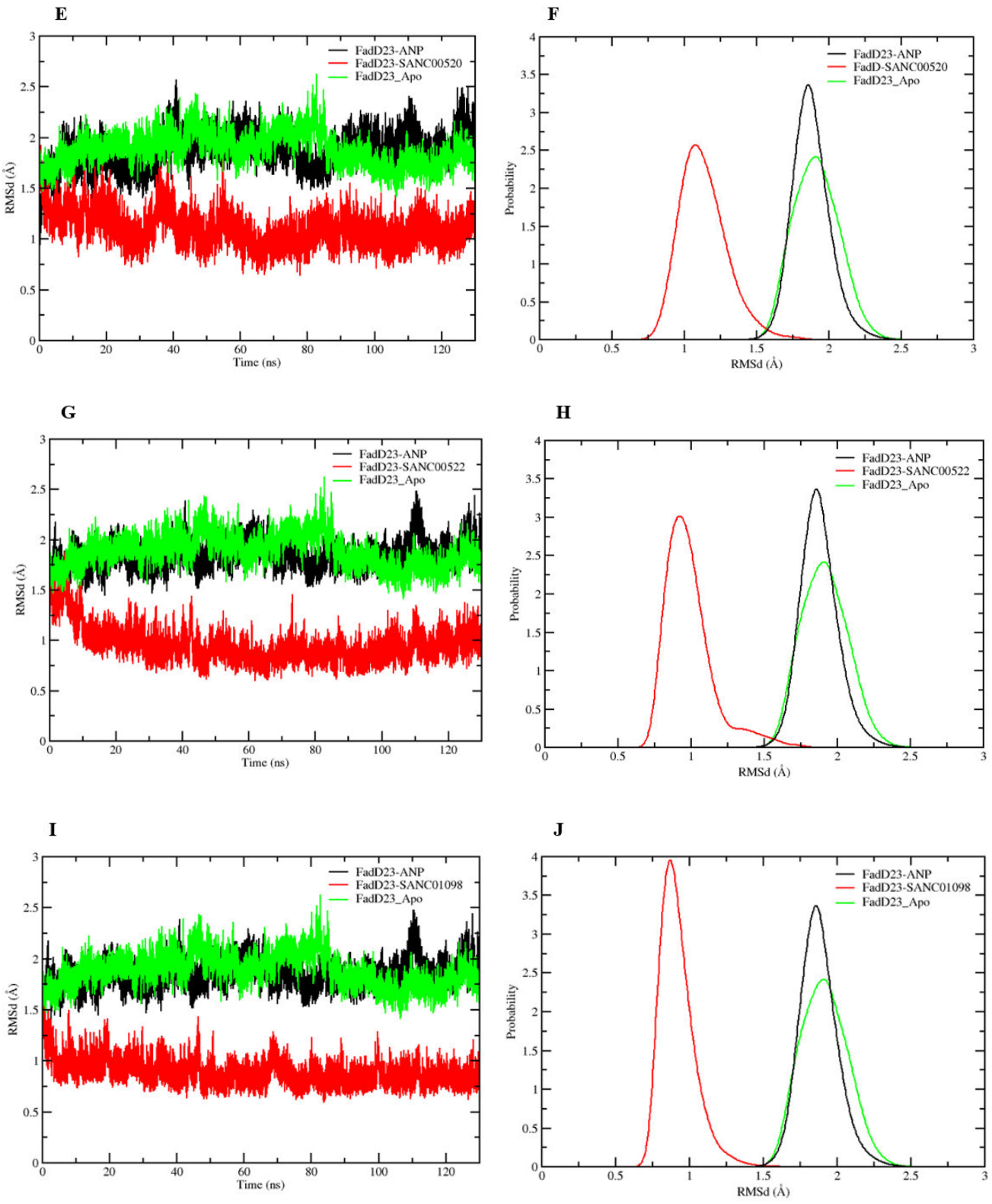
E
FadD23-ANP
FadD23-SANC00520
FadD23_Apo
RMSd (Å)
Time (ns)
F
FadD23-ANP
FadD-SANC00520
FadD23_Apo
Probability
RMSd (Å)
G
FadD23-ANP
FadD23-SANC00522
FadD23_Apo
RMSd (Å)
Time (ns)
H
FadD23-ANP
FadD23-SANC00522
FadD23_Apo
Probability
RMSd (Å)
I
FadD23-ANP
FadD23-SANC01098
FadD23_Apo
RMSd (Å)
Time (ns)
J
FadD23-ANP
FadD23-SANC01098
FadD23_Apo
Probability
RMSd (Å)

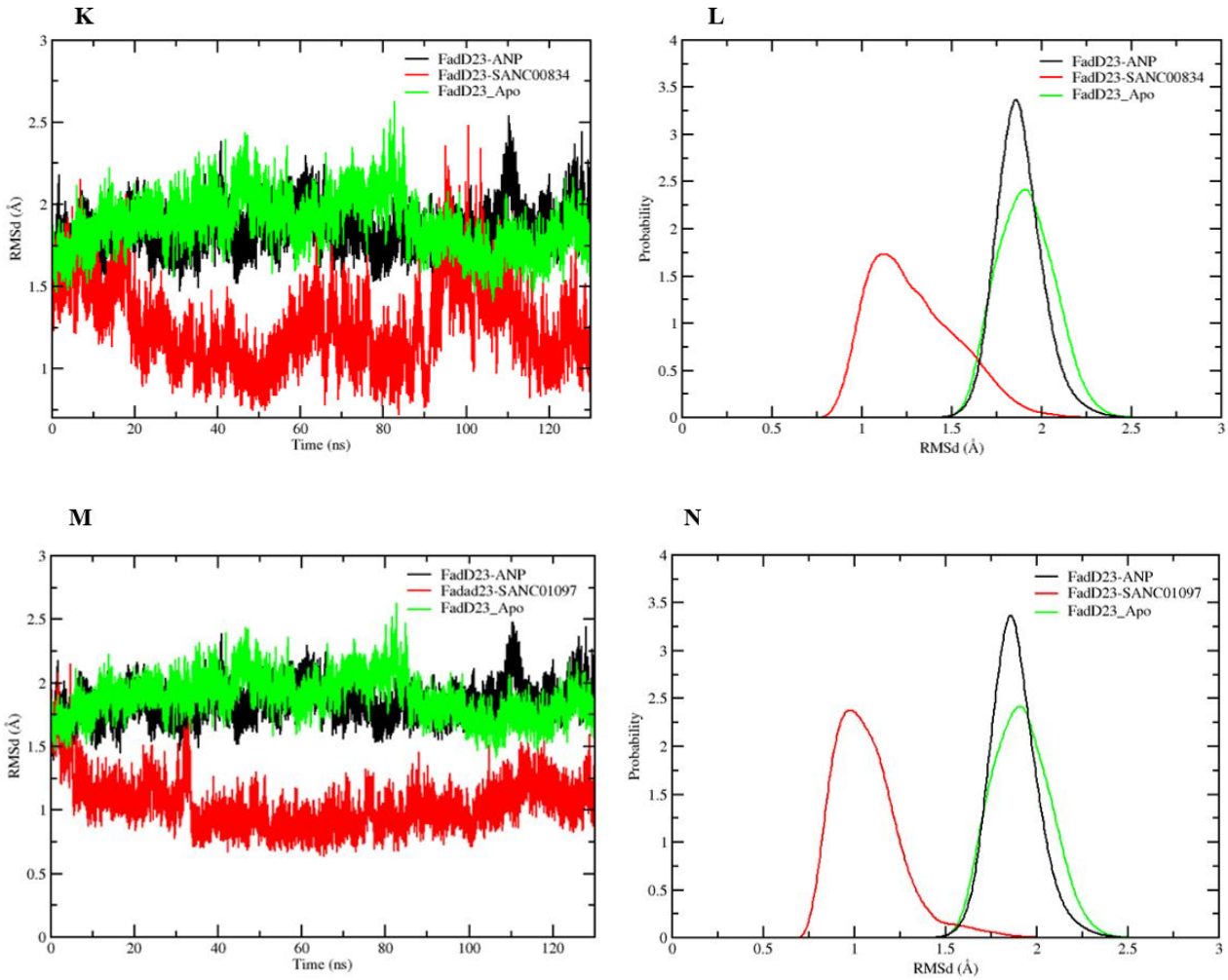

Figure 4.5: Graphs (C, E, G, I, K, and M) showing time evolution of average RMSd of Cα atoms in ANP and SANC complexes and Apo protein from MD simulations. Graphs D, F, H, J, and N demonstrate the RMSd probability distributions of FadD23 in the Apo state and in complex with ANP and SANC compounds during molecular dynamics simulations, illustrating ligand-dependent differences in conformational stability.

The stability and behaviour of these three systems in the graphs were further corroborated by the RMSd probability plots in Figure 4.5 (D, F, H, J, and N). In Figure 4.5 D, the FadD23–SANC00937 complex exhibited a narrow distribution centred at low RMSd (~0.93 Å), reflecting high structural stability. On the other hand, the FadD23_Apo form displayed higher and broader RMSd values (~1.9Å), indicating increased flexibility. Previous studies have also highlighted that the Apo form of FadDs was often in a dynamic state [17]. The FadD23-ANP complex also displayed high RMSd values, but with a sharper peak (at 1.8Å) than the Apo system, indicating intermediate stability. SANC00937 and SANC00522 (H) exhibited similar patterns. Although SANC00834 demonstrated an average RMSD of less than 2 Å, it

is the least stable among the selected compounds. The instability induced by this compound is evidenced by increased fluctuations, shown in Figure 4.5 (K), and this is further supplemented by the broad distribution of plot (L), which suggests that the RMSd values for this complex are widely dispersed, a characteristic that illustrates significant fluctuations likely due to conformational changes. In contrast, compound SANC01098 (I), despite having the second lowest docking score in the docking analysis, stood out as the most stable compound under physiological conditions. As the simulation progresses, the RMSd values of the complex gradually decrease, demonstrating the compound's increasing ability to stabilize FadD23. This enhanced stability is further validated by the narrow distribution of RMSd values observed in Figure 4.5 (J), which reflects minimal structural fluctuations.

The presence of the ligand enhanced the structural stability of FadD23 through favorable interactions such as hydrogen bonding, hydrophobic interactions [93], and salt bridges [94], all of which contribute to the stabilization of the protein-ligand complex in a specific conformation [95].

SANC01098 promotes increased folding and packing of FadD23 protein structure

Protein folding is a structural feature that defines protein stability and its functional propensity [66, 96]. To understand the impact of SANC binding on FadD23 and its influence on the protein's overall structural organization and dynamics, we calculated the radius of gyration (Rg) for all simulated systems and presented the results from

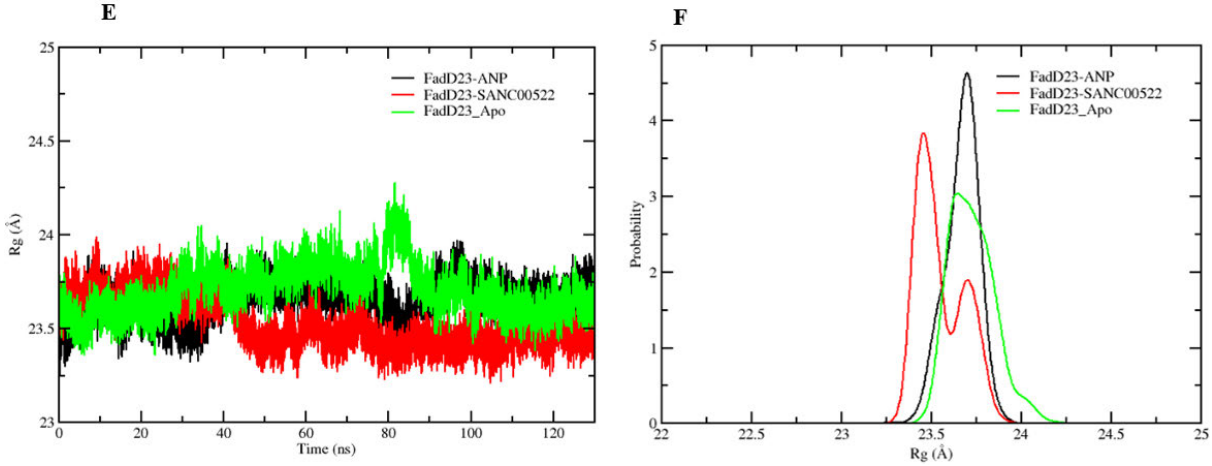

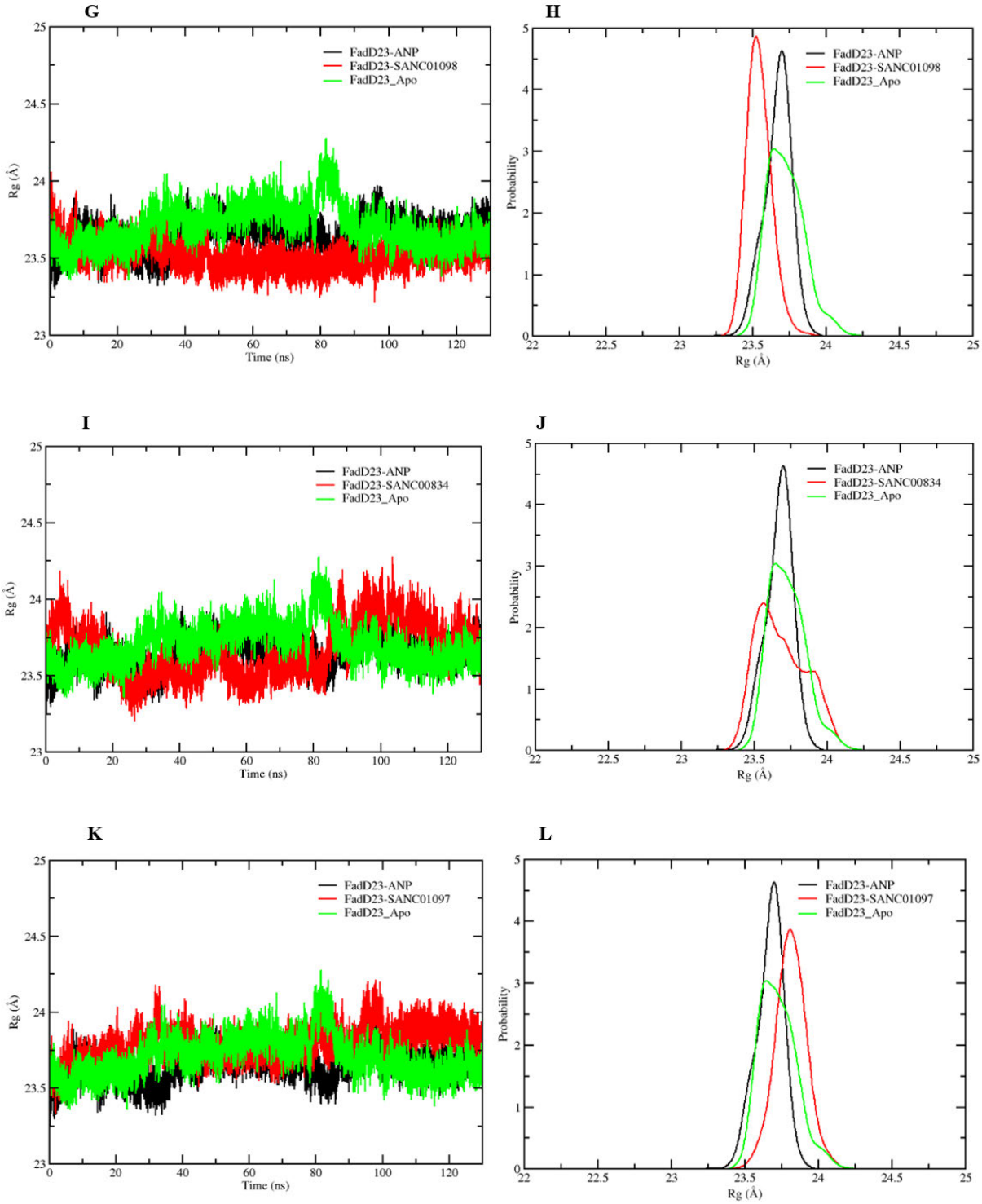
G
H
I
J
K
L
FadD23-ANP
FadD23-SANC01098
FadD23_Apo
FadD23-SANC00834
FadD23-SANC01097
Rg (Å)
Time (ns)
Probability

Figure 4.6 A-L.

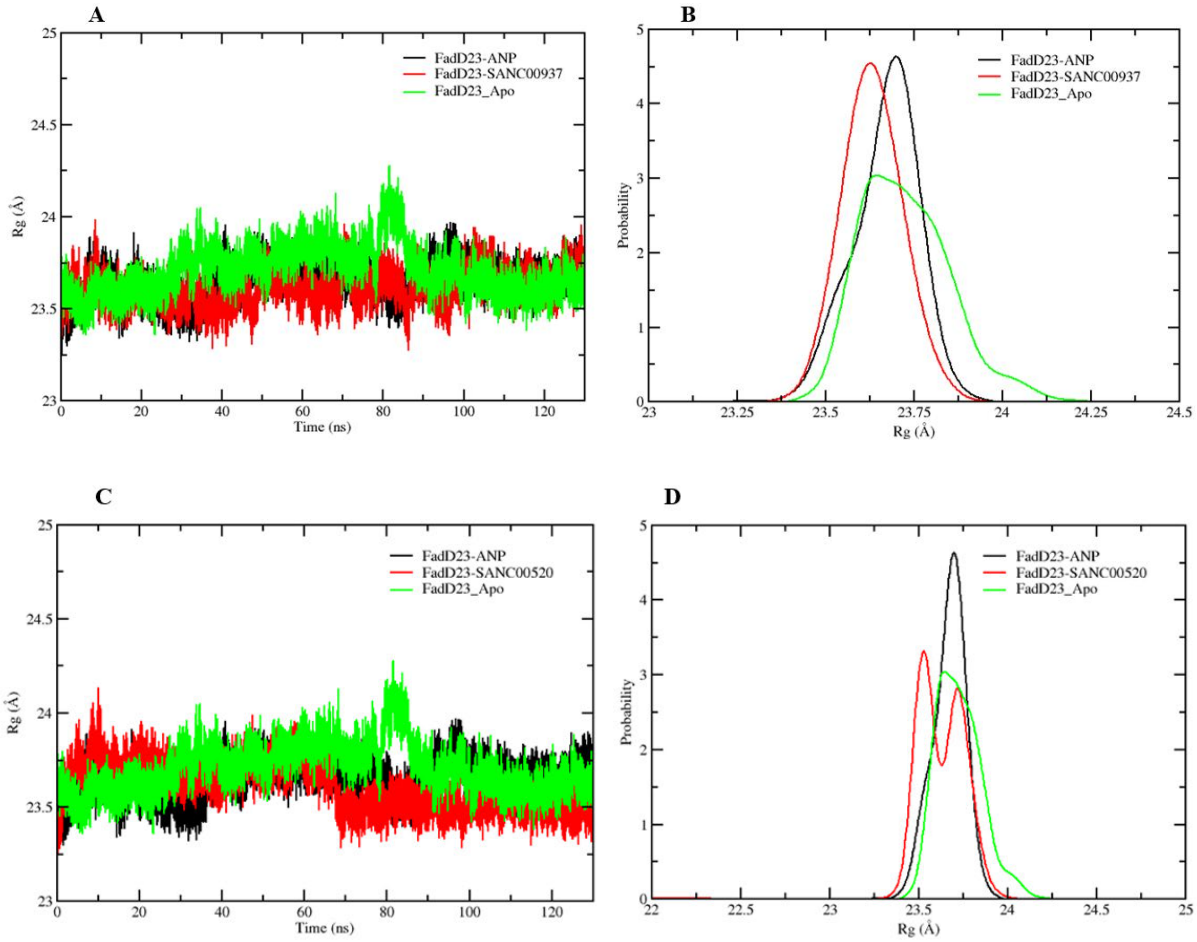
A
FadD23-ANP
FadD23-SANC00937
FadD23_Apo
Rg (Å)
Time (ns)
B
FadD23-ANP
FadD23-SANC00937
FadD23_Apo
Probability
Rg (Å)
C
FadD23-ANP
FadD23-SANC00520
FadD23_Apo
Rg (Å)
Time (ns)
D
FadD23-ANP
FadD23-SANC00520
FadD23_Apo
Probability
Rg (Å)

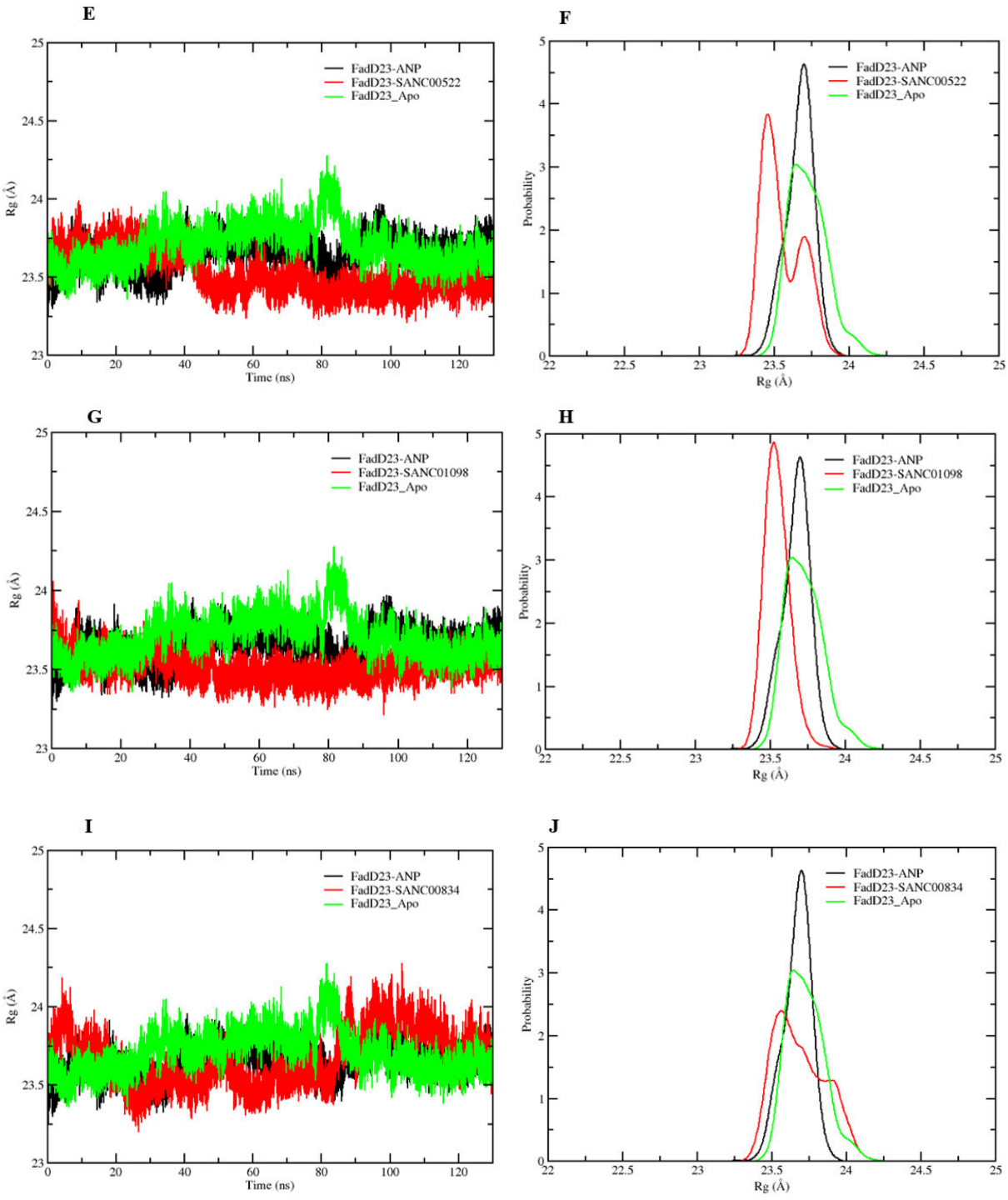
E
FadD23-ANP
FadD23-SANC00522
FadD23_Apo
Rg (Å)
Time (ns)
F
FadD23-ANP
FadD23-SANC00522
FadD23_Apo
Probability
Rg (Å)
G
FadD23-ANP
FadD23-SANC01098
FadD23_Apo
Rg (Å)
Time (ns)
H
FadD23-ANP
FadD23-SANC01098
FadD23_Apo
Probability
Rg (Å)
I
FadD23-ANP
FadD23-SANC00834
FadD23_Apo
Rg (Å)
Time (ns)
J
FadD23-ANP
FadD23-SANC00834
FadD23_Apo
Probability
Rg (Å)

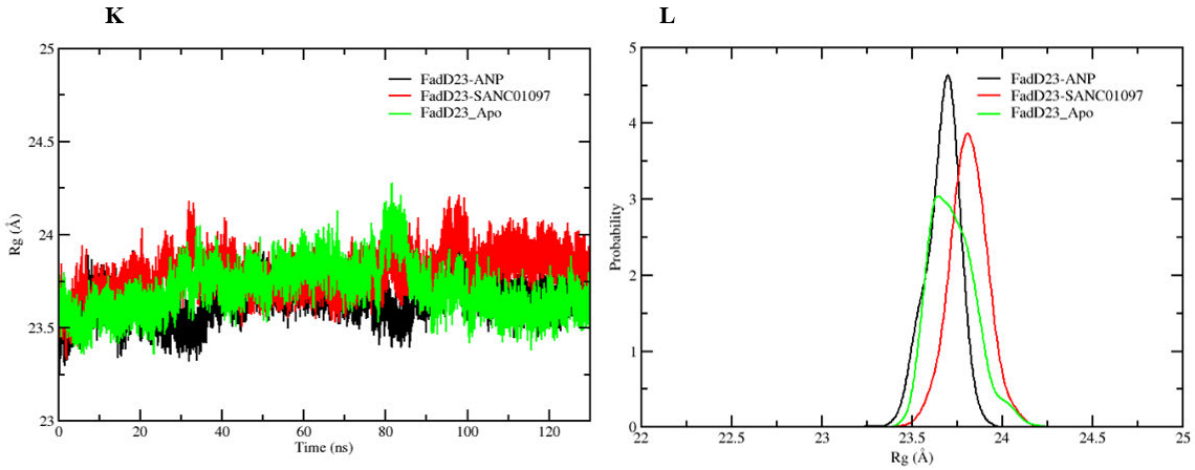

Figure 4.6: Graph (A-L) illustrates changes in the radius of gyration for ANP, SANC-bound complexes, and the Apo system over a 130nm simulation, supplemented by distribution plots.

The calculated average Rg values for FadD23-SANC00937 (A) and FadD23-ANP complexes were 23.61 Å and 23.65 Å, respectively, while for the Apo system, it was 23.70 Å. The average RMSd values for FadD23-SANC00520, FadD23-SANC00522, FadD23-SANC01098, FadD23-SANC00834, and FadD23-SANC01097 were 23.61 Å, 23.53 Å, 23.52 Å, 23.67 Å, and 23.79 Å, respectively. A lower Rg value indicates a more compact and stable protein structure, whereas a higher Rg suggests a less folded protein or a less stable complex [97]. Most systems showed similar levels of compactness, as indicated by their average Rg values. However, the FadD23-SANC01097 system in K and L displayed poor compactness over time, as shown by higher fluctuations exceeding those of the control and Apo system. The Rg values for this system were narrowly distributed toward higher values. The FadD23-SANC01098, SANC00937, SANC00520, SANC00834, and SANC00522 systems had slightly lower Rg compared to the other two systems, with SANC01098 having the lowest. This implies that ligand interactions induced a slightly higher packing density in the protein structure compared to the ANP and Apo systems. Although ligand binding clearly induced a relatively minute degree of structural density to the protein, this essentially informs of the relative overall complex stability introduced by the ligand.

These findings align with both the free binding energy and RMSd analysis. Furthermore, they're also supported by Rg distribution plots (

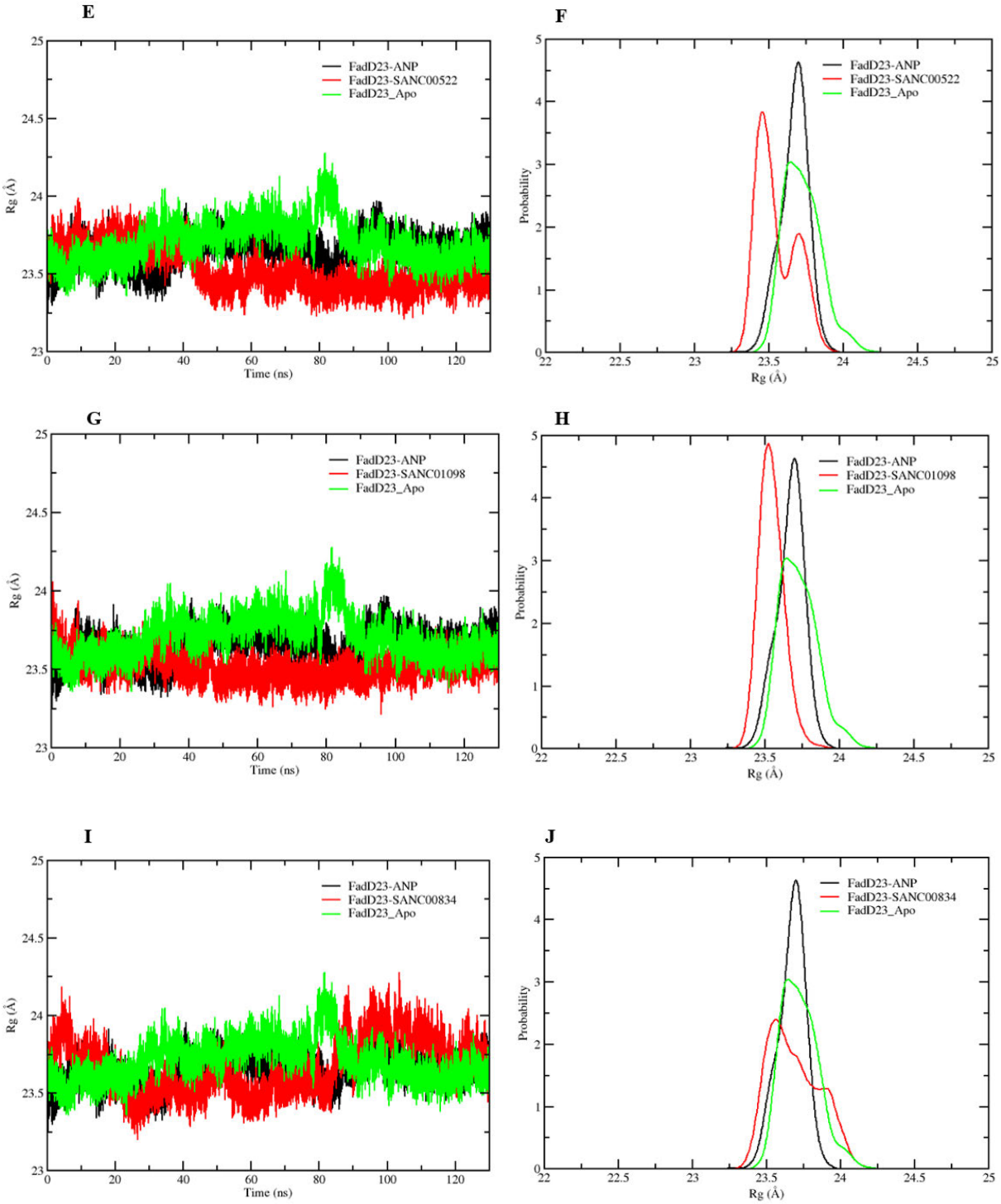

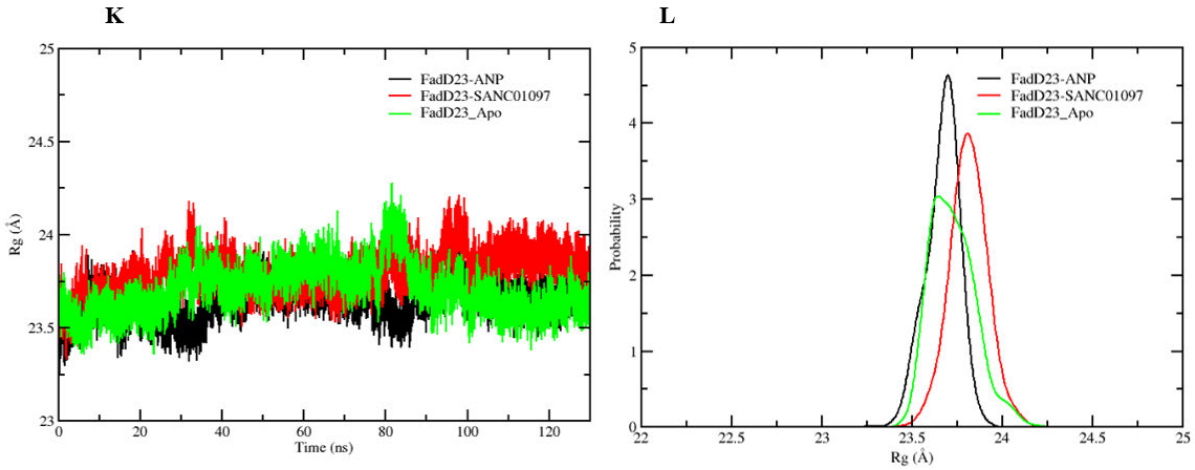

Figure 4.6), where the SANC01098 bound complex displayed a narrow peak centred around 23.5 Å, implying that the protein spent most of its simulation in a slightly compact state. The ANP-bound system presented a similar but slightly broader distribution, slightly shifted towards a higher Rg value (23.75 Å), portraying a more relaxed average conformation. The Apo system displayed an even broader, right-shifted distribution, consistent with increased conformational variability relative to the other two systems. Apart from compound SANC01097, all the other SANCs appeared to enhance the compactness and stability of FadD23as evident lower average Rg scores and their distribution toward the left lower values of the Rg distribution plot.

The binding affinity of SANC00937 to FadD23 is largely driven by Ser300, Ala328, and Glu301 interactions

The binding free energy achieved from FadD23-SANC00937 interaction was further decomposed to per amino acid contribution to identify key residues involved in ligand binding. Figure 4.8 and Figure 4.8 provide a graphical representation of per-residue energy decomposition results for FadD23-SANC00937 and FadD23-ANP interactions, respectively. In a FadD23-SANC00937 complex, a total of 12 residues formed contacts with the ligand. Out of the 12 residues, only Ser300 (-2.017 kcal/mol), Ala328 (-1.811 kcal/mol), and Glu301 (-1.214 kcal/mol) made prominent energy contributions to the total binding energy of the ligand (Table S0.1), with Ser300 being the highest contributor. FadD23-SANC00937 interaction sampled from the energy-minimized complex structure (Figure 4.8 B), Ser300 forms a h-bond (3.05 Å) interaction with the ligand, whereas in the first (Figure 4.8 A) and last (Figure 4.8 C) frames of the simulation form a hydrophobic interaction. The van der Waals forces (-2.404 kcal/mol) were the highest contributing energy component towards Ser300 total binding affinity contribution (Table S0.1). This supports the hydrophobic interactions observed in Figure 4.8 A and C.

Glu301 provides moderate stabilizing effects via van der Waals forces, with contributions from polar and non-polar solvation. This residue is positioned to enhance hydrophobic contact and provide additional binding support. Both Ser300 and Glu301 exhibit negative total binding energies, emphasizing their strong stabilizing roles. Ala328 and Gly330 showed favorable electrostatic contributions, accompanied by negative total binding energies, suggesting that these residues moderately contribute to the overall stability of the complex. Like Glu301, they are also positioned to facilitate both hydrophobic and h-bond interactions. Lys553 shows favorable contributions from electrostatic forces, van der Waals interactions, and non-polar solvation, leading to a slightly positive total binding energy. Gln274 and Cys298 demonstrate minimal energy contributions, indicating that these residues have a limited role in binding. In contrast, Arg460 and Ala332 made lower energy contributions, engaging in minor van der Waals and hydrophobic interactions that may fine-tune ligand orientation within the binding pocket. The binding of SANC00937 was largely influenced by electrostatic interactions, with the acidic residue Asp222 serving as the primary contributor, complemented by hydrogen bonds involving non-polar Gly330, polar Ser300, and non-polar Ala328. Further interactions include salt bridges involving basic residues Lys553 and Arg460.

In a FadD23-ANP complex, ANP binding was stabilized by 16 residues of the protein, whereby Ser300 (-1.768 kcal/mol), Tyr329 (-2.327 kcal/mol), Ile457 (-1.232 kcal/mol), Arg460 (-19.258 kcal/mol), and Arg555 (-1.072 kcal/mol) made prominent contributions to the total binding energy (Table S0.2). Arg460 made the highest contribution to ANP binding affinity. This large contribution could be attributed to multiple h-bond interactions it forms with oxygen atoms of the ligand (Figure 4.8). Electrostatic interaction energies (-139.804 kcal/mol) were the highest contributing energy component to Arg460's total energy contribution. Arg460 and Arg555 exhibited significantly high electrostatic and total binding energies. However, Ala328 presented a negative electrostatic impact with an ΔE_{ele} of 1.85 kcal/mol, accompanied by an ΔE_{vdw} value of -0.29 kcal/mol. Overall, the ΔG_{Total} for this residue was not prominent in both complexes.

The existence of prominently contributing residues to the binding affinity of both ligands was observed (Figure 4.7 and Figure 4.8) in both complexes. Ser300 interacted with both ligands but made the highest contribution to SANC00937 binding affinity than towards ANP. In the ANP complex, Ser300 formed a h-bond (3.10 Å) with a purine moiety of ANP, while in the SANC00937 complex, it formed a h-bond of similar strength (3.05 Å) with the ligand. Glu301 strengthened the binding of both ligands through hydrophobic interactions with a proximal hydrocarbon ring in SANC00937 and the purine ring of ANP. In Yans' crystallographic structure, Glu301 interacts with AMP to contribute to the stability of the protein-substrate complex [17]. Ala328 stabilized SANC00937 affinity through van der Waals forces, whereas in the ANP complex, it formed a moderate h-bond (2.95 Å) with N6 atom bound to C6 of the purine ring. This highlights the significance of this residue in the binding of both ligands in the ATP

binding site and essentially its importance in FadD23 inhibition. In the crystallographic structure, Ala328 is said to be involved in adenosine and ribose recognition [17]. The backbone oxygen of Ala328 forms a h-bond with the N37 of the adenosine in the AMP-PNP crystallographic structure in addition to this Ala328 is one of the hydrophobic residues that contribute to the hydrophobic environment that stabilizes the fatty acid chain in the acyl binding domain prior activation [17].

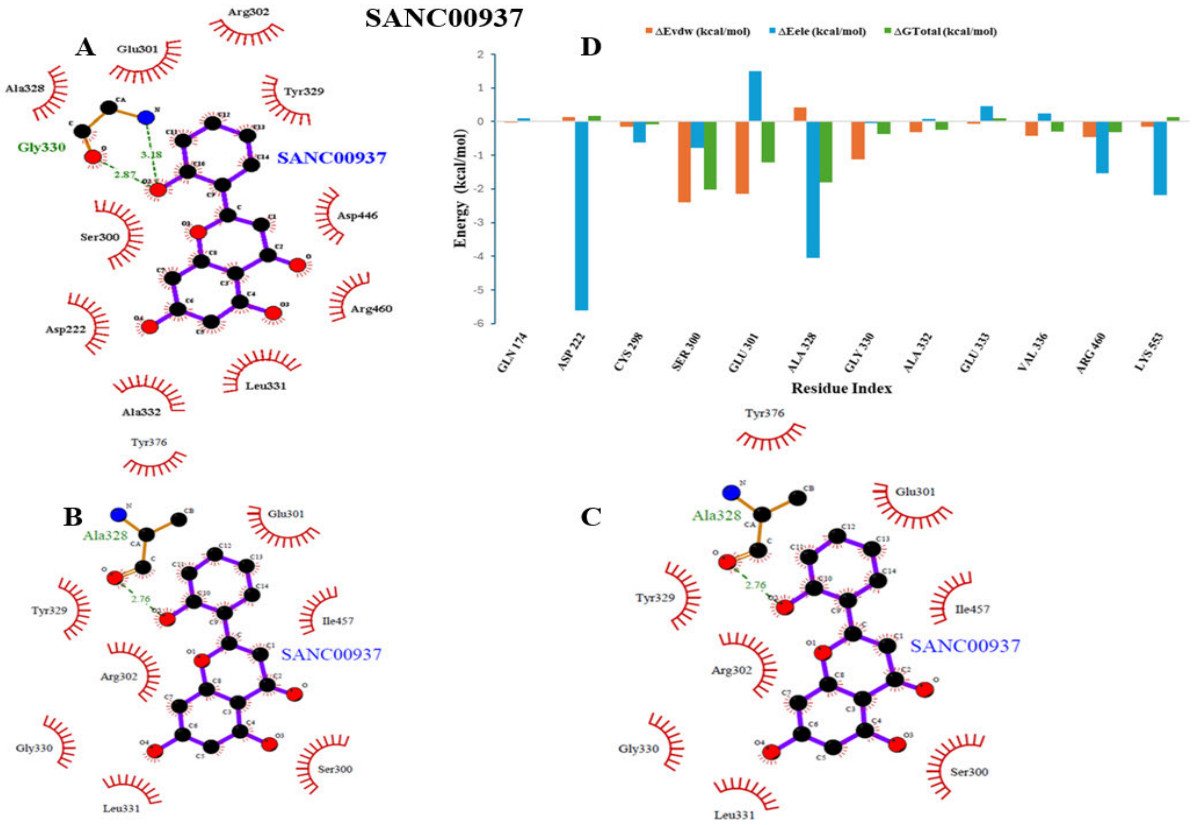

Figure 4.7: Per-residue Energy decompositions of FadD23-SANC00937 (**D**), supplemented by a 2D interaction diagram of SANC00937 surrounded by protein residues in the first frame (**A**), full mini dry (**B**), and last frame (**C**).

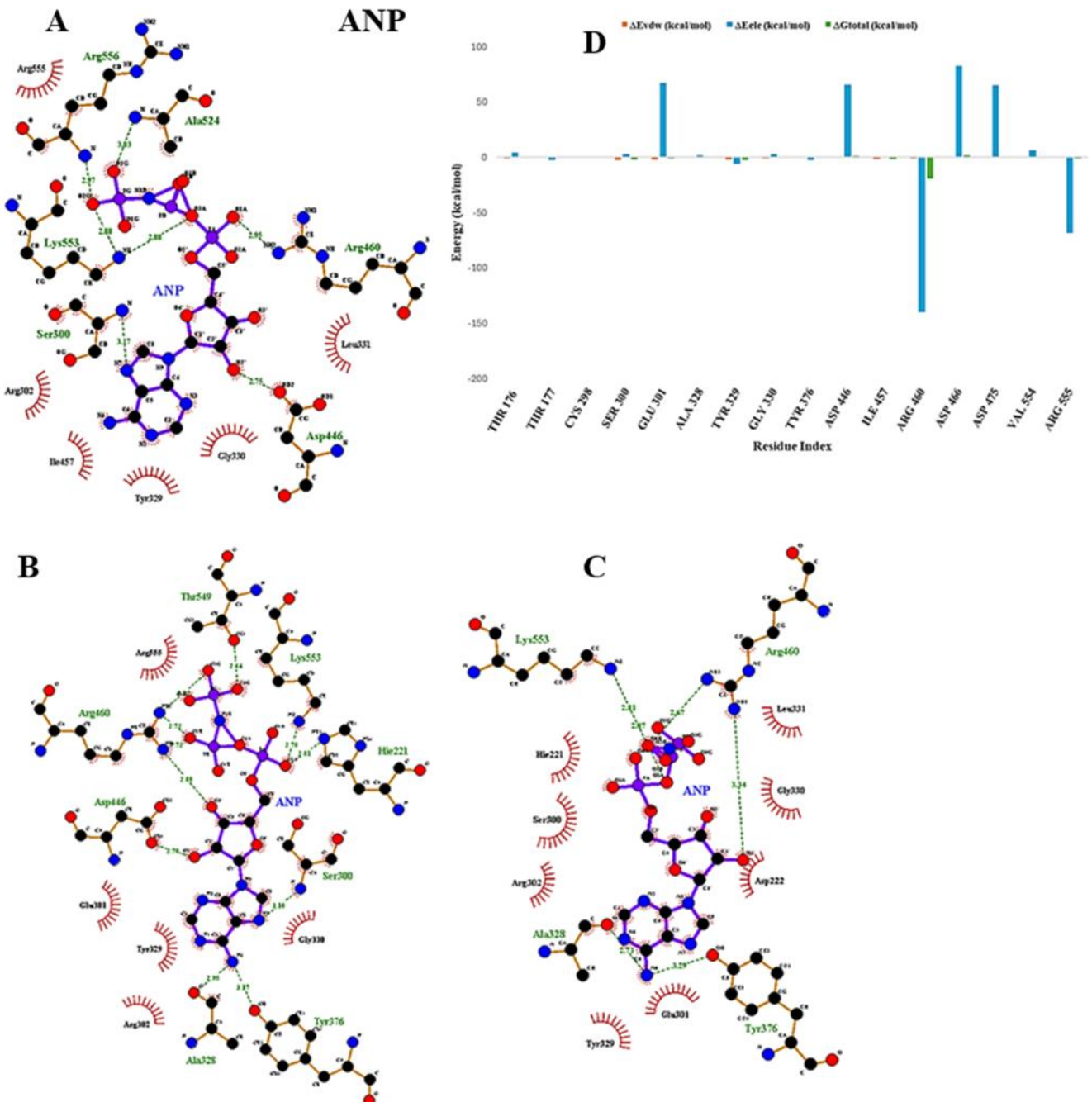

Figure 4.8: Per-residue Energy decompositions of FadD23-ANP (**D**) supplemented by a 2D interaction diagram of ANP surrounded by protein residue in the first frame (**A**), full mini dry (**B**), and last frame (**C**).

SANC00937 consistently reduced residue-level fluctuations across key structural regions of FadD23

The RMSf analysis was performed to evaluate the overall flexibility and mobility of the FadD23 protein residues in its Apo and ligand-bound state (ANP and SANC00937), especially those located at the active site of interest, which are vital for drug discovery [98, 99]. RMSf analysis provides a per-residue level insight into how ligand binding influences the stability or mobility of specific protein regions throughout the simulation. According to the RMSf analysis (Figure 4.9), the residues of all systems exhibit the same patterns characteristic of enzymes, with alternating flexible loops and stable secondary structure segments, with RMSf values ranging between 0.5 Å and 1.5 Å. This confirms that the overall fold of FadD23 remained intact throughout the simulation.

The FadD23-ANP complex (black) exhibited several high peaks, with fluctuations reaching 4 Å in the region around residue 115, which corresponds to region A of the N-terminus, and approximately 3.5 Å at residue Tyr468 within the antiparallel β-sheet region (residue 465–472) and additional peaks at residues Tyr170, Ala434, and Asp463, which correspond to the termini ends of the N-terminal regions [17, 100]. The elevated RMSf values suggest that ANP binding enhances a high degree of local flexibility in these regions.

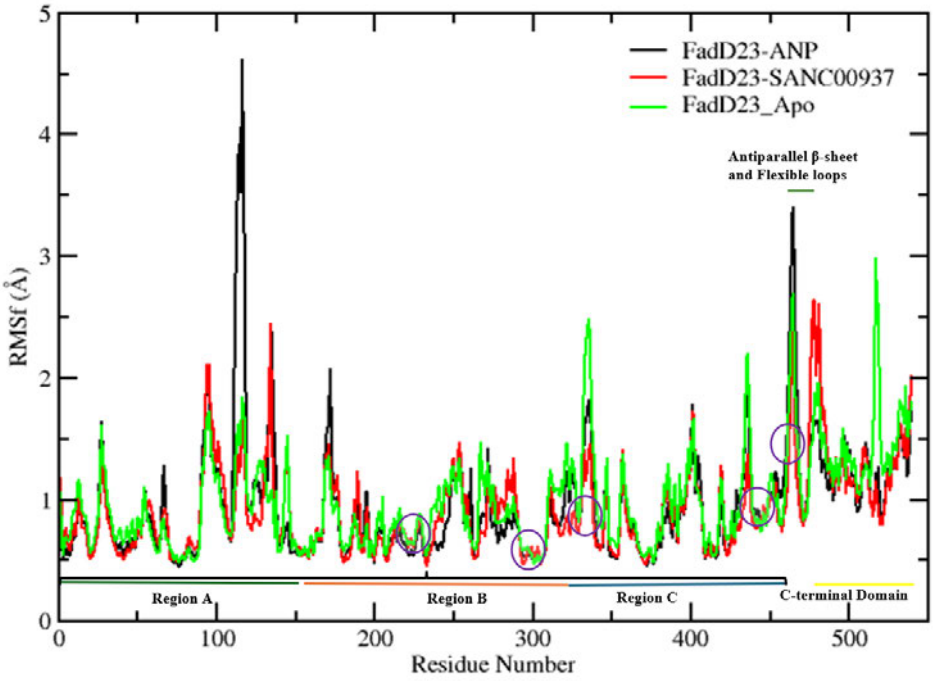

Figure 4.9: RMSf Analysis of FadD23 unbound (Green) and when bound to ANP (Black) and SANC00937 (Red). Purple circles indicate key residues.

In contrast, the FadD23-SANC00937 (red) displayed moderate fluctuations. The fluctuation patterns of this complex mirror both the Apo and ANP systems with minor variations in height. SANC00937 displayed lower RMSf values in some catalytic residues, with a few displaying higher peaks, indicating that SANC00937 restricted mobility more effectively, stabilising several flexible parts of the protein. Region B of the N-terminal appears to be the most rigid region (most reduced fluctuations), with few loop movements. Significant spikes in RMSf were noted around residue indices Pro95, an unknown missing residue 134, and Ile 400 in both complexes. According to Yan et al's crystallographic structure of FadD23, these regions represent the loop and termini regions, and this is expected for solvent-exposed and less ordered regions [17]. FadD23-SANC00937 complex displayed higher peaks in the range of residues 476-496 compared to the ANP complex. This region is part of the C-terminal domain (residue 473–576) and constitutes three peripheral helices and three inner sheets [17, 100]. The increased flexibility suggests that SANC00937 binding could interfere with the protein's normal function. This observation aligns with Teague et al.'s 2003 study on protein flexibility in drug discovery, which indicated that substrate binding reduces conformational entropy to stabilize the protein for catalysis, while inhibitors increase movement in certain regions, hindering the protein's activity [101]. , as observed with SANC00937 in some regions, especially in the C-terminal domain region. The average RMSf for the Apo form FadD23-SANC00937 and ANP system, respectively, is 0.95 Å. is 0.90 Å, and 0.94 Å.

The Apo protein showed moderate flexibility, with higher fluctuations in the loop and terminal regions in comparison to the other two systems. The presence of a ligand significantly stabilizes a protein by reducing its conformational freedom, particularly in regions involved in catalytic binding [92]. ANP appears to have a stronger stabilizing effect on selected regions, such as 213-312, 377-390, and 476-500, while SANC00937 induces slightly greater fluctuations in these areas. Yan et al. (2024) identified these regions as containing key residues like His221 and Asp446, along with hydrophobic residues such as Ala231, Val235, and Phe265, located at the end of the binding pocket (circled in Figure 4.9) [17]. These residues exhibit low RMSf values and maintain rigidity in the ANP complex.

Our docking analysis of the FadD23-SANC00937 showed that SANC00937 competes with ANP for the active site, simultaneously obstructing the entrance to the acyl binding domain, the hydrophobic pocket where the PLM molecule resides. As a result, the hydrophobic binding pocket residues remain unoccupied and often exhibit increased fluctuations. These findings correlate with the RMSd results, which demonstrate that ligand binding reduces local flexibility and aligns with the structural and functional findings of Yan et al.'s crystallographic (2023) study [17]. While RMSf provides an insight into how much each residue fluctuates over time, it does not provide information on how tightly packed the entire protein is around its centre of mass [102].

From the RMSf analysis, we observed that the binding of a ligand had a huge impact on the dynamic behaviour of FadD23. When ANP was bound, the protein residues in some regions became stable, and

this was indicated by low RMSf values. This decrease in flexibility suggests that ANP fits well in the protein, supporting its natural function. On the other hand, SANC00937 showed increased movement in certain segments, implying that the molecule disrupts the protein's normal functioning, which is consistent with the typical behaviour of an inhibitor [101]. In all, the RMSf analysis showed that SANC00937 binding reduces residue-level motion more effectively than both the Apo and ANP.

FadD23-SANC00937 stabilization by hydrogen bond formation

A hydrogen bond (h-bond) is a force of attraction that occurs when a slightly positive hydrogen atom, attached to a strongly electronegative atom (like oxygen, nitrogen, or fluorine), is drawn toward a nearby electronegative atom that has extra electrons (a lone pair) [103]. Some amino acids in proteins form h-bond interactions, among other means, with complexed ligands to stabilize complexes. H-bond formation plays a significant role in controlling the structural conformation of the protein, by influencing protein conformation and binding site dynamics, including ligand interactions [104].

In the FadD23-SANC00937 complex, h-bond formation between the ligand and protein was calculated and presented in Table S0.3. Thirty-five h-bonds were estimated between the ligand and residues Ala328, Asp222, Val336, Gly330, Arg460, Glu301, Ser300, Lys553, Glu333, Ala332, Gln174 and Cys298 in a 130 ns MD trajectory. Out of 35 estimated h-bonds, only 3 had a feasible probability of sustained occurrence: h-bond between the ligand and Ala328 O atom (89.18 %), Asp222 OD2 atom (33.56 %) and Asp222 OD1 atom (27.49 %). The calculated h-bond distances ranged from 2.65 Å to 2.95 Å. The oxygen atom of the Ala328 residue forms a moderate, predominantly electrostatic interaction with the hydrogen atom of the second atom of the ligand. This interaction occurred 89% of the simulation time and maintained an average distance of 2.69 Å. Furthermore, this interaction was well-aligned, with a bond angle of 160°, and a maximum lifetime of 230. This indicates that even though the interaction occurred frequently, it had a relatively short lifespan. In the FadD23-ANP complex, two h-bonds occurred at 19 % and 13 % of the simulation time between the H61 and the H62 atoms of ANP and Ala328. Both had an average distance of 2.87 Å, bond angles of 148°, and maximum lifetimes of 22 and 24, respectively. Yan et al. 2023 reported that the backbone oxygen of Ala328 and the OH groups of Tyr376 formed two h-bonds with the N37 atom of adenosine [17].

The next notable h-bond interaction occurred 33 % of the simulation time and was between the ligand and OD2 atom of Asp222. This interaction had the longest lifetime of 1040 in the simulation, suggesting its contribution in sustaining the complex. This interaction had an average distance of 2.64 Å and angle of 164°. The third notable h-bond occurred 27% of the simulation time, between OD1 atom of Asp222 and the first hydrogen atom of SANC00937. Asp222, which had the most significant electrostatic contribution in the SANC00937 complex, did not form h-bonds with ANP in this study. However, in the

AMP-PNP-FadD23 complex, Asp222 contributed to the stability of the FadD23-ANP complex by interacting with AMP (ANP) [17].

The oxygen atom of Val336, located at the base of adenosine's hydrophobic pocket in the AMP-PNP-FadD23 complex [17], forms a weak h-bond with the second hydrogen of SANC00937, which occurs 3% of the simulation time and has a maximum lifetime of 93. The oxygen atom of Gly330, another residue contributing to the stability of the AMP-PNP-FadD23 [17] complex forms a very weak interaction with the hydrogen of the ligand, which is present for only 1.88% of the simulation time. This interaction shows a marginal bond angle of 146.5°.

According to Hubbard et al. (2010), an ideal h-bond is typically characterized by a hydrogen-to-acceptor distance of less than 2.5 Å (often around 1.9 Å), with the angle between the donor, hydrogen, and acceptor usually falling between 90° and 180°, with 160° being the most common [105]. In the AMP-PNP–FadD23 complex, Arg460 forms a h-bond with the O27 atom of AMP-PNP through its NE atom, while the N-terminal nitrogen (Nα) of Ser300 participates in a similar interaction with the N09 atom of AMP-PNP [17]. In this study, these residues form weak interactions that are short-lived, with a probability of less than 5% with SANC00937. While Arg460, the most significant electrostatic contributor in the FadD23-ANP complex, formed hydrogen bonds that occurred 88%, 75% and 13% of the simulation time with longer lifespans as compared to SANC00937. The remaining hydrogen bonds formed by this residue were short-lived and weak.

Overall, an interatomic distance of 3 Å or greater generally signifies a weak electrostatic interaction, similar to a moderate h-bond or Van der Waals force [106]. The remaining interatomic residues have lower fractions, larger angles, and greater distances, which indicate weak or transient bond formation. These interactions likely contribute to the flexibility of the complex.

The SANC00937 ligand formed multiple stable hydrogen bonds with the protein residues Ala328, Asp222, Gly330, and Ser300. Among these, Ala328 and Asp222 emerged as the primary interacting residues. These hydrogen bonds were geometrically favourable and showed maximum lifetime contacts, with the second oxygen of Asp222 exhibiting the most prolonged interaction with SANC00937. Similarly, ANP formed several stable hydrogen bonds with residues Arg460, Ala328, and Lys553. Arg460 stood out as the main interacting residue for ANP, while Asp446 showed the longest interaction, and Lys553 contributed the most interactions overall. To analyse these interactions further, we closely examined the changes in the h-bond over 130 ns and plotted the distances (Figure 4.10-Figure 4.13).

The second oxygen atom of SANC00937 and the hydrogen atom of Ala328 (Ala328_O-H_O2_SANC00937) in Figure 4.10 and

Figure S.0.8 begin the simulation with increased distance fluctuations exceeding 3 Å during the first 8 ns of the simulation. However, they subsequently stabilized, maintaining a h-bond distance of

approximately 2.5 to 3.5 Å for the remainder of the simulation. The Ala328_O-H62_N6_ANP bond, on the other hand, remains intact throughout the simulation but shows frequent, short fluctuations ranging between 1.4 Å and 6.2 Å. Overall, SANC00937 formed a stronger and more consistent h-bond with Ala 328, whereas ANP formed a weak and fluctuating hydrogen bond. This interaction was further confirmed by the probability distribution plot (Figure 4.10-right), which displayed a sharp peak at about 2.80 Å in SANC00937, indicating that this is the most likely h-bond distance in the simulation, while ANP showed broader peaks centred around a different value, suggesting that the h-bond distance was maintained often in the simulation but across different conformations. Additionally, the 3D snapshots illustrate the h-bond interactions sampled from an MD trajectory, supporting the RMSd and probability distribution findings.

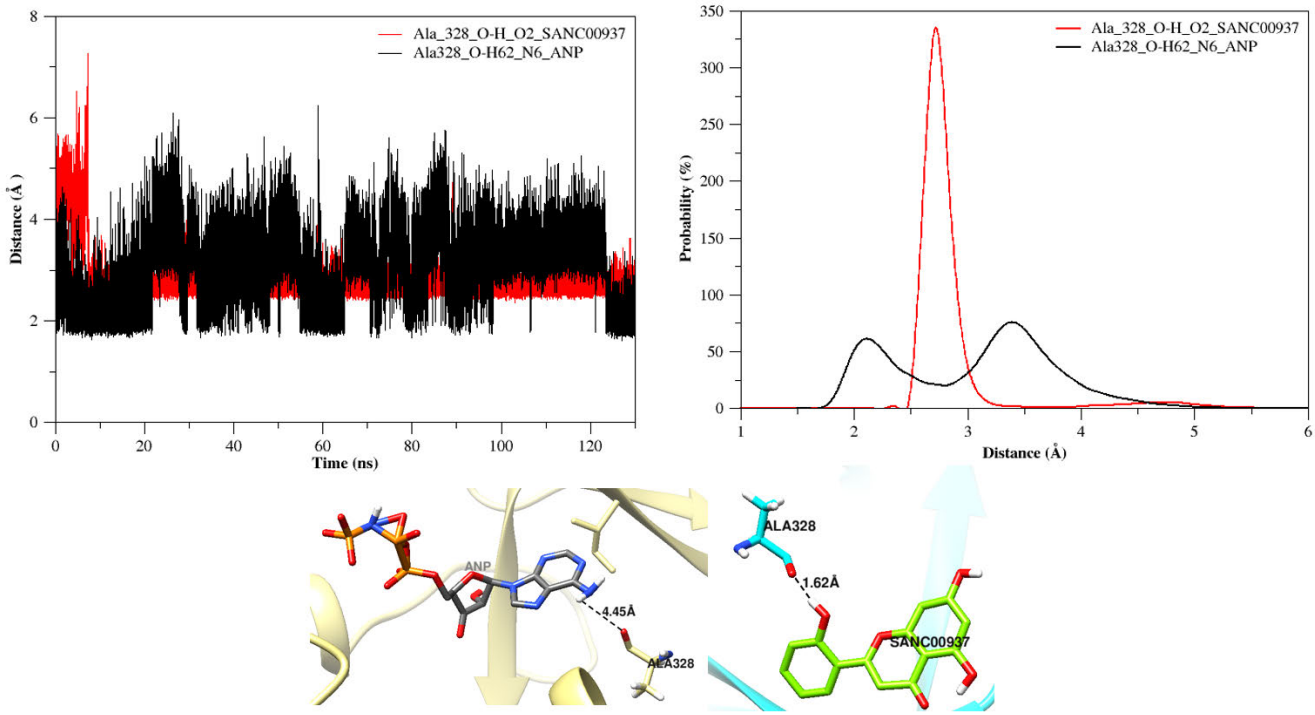

Figure 4.10: "Comparish-bond distances between Ala328-SANC00937 and Ala328-ANP, highlighting the stability and consistency of interactions over time. SANC00937 exhibits a narrower distance distribution and shorter interaction range, indicating a more reliable binding profile than ANP."

The h-bond OD2-H2 interaction only existed in SANC00937 and not in ANP. The bond fluctuates throughout the simulation but still maintains distances between 2-3.5 Å in most segments (Figure 4.11). This implies the bond is not persistent, it only exists for a short period. The probability distribution shows two distinct peaks: a main peak and a secondary peak. The main peak is sharp, narrow and centred at 2.8 Å, confirming that the bond forms at a h-bond distance range. The secondary peak is broad,

indicating that the distribution of this h-bond is widely spread, indicating instability. Overall, this implies that the bond is weak as opposed to other contacts, like that made by Ala328, observed in the trajectory. Even though the Asp222-SANC00937 bond showed dormancy in the other evaluations, it cannot be considered the key stabilizing bond for this interaction, since it often breaks.

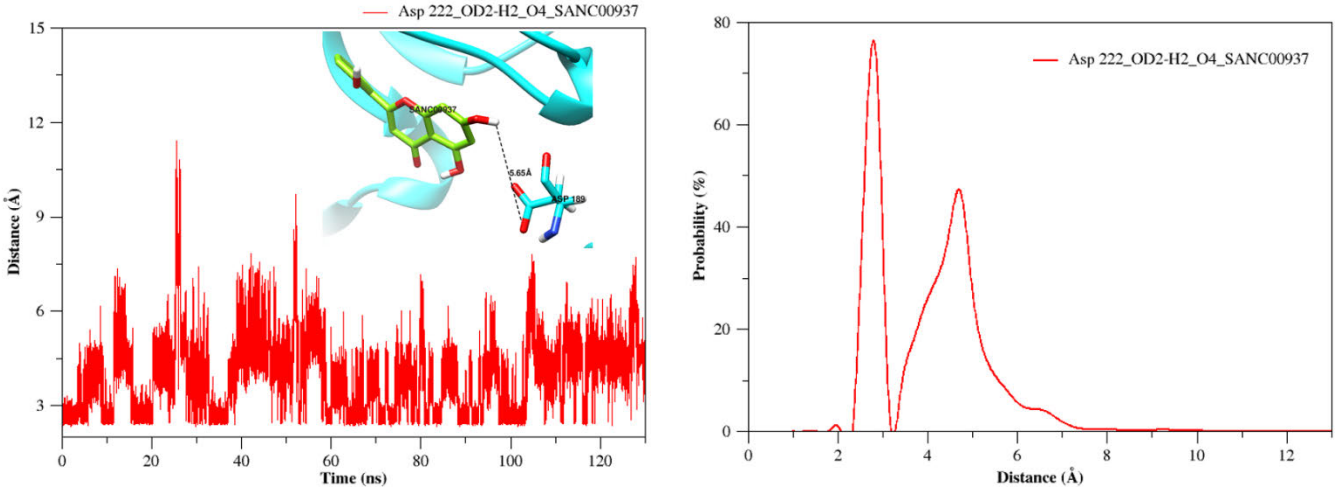

Figure 4.11: Graph showing time-evolution and probability distribution of the Asp222–SANC00937 hydrogen bond, showing fluctuating interaction distances with a dominant peak, indicating intermittent but recurrent bonding stability.

The Lys553-ANP interaction appeared steady, maintaining a distance between 1.6 Å – 4 Å throughout the simulation (Figure 4.12 and

Figure S.0.9). This means that the bond is persistent despite the fluctuations. The Lys553-SANC00937 bond fluctuates widely in a distance range of 2 Å - 6.5 Å, indicating the widening and shortening of the distance between Ly553 and the ligand over time.

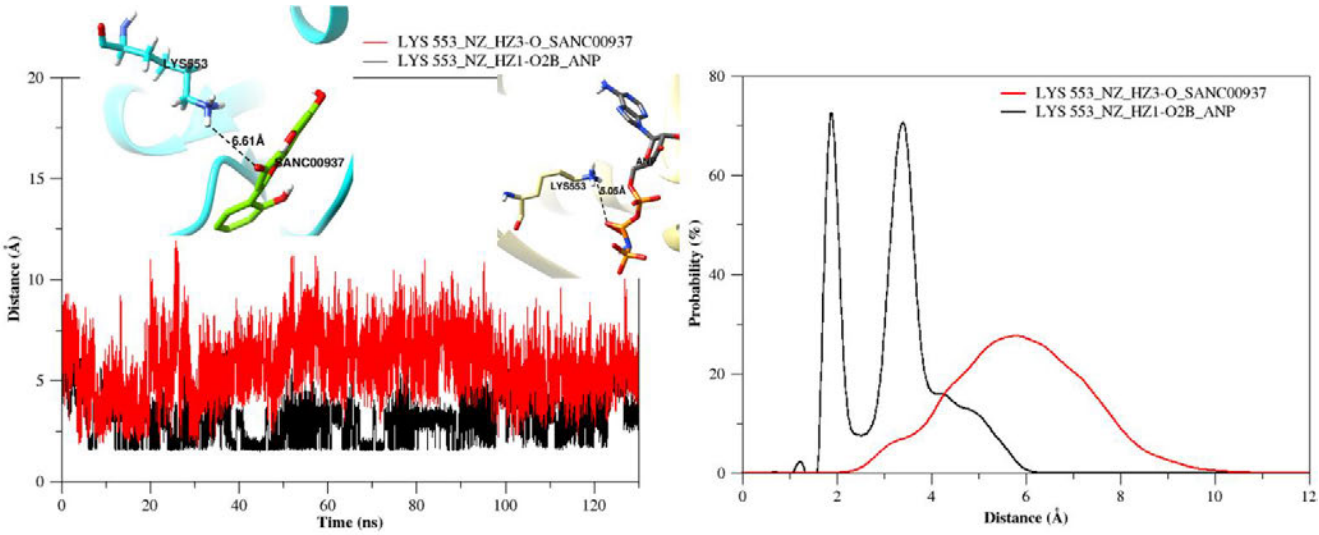

Figure 4.12: Time evolution and distribution of h-bond distances between Ala 328 and SANC00937 and ANP, showing increased h-bond distance in SANC00937 as evident by the broad distribution.

The h-bond distance between the HH12 atom of Arg460 and the oxygen of SANC00937 significantly increased with time, with distances ranging from 1.6 to 14.3 Å (Figure 4.13). This is beyond the acceptable cut-off of 3.5 Å for hydrogen bonds, indicating that the interaction between HH12 and O transitions from a h-bond to a weak electrostatic interaction and eventually no interaction. Arg 460 HH12 atom and O3A of ANP maintain a stable and consistent h-bond distance for the first 120 ns of the simulation. This is supported by the probability distribution plot, which shows a sharp, narrow peak at around 2 Å for this interaction. In contrast, the probability distribution for HH12 and O is broad. The snapshots further confirm these findings by providing actual h-bond distances. The average distance measured between Arg460 - SANC00937 and Arg460 – ANP were respectively 7.18 Å and 2.16 Å (Table S0.5), denoting intermittent interaction between the former, and sustained interaction between the latter.

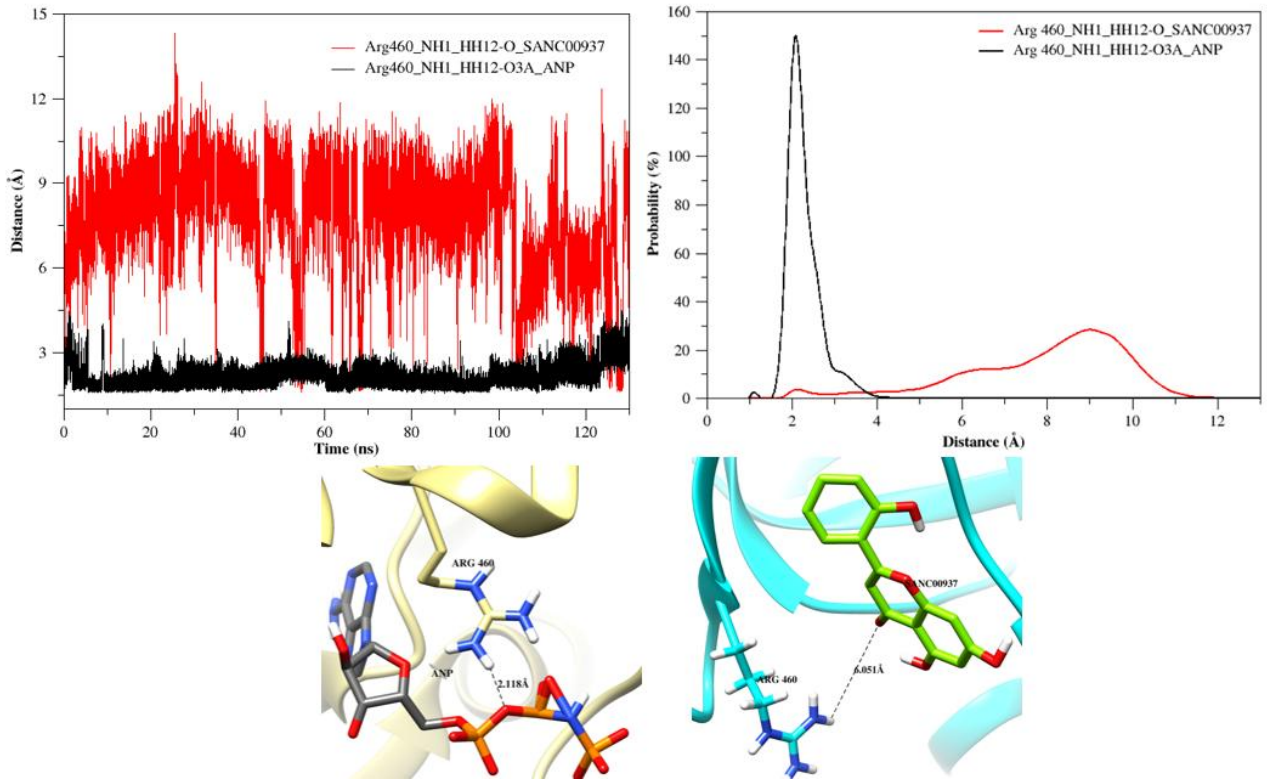

Figure 4.13: Comparison of time evolution and distribution of the h-bond distances between Arg460-SANC00937 and Arg460-ANP over 130 ns, showing that ANP maintains a more stable and consistent interaction an demonstrated by the narrower distance distribution.

Overall, SANC00937 forms a more stable and favourable h-bond with Ala 328 as opposed to ANP. However, ANP showed a stronger binding with Arg 460, while SANC00937 failed to sustain this interaction. The Asp222 h-bond is only dominant in SANC00937; however, it appears to be weak and non-stabilizing. With Lys 553, ANP showed a strong and favorable hydrogen bond.

Dictionary of Secondary Structure Elements (DSSP)

DSSP analysis was performed to examine the influence of the simulated ligands on the secondary structural elements of FadD23 and overall protein conformational dynamics. By monitoring changes in α-helices, β-sheets, turns, and coils, valuable insight into protein structure integrity is obtained and used to understand the impact of ligand binding to the protein (i.e., stabilization or destabilization of key structural motifs) [107]. Through this analysis, one could also uncover intricate structural features such as disordered regions, which are characterized by flexibility and lack of defined structure, as well as interaction sites where binding occurs within the protein [107]. In this study, DSSP was calculated for the overall FadD23 structure in the respective systems, and the results are presented in Figure 4.14.

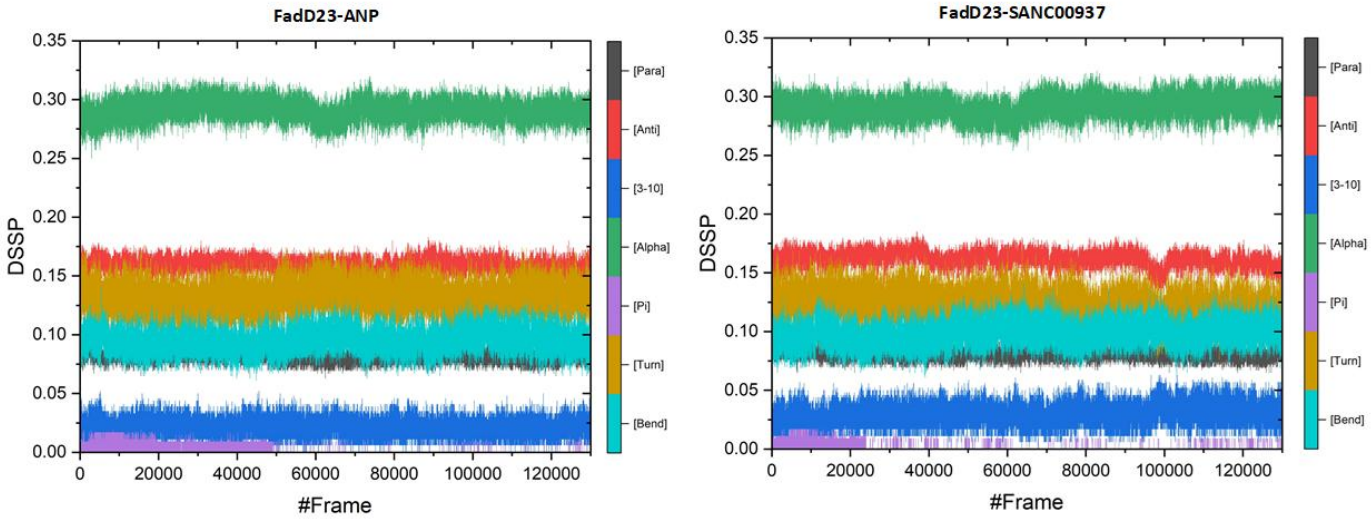

Figure 4.14: Time-evolution of secondary structure elements of a protein in simulated complexes

The deviation of structural elements (α-helices, β-sheets, turns, and coils) from the starting structure of FadD23 is relatively minimal for almost all structural elements except for the Pi structural element. Both ANP and SANC00937 systems are dominated by α-helices, followed by the anti and turns, while Pi remains relatively low. Pi-helices are generally rare and energetically less favourable secondary structural elements. The reduction in fluctuations indicates that ligand binding does not destabilize the protein. The reduction in pi-helices, especially in the SANC00937 complex, signifies a more compact and stable conformation in comparison to ANP.

We further examined the impact of ligand binding on individual residue structural organisation in FadD23 in the respective systems (Figure 4.15 – Figure 4.18). Panel A of Figure 4.15, comparatively depicts the change in the formation of parallel β-sheets in protein structure in respective complexes. The FadD23-SANC00937 complex exhibits a higher frequency and greater extent of parallel β-sheet formation in comparison to the FadD23-ANP complex. This is visible particularly between residues at positions 59-139, 174-292, and 500 which encompasses region A of the N-terminus and a few active site residues like His221, and Asp222, as well as the C-terminus which constitutes three peripheral helices and three inner sheets [17, 100]. In contrast, residues at position 360, 393, 397, 407, and 473 of the FadD23-ANP complex demonstrate the highest likelihood of parallel β-sheet formation. Panel B illustrates the formation of antiparallel β-sheets, highlighting that the SANC00937 complex once again presents a greater occurrence of antiparallel sheets, especially within the mid N-terminal and C-terminal regions (residues 300-539).

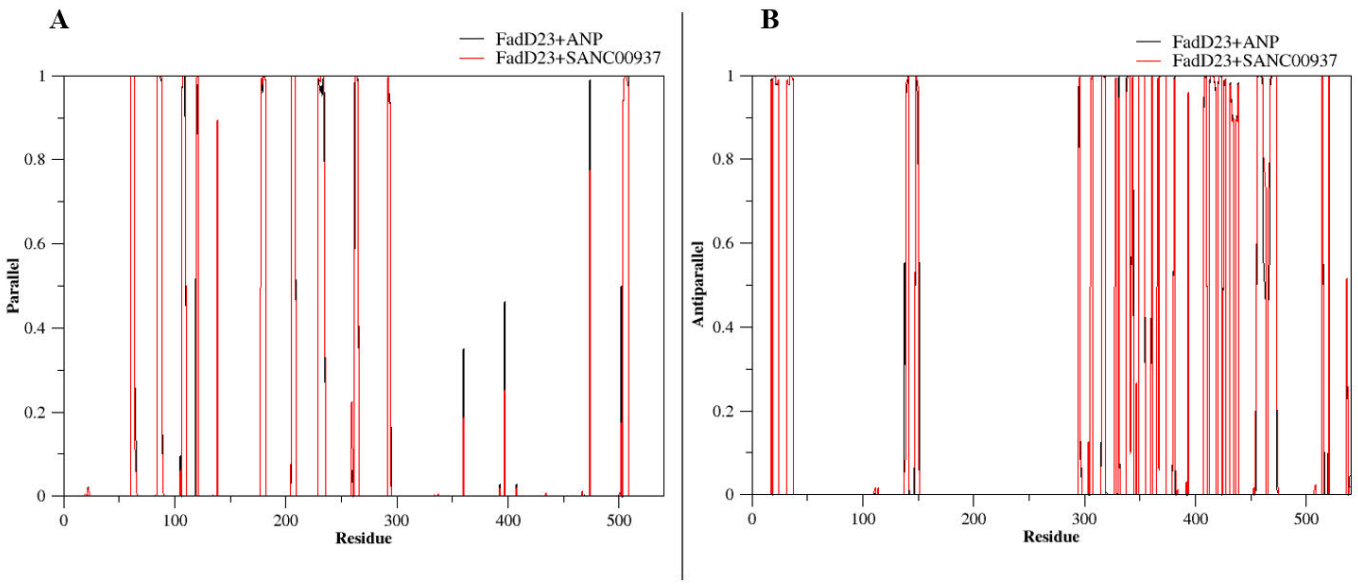

Figure 4.15: Comparison of per-residue secondary structure occupancy between the parallel (**A**) and antiparallel (**B**) sheet formation in FadD23-SANC00937 and FadD23-ANP complexes.

The alpha helix (C), also known as a key indicator of structural stability, was maintained throughout for both complexes (Figure 4.16). The FadD23-SANC00937 complex displayed more extended and consistent alpha-helical regions in several domains, especially between residues 1-104 and 150-284. The ANP complex showed dominance at residue 487. In panel D, both complexes exhibited scattered, irregular, and localized formation of the 310-helices, with the SANC00937 complex showing slightly higher frequencies and distribution. At residues 283 and 300, the ANP complex again showed dormancy.

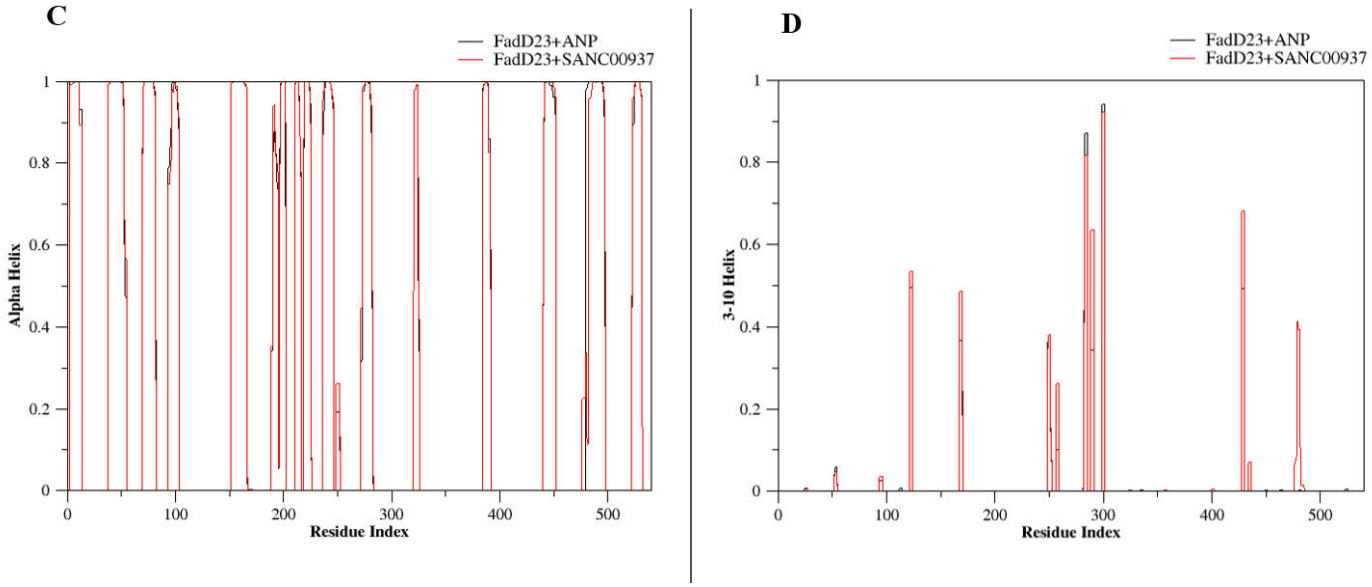

Figure 4.16: Comparison of per-residue secondary structure occupancy between the alpha helix (**C**) and 3_{10} (**D**) sheet formation in FadD23-SANC00937 and FadD23-ANP complexes.

In Figure 4.17, panel E shows a huge reduction in the formation of the pi-helix in both complexes, with SANC00937 showing the highest probability. In panel F, a wide distribution of Turn helices was observed in both complexes, but the SANC00937 complex demonstrated a greater number and density of turns compared to FadD23-ANP. Notably, in the residues 140-146 region, the ANP complex was predominant, as it was the only complex to display turn helices in this area.

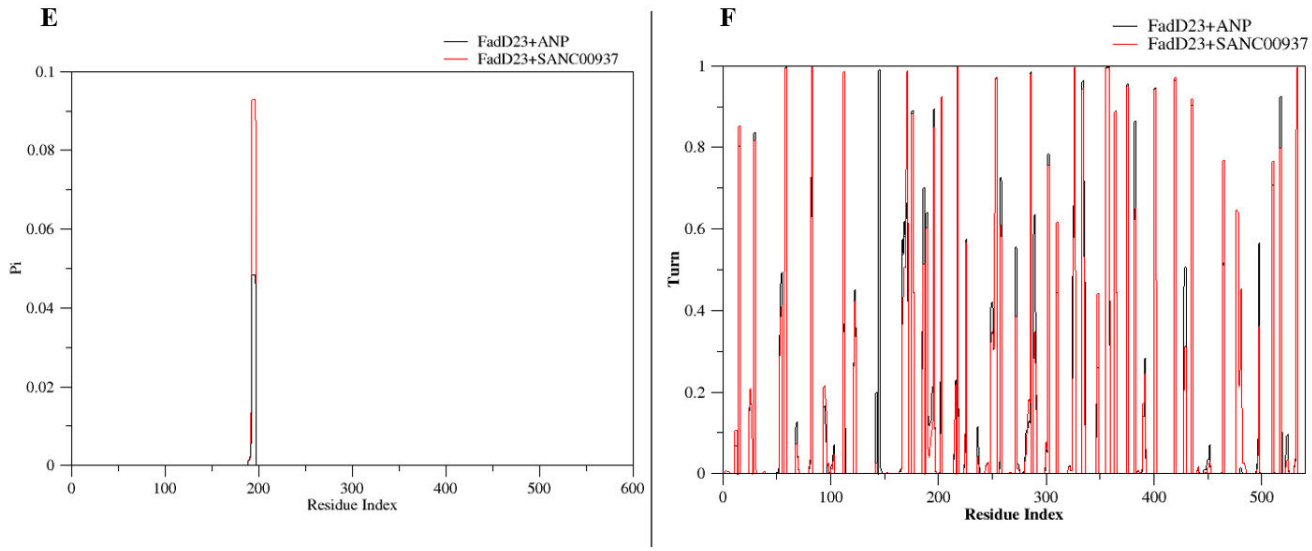

Figure 4.17: Comparison of per-residue secondary structure occupancy between the Pi (**E**) and the Turn (**F**) sheet formation in FadD23-SANC00937 and FadD23-ANP complexes.

In Figure 4.18 bend helices were observed throughout the simulation in both complexes; however, they were not uniformly distributed. The SANC00937 complex exhibited a greater frequency and density of bends across most residues. ANP showed dominance in a few residues.

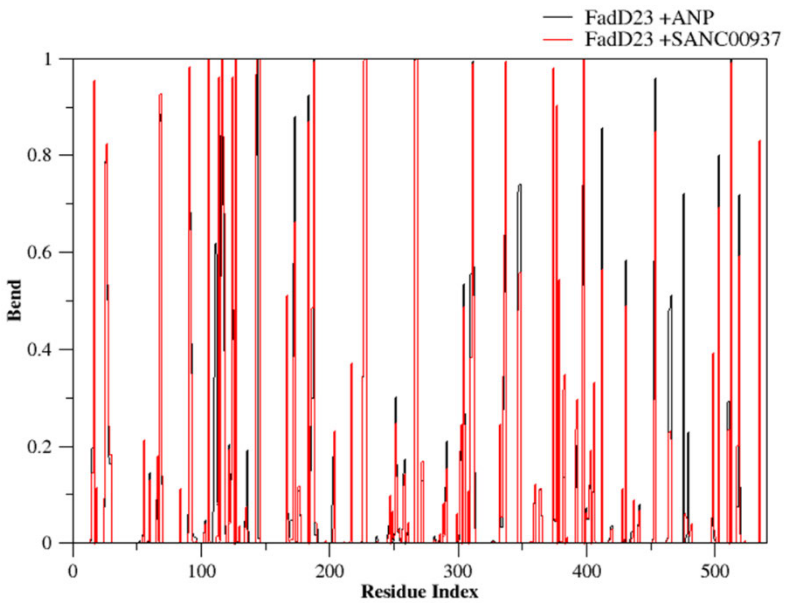

Figure 4.18: Comparison of per-residue secondary structure occupancy related to bend and sheet formation in FadD23-SANC00937 and FadD23-ANP complexes.

The secondary structure analysis confirmed that the core α-helical and β-sheet elements of FadD23 remained largely preserved across all simulations, indicating that ligand binding did not disrupt the protein's fundamental structural architecture.

4.4. Drug toxicity evaluation

The most crucial aspect of drug development is identifying the desired pharmacological properties of a potential inhibitor before determining whether a compound is suitable for further development. Utilizing the Swiss ADME tool [74], we evaluated the drug-like qualities, absorption potential, metabolic kinetics, safety flags, and synthetic feasibility of the seven compounds. The findings are presented in Table 4.3.

Compounds SANC00937, SANC00520, SANC00519, SANC00522, SANC00834, SANC01097, and SANC0109 displayed favorable physiological profiles that were consistent with drug-like molecules. Complying with Lipinski's rule of five, with no violations except for compound SANC00834 [108]. SANC01098 lacked most of the data. The molecular weights for all seven compounds ranged between 200.32 g/mol and 286.28 g/mol, which falls well within the acceptable range for drug candidates according to Lipinski's first rule, which states that an orally active drug exhibits a molecular weight of less than 500 g/mol [108]. Furthermore, most of the compounds also displayed high gastrointestinal absorption, which is associated with good oral bioavailability.

Compounds SANC00937, SANC00520, SANC00519, and SANC00522 displayed low fractions of sp^3 carbons and high levels of aromaticity. This could potentially impact their flexibility and binding specificity. In contrast, SANC00834, SANC01097, and SANC0109 displayed a higher fraction of sp^3 and increased flexibility due to an increased number of rotatable bonds, which in turn explains the enhanced membrane permeability (blood-brain permeability). Most of these compounds demonstrated acceptable hydrogen bond capacity and topological surface area (TPSA) below 140 $Å^2$. Generally, compounds with fewer h-bonds exhibit higher oral bioavailability because excessive h-bonds hinder passive diffusion through the lipid membrane [109]. This is a physiological trait that is essential for molecular recognition and binding to biological targets. [109]. No Pan-Assay Interference (PAIN) alerts were detected for any of the compounds. However, some compounds like SANC00519 and SANC00522 exhibit acceptor BRENK alerts, which could indicate potential reactivity concerns. The Cytochrome P450 inhibition profiles revealed possible risk for drug-drug interaction risks with most of the compounds except SANC01097. Most of the compounds, except SANC00834 (slightly above), showed lipophilicity, which is indicated by a consensus logP of less than 5 (maximum acceptable value is 5), according to Lipinski's rule [108].

Overall, most of these compounds showed promising drug-like properties, with SANC01097 showing the most favorable due to its high bioavailability score, lack of interference with major Cytochrome P-450 enzymes, and absence of structural alerts.

Table 4.3: Predicted physicochemical properties and toxicities of SANCDB compounds.

Compound ID	SANC00937	SANC00520	SANC00519	SANC00522	SANC00834	SANC01097	SANC01098
							
Formula	$C_{15}H_{10}O_5$	$C_{15}H_{12}O_5$	$C_{16}H_{14}O_5$	$C_{15}H_{12}O_3$	$C_{18}H_{30}O_2$	$C_{12}H_{24}O_2$	$C_{18}H_{32}O_2$
Molecular weight (g/mol)	270.24	272.25	286.28	240.25	278.43	200.32	280.4
Number of heavy atoms	20	20	21	18	20	14	20
Number of aromatic heavy atoms	16	12	12	12	0	0	0
Fraction Csp3	0.00	0.13	0.06	0.00	0.61	0.92	0.72
Number of rotatable bonds	1	1	4	3	13	10	14
Number of H-bond acceptors	5	5	5	3	2	2	2
Number of H-bond donors	3	3	3	2	1	1	1
Molar Refractivity	73.99	71.57	78.81	70.29	88.99	61.57	89.46
TPSA	90.90 Å²	86.99 Å²	86.99 Å²	57.53 Å²	37.30 Å²	37.30 Å²	37.30 Å²
Consensus $LogP_{o/w}$	2.15	1.86	2.38	2.75	5.09	3.51	No Data
Blood-brain barrier permeability	No	No	No	Yes	Yes	Yes	No Data
GI absorption	High	High	High	High	High	High	No Data
P-gp substrate	No	Yes	No	No	No	No	No Data
Synthetic accessibility	3.03	3.04	2.80	2.49	3.03	1.87	No Data

CYP-450 inhibitor	CYP1A2 / CYP2D6	CYP1A2 / CYP3A4	CYP1A2 / CYP2C9/ CYP3A4	CYP1A2 / CYP2C9/ CYP3A4	CYP1A2 / CYP2C9	None	No Data
Log Kp (skin permeation)	-5.70 cm/s	-6.11 cm/s	-5.81 cm/s	-5.26 cm/s	-3.41cm/s	-4.54 cm/s	No Data
Druglikeness violations	0 violations	0 violations	0 violations	0 violations	1 violation: Lipinski	0 violations	No Data
Bioavailability Score	0.55	0.55	0.55	0.55	0.85	0.85	No Data
PAINS	0 alert	0 alerts	0 alerts	0 alerts	0 alerts	0 alerts	0 alerts
Brenk	0 alert	0 alerts	1 alert: Michael_acceptor_1	1 alert: Michael_acceptor_1	1 alert: isolated alkene	0 alerts	0 alerts

The toxicity profiling of SANC00937 was carried out using ProTox [76] and presented in Table 4.4.

Table 4.4 shows that SANC00937 is predicted to have low acute toxicity and falls within a mild toxicological category. The compound shows low acute toxicity and minimal mutagenic/carcinogenic risk. It has the potential to cause endocrine disruption, respiratory irritation, moderate kidney toxicity, and mitochondrial stress. Ecotoxicity implies that the compound could have direct implications on nature. The compound shows no severe effects on major organs like the liver, heart, and skin.

Table 4.4: Predicted toxicity profile of SANC00937 using the ProTox webserver.

Parameter / Endpoint	**Prediction**	**Probability**	**Interpretation**
LD_{50} (oral)	3919 mg/kg	–	Low acute toxicity (Class 5 range)
Toxicity Class	Class 5	–	"May be harmful if swallowed"; mild acute toxicity
Hepatotoxicity	Inactive	0.69	No liver toxicity signal predicted
Neurotoxicity	Inactive	0.85	Low neurological risk
Nephrotoxicity	Active	0.63	Moderate alert for kidney toxicity
Respiratory toxicity	Active	0.84	Strong alert; potential respiratory irritation/toxicity

Parameter / Endpoint	Prediction	Probability	Interpretation
Cardiotoxicity	Inactive	0.88	No predicted cardiac involvement
Carcinogenicity	Inactive	0.69	Not carcinogenic
Mutagenicity	Inactive	0.74	No mutagenic potential
Cytotoxicity	Inactive	0.91	Very low general cytotoxicity
Immunotoxicity	Inactive	0.87	No immune toxicity predicted
Ecotoxicity	Active	0.53	Possible environmental risk
Clinical toxicity	Inactive	0.54	Low clinical toxicity alert
Nutritional toxicity	Active	0.67	Borderline to moderate nutritional disruption prediction
Nuclear receptor pathways	Mixed (AhR, ER, ER-LBD, Aromatase = Active)	0.82–1.00	Evidence of endocrine interaction, especially estrogenic pathways
Stress response pathways	Several active (MMP, p53, ATAD5)	0.99–1.00	Mitochondrial stress and DNA damage signalling activation
Molecular initiating events	All inactive	0.69–0.99	No direct receptor/channel mechanistic triggers
CYP Interactions (1A2, 2C19, 2C9, 2D6, 3A4, 2E1)	Mostly Active (1A2, 2C19, 2C9, 3A4)	0.89–1.00	Multiple CYP-mediated metabolic routes; potential drug–drug interactions

SANC00937 demonstrated favourable baseline safety profiles, with low acute oral toxicity (LD_{50} of 3919 mg/kg) and minimal risks for hepatotoxicity, cardiotoxicity, mutagenicity, cytotoxicity, and carcinogenicity. However, several minor toxicity alerts were highlighted, which raise important considerations for drug discovery. To ensure maximum safety regarding these compounds, *in vitro* renal and airway cytotoxicity assays should be considered to examine whether these alerts represent true biological risk or are model-driven false positives.

Table 4.5: Predicted toxicity profile of SANC01098 using the ProTox webserver.

Parameter / Endpoint	Prediction	Probability	Interpretation
LD_{50} (oral)	3919 mg/kg	–	Low acute toxicity (Class 6 range)

Parameter / Endpoint	Prediction	Probability	Interpretation
Toxicity Class	Class 6	–	"May be harmful if swallowed"; mild acute toxicity
Hepatotoxicity	Inactive	0.67	No liver toxicity signal predicted
Neurotoxicity	Inactive	0.83	Low neurological risk
Nephrotoxicity	Active	0.65	Moderate alert for kidney toxicity
Respiratory toxicity	Active	0.86	Strong alert; potential respiratory irritation/toxicity
Cardiotoxicity	Inactive	0.80	No predicted cardiac involvement
Carcinogenicity	Inactive	0.67	Not carcinogenic
Mutagenicity	Inactive	0.80	No mutagenic potential
BBB-Barier	Active	0.56	Can cross the blood–brain barrier
Cytotoxicity	Inactive	0.61	Very low general cytotoxicity
Immunotoxicity	Inactive	0.84	moderate systemic toxicity
Ecotoxicity	Active	0.52	Possible environmental risk
Clinical toxicity	Inactive	0.51	Low clinical toxicity alert
Nutritional toxicity	Active	0.65	Borderline to moderate nutritional disruption prediction
Nuclear receptor pathways	Mixed (ER, ER-LBD, Aromatase = Active)	0..66-0.77	Evidence of endocrine interaction, especially estrogenic pathways
Stress response pathways	Several active (MMP, P53, ATAD5)	0.57–0.86	Mitochondrial stress and DNA damage signalling activation

Parameter / Endpoint	Prediction	Probability	Interpretation
Molecular initiating events	Several active (TTR, GABAR, Ache)	0.5–0.96	• Potential neurological and endocrine interference
CYP Interactions (1A2, 2C19, 2C9, 2D6, 3A4, 2E1)	Mostly Active (1A2, 2C19, 2C9, 3A4)	0.90–1.00	Multiple CYP-mediated metabolic routes; potential drug–drug interactions

SANC01098 exhibits moderate safety characteristics, characterized by a moderate level of systemic toxicity, high organ-specific toxicity, and significant mechanistic toxicity, alongside a low risk of genotoxicity. Therefore, it may not be suitable for further drug development.

5. Chapter Five

Conclusion and future perspectives

5.1. Conclusion

Drug-resistant TB is a major obstacle to global TB control, and one that requires immediate and effective intervention. In this study, we explored the potential of natural compounds from SANCDB as inhibitors of *M. tuberculosis* FadD23, through the application of computational methods including virtual screening/molecular docking, molecular dynamics simulations, and *in silico* compound toxicity profiling. Several potential inhibitors were identified. SANC00937, a flavonoid isolated from the *G. africana* species found in the Northern Cape province of South Africa, demonstrated optimal binding to the ATP-binding site of FadD23, indicating a probability of competitive binding with ATP to the binding site. Although this compound is structurally different (and smaller) from ANP, it displayed a higher binding affinity to the protein compared to the native ANP. The redocking of the native ligand generated an RMSd exceeding 2Å. However, a visual inspection of the binding site confirmed that the ligand was accurately positioned within it, preserving similar interactions with the active site residues. Further analyses led to the conclusive realization that the elevated RMSd was caused by the oversized dimensions of the grid box and the rotational flexibility of the phosphate group. Investigations using post-MD simulations revealed that SANC01098 interacts more strongly with the binding site residues under physiological conditions, and several of which are crucial for the function of FadD23. While ADMET profiling also suggested that SANC00937 possessed desirable pharmacokinetic and safety properties. SANC01097, despite being unstable under physiological conditions (MD simulations) demonstrated the most favourable properties, which align well with the goal of this study - to identify potent and safe natural inhibitors of *M. tuberculosis* FadD23 within South Africa's rich biodiversity and characterize their potential inhibition mechanism. Although SANC01098 showed favorable results in molecular dynamics simulations, its pharmacokinetic properties do not meet the ideal criteria for drug development compounds. Therefore, as a precautionary measure, it would be advisable to conduct lab-based toxicity assessments for both SANC00937 and SANC01098 to validate their potential as promising therapeutic candidates for tuberculosis treatment targeting FadD23 in lipid metabolism.

5.2. Future Perspective

The overall findings of this study provide strong evidence that our South African natural compounds have the potential to serve as effective inhibitors. These results lay a solid foundation for advancing the search for new, effective, and safer TB treatments by inhibiting FadD23. However, following the docking limitation that led to RMSd exceeding 2 Å due to the use of a large grid box, which allowed increased conformational sampling and positional drifts. We propose that for future studies, we refine the grid box by adjusting the docking parameters to encapsulate the binding site and not the whole protein. This would improve pose accuracy in docking. Following these computational predictions, the next step would be to confirm them through laboratory experiments. The transition from *in silico* to lab-based experiments remains essential for turning these theoretical results into biological reality and ensuring the compounds' effectiveness, safety, and viability. However, this shift not only requires careful consideration of the specific assays to be employed but also involves significant cost implications, including expenses related to reagents, biological complexity, and infrastructure requirements. Especially since tuberculosis research requires biosafety level 3 (BSL-3) laboratories for safe handling. Experimental validation could include enzyme inhibition assays to evaluate the activity of the compounds against FadD23, while antimicrobial testing against *M. tuberculosis* may be excluded, as prior studies have already reported activity (0.1 M for SANC00937 and 100% inhibition at 50 µg/mL for SANC01098). Kinetic studies will assist us in examining the enzyme's kinetics (e.g., Vmax and Km) to understand how the inhibitor influences the enzyme's activity, while mechanism of action studies allow us to determine and understand the mechanism of inhibition to see whether it's competitive or non-competitive inhibition, giving us a deeper understanding of how the inhibitor interacts with the enzyme. This can be followed by binding studies, such as surface plasmon resonance or isothermal titration calorimetry, to confirm ligand–protein interactions. Performing cell-based assays using microbial strains would provide further insight into antimicrobial efficacy. To ensure maximum toxicity safety and prevent potential treatment disruptions, *in vitro* cytotoxicity assays (especially for renal and airway systems) using mammalian cells would assist in examining whether SwissADME and ProTox alerts represent true biological risks or are model-driven false positives. The identified compounds can be readily evaluated experimentally, as they are commercially available and the target protein can be obtained in recombinant form. SANC00937 (5,7,2′-trihydroxyflavone) is commercially available for online purchase from EvitaChem, and SANC01098 (linoleic acid) is commercially available from Thermo Fisher Scientific for research purposes. The recombinant FadD23 protein is available for research purchase through international commercial suppliers. Once all biological studies pass, the compound moves into the optimisation phase, where its drug potency is evaluated and later undergoes *in vivo* testing to determine therapeutic efficacy and safety. Future studies could also look into the use of current TB drugs and the SANC00937 for combination therapy, to improve treatment outcomes or slow down the development of resistance through synergistic effects, or maybe in developing newer

formulation strategies like inhalants, which would enhance the effectiveness of the drug by directly targeting the lungs, which is the primary site of TB infection directly.

References

1. Koch, R., T.D. Brock, and E.B. Fred, *The Etiology of Tuberculosis.* Reviews of Infectious Diseases, 1982. **4**(6): p. 1270–1274.
2. Daniel, T.M., *Pioneers of medicine and their impact on tuberculosis*. 2000: University Rochester Press.
3. World Health, O., *Global tuberculosis report 2024*. 2024, Geneva: World Health Organization.
4. Olivier, C. and L. Luies, *WHO Goals and Beyond: Managing HIV/TB Co-infection in South Africa.* SN Comprehensive Clinical Medicine, 2023. **5**(1).
5. Liu, X., D. Tang, M. Qi, and J.Q. He, *Efficacy of linezolid in the treatment of tuberculous meningitis: a meta-analysis.* Arch Med Sci, 2024. **20**(3): p. 1038–1042.
6. Mereškevičienė, R. and E. Danila, *The Adverse Effects of Tuberculosis Treatment: A Comprehensive Literature Review.* Medicina (Kaunas), 2025. **61**(5).
7. Garg, R., R.K. Garg, P. Garg, A. Srivastava, D.K. Bajaj, and S. Bhattacharya, *Linezolid induced lactic acidosis in tuberculosis: a systematic review of published case reports, case series*. 2024.
8. Ferreira, Â., P. Sobrosa, M. Costa, I. Miranda, and D. Guerra, *Linezolid Toxicity: A Clinical Case Report.* Cureus, 2024. **16**(3): p. e55672.
9. Conradie, F., A.H. Diacon, N. Ngubane, P. Howell, D. Everitt, A.M. Crook, C.M. Mendel, E. Egizi, J. Moreira, J. Timm, T.D. McHugh, G.H. Wills, A. Bateson, R. Hunt, C. Van Niekerk, M. Li, M. Olugbosi, and M. Spigelman, *Treatment of Highly Drug-Resistant Pulmonary Tuberculosis.* New England Journal of Medicine, 2020. **382**(10): p. 893–902.
10. Abou Hassan, O.K., M. Karnib, R. El-Khoury, G. Nemer, M. Ahdab-Barmada, and P. BouKhalil, *Linezolid Toxicity and Mitochondrial Susceptibility: A Novel Neurological Complication in a Lebanese Patient.* Front Pharmacol, 2016. **7**: p. 325.
11. Zhu, H., X. Zhou, Z. Zhuang, L. Li, J. Bi, and K. Mi, *Advances of new drugs bedaquiline and delamanid in the treatment of multi-drug resistant tuberculosis in children.* Frontiers in Cellular and Infection Microbiology, 2023. **Volume 13 - 2023**.
12. Hartkoorn, R.C., S. Uplekar, and S.T. Cole, *Cross-resistance between clofazimine and bedaquiline through upregulation of mmpl5 in mycobacterium tuberculosis.* Antimicrobial Agents and Chemotherapy, 2014. **58**(5): p. 2979–2981.
13. Ismail, N.A., S.V. Omar, L. Joseph, N. Govender, L. Blows, F. Ismail, H. Koornhof, A.W. Dreyer, K. Kaniga, and N. Ndjeka, *Defining Bedaquiline Susceptibility, Resistance, Cross-Resistance and Associated Genetic Determinants: A Retrospective Cohort Study.* EBioMedicine, 2018. **28**: p. 136–142.

14. Kurahara, Y., Y. Tanaka, T. Kobayashi, S. Yoshida, and K. Tsuyuguchi, *Changes in skin discoloration according to clofazimine dosage in nontuberculous mycobacterial pulmonary disease.* Journal of Infection and Chemotherapy, 2025. **31**(1): p. 102441.
15. Nair, P., T. Hasan, K. Zaw, S. Allamuratova, A. Ismailov, P. Mendonca, Z. Bekbaev, N. Parpieva, J. Singh, and N. Sitali, *Acquired bedaquiline resistance in Karakalpakstan, Uzbekistan.* The International Journal of Tuberculosis and Lung Disease, 2022. **26**(7): p. 658–663.
16. World Health, O., *WHO consolidated operational handbook on tuberculosis: module 4: treatment and care*. 2025, Geneva: World Health Organization.
17. Yan, M., L. Cao, L. Zhao, W. Zhou, X. Liu, W. Zhang, and Z. Rao, *The Key Roles of Mycobacterium tuberculosis FadD23 C-terminal Domain in Catalytic Mechanisms.* Frontiers in Microbiology, 2023. **14**.
18. Gilmore, S.A., M.W. Schelle, C.M. Holsclaw, C.D. Leigh, M. Jain, J.S. Cox, J.A. Leary, and C.R. Bertozzi, *Sulfolipid-1 Biosynthesis Restricts Mycobacterium tuberculosis Growth in Human Macrophages.* ACS Chemical Biology, 2012. **7**(5): p. 863–870.
19. Goren, M.B., P. D'Arcy Hart, M.R. Young, and J.A. Armstrong, *Prevention of phagosome-lysosome fusion in cultured macrophages by sulfatides of Mycobacterium tuberculosis.* Proceedings of the National Academy of Sciences, 1976. **73**(7): p. 2510–2514.
20. Pabst, M.J., J.M. Gross, J.P. Brozna, and M.B. Goren, *Inhibition of macrophage priming by sulfatide from Mycobacterium tuberculosis.* J Immunol, 1988. **140**(2): p. 634–40.
21. Brozna, J.P., M. Horan, J.M. Rademacher, K.M. Pabst, and M.J. Pabst, *Monocyte responses to sulfatide from Mycobacterium tuberculosis: inhibition of priming for enhanced release of superoxide, associated with increased secretion of interleukin-1 and tumor necrosis factor alpha, and altered protein phosphorylation.* Infect Immun, 1991. **59**(8): p. 2542–8.
22. Sachdeva, K., M. Goel, M. Sudhakar, M. Mehta, R. Raju, K. Raman, A. Singh, and V. Sundaramurthy, *Mycobacterium tuberculosis (Mtb) lipid mediated lysosomal rewiring in infected macrophages modulates intracellular Mtb trafficking and survival.* Journal of Biological Chemistry, 2020. **295**(27): p. 9192–9210.
23. Seeliger, J.C., C.M. Holsclaw, M.W. Schelle, Z. Botyanszki, S.A. Gilmore, S.E. Tully, M. Niederweis, B.F. Cravatt, J.A. Leary, and C.R. Bertozzi, *Elucidation and chemical modulation of sulfolipid-1 biosynthesis in Mycobacterium tuberculosis.* J Biol Chem, 2012. **287**(11): p. 7990–8000.
24. Umar, I., S.-e.-J. Gulzar, and V. Sundaramurthy, *M. tuberculosis surface sulfoglycolipid SL-1 activates the mechanosensitive channel TRPV4 to enhance lysosomal biogenesis and exocytosis in macrophages.* Molecular Biology of the Cell, 2025. **36**(6): p. ar76.
25. Sachdeva, K., M. Goel, M. Sudhakar, M. Mehta, R. Raju, K. Raman, A. Singh, and V. Sundaramurthy, *Mycobacterium tuberculosis (Mtb) lipid mediated lysosomal rewiring in*

infected macrophages modulates intracellular Mtb trafficking and survival. J Biol Chem, 2020. **295**(27): p. 9192–9210.

26. Ruhl, C.R., B.L. Pasko, H.S. Khan, L.M. Kindt, C.E. Stamm, L.H. Franco, C.C. Hsia, M. Zhou, C.R. Davis, T. Qin, L. Gautron, M.D. Burton, G.L. Mejia, D.K. Naik, G. Dussor, T.J. Price, and M.U. Shiloh, *Mycobacterium tuberculosis Sulfolipid-1 Activates Nociceptive Neurons and Induces Cough.* Cell, 2020. **181**(2): p. 293–305.e11.
27. Behr, M.A., P.H. Edelstein, and L. Ramakrishnan, *SLeuthing Tuberculous Cough.* Cell, 2020. **181**(2): p. 230–232.
28. Han, J., X. Liu, L. Zhang, R.J. Quinn, and Y. Feng, *Anti-mycobacterial natural products and mechanisms of action.* Natural Product Reports, 2022. **39**(1): p. 77–89.
29. Hatherley, R., D. Brown, T. Musyoka, D. Penkler, N. Faya, K. Lobb, and O. Tastan Bishop, *SANCDB: a South African natural compound database.* Journal of cheminformatics, 2015. **7**.
30. Atanasov, A.G., S.B. Zotchev, V.M. Dirsch, and C.T. Supuran, *Natural products in drug discovery: advances and opportunities.* Nat Rev Drug Discov, 2021. **20**(3): p. 200–216.
31. Cazzaniga, G., M. Mori, L.R. Chiarelli, A. Gelain, F. Meneghetti, and S. Villa, *Natural products against key Mycobacterium tuberculosis enzymatic targets: Emerging opportunities for drug discovery.* European Journal of Medicinal Chemistry, 2021. **224**: p. 113732.
32. Kumar, G. and A. C, *Natural products and their analogues acting against Mycobacterium tuberculosis: A recent update.* Drug Dev Res, 2023. **84**(5): p. 779–804.
33. Diallo, B.N., M. Glenister, T.M. Musyoka, K. Lobb, and Ö. Tastan Bishop, *SANCDB: an update on South African natural compounds and their readily available analogs.* J Cheminform, 2021. **13**(1): p. 37.
34. Sulyman, A.O., J. Fulcher, S. Crossley, A.A. Fatokun, and F.J. Olorunniji, *Shikonin and Juglone Inhibit Mycobacterium tuberculosis Low-Molecular-Weight Protein Tyrosine Phosphatase a (Mt-PTPa).* BioTech, 2023. **12**(3): p. 59.
35. Berman, H.M., J. Westbrook, Z. Feng, G. Gilliland, T.N. Bhat, H. Weissig, I.N. Shindyalov, and P.E. Bourne, *The Protein Data Bank.* Nucleic Acids Research, 2000. **28**(1): p. 235–242.
36. Pettersen, E.F., Goddard, T.D., Huang, C.C., Couch, G.S., Greenblatt, D.M., Meng, E.C., and Ferrin, T.E. , *UCSF Chimera - A Visualization System for Exploratory Research and Analysis.* J. Comput. Chem, 2004. **25**((13)): p. 1605–1612.
37. Sali, A. and T.L. Blundell, *Comparative protein modelling by satisfaction of spatial restraints.* J Mol Biol, 1993. **234**(3): p. 779–815.
38. Hanwell, M.D., D.E. Curtis, D.C. Lonie, T. Vandermeersch, E. Zurek, and G.R. Hutchison, *Avogadro: an advanced semantic chemical editor, visualization, and analysis platform.* Journal of Cheminformatics, 2012. **4**(1): p. 17.

39. Trott, O. and A.J. Olson, *AutoDock Vina: Improving the speed and accuracy of docking with a new scoring function, efficient optimization, and multithreading.* Journal of Computational Chemistry, 2010. **31**(2): p. 455–461.
40. Hassan, N.M., A.A. Alhossary, Y. Mu, and C.-K. Kwoh, *Protein-Ligand Blind Docking Using QuickVina-W With Inter-Process Spatio-Temporal Integration.* Scientific Reports, 2017. **7**(1): p. 15451.
41. Zhang, Y., M. Luo, P. Wu, S. Wu, T.-Y. Lee, and C. Bai, *Application of Computational Biology and Artificial Intelligence in Drug Design.* International Journal of Molecular Sciences, 2022. **23**(21): p. 13568.
42. Sarthak Pal1 , M.C., Kanishak Kala3, *Autodock & Autodock Vina: Development, Capabilities, & Applications*

in Molecular Docking. International Journal of Pharmaceutical Sciences, 2025. **3**(5): p. 3005–3019.
43. Fuhrmann, J., A. Rurainski, H.-P. Lenhof, and D. Neumann, *A new Lamarckian genetic algorithm for flexible ligand-receptor docking.* Journal of Computational Chemistry, 2010. **31**(9): p. 1911–1918.
44. Martis, E.A.F. and S. Téletchéa, *Ten quick tips to perform meaningful and reproducible molecular docking calculations.* PLoS Comput Biol, 2025. **21**(5): p. e1013030.
45. Jubb, H.C., A.P. Higueruelo, B. Ochoa-Montaño, W.R. Pitt, D.B. Ascher, and T.L. Blundell, *Arpeggio: A Web Server for Calculating and Visualising Interatomic Interactions in Protein Structures.* J Mol Biol, 2017. **429**(3): p. 365–371.
46. Cock, P.J., T. Antao, J.T. Chang, B.A. Chapman, C.J. Cox, A. Dalke, I. Friedberg, T. Hamelryck, F. Kauff, B. Wilczynski, and M.J. de Hoon, *Biopython: freely available Python tools for computational molecular biology and bioinformatics.* Bioinformatics, 2009. **25**(11): p. 1422–3.
47. O'Boyle, N.M., M. Banck, C.A. James, C. Morley, T. Vandermeersch, and G.R. Hutchison, *Open Babel: An open chemical toolbox.* J Cheminform, 2011. **3**: p. 33.
48. DeLano, W.L., *PyMOL: An Open-Source Molecular Graphics Tool.* CCP4 Newsletter on Protein Crystallography, 2002. **40**: p. 82–92.
49. Arslan, N., *Molecular Docking Study of Four Chromene Derivatives as Novel HIV-1 Integrase Inhibitors.* Journal of the Turkish Chemical Society, Section A: Chemistry, 2019. **6**: p. 133–142.
50. Case, D., I. Ben-Shalom, S.R. Brozell, D.S. Cerutti, T. Cheatham, V.W.D. Cruzeiro, T. Darden, R. Duke, D. Ghoreishi, M. Gilson, H. Gohlke, A. Götz, D. Greene, R. Harris, N. Homeyer, Y. Huang, S. Izadi, A. Kovalenko, T. Kurtzman, and P.A. Kollman, *Amber 2018*. 2018.
51. Gordon, J.C., J.B. Myers, T. Folta, V. Shoja, L.S. Heath, and A. Onufriev, *H++: a server for estimating p Ka s and adding missing hydrogens to macromolecules.* Nucleic Acids Research, 2005. **33**(suppl_2): p. W368–W371.

52. Maier, J.A., C. Martinez, K. Kasavajhala, L. Wickstrom, K.E. Hauser, and C. Simmerling, *ff14SB: Improving the Accuracy of Protein Side Chain and Backbone Parameters from ff99SB.* Journal of Chemical Theory and Computation, 2015. **11**(8): p. 3696–3713.
53. Wang, J., R.M. Wolf, J.W. Caldwell, P.A. Kollman, and D.A. Case, *Development and testing of a general amber force field.* J Comput Chem, 2004. **25**(9): p. 1157–74.
54. Wang, J., W. Wang, P. Kollman, and D. Case, *ANTECHAMBER: an accessory software package for molecular mechanical calculations.* Journal of Chemical Information and Computer Sciences - JCISD, 2000. **222**.
55. Jorgensen, W.L., J. Chandrasekhar, J.D. Madura, R.W. Impey, and M.L. Klein, *Comparison of simple potential functions for simulating liquid water.* The Journal of Chemical Physics, 1983. **79**(2): p. 926–935.
56. Petersen, H.G., *Accuracy and efficiency of the particle mesh Ewald method.* The Journal of Chemical Physics, 1995. **103**(9): p. 3668–3679.
57. Ryckaert, J.-P., G. Ciccotti, and H. Berendsen, *Numerical Integration of the Cartesian Equations of Motion of a System with Constraints: Molecular Dynamics of n-Alkenes.* J. Comp. Phys., 1976. **23**: p. 327–341.
58. Yan, F., X. Liu, S. Zhang, Q. Zhang, and J. Chen, *Understanding conformational diversity of heat shock protein 90 (HSP90) and binding features of inhibitors to HSP90 via molecular dynamics simulations.* Chemical Biology & Drug Design, 2019. **95**: p. 87–103.
59. Davidchack, R., R. Handel, and M. Tretyakov, *Langevin thermostat for rigid body dynamics.* The Journal of chemical physics, 2009. **130**: p. 234101.
60. Pan, D., J. Li, L.X. Zhang, and S. Xueming, *Application of Berendsen barostat in dissipative particle dynamics for nonequilibrium dynamic simulation.* The Journal of Chemical Physics, 2017. **146**: p. 124108.
61. Roe, D.R. and T.E. Cheatham, 3rd, *PTRAJ and CPPTRAJ: Software for Processing and Analysis of Molecular Dynamics Trajectory Data.* J Chem Theory Comput, 2013. **9**(7): p. 3084–95.
62. Jain, A.N., *Bias, reporting, and sharing: computational evaluations of docking methods.* Journal of Computer-Aided Molecular Design, 2008. **22**(3): p. 201–212.
63. Amaro, R.E., J. Baudry, J. Chodera, Ö. Demir, J.A. McCammon, Y. Miao, and J.C. Smith, *Ensemble Docking in Drug Discovery.* Biophysical Journal, 2018. **114**(10): p. 2271–2278.
64. Maia, E.H.B., L.C. Assis, T.A. de Oliveira, A.M. da Silva, and A.G. Taranto, *Structure-Based Virtual Screening: From Classical to Artificial Intelligence.* Frontiers in Chemistry, 2020. **Volume 8 - 2020**.
65. Saenz-Méndez, P., S. Genheden, A. Reymer, and L. Eriksson, *Computational Chemistry and Molecular Modelling Basics*. 2017. p. 1–38.
66. Lobanov, M.Y., N.S. Bogatyreva, and O.V. Galzitskaya, *Radius of gyration as an indicator of protein structure compactness.* Molecular Biology, 2008. **42**(4): p. 623–628.

67. Genheden, S., A. Reymer, P. Saenz-Méndez, and L.A. Eriksson, *Computational Chemistry and Molecular Modelling Basics*, in *Computational Tools for Chemical Biology*, S. Martín-Santamaría, Editor. 2017, The Royal Society of Chemistry. p. 0.
68. Srinivasan, J., T.E. Cheatham, P. Cieplak, P.A. Kollman, and D.A. Case, *Continuum Solvent Studies of the Stability of DNA, RNA, and Phosphoramidate−DNA Helices.* Journal of the American Chemical Society, 1998. **120**(37): p. 9401–9409.
69. Genheden, S. and U. Ryde, *The MM/PBSA and MM/GBSA methods to estimate ligand-binding affinities.* Expert Opin Drug Discov, 2015. **10**(5): p. 449–61.
70. Wang, C., P.H. Nguyen, K. Pham, D. Huynh, T.B.N. Le, H. Wang, P. Ren, and R. Luo, *Calculating protein–ligand binding affinities with MMPBSA: Method and error analysis.* Journal of Computational Chemistry, 2016. **37**(27): p. 2436–2446.
71. Chaudhary, N. and P. Aparoy, *Application of per-residue energy decomposition to identify the set of amino acids critical for in silico prediction of COX-2 inhibitory activity.* Heliyon, 2020. **6**(10): p. e04944.
72. Halder, A. and B. Honarparvar, *Molecular alteration in drug susceptibility against subtype B and C-SA HIV-1 proteases: MD study.* Structural Chemistry, 2019. **30**.
73. Case, D.A., H.M. Aktulga, K. Belfon, D.S. Cerutti, G.A. Cisneros, V.W.D. Cruzeiro, N. Forouzesh, T.J. Giese, A.W. Götz, H. Gohlke, S. Izadi, K. Kasavajhala, M.C. Kaymak, E. King, T. Kurtzman, T.-S. Lee, P. Li, J. Liu, T. Luchko, . . . K.M. Merz, Jr., *AmberTools.* Journal of Chemical Information and Modeling, 2023. **63**(20): p. 6183–6191.
74. Daina, A., O. Michielin, and V. Zoete, *SwissADME: a free web tool to evaluate pharmacokinetics, drug-likeness and medicinal chemistry friendliness of small molecules.* Scientific Reports, 2017. **7**(1): p. 42717.
75. Knox, C., M. Wilson, C.M. Klinger, M. Franklin, E. Oler, A. Wilson, A. Pon, J. Cox, N.E.L. Chin, S.A. Strawbridge, M. Garcia-Patino, R. Kruger, A. Sivakumaran, S. Sanford, R. Doshi, N. Khetarpal, O. Fatokun, D. Doucet, A. Zubkowski, . . . D.S. Wishart, *DrugBank 6.0: the DrugBank Knowledgebase for 2024.* Nucleic Acids Res, 2024. **52**(D1): p. D1265–d1275.
76. Banerjee, P., E. Kemmler, M. Dunkel, and R. Preissner, *ProTox 3.0: a webserver for the prediction of toxicity of chemicals.* Nucleic Acids Res, 2024. **52**(W1): p. W513–w520.
77. Njue, A.W., J. Omolo, M.K. Langat, D. A. Mulholland, and N.M. Kimani, *Ergostanes and Cytochalasin From the Fruiting Bodies of Xylaria longipes Nitschke and Their Cytotoxicity Evaluation.* Journal of Chemistry, 2026. **2026**(1): p. 2027635.
78. Shukla, R. and T.R. Singh, *High-throughput screening of natural compounds and inhibition of a major therapeutic target HsGSK-3β for Alzheimer's disease using computational approaches.* Journal of Genetic Engineering and Biotechnology, 2021. **19**(1): p. 61.
79. Bolivar Avila, S., *Validation of Docking Methodology (Redocking)*. 2024.

80. Sousa, S.F., P.A. Fernandes, and M.J. Ramos, *Protein-ligand docking: current status and future challenges.* Proteins, 2006. **65**(1): p. 15–26.
81. Mativandlela, S.P., J.J. Meyer, A.A. Hussein, P.J. Houghton, C.J. Hamilton, and N. Lall, *Activity against Mycobacterium smegmatis and M. tuberculosis by extract of South African medicinal plants.* Phytother Res, 2008. **22**(6): p. 841–5.
82. Mativandlela, S.P.N., T. Muthivhi, H. Kikuchi, Y. Oshima, C. Hamilton, A.A. Hussein, M.L. van der Walt, P.J. Houghton, and N. Lall, *Antimycobacterial Flavonoids from the Leaf Extract of Galenia africana.* Journal of Natural Products, 2009. **72**(12): p. 2169–2171.
83. Masoko, P., I.H. Mabusa, and R.L. Howard, *Isolation of alpha-linolenic acid from Sutherlandia frutescens and its inhibition of Mycobacterium tuberculosis' shikimate kinase enzyme.* BMC Complementary and Alternative Medicine, 2016. **16**(1): p. 366.
84. Saravanakumar, D.E.M., P.I. Folb, B.W. Campbell, and P. Smith, *Antimycobacterial Activity of the Red Alga Polysiphonia virgata.* Pharmaceutical Biology, 2008. **46**(4): p. 254–260.
85. Case, D.A., H.M. Aktulga, K. Belfon, D.S. Cerutti, G.A. Cisneros, V.W.D. Cruzeiro, N. Forouzesh, T.J. Giese, A.W. Götz, H. Gohlke, S. Izadi, K. Kasavajhala, M.C. Kaymak, E. King, T. Kurtzman, T.S. Lee, P. Li, J. Liu, T. Luchko, . . . K.M. Merz, Jr., *AmberTools.* J Chem Inf Model, 2023. **63**(20): p. 6183–6191.
86. Bosshard, H.R., D.N. Marti, and I. Jelesarov, *Protein stabilization by salt bridges: concepts, experimental approaches and clarification of some misunderstandings.* J Mol Recognit, 2004. **17**(1): p. 1–16.
87. Nene, T., D. Basumatary, M. Yadav, and H. Yadav, *Electrostatic and Van Der Waals Forces*. 2021. p. 55–89.
88. Reva, B.A., A.V. Finkelstein, and J. Skolnick, *What is the probability of a chance prediction of a protein structure with an rmsd of 6 å?* Folding and Design, 1998. **3**(2): p. 141–147.
89. Wang, L., B.J. Berne, and R.A. Friesner, *Ligand binding to protein-binding pockets with wet and dry regions.* Proc Natl Acad Sci U S A, 2011. **108**(4): p. 1326–30.
90. Erman, B., *Effects of ligand binding upon flexibility of proteins.* Proteins, 2015. **83**(5): p. 805–8.
91. Hussain, T., S. Ullah, S. Alrokayan, S. Alamery, A.A. Mohammed, S.A. Ejaz, M. Aziz, and J. Iqbal, *Synthesis, characterization and biological evaluation of pyrazole-based benzene sulfonamides as inhibitors of human carbonic anhydrase II, IX and XII.* RSC Advances, 2023. **13**(27): p. 18461–18479.
92. Hollingsworth, S.A. and R.O. Dror, *Molecular Dynamics Simulation for All.* Neuron, 2018. **99**(6): p. 1129–1143.
93. Patil, R., S. Das, A. Stanley, L. Yadav, A. Sudhakar, and A.K. Varma, *Optimized Hydrophobic Interactions and Hydrogen Bonding at the Target-Ligand Interface Leads the Pathways of Drug-Designing.* PLoS ONE, 2010. **5**(8): p. e12029.

94. Takano, K., K. Tsuchimori, Y. Yamagata, and K. Yutani, *Contribution of salt bridges near the surface of a protein to the conformational stability.* Biochemistry, 2000. **39**(40): p. 12375–81.
95. Klebe, G., *Protein–Ligand Interactions as the Basis for Drug Action*, in *Drug Design: Methodology, Concepts, and Mode-of-Action*, G. Klebe, Editor. 2013, Springer Berlin Heidelberg: Berlin, Heidelberg. p. 61–88.
96. Amirabadi, D.G., *Understanding the Radius of Gyration in Protein Design & Bioinformatics*. 2024: neurosnap.
97. Lobanov, M., N. Bogatyreva, and O. Galzitskaya, *Radius of gyration as an indicator of protein structure compactness.* Mol Biol, 2008. **42**: p. 623–628.
98. Adelusi, T.I., A.-Q.K. Oyedele, I.D. Boyenle, A.T. Ogunlana, R.O. Adeyemi, C.D. Ukachi, M.O. Idris, O.T. Olaoba, I.O. Adedotun, O.E. Kolawole, Y. Xiaoxing, and M. Abdul-Hammed, *Molecular modeling in drug discovery.* Informatics in Medicine Unlocked, 2022. **29**: p. 100880.
99. Yan, F., X. Liu, S. Zhang, J. Su, Q. Zhang, and J. Chen, *Binding difference of inhibitors ACD and TDZ to A-FABP revealed by molecular dynamics simulations.* Journal of Atomic and Molecular Sciences, 2018. **8**: p. 97–104.
100. Yan, M., M. Ma, R. Chen, Y. Cao, W. Zhang, and X. Liu, *Structural basis for the development of potential inhibitors targeting FadD23 from Mycobacterium tuberculosis.* Acta Crystallogr F Struct Biol Commun, 2023. **79**(Pt 8): p. 208–216.
101. Teague, S., *Teague, S.J. Implications of protein flexibility for drug discovery. Nat. Rev. Drug Discov. 2, 527−541.* Nature reviews. Drug discovery, 2003. **2**: p. 527–41.
102. Christopher Barnett, T.S., Simon Bray, Nadia Goué. *Analysis of molecular dynamics simulations (Galaxy Training Materials).* 2025 [cited 2025 30/05]; Available from: https://training.galaxyproject.org/training-material/topics/computational-chemistry/tutorials/analysis-md-simulations/tutorial.html.
103. Patel, K., *Chapter 1 - Structural organization of peptides*, in *De Novo Peptide Design*, V. Ramakrishnan, K. Patel, and R. Goyal, Editors. 2023, Academic Press. p. 1–33.
104. Shah, T.R. and A. Misra, *8 - Proteomics*, in *Challenges in Delivery of Therapeutic Genomics and Proteomics*, A. Misra, Editor. 2011, Elsevier: London. p. 387–427.
105. Hubbard, R.E. and M. Kamran Haider, *Hydrogen Bonds in Proteins: Role and Strength*, in *eLS*.
106. Jeffrey, G.A., *An Introduction to Hydrogen Bonding*. 1997: Oxford University Press.
107. Reeb, J. and B. Rost, *Secondary Structure Prediction*, in *Encyclopedia of Bioinformatics and Computational Biology*, S. Ranganathan, et al., Editors. 2019, Academic Press: Oxford. p. 488–496.
108. Lipinski, C., F. Lombardo, B.W. Dominy, and P.J. Feeney, *Experimental and computational approaches to estimate solubility and permeability in drug discovery and development settings.* Adv. Drug Delivery Rev., 1997. **3**: p. 23–25.

109. Veber, D.F., S.R. Johnson, H.-Y. Cheng, B.R. Smith, K.W. Ward, and K.D. Kopple, *Molecular Properties That Influence the Oral Bioavailability of Drug Candidates.* Journal of Medicinal Chemistry, 2002. **45**(12): p. 2615–2623.

Supplementary Information

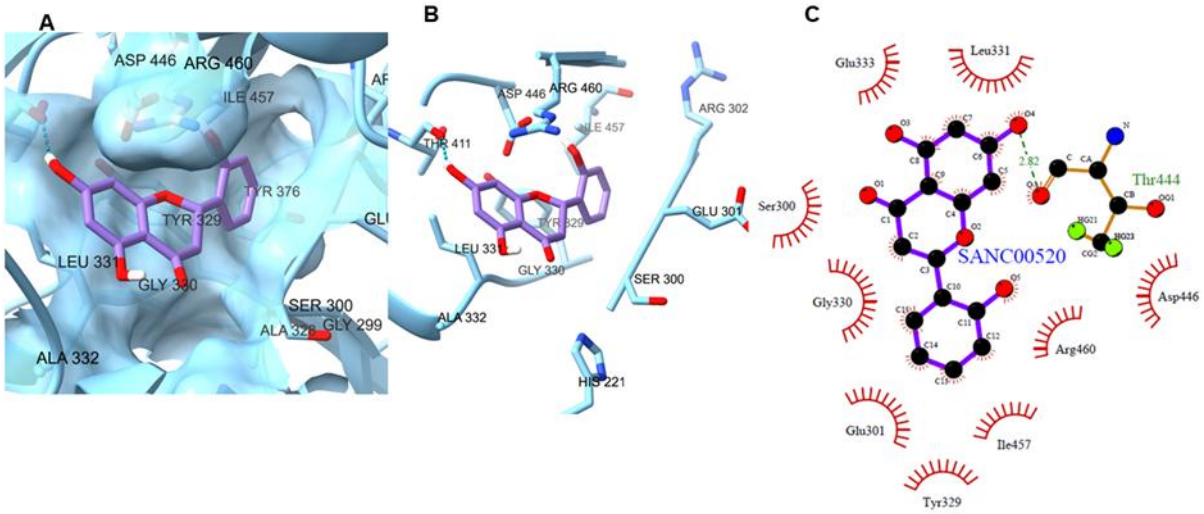

Figure S.0.1: A depiction of SANC00520 docked to FadD23 ANP binding site. **A** shows 3D conformation of the ligand (purple) in the ANP binding pocket presented with a surface; **B** shows h-bondformation between the ligand and Thr 444; and **C** shows ligand interaction with binding pocket residues – h-bondformation with Thr 444 and hydrophobic interactions with other residues within a 4 Å radius of the ligand.

.

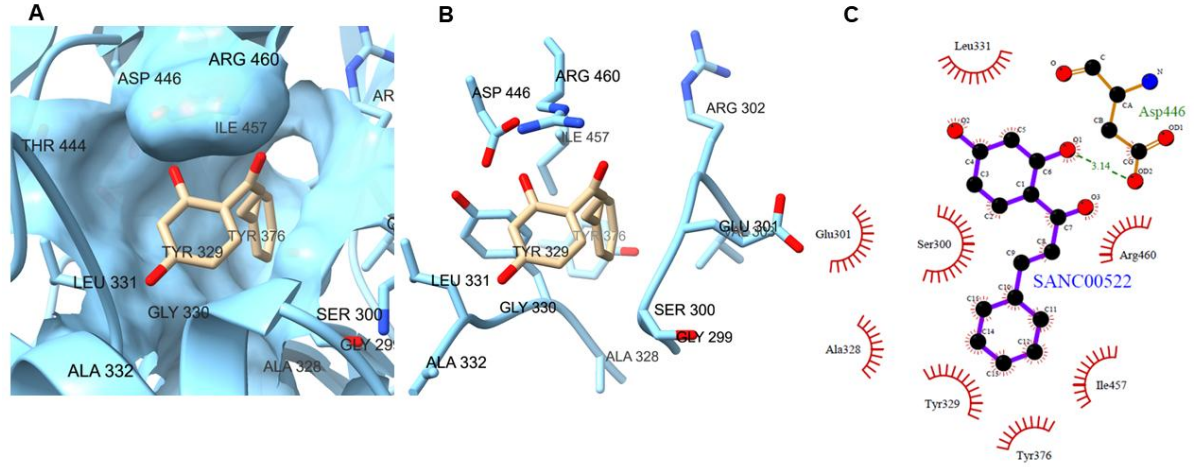

Figure S.0.2: A depiction of SANC00522 docked to FadD23 ANP binding site. **A** shows 3D conformation of the ligand (tan) in the ANP binding pocket presented with a surface; **B** shows the ligand and surrounding residues; and **C** shows ligand interaction with binding pocket residues – h-bondformation with Asp 446, and hydrophobic interactions with other residues within a 4 Å radius of the ligand.

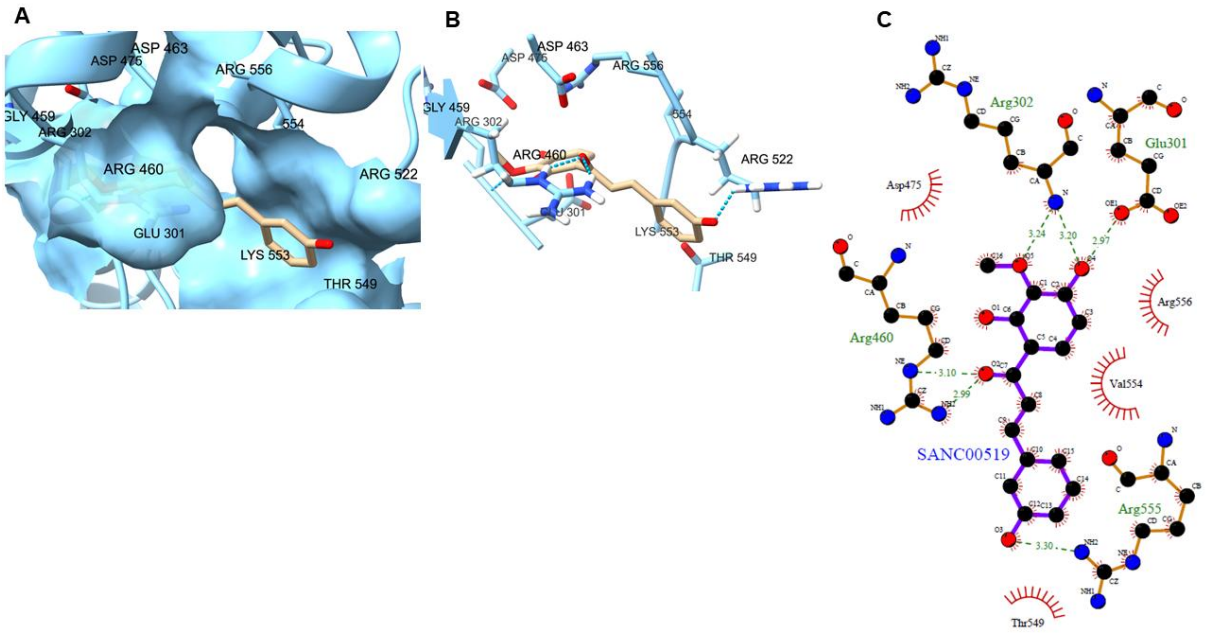

Figure S.0.3: A depiction of SANC00519 docked to FadD23 ANP binding site. **A** shows 3D conformation of the ligand (tan) in the ANP binding pocket presented with a surface; **B** shows the ligand and possible h-bondformation with Arg 522, Arg 460 and Arg 302; **C** shows ligand h-bondformation with Arg 460, Arg 302, Glu 301 and Arg 555; ligand hydrophobic interactions with residues Asp 475, Arg 556, Val 554, and Thr549.

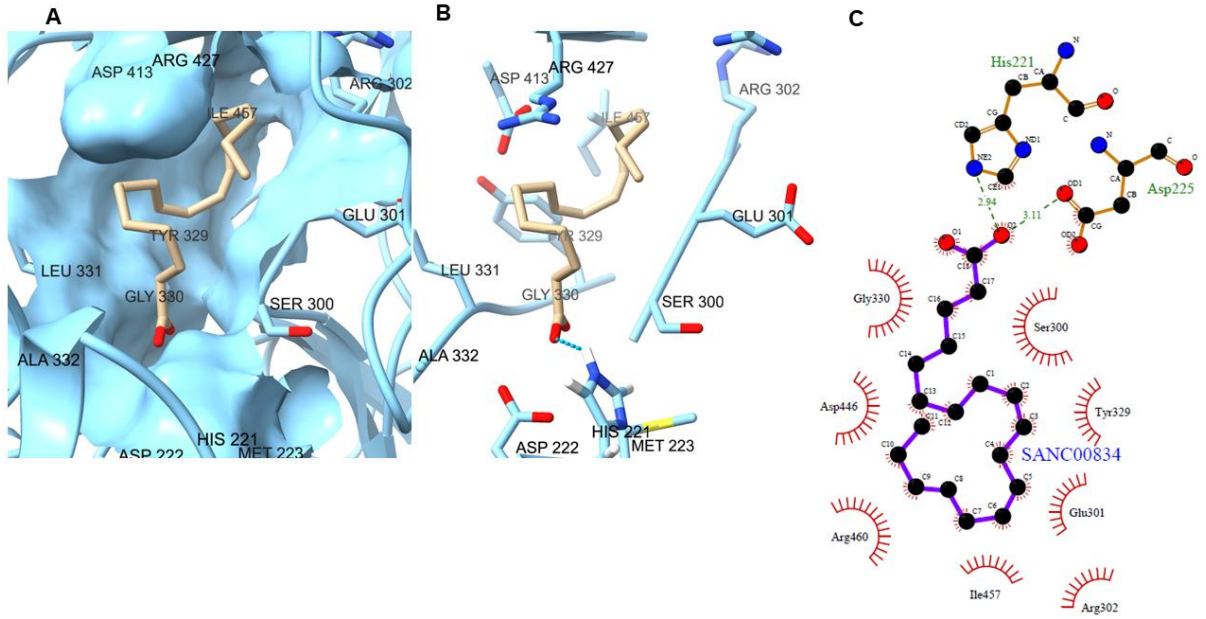

Figure S.0.4: A depiction of SANC00834 docked to FadD23 ANP binding site. **A** shows 3D conformation of the ligand (tan) in the ANP binding pocket presented with a surface; **B** possible h-bondformation between ligand and His 221; **C** shows ligand h-bondformation with His 221 and Asp

225; ligand hydrophobic interactions with Gly 330, Asp 446, Arg 460, Ile 457, Arg 302, Glu 301, Tyr 329 and Ser 300.

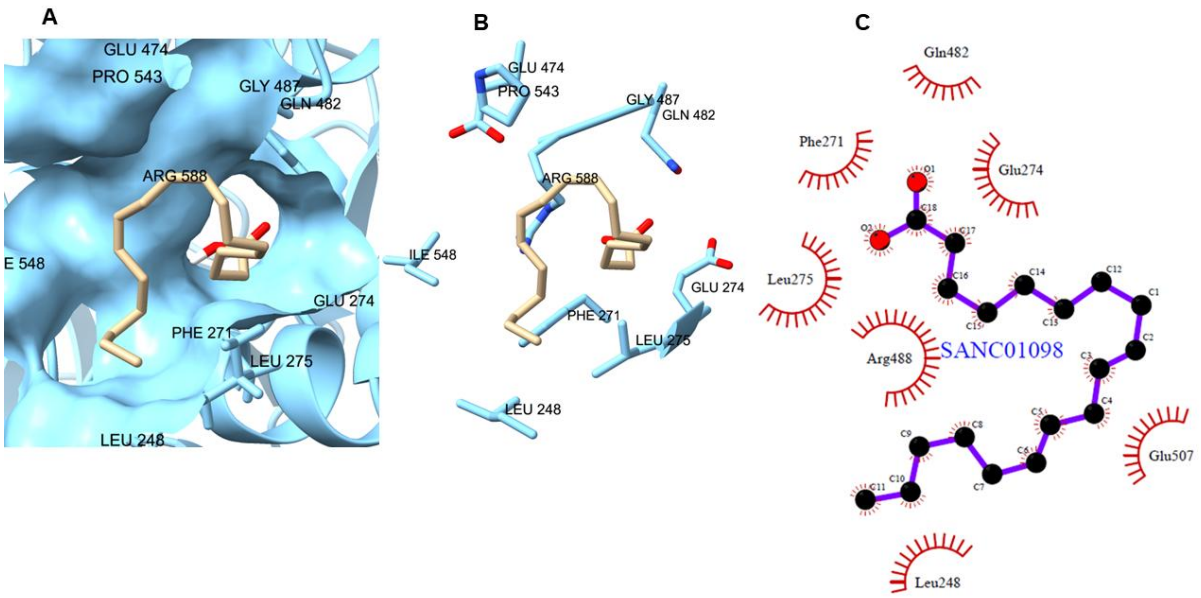

Figure S.0.5: A depiction of SANC01098 docked to FadD23 surface. **A** shows ligand conformation bound adjacent to ANP binding site; **B** ligand surrounded by binding site residues; **C** ligplot showing hydrophobic interactions between ligand and residues within a 4 Å radius of the ligand.

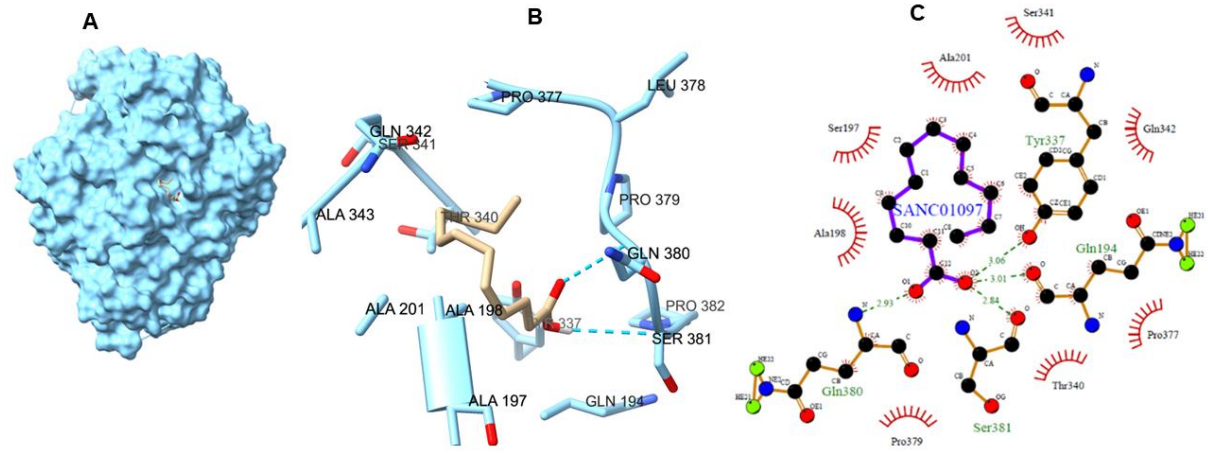

Figure S.0.6: A depiction of SANC01097 docked to FadD23 surface. **A** shows ligand conformation bound at the back of the protein, behind the ANP binding site; **B** possible h-bondformation between ligand and Ser 381 and Gln 380; **C** ligplot showing ligand h-bondformation with Gln 380, Ser 381, Gln

194 and Tyr 342; hydrophobic interactions between ligand and Ala 198, Al 201, Ser 341, Gln 342, Pro 377, Thr 340 and Pro 379.

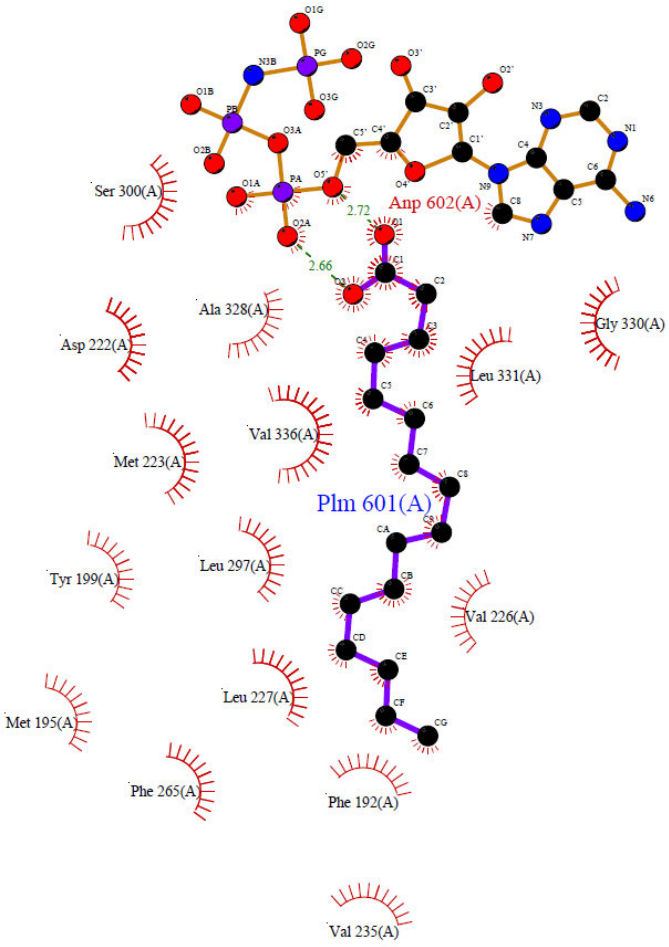

Figure S.0.7: Ligplot image presenting ANP and PLM interaction with residues in the ATP binding site of FadD23 [17].

Table S0.1: Per-residue decomposition analysis of the FadD23-SANC00937 system over a 130 ns trajectory.

Residue	ΔE_{vdw}	ΔE_{ele}	ΔG_{polar}	$\Delta G_{non\text{-}polar}$	ΔG_{total}
GLN 174	-0.034±0.035	0.093±0.124	-0.044 ± 0.123	-0.000 ± 0.002	0.014±0.048
ASP 222	0.134±1.009	-5.610±4.676	5.781 ± 3.802	-0.143 ± 0.039	0.162±0.628
CYS 298	-0.152±0.051	-0.617±0.230	0.694 ± 0.220	-0.002 ± 0.003	-0.078±0.075
SER 300	-2.404±0.315	-0.788±0.477	1.485 ± 0.466	-0.311 ± 0.054	-2.017±0.450
GLU 301	-2.140±0.406	1.500±0.936	-0.423 ± 0.742	-0.150 ± 0.027	-1.214±0.427
ALA 328	0.412±0.680	-4.041±1.281	1.855 ± 0.474	-0.036 ± 0.013	-1.811±0.635
GLY 330	-1.130±0.434	-0.049±0.661	0.946 ± 0.416	-0.138 ± 0.031	-0.372±0.596
ALA 332	-0.320±0.224	0.071±0.238	0.034 ± 0.219	-0.023 ± 0.023	-0.238±0.204
GLU 330	-0.066±0.051	0.451±0.617	-0.287 ± 0.577	-0.001 ± 0.007	0.097±0.063
VAL 336	-0.416± 0.285	0.244±0.860	-0.076 ± 0.408	-0.044 ± 0.028	-0.292±0.427
ARG 460	-0.454±0.513	-1.536±1.451	1.787 ± 1.517	-0.113 ± 0.113	-0.315±0.442
LYS 553	-0.160±0.130	-2.182±1.255	2.528 ± 1.370	-0.048 ± 0.051	0.138±0.236

Table S0.2: Per-residue decomposition analysis of the FadD23-ANP system over a 130 ns trajectory.

Residue	ΔE_{vdw}	ΔE_{ele}	ΔG_{polar}	$\Delta G_{non\text{-}polar}$	ΔG_{total}
THR 176	-0.769 ± 0.428	4.124 ± 3.176	-3.726 ± 2.310	-0.162 ± 0.055	-0.533 ± 1.190
THR 177	-0.229 ± 0.115	-2.155 ± 1.790	2.011 ± 1.656	-0.011 ± 0.015	-0.384 ± 0.276
CYS 298	-0.180 ± 0.095	-0.428 ± 0.789	0.417 ± 0.770	-0.004 ± 0.005	-0.195 ± 0.148
SER 300	-2.211 ± 0.598	2.926 ± 3.001	-2.242 ± 2.428	-0.242 ± 0.073	-1.768 ± 1.116
GLU 301	-1.733 ± 0.529	67.090 ± 4.390	-66.096 ± 4.105	-0.099 ± 0.049	-0.838 ± 0.736
ALA 328	-0.291 ± 0.318	1.849 ± 0.574	-1.721 ± 0.376	-0.019 ± 0.015	-0.181 ± 0.337
TYR 329	-2.027 ± 0.575	-5.814 ± 0.648	5.677 ± 0.456	-0.162 ± 0.030	-2.327 ± 0.752
GLY 330	-0.582 ± 0.328	2.683 ± 0.480	-2.303 ± 0.467	-0.086 ± 0.039	-0.288 ± 0.317
TYR 376	-0.304 ± 0.269	-2.175 ± 1.743	2.091 ± 1.104	-0.063 ± 0.028	-0.452 ± 0.709

ASP 446	-0.171 ± 0.676	65.814 ± 3.425	-64.186 ± 2.827	-0.078 ± 0.024	1.379 ± 0.813
ILE 457	-1.172 ± 0.559	-0.539 ± 0.655	0.586 ± 0.594	-0.107 ± 0.048	-1.232 ± 0.565
ARG 460	-0.951 ± 1.186	-139.804 ± 4.930	122.044 ± 2.814	-0.024 ± 0.023	-19.258 ± 2.758
ASP 466	-0.275 ± 0.102	82.563 ± 6.172	-80.629 ± 5.525	-0.024 ± 0.023	1.635 ± 0.714
ASP 475	-0.147 ± 0.114	65.344 ± 4.124	-64.521 ± 3.888	-0.011 ± 0.023	0.665 ± 0.226
VAL 554	-0.154 ± 0.129	6.528 ± 1.759	-6.152 ± 1.346	-0.011 ± 0.016	0.212 ± 0.372
ARG 555	-0.260 ± 0.366	-68.386 ± 14.742	67.629 ±13.375	-0.055 ± 0.084	-1.072 ± 1.890

Table S0.3: H-bond interactions between FadD23 and ligand SANC00937.

#Acceptor	Donor H	Donor	Frames	Probability (%)	$Dist_{avg}$ (Å)	Ang_{avg} (°)	$Lifetime_{max}$
ALA_328@O	LIG@H	LIG@O2	115937	89.18	2.6859	160.4306	230
ASP_222@OD2	LIG@H2	LIG@O4	43625	33.56	2.6358	164.2718	1040
ASP_222@OD1	LIG@H2	LIG@O4	35738	27.49	2.6416	164.1602	510
VAL_336@O	LIG@H2	LIG@O4	4047	3.11	2.7443	155.0090	93
GLY_330@O	LIG@H	LIG@O2	2440	1.88	2.7687	146.0545	15
LIG@O	ARG_460@HH12	ARG_460@NH1	1335	1.03	2.8392	151.6813	15
ASP_222@OD2	LIG@H1	LIG@O3	1322	1.02	2.6587	164.8752	110
ASP_222@OD1	LIG@H1	LIG@O3	1235	0.95	2.6557	164.7141	109
LIG@O2	GLU_301@H	GLU_301@N	968	0.74	2.9220	142.4814	3
LIG@O2	GLY_330@H	GLY_330@N	638	0.49	2.9264	152.3602	5
LIG@O	ARG_460@HH22	ARG_460@NH2	582	0.45	2.8463	152.5051	12
LIG@O3	ARG_460@HH12	ARG_460@NH1	295	0.23	2.8872	148.2106	5
LIG@O4	SER_300@HG	SER_300@OG	151	0.12	2.8912	159.9209	4
LIG@O2	SER_300@H	SER_300@N	98	0.08	2.9174	143.4670	3
LIG@O3	ARG_460@HH22	ARG_460@NH2	62	0.05	2.9060	150.7839	4
LIG@O	ARG_460@HH11	ARG_460@NH1	60	0.05	2.8743	156.3737	5
GLY_330@O	LIG@H2	LIG@O4	40	0.03	2.8092	161.4955	5
LIG@O	LYS_553@HZ3	LYS_553@NZ	36	0.03	2.8525	147.7108	9
GLU_333@OE2	LIG@H1	LIG@O3	27	0.02	2.7464	162.0846	14
GLU_301@O	LIG@H	LIG@O2	24	0.02	2.7978	149.1585	2
GLU_301@OE1	LIG@H1	LIG@O3	21	0.02	2.7344	157.5157	5
LIG@O	LYS_553@HZ2	LYS_553@NZ	15	0.01	2.8675	143.0988	2
LIG@O	LYS_553@HZ1	LYS_553@NZ	12	0.01	2.8920	144.1042	2

LIG@O1	SER_300@H	SER_300@N	12	0.01	2.9218	144.5576	1
LIG@O4	ALA_332@H	ALA_332@N	11	0.01	2.9357	141.9973	1
ASP_222@O	LIG@H2	LIG@O4	9	0.01	2.8563	159.5693	3
LIG@O3	LYS_553@HZ3	LYS_553@NZ	9	0.01	2.9455	140.9214	1
LIG@O4	GLN_174@HE21	GLN_174@NE2	8	0.01	2.9051	147.0266	1
LIG@O3	LYS_553@HZ2	LYS_553@NZ	7	0.01	2.9226	144.1158	1
LIG@O3	ALA_332@H	ALA_332@N	7	0.01	2.9255	153.8247	1
LIG@O1	GLY_330@H	GLY_330@N	7	0.01	2.9363	145.1536	1
LIG@O3	LYS_553@HZ1	LYS_553@NZ	5	0.00	2.9262	146.5282	1
SER_300@O	LIG@H1	LIG@O3	3	0.00	2.8456	144.3501	1
GLU_301@OE2	LIG@H1	LIG@O3	2	0.00	2.9210	160.1411	1
CYS_298@O	LIG@H	LIG@O2	1	0.00	2.8909	161.9290	1

Table S0.4: H-bond interactions between FadD23 and ligand ANP over 130ns.

#Acceptor	Donor H	Donor	Frames	Probability (%)	$Dist_{avg}$ (Å)	Ang_{avg} (°)	$Lifetime_{max}$
ANP_540@O1B	ARG_427@HH22	ARG_427@NH2	528150	88.02	2.7919	162.2028	729
ANP_540@O2B	ARG_427@HH12	ARG_427@NH1	450773	75.13	2.7517	162.6186	994
ASP_413@OD2	ANP_540@HO2'	ANP_540@O2'	359512	59.92	2.6958	165.4009	1131
ASP_413@OD1	ANP_540@HO2'	ANP_540@O2'	157608	26. 7	2.7071	163.6116	508
ANP_540@O1B	ARG_427@HH12	ARG_427@NH1	118983	19.83	2.8326	149.7171	169

Table S0.5: The average h-bond distance between key residues of FadD23

H-BOND	Average Distance (Å)
Ala 328_O-H_O2_SANC00937	2.80
Ala 328_O-H62_N6_ANP	3.00
Arg 460_NH1_HH12-O_SANC00937	7.81
Arg 460_NH1_HH12-O3A_ANP	2.16
LYS 553_NZ_HZ3-O_SANC00937	5.75
LYS 553_NZ_HZ1-O2B_ANP	4.63
Asp 222_OD2-H2_O4_SANC00937	3.93

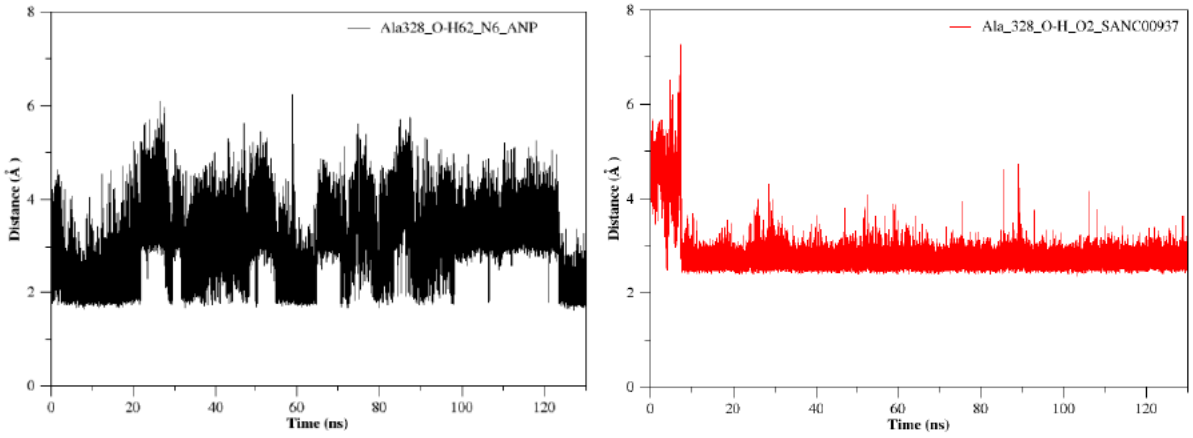

Figure S.0.8: Graphical representation of the h-bond distance between Ala_328_O-H_O2_SANC00937 (red) and Ala328_O-H62_N6_ANP (black) over 130 ns.

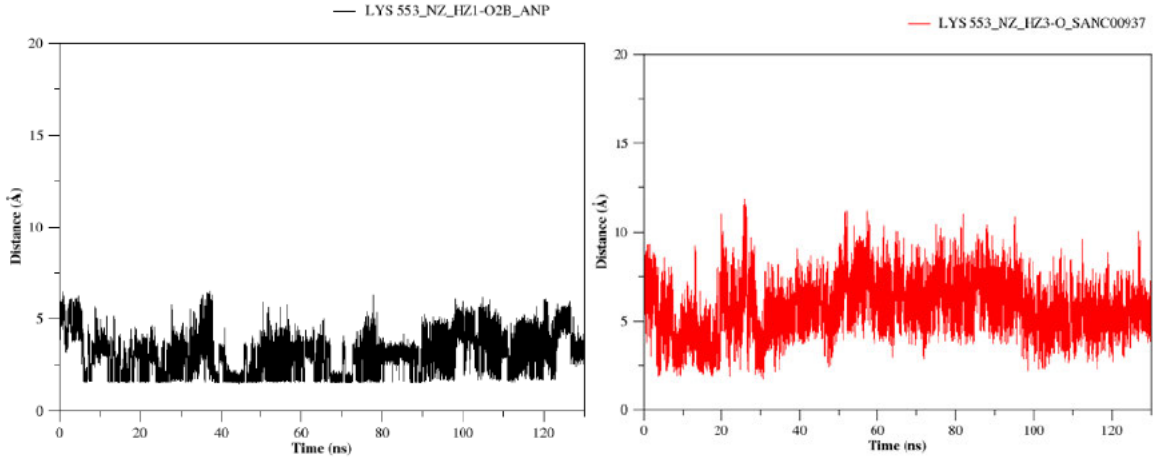

Figure S.0.9: Graphical analysis of the h-bonddistance between LYS 553_NZ_HZ1-O2B_ANP (black) and LYS 553_NZ_HZ3-O_SANC00937 (red) over 130 ns.